Shock compression of water and solutions of ammonium nitrate

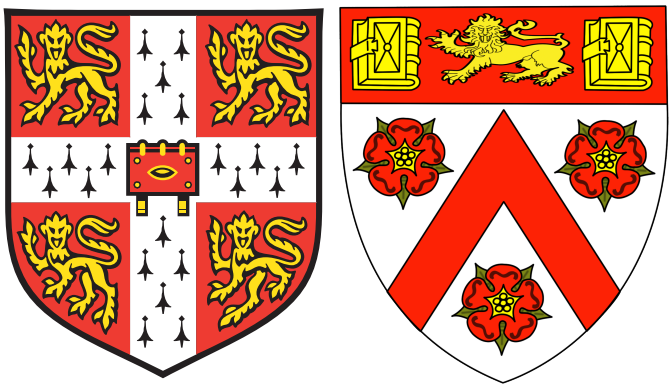

Michael James Morley
Trinity College
&
Fracture and Shock Physics, Cavendish Laboratory
University of Cambridge

A Thesis Submitted for the Degree of Doctor of Philosophy
June 2011

SHOCK COMPRESSION OF WATER AND SOLUTIONS OF AMMONIUM NITRATE

Michael James Morley

Modern mining explosives employ solutions of ammonium nitrate, where the solution is the oxidising component of a fuel/oxidiser mixture. This thesis is primarily concerned with the shock response of water and of aqueous solutions of ammonium nitrate. Of particular interest are the temperatures induced through shock compression. An experimental facility, using a single-stage gas gun in the 'plate impact' configuration, is described, along with associated experimental diagnostics. Measurements of, and improvements to, the tilt at impact are reported. The problem of shock temperature is discussed, including a brief review of the relevant literature. It is demonstrated that direct measurement of shock temperature is a complex issue that is not yet fully understood, whereas determination of temperature from an equation of state is an established technique.

In a series of experiments, plate impact techniques were utilised to determine the Hugoniot and, through shock/reload experiments, the equation of state of water and aqueous solutions of ammonium nitrate. In-situ manganin gauges were used to measure stresses in the liquids and, from the arrival times of the shock wave, determine the shock velocity. Linear shock velocity–particle velocity Hugoniots for the liquids were determined, up to particle velocities of $1\,\mathrm{km\,s^{-1}}$, with uncertainties on the intercept and slope of these Hugoniots of $5\,\%$. A Mie-Grüneisen equation of state was used to describe the shock/reload experiments. Approximate calculations of shock temperature are reported. Increasing ammonium nitrate concentrations resulted in greater calculated temperatures. It was demonstrated that the liquids investigated in this thesis show a temperature dependence of the Grüneisen parameter, Γ, which cannot be accommodated in the model. The present work is believed to be the first demonstration of this effect in shock compressed liquids. The data presented provide constraints on future theoretical development of equations of state.

RELATED PUBLICATIONS

Some of the results presented in Chapter 4 were presented at the Sixteenth Biennial International Conference of the American Physical Society Topical Group on Shock Compression of Condensed Matter:

> M. Morley, D. J. Chapman, and W. G. Proud. Temperature measurements at material interfaces with thin-foil gauges. In Elert, M. L. and Butler, W. T. and Furnish, M. D. and Anderson, W. W. and Proud, W. G., editors, *Shock Compression of Condensed Matter — 2009*, pages 599–6014. American Institute of Physics, 2009.

Some of the results presented in Chapter 5 have been used in the development of models of shock wave structure:

> K. B. Jordan *Direct Numeric Simulation of Shock Wave Structure without the Use of Artificial Viscosity*. PhD thesis. Marquette University, 2011.

Some of the results presented in Chapters 5 and 6 were presented at the Sixteenth Biennial International Conference of the American Physical Society Topical Group on Shock Compression of Condensed Matter:

> M. Morley, D. J. Chapman, and W. G. Proud. Equation of state data from off-Hugoniot measurements in multiply-shocked liquids. In Elert, M. L. and Butler, W. T. and Furnish, M. D. and Anderson, W. W. and Proud, W. G., editors, *Shock Compression of Condensed Matter — 2009*, pages 560–563. American Institute of Physics, 2009.

Some of the results presented in Chapters 5 and 6 will be presented at the Seventeenth Biennial International Conference of the American Physical Society Topical Group on Shock Compression of Condensed Matter:

> M. Morley and D. M. Williamson. Shock/reload response of water and aqueous solutions of ammonium nitrate. In *Shock Compression of Condensed Matter — 2011*. American Institute of Physics, *in preparation*.

DECLARATION

This thesis is the result of my own work and includes nothing which is the outcome of work done in collaboration, except where noted in the text. It is not substantially the same as any that I have submitted or will be submitting for a degree or diploma or other qualification at this or any other University and satisfies the word limit prescribed by the Faculty Board of Physics and Chemistry.

ACKNOWLEDGEMENTS

This work has been supported financially by Orica Mining Services and I would like to extend my thanks to Richard Goodridge and the team at Kurri Kurri for their assistance and hospitality. In particular, I am grateful to Drs. Jim Chan, Ian Kirby, and Alan Minchinton for their advice and words of wisdom. I am grateful for the supervision that has been afforded to me by Drs. Bill Allison and David Williamson, and to Dr. Bill Proud for arranging the funding of this project.

I must acknowledge Dr. David Chapman, now at the Institute for Shock Physics, Imperial College, who early on pointed me in interesting directions. I should also thank Dr. Chris Braithwaite, for his advice and assistance with VISAR measurements, and David Bell, for his assistance with interferometeric and optical diagnostics. To the others of the Fracture and Shock Physics Group - Hannah Brierley, Adam Collins, Dr. Dan Drodge, Tuuli Gröhn, Simon Kirk, Nick Taylor and Dr. Stephen Walley - who were always on hand for useful advice or a pint, often simultaneously, thank you. I am particularly grateful to Amy Adams, of the University of Florida, who helped me stay sane during a difficult summer, and believed in me even when I didn't.

Without the invaluable mechanical skills of Rik Balsod, Ray Flaxman, Dave Johnson, Peter Norman, Nigel Palfrey, Chris Summerfield, and the other staff of the Mott and Main Workshops, I doubt whether any of the experiments I conducted would have progressed beyond a roughly-drawn sketch. I learnt much from their advice and expertise, and owe them a debt of gratitude. In the wider Cavendish, Chris, Jacqui, Jess, Lisa, and Susan - amongst others - have made my time here far more enjoyable than it might otherwise have been. Further thanks should be given to Drs. Bill Allison, Chris Braithwaite, David Chapman, and Daniel Eakins (of the Institute of Shock Physics, Imperial College) who kindly gave up their time to proof-read my thesis, and who offered valuable and useful insights.

It would be remiss of me not to thank my parents who, years ago, started me on the road that lead to this document and to whom I shall remain eternally indebted.

Finally, and most importantly, I must thank Rachael, who has helped in ways she can't imagine, and who proof-read much of what follows. Without her love and support, I doubt I could have found the motivation to finish this thesis.

CONTENTS

CHAPTER 1

INTRODUCTION

Jones, Scott and Co. was formed over 130 years ago as a supplier of explosives to the newly-discovered Victorian gold fields. Since then, first as part of *Nobel*, then *ICI*, and now as *Orica*, the company has become one of the largest producers of commercial explosives anywhere in the world [Orica, 2004] with dozens of major manufacturing locations across the world (Figure 1.1).

In 2010, *Orica Mining Services* recorded annual earnings in excess of half a billion pounds, with nearly two-thirds of this being generated from Australian operations [Orica, 2010]. A large proportion of this revenue is generated through sales to coal mines in New South Wales, where the port of Newcastle sees coal exports of over 90 million tons per annum [Port Waratah Coal Services, 2011]. Affecting the underlying profitability of all mining operations is, of course, the price of raw materials, *i.e.*, of the explosives themselves. The production of ammonium nitrate produces significant amounts of carbon dioxide; for environmental reasons, and under the continued threat of the introduction of a carbon tax [Commonwealth of Australia, 2011], it would be desirable to reduce *Orica*'s carbon footprint. One way to achieve this would be simply to reduce the amount of ammonium nitrate incorporated in emulsion explosives. It is not immediately clear how much ammonium nitrate can be removed whilst retaining the necessary explosive output. The experimental development and testing of a new explosive formulation is, however, an expensive and time-consuming processs. A theoretical framework, enabling prediction of the behaviour of novel explosives, is therefore desirable. Indeed, accompanying the development of new explosives has been a development of computational models - first in one-dimensional models [Chan, 1982; Kirby and Chan, 1986], and then two-dimensionally [Chan, 2007; Kirby and Chan, 2002]. *Orica*'s present model is implemented in the 'Commerical Properties of Explosives' (CPeX) code [Chan, 2011]. More recently, there has been a move towards developing holistic models, that model the entirety of the blasting process, from explosive behaviour, through explosive/rock interaction, to fragmentation behaviour of the rock. One such approach is the *De Beers*-led 'Hybrid Stress Blasting Model' [Braithwaite, 2009]. *Orica*'s 'Mechanistic Blast-

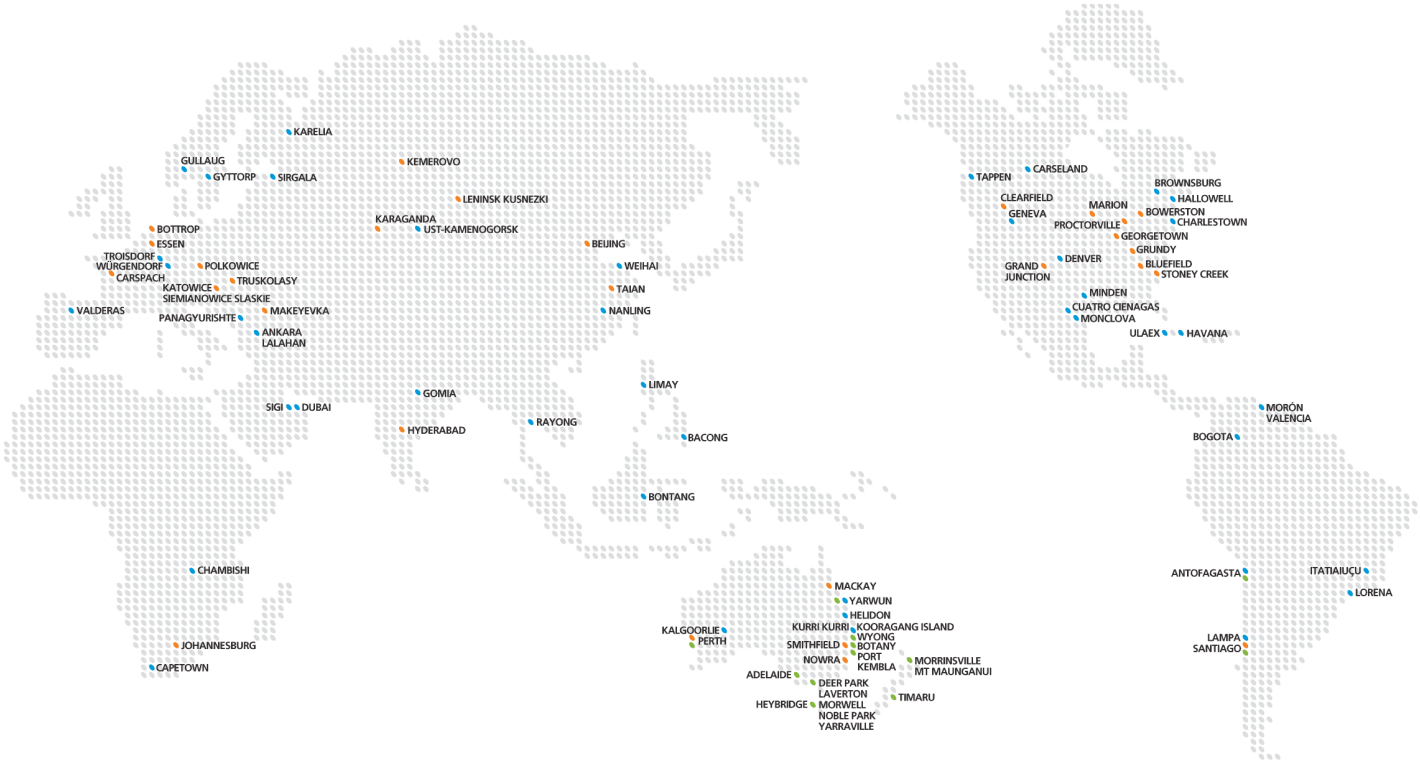

Figure 1.1: *Orica*'s major manufacturing locations, adapted from Orica [2010]. The map does not show smaller regional manufacturing sites, such as the Roburite plant near Wigan.

ing Model', when combined with the CPeX model of detonation behaviour, fulfils much the same role [Chan, 2011]. Predicting the behaviour of novel emulsion compositions requires developing knowledge of the behaviour of the constituent ingredients at the pressures, and over the time scales, that would be found in a mine. Of particular interest are the temperature rises that occur due to the passage of the shock, as reaction in ammonium nitrate is, to a large extent, thermally activated. This thesis considers aqueous solutions of ammonium nitrate. Using established shock compression techniques, the high pressure (several giga-Pascal), dynamic (few micro-seconds) behaviour of these solutions is investigated, in well-defined laboratory conditions. That ammonium nitrate solutions can be considered explosives is a fact largely neglected by the present work, which focusses on the behaviour of the unreacted solutions.

It is both interesting and instructive to consider, from an historical viewpoint, the development of the explosives that are used in the mining industry. Gunpowder was discovered in antiquity in China, although it was not until the seventeenth century, in Hungary, that it saw widespread (albeit rather dangerous) use in mining [Dolan and Langer, 1997]. The development of dynamites - the first high explosive - by Alfred Nobel in the 1860s, together with his invention of the blasting cap, or detonator, led to marked improvements in safety. The first use of ammonium nitrate as a component in explosives came at this time with its inclusion in dynamite formulations [Cook, 1974]. By the 1960s, dynamites were being replaced in the mining industry by cheaper explosives based around the mixture of granular ammonium nitrate with fuel oil (ANFO). The properties of the granular ammonium nitrate used in ANFO have recently been studied in this laboratory [Taylor, 2011]. ANFO delivers a large amount of blasting energy whilst being cheap to produce, however, it suffers a major drawback. Mines, by their very nature - as large holes in the ground - tend to be damp environments, and often bore holes contain a large amount of water. The addition of more than $10\,\%$ water to ANFO causes it to fail to detonate. Ammonium nitrate is highly hygroscopic, and the addition of fuel oil only enhances this unfortunate property [Hustrulid, 1999], preventing the use of ANFO in damp bore holes. A solution to this problem came with the development, first of 'slurry', and then, of 'emulsion' explosives [Cook, 1974; Sudweeks, 1985]. In an ammonium nitrate emulsion explosive, a solution of ammonium nitrate is mixed with a fuel to create a water-in-oil type emulsion. Micrographs of two such emulsions are shown in Figure 1.2. Droplets of am-

monium nitrate solution are coated entirely in fuel, providing an intimate mixing of fuel and oxidiser, and effectively water-proofing the explosive, through the immiscibility of the oil phase with any surrounding water. Ammonium nitrate emulsions are now widely used in the industry. Indeed, Orica are currently seeking to create a new emulsion manufacturing plant at their technical centre in Kurri Kurri, near Newcastle [Orica, 2009].

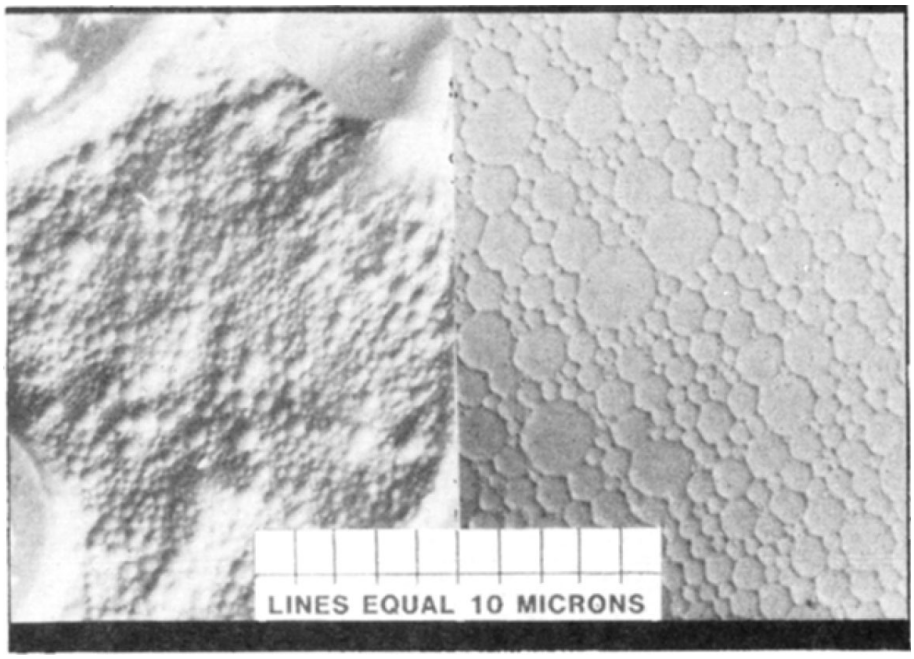

Figure 1.2: Micrographs of two ammonium nitrate emulsions, from Sudweeks [1985]. The circular droplets are the ammonium nitrate solution, which is surrounded by a continuous oil phase.

Galbraith [1997] reported four experiments conducted in the 'ring-up' configuration to measure the principal Hugoniot of a variety of ammonium nitrate solutions, and one similar experiment on pure water. In this geometry, the sample is confined between two high-impedance anvils and is thus subject to the action of a number of shocks which 'ring-up' the stress in the the sample. These reflected shocks result in states that do not lie on the principal Hugoniot of the sample. A given stress in the 'ring-up' geometry is reached for a lower entropy rise than would be the case for a single shock wave. The lower entropy rise results in a lower thermal pressure and, ultimately means that a

given stress in the 'ring up' geometry is reached at higher density and, hence, lower particle velocity than the same stress on the principal Hugoniot. If an equation of state is available, then the exact difference between the principal Hugoniot and multiple shock state can be calculated. Applying an equation of state for water [Gurtman et al., 1971], it can be shown that, for the experiment on water reported by Galbraith, the first reflected shock state is at a stress approximately $2\,\%$ below the Hugoniot. It can be assumed that the ammonium nitrate solutions show a similar magnitude of displacement between the principal Hugoniot and first reflected shock state. Galbraith comments that this displacement is within the experimental uncertainty of the diagnostics and, thus, can be neglected. Galbraith assumed that subsequent states in the 'ring-up' lie similarly below the Hugoniot. However, it can also be shown from the equation of state that these states lie progressively further below the Hugoniot, with the difference in some of the stresses reported by Galbraith being as much as $10\,\%$. Hence, the Hugoniots reported by Galbraith underestimate the Hugoniot stress in the liquid by as much as $10\,\%$. An additional complication arises from the specific diagnostic employed by Galbraith. In order to measure the longitudinal stress in the liquid, manganin gauges were employed. The particular gauges in use at the time had 'legs', which extend out of the target enabling electrical contacts to be made, that are also made from manganin. The measured resistance change is, therefore, dependent not only on the stress experience by the gauge grid, but also by the pressure experienced by the legs, which may have a significant deviatoric component (*i.e.*, a lateral stress). Such effects have recently been reported on for lateral stress gauges by others in this Laboratory [Chapman et al., 2009]. The effect of the manganin legs on measured stress was not understood at the time of Galbraith's work, but generally appears to result in stresses that, when reduced from the measured resistance change, are around $2\,\%$ lower than the stress that was present in the experiment. Because of these two effects, whilst Galbraith's data comprise the best results on the Hugoniot of ammonium nitrate solutions that has been reported in the open literature, advances that have been made in the past decade now enable measurements of a greater accuracy to be made.

Chapter 2 of this thesis develops a mathematical formulation of the propagation of shock waves and introduces the Mie-Grüneisen equation of state, an equation that is widely used in the literature and believed by Orica to provide an appropriate description of emulsion explosives [Chan, 2011]. In Chapter 3, the experimental technique of 'plate impact' is described; particular attention

is paid to diagnostics for measuring stress in dynamic experiments. The existing experimental facilities in the Cavendish Laboratory are described, and reductions of the tilt at impact reported on. Chapter 4 discusses techniques for measuring shock temperature that have been reported in the literature and presents new experimental results on the use of thin-foil thermistors. From these, it is concluded that direct measurement of temperature is an expensive and complex issue that remains largely unsolved. The calculation of temperature from equations of state is, however, an established technique, and a method for so doing is described. In Chapters 5 and 6, measurements are made of the Hugoniots and equations of state of water and ammonium nitrate solutions, investigating the effects of initial temperature and ammonium nitrate concentration on the resultant behaviour. The results reported enable approximate calculations of shock temperatures to be made. Finally, Chapter 7 critically assesses the present data and discusses the applicability of the Mie-Grüneisen equation of state to the liquids studied in this thesis. It is demonstrated that the assumptions underpinning Mie-Grüneisen equation are unlikely to apply to water and ammonium nitrate solutions in the range of stresses considered in the present work. Complexities in the theoretical modeling of water are discussed, and it is demonstrated that whilst surprisingly little is well understood about the shock response of water and aqueous solutions at low stresses, the results presented in this thesis are an important test of the common assumptions made when dealing with such materials.

1.1 Bibliography

C. H. Braithwaite. *High Strain Rate Properties of Geological Materials*. PhD thesis, University of Cambridge, 2009.

J. Chan. Personal communication, 2011. Orica Mining Services.

S. K. Chan. A theory to predict the velocity-diameter relation of explosives. In *Seventh Symposium (International) on Detonation — 1981*, pages 589–601. Office of Naval Research, 1982.

S. K. Chan. Prediction of confinement effects on detonation with an analytical two-dimensional model. In *Thirteenth Symposium (International) on Detonation — 2006*, pages 224–232. Office of Naval Research, 2007.

D. J. Chapman, C. H. Braithwaite, and W. G. Proud. Calibration of wire-like manganin gauges for use in planar shock-wave experiments. In M. L. Elert, W. T. Butler, M. D. Furnish, W. W. Anderson, and W. G. Proud, editors, *Shock Compression of Condensed Matter — 2009*, pages 603–606. American Institute of Physics, 2009.

Commonwealth of Australia. Department of Climate Change and Energy Efficiency, 2011. URL `http://www.climatechange.gov.au/`.

M. A. Cook. *The Science of Industrial Explosives*. Ireco Chemicals, 1974.

J. E. Dolan and S. S. Langer, editors. *Explosives in the Service of Man*. The Royal Society of Chemistry, 1997.

S. Galbraith. *The responses of potassium chloride, ammonium nitrate solutions, and emulsion explosives to plate impact loading*. PhD thesis, University of Cambridge, 1997.

G. A. Gurtman, J. W. Kirsch, and C. R. Hastings. Analytical equation of state for water compressed to 300 kbar. *Journal of Applied Physics*, 42(2):851–857, 1971.

W. Hustrulid. *Blasting principles for open pit mining*, volume 1 - General design concepts. A. A. Balkema, 1999.

I. J. Kirby and S. K. Chan. A small divergent detonation theory for intermolecular explosives. In *Eighth Symposium (International) on Detonation — 1985*, pages 176–186. Office of Naval Research, 1986.

I. J. Kirby and S. K. Chan. Analysis of VOD-diameter data using an analytical two-dimensional non-ideal detonation model. In M. D. Furnish, M. Elert, T. P. Russell, and C. T. White, editors, *Shock Compression of Condensed Matter — 2005*. American Institute of Physics, 2002.

Orica. Orica Limited — History, 2004. URL `http://www.orica.com/BUSINESS/COR/orica/COR00254.nsf/Page/About_OricaHistory`.

Orica. Proposed Ammonium Nitrate Emulsion (ANE) Production Facility and Continued Operations of Orica Mining Services Technology Centre, 2009. URL `http://www.oricaminingservices.com/download/file_id_8072/`.

Orica. On Solid Ground, 2010. URL `http://www.orica.com/BUSINESS/COR/orica/COR00254.nsf/Page/InvestorsReports`. Orica Annual Report.

Port Waratah Coal Services. PWCS Operating Statistics, 2011. URL `http://www.pwcs.com.au/display/assets/download.php?id=498`.

W. B. Sudweeks. Physical and chemical properties of industrial slurry explosives. *Industrial & Engineering Chemistry Product Research and Development*, 24(3):432–436, 1985.

N. Taylor. *Hot spots in Ammonium Nitrate*. PhD thesis, University of Cambridge, 2011.

CHAPTER 2

FUNDAMENTALS OF SHOCK WAVE PROPAGATION

The equations governing the propagation of shocks (*i.e.*, discontinuous flows) were derived in the latter half of the 1800s [Hugoniot, 1887, 1889; Rankine, 1869], but it was only in the 1940s - as part of the War effort - that the experimental study of shock waves in condensed matter, and the development of a theoretical framework to support such experiments, began. An historical overview of this early experimental programme is given by Taylor [1984].

Shock waves are the necessary and unavoidable result of matter moving at velocities greater than those at which the surrounding media can move out of the way: a shock wave, therefore, is supersonic with respect to the material into which it propagates.

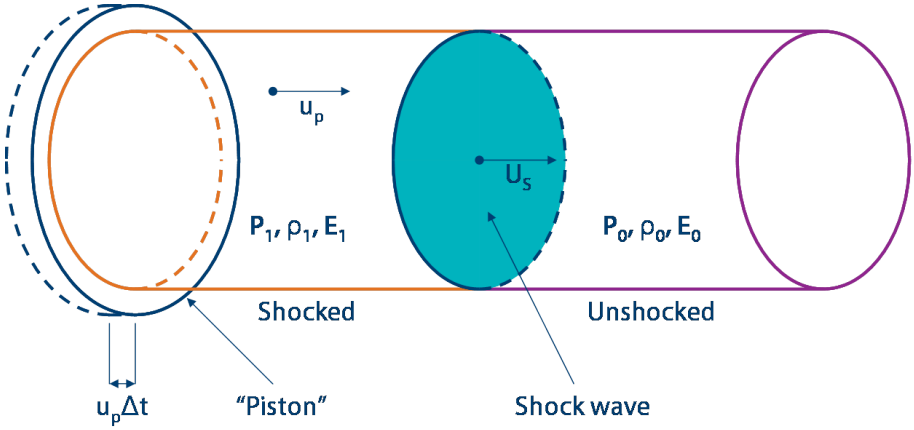

Figure 2.1: A rigid piston, moving at u_p, impinges on a column of fluid. The resultant shock wave propagates through the fluid at U_S, taking the material from its initial state, 0, to a state of elevated pressure, density, and internal energy, labelled 1.

Figure 2.1 shows a piston driving a shock wave into column of fluid. In this simplified system, it is assumed that the resultant flow is steady, body forces may be neglected, and the initial and final states are in mechanical equilibrium. Additionally, it is assumed that the material has zero strength, is inviscid, and that no reactions or phase changes occur. Following the derivations

presented by, amongst others, Asay and Shahinpoor [1993, Chapter 2] and Davison [2008, Chapter 3], this chapter considers such a simplified system, and shows it is possible to derive a series of conservation equations and the mathematical description of a planar longitudinal shock.

2.1 Planar longitudinal shock waves

Considering the piston in Figure 2.1, per unit time, the discontinuity moves through a mass of material $\rho_0 U_S A$, where ρ_0 is the initial density of the fluid, U_S is the velocity of the discontinuity and A is its area. The material behind the discontinuity is at some higher density ρ_1 and the mass of material between the piston and the discontinuity is $\rho_1(U_S - u_p)A$ where u_p is the particle velocity of the material and is identical to the velocity of the piston. Conservation of mass is expressed by equating these terms and dividing by the area A:

$$\rho_0 U_S = \rho_1(U_S - u_p). \tag{2.1}$$

Conservation of momentum can be derived by considering a tube of unit area parallel to the plane normal of the discontinuity and with one face on either side of the discontinuity. The difference in force over this unit area, then, is identical to the change in pressure $P_1 - P_0$ between the two faces, and is equal to the change in momentum due to the acceleration of the mass element $\rho_0 U_S$ to the particle velocity u_p. Thus, conservation of momentum is expressed as

$$P_1 - P_0 = \rho_0 U_S u_p, \tag{2.2}$$

where P_0 is the initial pressure of the material and P_1 the pressure behind the discontinuity.

In a time interval Δt, the work done per unit area by the piston is $P_1 u_p \Delta t$ and is equal to the increase in the kinetic and internal energies of the material. The mass accelerated in this time interval is $\rho_0 U_S \Delta t$, and it is accelerated to the particle velocity u_p; the change in internal energy is the difference in specific internal energy, $E_1 - E_0$, multiplied by this mass element. Hence, conservation of energy gives the expression

$$P_1 u_p = \frac{1}{2}(\rho_0 U_S u_p^2) + \rho_0 U_S (E_1 - E_0), \tag{2.3}$$

as the time interval Δt cancels from both sides.

These three equations combined are termed the 'jump conditions' and express the conservation of mass, momentum, and energy between an initial and final state. It is not necessary that there is a discontinuity between the two states, as this was not a requirement of the derivation, and so the equations hold as true for steady compressions as they do for shock discontinuities. What is required is that the initial and final states are uniform and in mechanical equilibrium. This latter condition merely requires that the state behind the shock is changing slowly with respect to rate of change at the shock itself: thus the jump conditions, whilst not strictly valid, are a useful approximation for decompression waves or in the case of chemical reaction or some rate-dependent behaviour (e.g., a viscoelastic response) occurring, provided the final state only varies slowly with time.

Equations 2.1, 2.2, and 2.3 may be combined to eliminate the velocities to give the Rankine-Hugoniot equation, which relates the change in internal energy to the changes in specific volume and pressure:

$$E_1 - E_0 = \frac{1}{2}(V_0 - V_1)(P + P_0), \tag{2.4}$$

where the densities have been replaced by the specific volumes ($V \equiv 1/\rho$).

The jump conditions can be generalised to cover the transition from one steady state to another, where the material in the initial state moves with some velocity u_1 with respect to an arbitrary reference frame:

$$\rho_1/\rho = (u_p - u_1)/(U_S - u_1), \tag{2.5}$$

$$P - P_1 = \rho_1(U_S - u_1)(u_p - u_1), \tag{2.6}$$

$$E - E_1 = \frac{1}{2}(P + P_1)(V_1 - V). \tag{2.7}$$

The jump conditions, then, give a set of three equations in five variables (P,V,E,U_S,u_p); an additional equation - the 'equation of state' $E(P, V)$ - is required to close the system. This equation describes the behaviour of the material, and is not derivable from the idealised system described above. One such equation of state is the Mie-Grüneisen equation, discussed in §2.4. Thus, after the addition of an equation of state to the jump conditions, a single independent variable exists defining a curve in a five-dimensional parameter space: the 'Hugoniot.' (This curve, as discussed in §2.2 below, may be represented in any two-dimensional plane). The Hugoniot does not represent a thermodynamic path but is merely the locus of possible states, centered on

some initial state, achievable through the action of a single shock on a material. The term 'principal Hugoniot' is used to describe the Hugoniot centered on the zero pressure state (*i.e.*, the ambient state of the material).

By equating the total differential of the Rankine-Hugoniot Equation (2.4) to the differential form of the first law of thermodynamics, $dE = TdS - PdV$, an expression for the entropy, S, on the Hugoniot may be obtained:

$$TdS = \frac{1}{2}(V_0 - V_1)dP + \frac{1}{2}(P + P_0)dV. \tag{2.8}$$

Expanding the entropy as a Taylor series along the Hugoniot gives:

$$S = S_0 + \left.\frac{dS}{dV}\right|_0 (V - V_0) + \frac{1}{2!}\left.\frac{d^2S}{dV^2}\right|_0 (V - V_0)^2 + \frac{1}{3!}\left.\frac{d^3S}{dV^3}\right|_0 (V - V_0)^3 + \cdots. \tag{2.9}$$

From Equation 2.8 it is clear that the first order derivative in the expansion is zero:

$$\left.\frac{dS}{dV}\right|_0 = \frac{1}{2T}\left[P - P_0 + (V_0 - V)\frac{dP}{dV}\right]_{P=P_0, V=V_0}. \tag{2.10}$$

Similarly, the second order derivative is

$$\left.\frac{d^2S}{dV^2}\right|_0 = \frac{1}{2T}\left[\frac{dP}{dV} - 2(V_0 - V)^2\frac{dP}{dV} + (V_0 - V)\frac{d^2P}{dV^2}\right]_{P=P_0, V=V_0}, \tag{2.11}$$

which is also zero. The third order derivative is non-zero, and hence the entropy along the Hugoniot is

$$S - S_0 = \frac{1}{12T_0}\frac{d^2P}{dV^2}(V_0 - V)^3 + O(V_0 - V)^4. \tag{2.12}$$

The entropy, then, is constant along the Hugoniot to third order in strain. It is therefore, for weak shocks, often reasonable to approximate the Hugoniot to a line of constant entropy: the isentrope. As the shock process is sufficiently rapid that no heat is transferred to the surrounding material, the second law of thermodynamics requires the entropy change, $S - S_0$, to be positive. Thus, the shock is thermodynamically stable if

$$\left.\frac{d^2P}{dV^2}\right|_S > 0. \tag{2.13}$$

This is equivalent to requiring the P–V Hugoniot to be concave upwards everywhere. It is important to recall that the Hugoniot is not a thermodynamic

curve and does not represent the loading path of the material; this point is discussed further in §2.2 below.

Temperature is defined thermodynamically as the reciprocal of the partial derivative of entropy with respect to energy:

$$T \equiv \left(\frac{\partial S}{\partial E} \right)^{-1}. \tag{2.14}$$

Thus, the entropy rise associated with the passage of a shock wave leads to a temperature rise in the shocked material. This temperature rise is discussed further in Chapter 4.

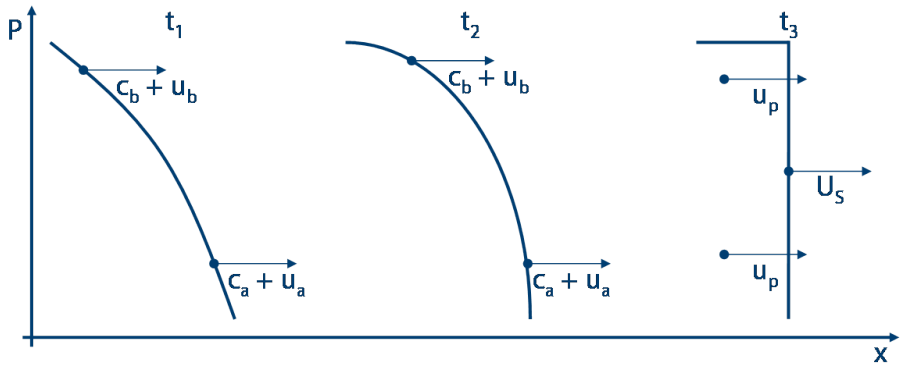

Figure 2.2: A compressive wave propagating into a material whose sound speed increases with pressure, shown as a function of distance and pressure, at three different times. The sound speed, c_b, in the higher pressure state is greater than that at lower pressures, c_a, and hence the higher pressure portions of the wave front will catch the lower pressure sections. This results in the formation of a shock discontinuity moving at a single velocity U_S in, and imparting a particle velocity u_p to, the shocked material.

In most materials, sound speed is an increasing function of pressure. As shown in Figure 2.2, it is this property which allows a compressive wave to steepen into a shock discontinuity. The sound speed in the higher pressure state is greater than that in the lower pressure state, and thus compressional waves propagating in the higher pressure region travel faster than those in the lower pressure region. Of course, in the laboratory frame, both propagate at a velocity equal to the local sound speed plus the material's particle velocity. Thus, waves from the higher pressure region catch those from the lower pressure region, resulting in the steepening of the wave front until it becomes

a single discontinuity travelling into unshocked material at the shock velocity, which is itself supersonic with respect to the unshocked material. Some materials do not exhibit this behaviour. For example, at low pressures, the sound speed in fused silica decreases with pressure and, hence, shocks are not supported [Asay and Shahinpoor, 1993].

It follows that, in addition to being supersonic with respect to the unshocked material, the shock must be subsonic with respect to the material behind it: if this were not the case, then compressional disturbances behind the shock would not be able to catch it. Thence, the shock would not be stable with respect to trailing perturbations. Therefore, it is these three conditions - that sound speed increases with pressure, the shock is supersonic with respect to the material ahead of it and subsonic with respect to that behind it - that are required to ensure that a shock is stable.

In a real material, especially at moderate to low pressures, a shock is not a true discontinuity and its sharpness is limited by dissipative processes including heat transport and viscosity. For example, in a viscous material, an infinite velocity gradient cannot be supported. Hence, in experimental measurements, shock rise times of several tens to hundreds of nanoseconds are not uncommon, depending on the material. A final complication occurs when the sound speed is not a continuous function of pressure: for example, in the vicinity of a phase change or in an elastic-plastic material, the discontinuity in sound speed will result in the emergence of a two-wave structure.

A material, once in an elevated pressure state, must, necessarily, return to ambient pressure: the mechanism through which this is achieved is that of the release, or rarefaction. Release waves spread as they propagate, and are often termed 'release fans' as a consequence. Such a spreading is shown in Figure 2.3; it should be obvious that the mechanism responsible for steepening a shock is similarly responsible for the spreading of a release fan: the decrease of sound speed with decreasing pressure results in the front portion of the release out-running the trailing portions. The degree of 'fanning' depends on the material and in many cases it is more useful to consider only the lead characteristic of the release.

Whereas a shock, which is limited by dissipative processes, is irreversible and results in an increase in entropy, a release is (at least in an inviscid fluid) a nearly isentropic process. Therefore, an irreversible rise in entropy occurs in a medium that is shocked to some state and then returned to ambient conditions by the action of release waves.

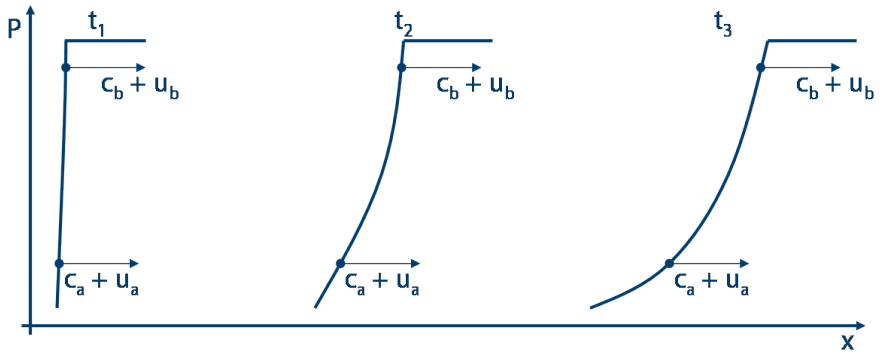

Figure 2.3: The same mechanism that results in the sharpening of the shock shown in Figure 2.2 is also responsible for the spreading of a release wave. Portions of the release wave in the lower pressure regions travel slower than those in the higher pressure regions and hence trail behind. This results in the spreading of the wave into a 'release fan'.

2.2 Graphical representations

The principal Hugoniot of a material is often represented in U_S–u_p space, as the experimental determination of this relationship is common. It is observed empirically that, for the vast majority of materials, the velocity of the shock wave generated under plate-impact type loading is linearly proportional to the particle velocity imparted at impact. This result, sometimes termed the shock equation of state, is conventionally expressed in the form

$$U_S = c_0 + Su_p, \tag{2.15}$$

where c_0 and S are material constants. c_0 is usually found to be approximately equal to the bulk soundspeed at zero pressure and S is positive for most materials. The values of c_0 and S are tabulated for a wide range of materials in Asay and Shahinpoor [1993, Appendix C] and Marsh [1980]. Such a linear relationship between shock and particle velocities gives a Hugoniot in pressure–particle velocity space that is curved upwards. In some materials, such as nylon, there is a weak quadratic dependence of shock velocity on particle velocity, and an extra term may be added to Equation 2.15 to capture any such behaviour.

The shock impedance, $Z \equiv \rho_0 U_S$, indicates the ability of a material to support pressure under the action of a shock wave. For a given particle ve-

locity u_p a material of higher impedance will support a higher pressure than a lower impedance one. It is often convenient to consider impedance in the limit of a weak shock, where Z_0 is given by $\rho_0 c_L$, where c_L is the longitudinal sound speed at zero pressure; this quantity allows for easy comparison between materials. In general, materials with a high impedance have a high density, although this is not always the case: sapphire, for example, has a high impedance due to its very high sound speed.

It is both useful and instructive to consider the graphical representations of the results derived above. Three representations are commonly encountered in the design and analysis of shock experiments: x–t diagrams, P–v, and P–u_p diagrams.

x-t diagrams are instructive in showing the propagation of shocks and releases through a series of materials, and are helpful in determining what interactions may occur at boundaries or between various waves. Figure 2.4 shows an example x-t for a symmetric plate impact experiment. A flyer plate is fired at some velocity into a stationary target of the same material, producing shocks in both. These shocks, upon reaching the rear surfaces of both flyer and target, are reflected as release waves that propagate back into each plate.

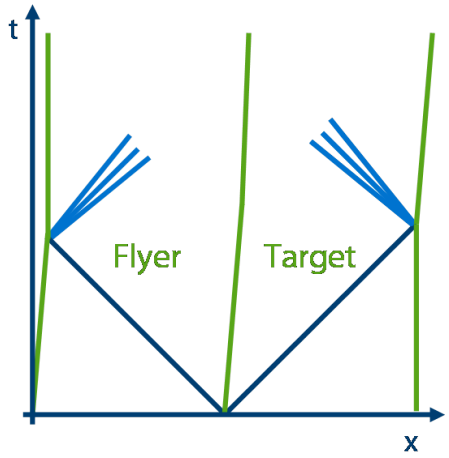

Figure 2.4: An x-t diagram for a symmetric plate impact experiment. Shocks are generated at impact that propagate into the target and flyer at identical velocities; upon reaching the free surfaces, these shocks are reflected as release fans.

If, as is shown in Figure 2.5, the target plate was not backed by a free surface but by a material of higher impedance then, upon reaching the interface,

there is a shock transmitted into the rear anvil, and one reflected into the target plate. It should be noted that this reflected shock acts to increase the pressure in the target plate, whilst simultaneously lowering its particle velocity (as it propagates in the opposite direction).

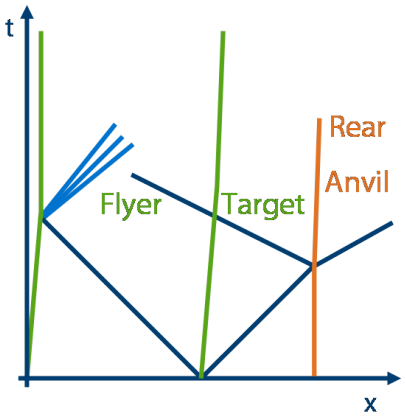

Figure 2.5: An x-t diagram for a symmetric plate impact experiment backed by a material of higher impedance. Upon reaching this interface, the shock is reflected back into the target material; in addition, a shock propogates into the rear material.

The jump conditions, Equations 2.1 - 2.3, can be solved for the shock and particle velocities:

$$U_S = V_0\sqrt{(P-P_0)/(V_0-V)}, \tag{2.16}$$

$$u_p = \sqrt{(P-P_0)(V_0-V)}. \tag{2.17}$$

Figure 2.6 shows a Hugoniot in P–V space. The chord connecting the initial and final state, which has slope $(U_S/V_0)^2$, is termed the 'Rayleigh line' and represents the loading path between the initial and final states. From Equation 2.17, it is clear that specific kinetic energy is $(P-P_0)(V_0-V)/2$ and is the triangle below the Rayleigh line. The increase in specific internal energy is given by the Rankine-Hugoniot Equation (Equation 2.4) and is the total area below the Rayleigh line. In the case that $P_0 = 0$, which is approximately true in the case when the initial state is at ambient pressure, then the internal and kinetic energy generated are equal.

As shown in Equation 2.12, the Hugoniot is isentropic to third order in strain. Therefore, it is reasonable to approximate the release by the Hugoniot.

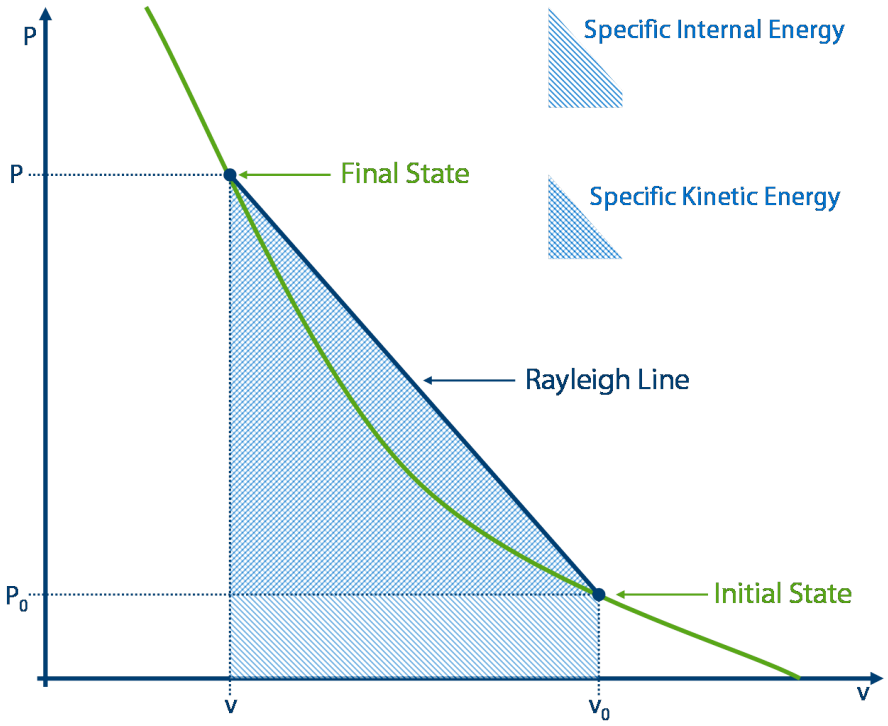

Figure 2.6: In P–v space, the chord between the initial and final states - the Rayleigh line - gives the loading path of a material under single-shock loading. The specific kinetic energy imparted by the shock wave is given by the area of the triangle below the Rayleigh line; the specific internal energy rise is given by the total area under the Rayleigh line. As the Hugoniot is isentropic to third order in strain, and hence a good approximation of the release isentrope, the area between the Hugoniot and the Rayleigh line represents approximately the 'waste heat' irreversibly gained by a material that is shocked to some state and then released to ambient conditions.

Thus, the internal energy returned to the surroundings upon release may be approximated by the area under the Hugoniot. Hence, the irreversible nature of the shock process leads to 'waste heat' which is the internal energy retained and is approximately given by the area between the Hugoniot and Rayleigh line.

P–u_p diagrams enable determination of the pressure and particle velocity states resulting from a given interaction. In order that an interface does not separate, it is necessary that particle velocity be conserved across it; similarly the pressures must be identical. As the equations derived above are invariant under transformation of the reference frame, it should be obvious that Hugoniots in pressure-particle velocity space may simply be translated along the particle velocity axis or rotated through the pressure axis to match the particular shock under consideration. As is shown in Figure 2.7, which corresponds to the experiment represented in Figure 2.4, the Hugoniot of the flyer is translated such that it is centered on the impact velocity and reflected - for the shock in the flyer travels in the opposite direction. It is easy to see, therefore, that the particle velocity in such a symmetric impact is half the impact velocity.

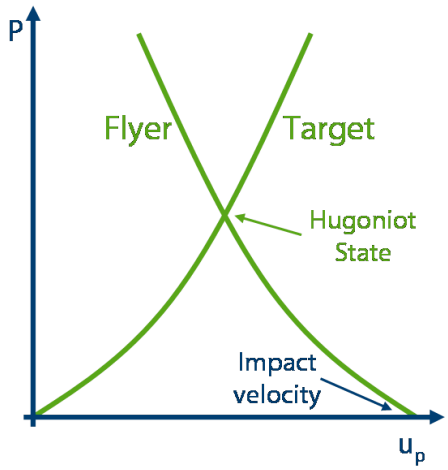

Figure 2.7: A P–u_p diagram for a symmetric plate impact. The flyer Hugoniot is reflected, as it travels in the opposite direction, and is translated so that it is centered on the impact velocity. The Hugoniot state is given by the intersection of the two Hugoniots; in the symmetric case, the particle velocity is simply half the impact velocity.

If, instead of the higher impedance material of Figure 2.5, the target plate

was backed by a material of lower impedance, then, whilst a shock would still propagate into the rear material, a release would propagate back into the target plate. The corresponding P–u_p diagram is shown in Figure 2.8. The target material is as expected, shocked to the same state as in Figure 2.7. However, the release process then takes it to a state lying on the rear material's Hugoniot. As, in most materials, it is reasonable to consider that releases are nearly isentropic, and the Hugoniot and isentrope differ only by terms that are third-order in strain, it is conventional to approximate the release path by the isentrope and, hence, by the Hugoniot. Hence, this final state lies on the intersection between the rear material's Hugoniot and that of the flyer plate.

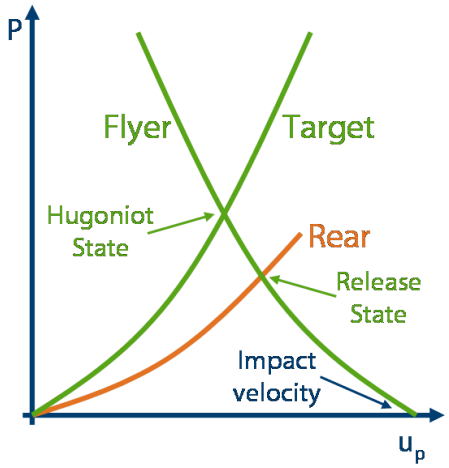

Figure 2.8: For a target material backed, not by a free surface, but by a material of lower impedance, the P–u_p diagram enables both the Hugoniot and release state to be found. As in Figure 2.7, the Hugoniot state is given by the intersection of the target and flyer Hugoniots. Approximating the release isentrope of the target by its Hugoniot, the release state is the intersection of the rear material's Hugoniot with a Hugoniot for the target material that passes through the previously-calculated Hugoniot state; in the case of a symmetric impact, this is identical to the flyer Hugoniot.

2.3 Ideal Elastic-Plastic materials

The preceding discussions have explicitly neglected the effect of material strength on the response of materials to shocks. At high pressures, or for weak materials, this assumption seems justified, as the effect of strength is consid-

ered to be negligible and the material behaves as an inviscid fluid. However, at moderate shock pressures, many materials exhibit a 'deviatoric' response [Chartagnac, 1982]. Whilst it is not necessary, in the context of the present discussion, to consider the full mathematical treatment of such materials, the qualitative response of one such material - the ideal elastic-plastic material - is discussed below.

The hydrodynamic pressure P is equal to the mean stress and under conditions of uniaxial strain, is $\frac{1}{3}(\sigma_x + 2\sigma_y)$, where σ_x is the longitudinal stress and σ_y the deviatoric strain. Combining this with the Tresca (or, equivalently, von Mises) yield criteria, $2\tau = \sigma_x - \sigma_y$, the forward yield condition is satisfied [Kanel et al., 2004] when

$$|\sigma_x - P| = \frac{2}{3}Y, \tag{2.18}$$

where the yield strength Y is simply twice the shear strength τ at the onset of yield, giving the offset loading cycle shown in Figure 2.9.

For stresses below the 'Hugoniot elastic limit' (HEL) of the material, the response is entirely elastic and consists of a single elastic wave. The response above the HEL is shown schematically in Figure 2.10 and exhibits a so-called 'two wave' response. The first wave is an elastic wave, of stress-amplitude equal to the HEL, and runs ahead of the plastic shock: for this reason, it is conventially refered to as the 'elastic precursor'. The release behaviour is similar: the initial unloading is elastic, and occurs before plastic unloading. The gradual nature of both unloading segments is due to the dispersive nature of release waves, shown in Figure 2.3.

2.4 The Mie-Grüneisen Equation of State

The thermodynamic Grüneisen parameter, Γ, is defined [McQueen, 1989] as

$$\Gamma = v\frac{\partial P}{\partial E}\bigg|_v. \tag{2.19}$$

This equation can be used [e.g., Davison, 2008] to relate the energy on the principal Hugoniot, E_H, along an isochor, to an energy state not on the principal Hugoniot:

$$P - P_H = \frac{\Gamma}{v}(E - E_H), \tag{2.20}$$

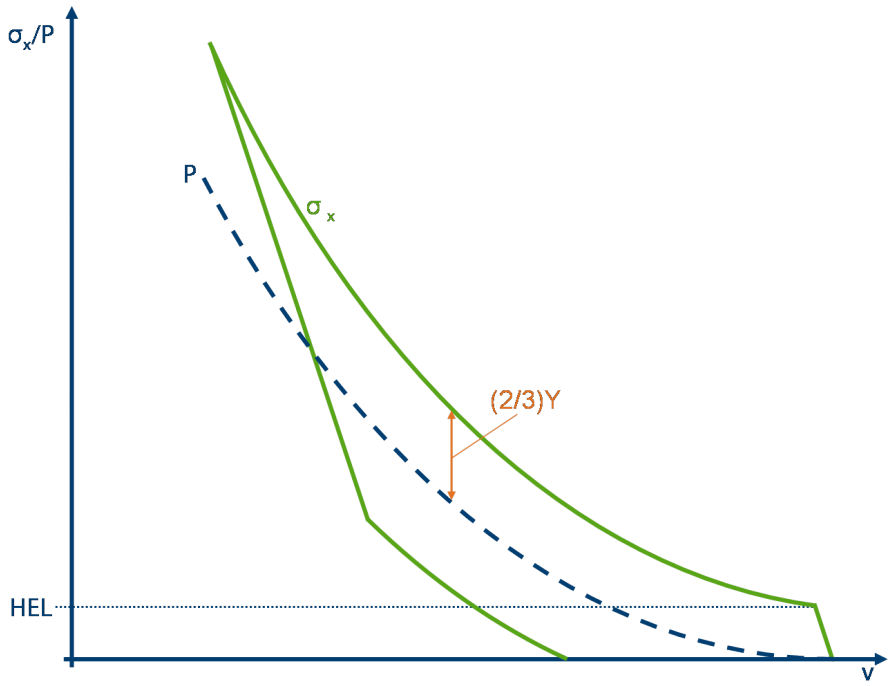

Figure 2.9: Loading and unloading, in P–v space for an ideal elastic-plastic material. The longitudinal stress increases elastically until the forward yield criterion is reached. The plastic portion is given by a curve identical to the Hugoniot (the dashed line, often termed the 'hydrostat') that is displaced above it by two-thirds the yield strength Y. The unloading is similar: first, the unloading is elastic continuing until the reverse yield criterion is reached. Plastic unloading occurs along a line parallel to the Hugoniot, displaced below the hydrostat by two-thirds the yield strength.

where P_H is the pressure on the principal Hugoniot. Equation 2.20 is often refered to as the 'Mie-Grüneisen equation' [Davison, 2008] is a P–V–E equation of state. A 'Mie-Grüneisen material' is one in which Γ is a function of volume alone.

It is instructive to consider the origin of Equation 2.20. The following derivation follows those given by Rice et al. [1958] and [Eliezer et al., 2002]. Consider a solid of N atoms to be composed of N simple harmonic oscillators. Neglecting any phonon-electron interactions, the thermodynamic functions of the system can be considered as a superposition of terms [Eliezer et al., 2002]. The pressure is expressed as $P = P_c + P_{Ta} + P_{Te}$, where the subscript c denotes the pressure at 0 K. P_{Ta} is the contribution to pressure due to vibration

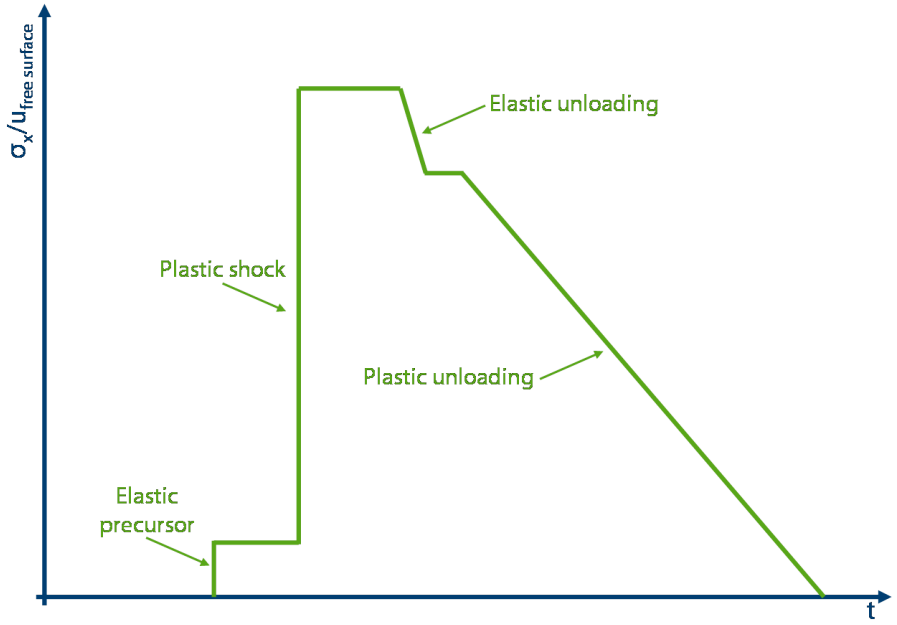

Figure 2.10: Representative wave profile for the ideal elastic-plastic material shown in Figure 2.9. A similar profile would be found in both stress and free surface velocity and consists of an initial elastic response (the 'elastic precursor') followed by the plastic shock. The release process is similar and consists of elastic unloading followed by plastic unloading.

of the atoms. P_{Te} is the electronic contribution, and can be neglected over the pressure and temperature range relevant to the present work. Similarly, the internal energy can be considered as $E = E_c + E_{Ta} + E_{Te}$. Following the derivation given by Rice et al. [1958], the energy and pressure of such a system is calculated below. The energy levels of the oscillators are [Ashcroft and Mermin, 1976]

$$E_j = \left(n + \frac{1}{2}\right) h\nu_j, \tag{2.21}$$

where the eigenfrequencies ν_j are functions of volume alone, $j = 1, 2, \cdots, 3N$ for the $3N$ independent degrees of freedom, $n = 0, 1, \cdots, \infty$ is the excitation number of the particular mode, and h is Planck's constant. The partition function for the oscillator system is then

$$Z = \prod_{j=1}^{3N} \left(\sum_{n=0}^{\infty} \left(e^{-(n+\frac{1}{2}h\nu_j)/kT} \right) \right), \tag{2.22}$$

where k is the Boltzman constant. The sum over the excitation numbers is a convergent geometric series, and so the partition function becomes

$$Z = \prod_{j=1}^{3N} \left(\frac{e^{-h\nu_j/2kT}}{1 - e^{-h\nu_j/kT}} \right). \tag{2.23}$$

The Helmholtz free energy, F, is defined as

$$F = -kT \ln(Z), \tag{2.24}$$

and so the Helmholtz free energy of the solid is

$$F = \phi(v) + \sum_{j=1}^{3N} \frac{h\nu_j}{2} + kT \sum_{j=1}^{3N} \ln \left(1 - e^{-h\nu_j/kT} \right), \tag{2.25}$$

where the term $\phi(v)$ is the potential energy of the atoms at rest. The pressure is defined as the negative of the volume derivate of F at constant T

$$P = -\left. \frac{\partial F}{\partial V} \right|_T = -\frac{d\phi(v)}{dV} + \frac{1}{V} \sum_{j=1}^{3N} \left[\Gamma_j \left(\frac{h\nu_j}{2} + \frac{h\nu_j}{\left(e^{h\nu_j/kT} - 1 \right)} \right) \right], \tag{2.26}$$

where Γ_j is defined as

$$\Gamma_j \equiv -\frac{d\ln(\nu_j)}{d\ln(V)}. \tag{2.27}$$

The internal energy can be determined from the Helmholtz free energy through the relation

$$E = F - T \left. \frac{\partial F}{\partial T} \right|_V, \tag{2.28}$$

and so the internal energy is

$$E = \phi(v) + \sum_{j=1}^{3N} \left[\frac{h\nu_j}{2} + \frac{h\nu_j}{\left(e^{h\nu_j/kT} - 1 \right)} \right]. \tag{2.29}$$

Considering Einstein's model of solids [Eliezer et al., 2002], the eigenfrequencies of the oscillators are identical: $\nu_j \equiv \nu$ for all values of j. Hence, $\Gamma_j \equiv \Gamma$ for all j and Equation 2.27 becomes

$$\Gamma \equiv -\frac{V}{\nu}\frac{d\nu}{dV}, \tag{2.30}$$

and as, in a real solid, the eigenfrequencies are functions of volume alone, so too is Γ. The sums over j in Equations 2.26 and 2.29 are then trivially solved and the pressure (Equation 2.26) becomes

$$P = -\frac{d\phi(v)}{dV} + \frac{3N\Gamma}{V}\left[\frac{h\nu_j}{2} + \frac{h\nu_j}{\left(e^{h\nu_j/kT}-1\right)}\right], \tag{2.31}$$

and Equation 2.29 is

$$E = \phi(v) + 3N\left[\frac{h\nu_j}{2} + \frac{h\nu_j}{\left(e^{h\nu_j/kT}-1\right)}\right]. \tag{2.32}$$

Combining these equations, we have the Mie-Grüneisen equation of state referenced to the 'cold compression curve'

$$P - P_c = \frac{\Gamma}{v}(E - E_c), \tag{2.33}$$

as $\phi(v) \equiv E_c$ and $-d\phi(v)/dV \equiv P_c$ are the energy and pressure at 0 K. Differentiating Equation 2.33, we recover the definition of Γ given in Equation 2.19. As Γ is a function solely of volume (Equation 2.30), then Equation 2.33 can be referenced to pressures and energies at any temperature. Replacing the cold compression curve with the Hugoniot, the familar Mie-Grüneisen equation (Equation 2.20) is recovered:

$$P - P_H = \frac{\Gamma}{v}(E - E_H). \tag{2.34}$$

It should be stressed that this final step is valid if, and only if, Γ is a function of volume alone. The Mie-Grüneisen equation can similarly be derived in the context of Debye theory, where there is a spectrum of eigenfrequencies ν_j. As noted by [Ashcroft and Mermin, 1976], all the eigenfrequencies scale linearly with the Debye frequency, ω_D:

$$\Gamma_j = -\frac{d\ln(\omega_D)}{d\ln(V)}, \tag{2.35}$$

and, therefore, Γ_j is independent of j and therefore the same for all the eigenfrequencies. Consequently, $\Gamma \equiv \Gamma_j$, which is now a function of volume alone, can be taken outside the sum over j in Equation 2.26, and by substituting the energy (Equation 2.29), Equations 2.33 and 2.34 can be recovered.

The physics underlying the foregoing discussion is generally neglected and the Mie-Grüneisen equation is often applied to materials that would not conventionally be described as a collection of harmonic oscillators. In these cases, it should be regarded as simply a P–V–E equation of state that can be used to describe shock experiments. It has been experimentally demonstrated that the Mie-Grüneisen equation provides an appropriate description of the behaviour of many materials, including mixtures of different materials [McQueen, 1989], porous solids [Meyers, 1994], and liquids (including water) [Davis, 1973; Gurtman et al., 1971]. Further, the equation can be used to calculate Hugoniots that are not centered on the ambient conditions (*i.e.*, those due to multiple shock compression) [McQueen, 1989]. For a material that is first shocked to a state (P_1, V_1), the locus of second shock states (P_2, V_2) is given by:

$$P_2 = \frac{P_H - (\Gamma/V_2)[(P_H - P_1)(V_0 - V_2)/2]}{1 - (\Gamma/V_2)(V_1 - V_2)/2}, \tag{2.36}$$

where P_H is the pressure on the principal Hugoniot at the volume V_2. Thus, the loci of reflected shocks may be calculated given knowledge of Γ; alternatively, Γ may be determined from experimental measurement of reflected shock states [e.g., Mitchell and Nellis, 1982].

2.5 Summary

- A theoretical description of ideal planar shock waves has been described.
- Two equations of state governing material response have been presented.
- It has been shown that the passage of a shock wave through a material leads to an irreversible rise in entropy and temperature.

2.6 Bibliography

J. R. Asay and M. Shahinpoor, editors. *High-pressure shock compression of solids*. Springer, 1993.

N. Ashcroft and N. Mermin. *Solid state physics*. Holt, Rinehart and Winston, 1976.

P. F. Chartagnac. Determination of mean and deviatoric stresses in shock loaded solids. *Journal of Applied Physics*, 53(2):948–953, 1982.

R. O. Davis. Further comments on thermodynamic response of Mie-Gruneisen materials. *Zeitschrift für Physik B Condensed Matter*, 17:63–70, 1973.

L. Davison. *Fundamentals of shock wave propagation in solids*. Springer, 2008.

S. Eliezer, A. Ghatak, and H. Hora. *Fundamentals of equations of state*. World Scientific, 2002.

G. A. Gurtman, J. W. Kirsch, and C. R. Hastings. Analytical equation of state for water compressed to 300 kbar. *Journal of Applied Physics*, 42(2):851–857, 1971.

H. Hugoniot. On the propagation of motion in bodies and in perfect gases in particular - I. *Journal de l'École Polytechnique*, 57:3–97, 1887.

H. Hugoniot. On the propagation of motion in bodies and in perfect gases in particular - II. *Journal de l'École Polytechnique*, 58:1–125, 1889.

G. I. Kanel, S. V. Razorenov, and V. E. Fortov. *Shock-Wave Phenomena and the properties of condensed matter*. Springer, 2004.

S. P. Marsh, editor. *LASL Shock Hugoniot Data*. University of California Press, 1980.

R. G. McQueen. Shock-waves in condensed media: Their properties and the equation of state of materials derived from them. In *Enrico Fermi summer course CX11: nuclear collisions from the mean field into the fragmentation regime*, 1989.

M. A. Meyers. *Dynamic Behavior of Materials*. John Wiley & Sons, 1994.

A. C. Mitchell and W. J. Nellis. Equation of state and electrical conductivity of water and ammonia shocked to the 100 GPa (1 Mbar) pressure range. *Journal of Chemical Physics*, 76:6273–6281, 1982.

W. J. M. Rankine. On the thermodynamic theory of waves of finite longitudinal disturbance. *Proceedings of the Royal Society of London*, 18:80–83, 1869.

M. Rice, R. McQueen, and J. M. Walsh. Compression of solids by strong shock waves. In F. Seitz and D. Turnbull, editors, *Advances in Research and Applications*, volume 6 of *Solid State Physics*, pages 1–63. Academic Press, 1958.

J. W. Taylor. Thunder in the mountains. In J. R. Asay, R. A. Graham, and G. K. Straub, editors, *Shock Waves in Condensed Matter — 1983*, pages 3–15. American Institute of Physics, 1984.

CHAPTER 3

EXPERIMENTAL TECHNIQUES

In Chapter 2, the equations governing the propagation of planar longitudinal shocks in condensed media were derived. The practicalities of generating a planar longitudinal shock and measuring the resultant longitudinal stress are now considered. A number of experimental techniques for the production of well-defined planar shock waves in laboratory conditions are available [Asay and Shahinpoor, 1993, §3.2 – §3.4]. In the present thesis, a single-stage gas gun is used in the so-called 'plate-impact' geometry to produce shock stresses to $30\,\mathrm{GPa}$.

3.1 The Cavendish plate-impact facility

The experiments described in this thesis were performed on the Cavendish plate-impact facility. The facility was originally designed to investigate the behaviour of hard ceramics above their elastic limits [Bourne et al., 1995], although it has subsequently been used to investigate a wide range of phenomena under uniaxial plate-impact and ballistic loading [*e.g.*, Braithwaite, 2009; Chapman, 2009; Forde, 2000; Hammond, 2004; Murray, 1997; Willmott, 2004]. The facility, shown in Figure 3.1, consists of a single-stage light-gas gun, with a $5\,\mathrm{m}$ barrel with $50.8\,\mathrm{mm}$ interior bore, and associated diagnostics.

The gun employs a 'wrap-around' breech, where the projectile seals the openings of the gas reservoirs [Fowles et al., 1970]. The reservoirs have a volume of $0.02\,\mathrm{m}^3$; release of the gas in these reservoirs - either compressed air or helium - accelerates the projectile along the barrel. In order to avoid an air-blast ahead of the projectile disturbing the target, and to ensure that the gun is effectively silenced, the target area is part of a sealed expansion chamber, of total volume $2.2\,\mathrm{m}^3$, which is evacuated to below $15\,\mathrm{mbar}$ prior to firing.

The details of the operation of the plate impact facility are adequately described elsewhere (*e.g.*, Bourne et al. [1995], Murray [1997], Braithwaite [2009]). However, aspects relevant to the experiments described in this thesis are discussed in detail below.

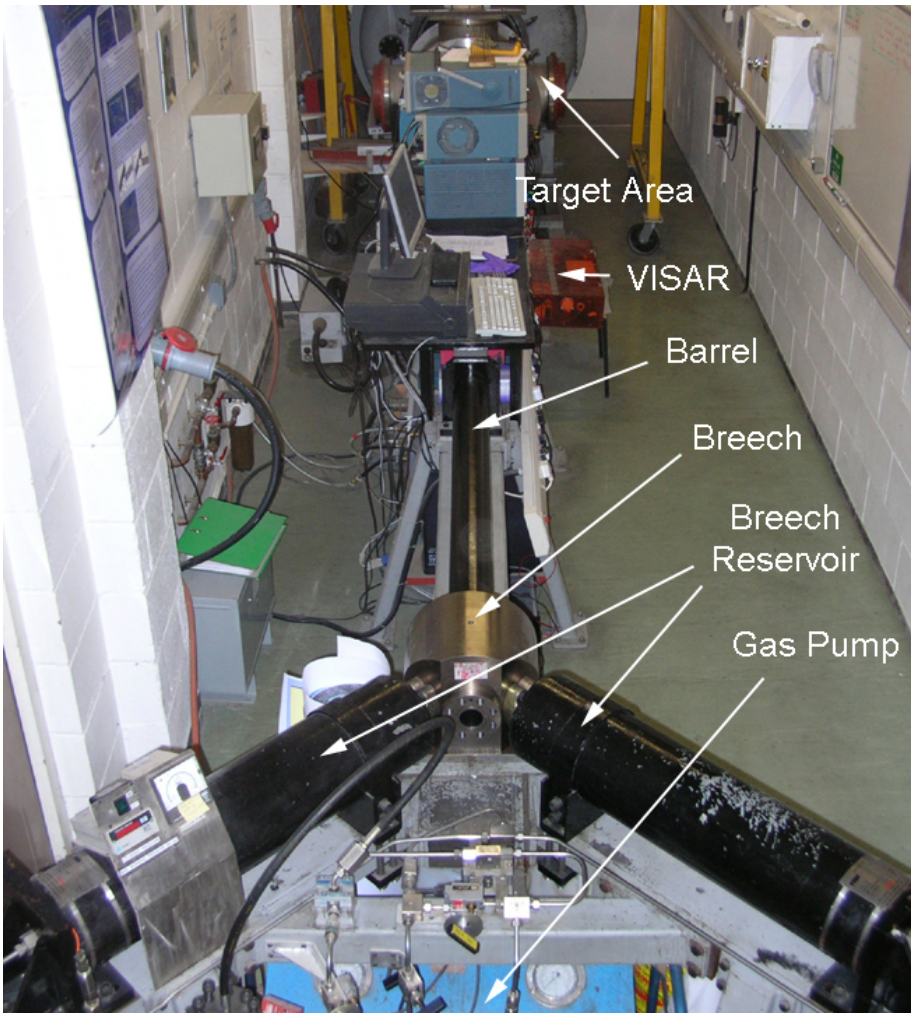

Figure 3.1: The single-stage light-gas gun in the Cavendish plate-impact facility. The gun utilises a 'wrap-around' breech, with the projectile forming the seal of the high-pressure breech reservoir. A sabot is inserted in the breech and held in place by a vacuum drawn behind it. The central section of the target area is bolted in place before an experiment is performed, and the entire barrel and expansion chamber are evacuated. The breech reservoirs are filled with air or helium, either directly or via a gas pump to obtain pressures as high as $350\,\mathrm{bar}$. When the vacuum behind the projectile is released, the projectile drifts forward through the breech until the reservoirs are no longer sealed. The projectile is then accelerated along the barrel and into the target area. Various diagnostics are available, including a laser-based interferometer system (VISAR). From Braithwaite [2009].

Figure 3.2 shows the target area of the plate impact facility. The target plate, holding the specimen mount, is attached by three adjustable threaded rods to a collar mounted on the muzzle of the gun. It is by the adjustment of these three rods that the sample may be aligned perpendicular to the barrel of the gun.

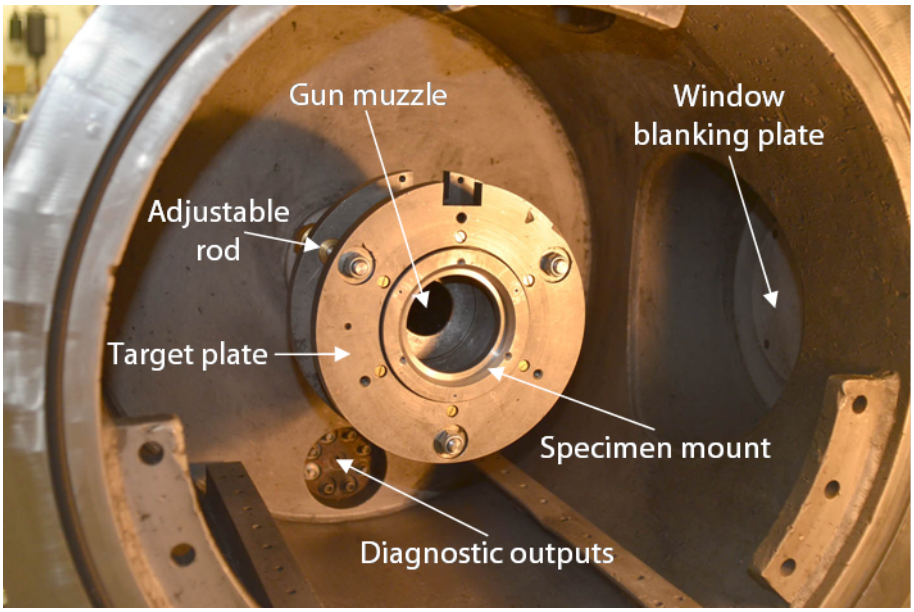

Figure 3.2: Target area of the plate impact facility. The specimen mount is held within an adjustable target plate attached to the muzzle of the gun. Three threaded rods, of which one is labelled, are used to adjust the tilt of the the target plate (and, hence, the target itself) with respect to the axis of the barrel. A number of BNC connections enable diagnostic outputs from within the target chamber. In addition, a number of windows for high speed photography are available. When not in use, these are covered with aluminium blanking plates.

A brass plug, with a hardened steel face, is inserted into the muzzle of the gun. The face of the plug is machined so that it is perpendicular to the axis of the barrel. An electronic dial indicator, the probe of which is mounted in a disc that can be held against the sample mount, is used to measure the position of the mount with respect to the face of the alignment plug. By repeated measurement of the displacement at three points, and careful adjustment of the threaded rods, it is possible to bring the specimen mount into alignment. The mount is considered aligned when the displacements measured at three

points differ by no more than $\pm 1\ \mu\mathrm{m}$.

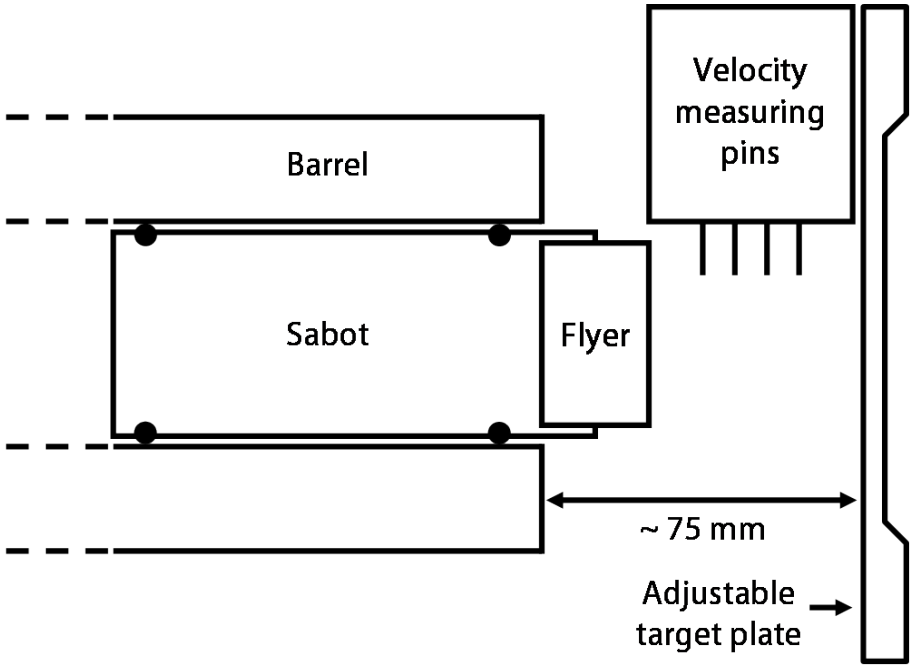

Figure 3.3: Schematic representation of the target area of the plate impact facility. For clarity, the adjustable rods on which the target plate is mounted (Figure 3.2) are not shown. On exiting the muzzle, the flyer makes contact with a series of pairs of thin conducting pins. The pins form an electrical circuit, which is completed at impact, producing a pulse on an oscilloscope. The velocity of the projectile is determined from the average time between pulses.

The target area is shown schematically in Figure 3.3. For clarity, the adjustable rods on which the target plate is mounted are not shown. Projectile velocity is measured immediately prior to impact. A series of eight thin ($0.3\,\mathrm{mm}$ diameter) pins, of either graphite or brass, are arranged in pairs above the path of the projectile and protrude approximately $5\,\mathrm{mm}$ vertically downwards in front of the flyer plate. As the flyer plate impacts each pair of pins, an electrical circuit is completed and a corresponding pulse recorded on an oscilloscope. The time between each pulse enables the velocity to be determined, and the impact velocity is given by the average velocity recorded from the four pairs of pins (three timings).

Experiments E081026A (flyer velocity $0.697\,\mathrm{mm}\mu\mathrm{s}^{-1}$, brass pins) and E081027A (flyer velocity $0.394\,\mathrm{mm}\mu\mathrm{s}^{-1}$, graphite pins) enabled an independent measure-

ment of projectile velocity by the use of streak photography [Courtney-Pratt, 1949]. Streak records, obtained with a DRS Lightning Digistreak camera, were compared to the measured velocity; an extract from such a streak record is shown in Figure 3.4. In each case, the velocities determined by the pins and by the streak record agree to within $1\,\%$. It is therefore concluded that the error on the measured impact velocity is $1\,\%$.

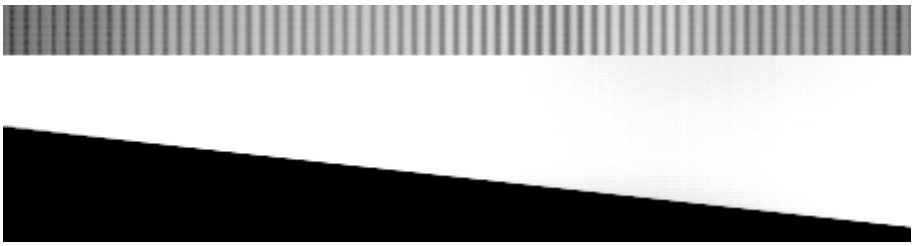

Figure 3.4: Extract from the streak image of E081026A. The black object is the leading edge of a flyer, travelling from left to right at $0.697\,\mathrm{mm}\mu\mathrm{s}^{-1}$. The time axis is increasing vertically downwards, with each pixel representing approximately $1.8\,\mu\mathrm{s}$. The vertical lines are spaced $1\,\mathrm{mm}$ apart, and are from a calibration image that has been artificially added to the image.

3.2 In-situ stress measurements

In-situ measurements of longitudinal stress are a key diagnostic in the experiments described in this thesis. One such diagnostic is the thin-foil piezoresistive gauge [Asay and Shahinpoor, 1993, §3.9.1]: the pressure-dependent resistance of a thin metallic foil can be used to measure the applied pressure.

The pioneering work of Bridgman [1917] measured the effect of static pressure on the resistance of a range of metals. Lawson [1956] discusses the use of pressure-dependent resistance to construct pressure gauges for high-pressure experiments. For such a gauge to be of use, it must be sensitive to the applied pressure, insensitive to temperature changes, and, preferably, must exhibit linear behaviour over the pressure range of interest. For these reasons manganin (an alloy of copper, manganese, and nickel), which has a low temperature coefficient of resistance and approximately linear pressure coefficient, has been used as piezoresistive pressure gauge. As the resistance change is dependent on the mode of the applied strain [Lawson, 1956], the resistance change due to an applied hydrostatic pressure is not the same as that due to an equivalent

uniaxial dynamic strain. Considering manganin as a perfect elastic-plastic material, Barsis et al. [1970] were able to measure the piezo-resistive coefficients in manganin under shock loading.

Figure 3.5 shows a commercial manganin foil gauge. It is a 'grid-like' gauge (LM-SS-125CH-048) and is supplied by Vishay Measurements Group U.K. Ltd. The nominal resistance of the gauge grid is $48\,\Omega \pm 1\,\%$ and it is mounted on a glass-fibre-reinforced epoxy-phenolic substrate.

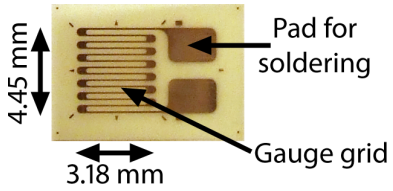

Figure 3.5: Thin-foil manganin gauges used in this work were supplied by Vishay Micro-Measurements, and consist of $48\,\Omega$ gauge (LM-SS-125CH-048) on a glass-fibre-reinforced epoxy-henolic substrate. As targets are larger than the gauges, in order to extract a signal from a gauge, 'legs' of copper shim are attached using a low-melting point solder.

The gauges pictured are embedded in experiments using a slow-setting low-viscosity epoxy. As the gauges are much smaller than the targets, in order to extract signals from the gauges 'legs' of $25\,\mu$m-thick copper shim are attached to the gauge with a low-melting-point Indalloy solder. When embedding gauges between conducting surfaces, $25\,\mu$m-thick sheets of either mylar or teflon (PTFE) are used to insulate the gauge. Samples are clamped between glass plates whilst the epoxy dries. The low-viscosity and long curing time ensure that, during the clamping process, any bubbles in the epoxy flow outwards, and ensures a uniform and thin glue layer. Total overall thicknesses of gauge packages are around $100\,\mu$m.

A Wheatstone bridge [Horowitz and Hill, 1989] is a measuring device capable of accurately determining, through a differential measurement, an unknown electrical resistance. For the bridge circuit shown in Figure 3.6, the output voltage is proportional to the size of the unknown resistance R_x and, hence, recording this voltage when the unknown resistance is a manganin gauge allows determination of the resistance of the gauge element. Using Kirchoff's Laws, the output voltage in an Wheatstone bridge may be calculated:

$$V_{\text{out}} = \left(\frac{R_x}{R_3 + R_x} - \frac{R_2}{R_1 + R_2} \right) V_{\text{supply}}, \tag{3.1}$$

where V_{supply} is termed the 'excitation voltage' of the bridge. The output voltage is zero, and the bridge described as 'balanced' when

$$\frac{R_x}{R_3} = \frac{R_2}{R_1}. \tag{3.2}$$

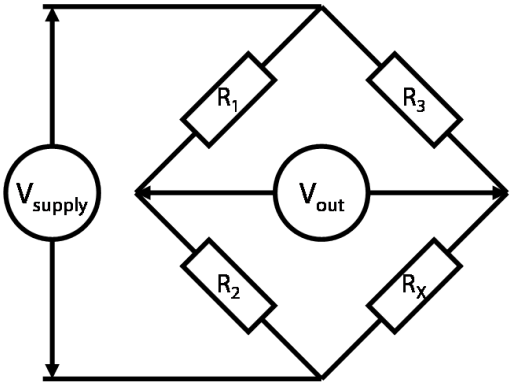

Figure 3.6: A Wheatstone bridge. The bridge is 'balanced', and V_{out} is zero, when $R_X = \frac{R_2}{R_1} R_3$.

In order to be sensitive to small resistance changes, the excitation voltage of the bridge must be large (of order $100\,\text{V}$). For the $48\,\Omega$ gauges used in this work, the resultant current in the gauge (around $2\,\text{A}$) would damage the gauge if applied continuously. Pulsed power supplies (Dynasen CK1-50/0.050-300 and Dynasen CK2-50/0.050-300) are used in this Laboratory to measure resistance histories of piezoresistive gauges. The power supplies have been modified in-house [Bourne and Rosenberg, 1997] in order to more accurately capture the fast transient resistance changes in gauges under shock compression.

Whilst the output of the Dynasen power supplies is roughly linear with respect to changes in the gauge's resistance, the output voltage changes with both the excitation voltage of the bridge and the resistance value at which it is balanced. In order to calibrate the bridge, and to enable the calculation of stress, the output voltage as a function of gauge resistance is measured before every experiment. The power supplies have an adjustable 'balance' resistance. Once a gauge has been connected to the power supply, the balance

resistance is adjusted such that the output voltage of the bridge is zero. After the bridge has been balanced, a number of well-defined resistances are placed in series with the gauge. These 'shunt' resistors mimic the effect of a changing resistance in the gauge. A typical shunt calibration is shown in Figure 3.7. A simple quadratic relation is used to fit the output voltage to a resistance change.

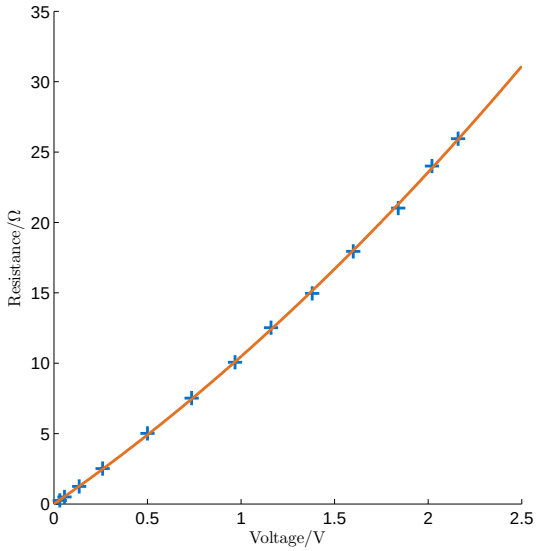

Figure 3.7: Gauge calibration, from experiment E090624B, to $\frac{\Delta R}{R_0} \approx 0.5$. The calibration curve is described by the equation $R = aV + bV^2$, with $a = 9.1699\,\Omega\mathrm{V}^{-1}$ and $b = 1.3072\,\Omega\mathrm{V}^{-2}$.

The calibration, relating the change in resistance of the gauge to the stress in the gauge, is dependent only on the geometry of the gauge element and, so, the calibration of foil-like manganin gauges to $18.1\,\mathrm{GPa}$ in plate impact experiments, reported by Rosenberg et al. [1980], can be applied to the gauges used in the present work. They found that the response of the gauge is elastic-plastic. Below the yield strength of the gauge, the gauge behaves elastically, and the resistance change varies linearly with stress:

$$\sigma = \frac{1}{k}\frac{\Delta R}{R_0}, \tag{3.3}$$

where $k = 1.95 \times 10^{-2}\,\mathrm{GPa}^{-1}$ is the one-dimensional piezoresistive constant

given by Rosenberg and Partom [1985]. The onset of plastic behaviour and, hence, the HEL of the gauge, is at a stress of $1.5\,\mathrm{GPa}$ [Rosenberg et al., 1980] Above the HEL, Rosenberg et al. [1980] fitted a fourth-order polynomial function to their data:

$$\sigma = A_0 + A_1\left(\frac{\Delta R}{R_0}\right) + A_2\left(\frac{\Delta R}{R_0}\right)^2 + A_3\left(\frac{\Delta R}{R_0}\right)^3 + A_4\left(\frac{\Delta R}{R_0}\right)^4, \qquad (3.4)$$

where $A_0 = 0.572\,\mathrm{GPa}$, $A_1 = 29.59\,\mathrm{GPa}$, $A_2 = 95.20\,\mathrm{GPa}$, $A_3 = -312.74\,\mathrm{GPa}$, and $A_4 = 331.77\,\mathrm{GPa}$. The fit, shown in Figure 3.8, passes within $2\,\%$ of all data points, with a standard deviation of $0.1\,\mathrm{GPa}$. Within error, this fit applies to multiple-shock loading as well as to single shocks [Rosenberg and Partom, 1985].

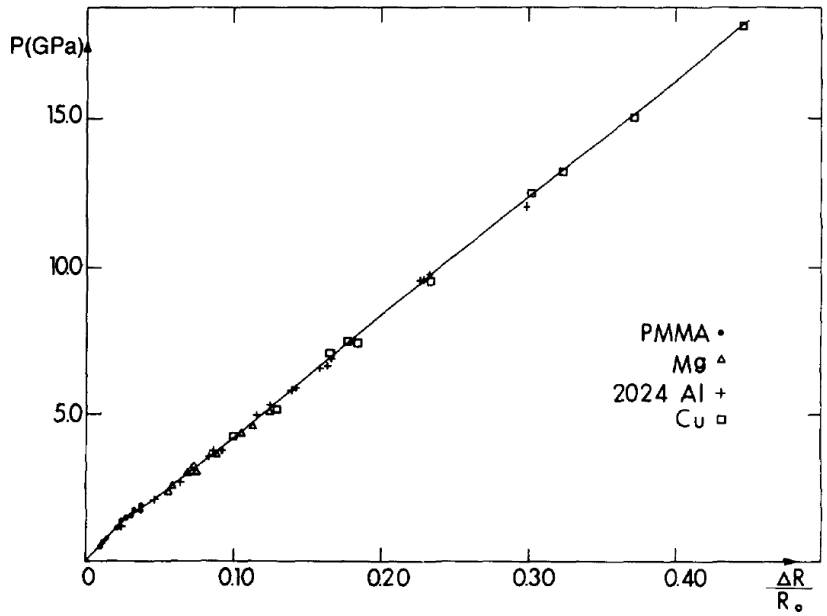

Figure 3.8: Calibration for manganin gauges, from Rosenberg et al. [1980]; the different data points represent different target materials. The fit is described by Equations 3.3 and 3.4 and passes within $2\,\%$ of all data points.

Due to the elastic-plastic nature of manganin, resistive hysteresis is observed on unloading. This hysteresis has been calibrated in the range 1.5–$15\,\mathrm{GPa}$ by Yaziv et al. [1980]. The calibration relates the in-material stress on unloading to the peak stress the gauge has been subjected to and the ratio of

measured resistance changes at each point. The normalised data obtained by Yaziv et al. [1980], relating the ratio of stresses to the ratio of resistances, is shown in Figure 3.9.

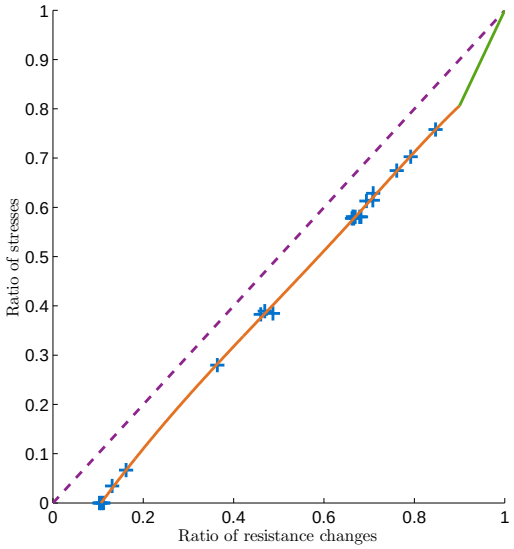

Figure 3.9: Manganin exhibits a strong resistive hysteresis upon unloading. Data relating the resistance changes and stress in the partially unloaded states to those at the peak stress are from from Yaziv et al. [1980]. The unloading data is described, in the plastic region, by Equation 3.5. For stresses above $80\,\%$ of the peak stress, the fit is undefined and ideal reverse elastic yielding has been assumed.

A non-linear least-squares method was used in Matlab to fit a fifth-order polynomial to the data:

$$\begin{aligned}\frac{\sigma_{\text{release}}}{\sigma_{\text{peak}}} = M_0 \quad &+ \quad M_1\left(\frac{\Delta R_{\text{release}}}{\Delta R_{\text{peak}}}\right) \\ &+ \quad M_2\left(\frac{\Delta R_{\text{release}}}{\Delta R_{\text{peak}}}\right)^2 + M_3\left(\frac{\Delta R_{\text{release}}}{\Delta R_{\text{peak}}}\right)^3 \\ &+ \quad M_4\left(\frac{\Delta R_{\text{release}}}{\Delta R_{\text{peak}}}\right)^4 + M_5\left(\frac{\Delta R_{\text{release}}}{\Delta R_{\text{peak}}}\right)^5,\end{aligned} \tag{3.5}$$

where $M_0 = -0.1375$, $M_1 = 1.3995$, $M_2 = -0.3768$, $M_3 = -1.1112$, $M_4 = 2.5171$, and $M_5 = -1.3515$.

The fit, which passes within $1\,\%$ of the data, is valid to

$$\frac{\Delta R_{\text{release}}}{\Delta R_{\text{peak}}} = 0.9, \text{and} \frac{\sigma_{\text{release}}}{\sigma_{\text{peak}}} = 0.8. \tag{3.6}$$

As noted by Yaziv et al. [1980], the calibration above this region is uncertain and difficult to determine experimentally. In the analysis discussed below, the resistive hysteresis is taken to be linear in this region, as the gauge is assumed to undergo reverse yielding and hence, initially, unloads elastically.

The data reduction procedure, then, for manganin gauges combines the calibration results described above. The initial resistance of the gauge, R_0, is measured at multiple stages during the construction of a target to ensure that no damage (indicated by a resistance that differs greatly from the nominal gauge resistance) has occurred. A four-terminal digital multimeter (Keithley 2100) enables high-precision measurements of the initial resistance to be made. Simple Matlab routines have been written to calculate the fitting parameters necessary to convert bridge output voltages into resistance change (Figure 3.7) and to reduce the data to a stress–time history using Equations 3.3, 3.4, and 3.5.

3.3 Particle velocity diagnostics

In addition to measurements of in-material longitudinal stresses, direct measurements of particle velocity have been accomplished through the use of interferometric techniques. One diagnostic that has been used on the Cavendish plate-impact facility is the VISAR interferometer. The *Velocity Interferometer System for Any Reflector* (VISAR) was developed by Barker and Hollenbach [1972]. A detailed overview of the development of VISAR is not relevant to the present discussion, and the interested reader is directed to the historical overview given by Barker [2000] or the technical descriptions given by Dolan [2006]. The basic principal of all VISAR systems is to interfere laser light that has been reflected from a target at two different times. Due to the relativistic Doppler effect, light reflected from a moving surface undergoes a change in phase [Barker and Hollenbach, 1972]. The fringe pattern that results from interfering light reflected from the moving surface at two different times is related to the relative changes in phase and, hence, to the velocity of the surface.

The VISAR system used with the plate impact facility uses the 'modified quadrature' or 'push-pull' design proposed by Hemsing [1979]. Figure 3.10

shows schematically Hemsing's VISAR interferometer. The particular system available in the Cavendish (VMBV-04-1027-532, produced by Valyn V.I.P. Ltd.) is capable of simultaneous measurements at up to three distinct points, using a neodymium-doped yttrium orthovanadate (Nd:YVO_4) solid-state laser, frequency doubled by a LiB_3O_5 crystal to $532\,\mathrm{nm}$ (Coherent Verdi V5). Light for each beam is carried to the target in a $50\,\mu\mathrm{m}$-core optical fibre, and returned to the interferometer in a $300\,\mu\mathrm{m}$-core fibre. The interferometer is schematically identical to that shown in Figure 3.10. After passing through a collimator, an ultranarrow bandpass filter (UBNP) prevents light not at the laser wavelength from entering the interferometer. Light from each beam is split by the principal beam splitter, BS, with half traveling through the delay leg. The uncompensated components that make up the delay leg are the remaining glass of the beam splitter, up to four etalons, E, and the waveplate, WP. The wave plate can be rotated axially to ensure the phase difference between the two polarisations, β, is $\pi/2$. This splitting of polarisations ensures that whenever the interference in one polarisation results in a minimum of the detected signal, the other polarisation gives a maximum, resulting in no loss of sensitivity near the minima. Upon reflection at the mirror M2, this delayed light passes back to the beam splitter. The remaining light travels through free space to the mirror, M1, in the reference leg before returning to the beam splitter. M1 is mounted on three piezoelectric elements, the voltage supplied to which can be adjusted to align the interferometer. Finally, this recombined light travels to the two polarising beam splitters. The four output beams associated with each input beam are collected into optical fibres, that take the outputs to a separate 'beam module'. The beam modules contain the necessary optoelectronic components to allow for velocity histories to be reduced from the ouptut beams of the interferometer.

The details of the analysis are not relevant to the present discussion and have been described adequately elsewhere [Dolan, 2006; Hemsing, 1979]. A detailed analysis of the performance of the VISAR system used in the Cambridge plate impact facility is reported by Chapman [2009].

3.4 Sample preparation and design

In addition to requiring that the target is well-aligned, as discussed above, it is important that the flyer plate and target plates are machined both flat and parallel, as any mis-machining will have the same effect as a poorly-aligned

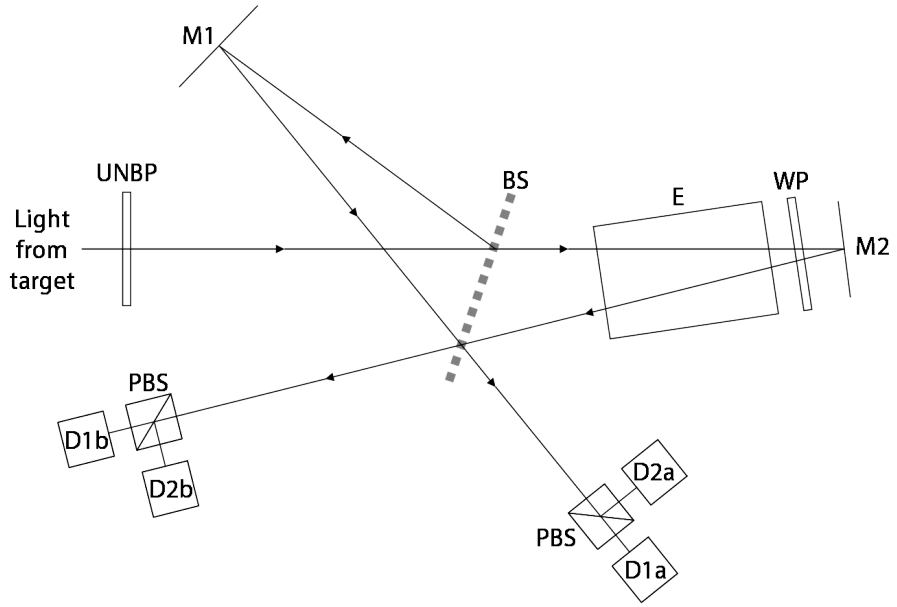

Figure 3.10: Hemsing's modified quadrature VISAR interferometer, the 'push-pull' VISAR after Dolan [2006]. The interferometer consists of a principal beam splitter (BS), a number of glass etalons (E), a one-eighth waveplate (WP), two mirrors (M1, M2), polarising beam splitters (PBS) and photomultipliers (D1a, D1b, D2a, D2b). Light not at the laser wavelength is rejected by an ultra-narrow bandpass filter (UNBP).

target.

A vacuum chuck has been designed in-house to enable the machining of target plates to the required degree of planarity. The chuck is fixed to the bed of a CNC mill, and skimmed flat. Target plates are then skimmed to near the final thickness by placing them on the chuck and skimming one face. The plates are turned over and the reverse face is then skimmed to reduce the plate to the required thickness. This also ensures that both faces are parallel. With this process, plates as thin as $1\,\mathrm{mm}$ are skimmed flat, and parallel, to, typically, better than $\pm 2\,\mu\mathrm{m}$.

For reasons discussed in Section 3.5 below, two main sabot designs were used in the experiments reported in this thesis: the older 'Mark II' polycarbonate design (Figure 3.11), and the new 'Mark III' nylon design (Figure 3.12).

Both designs have three variants: the 'standard', which has a solid polymer body; the 'lightweight', which has material drilled from it, and allows

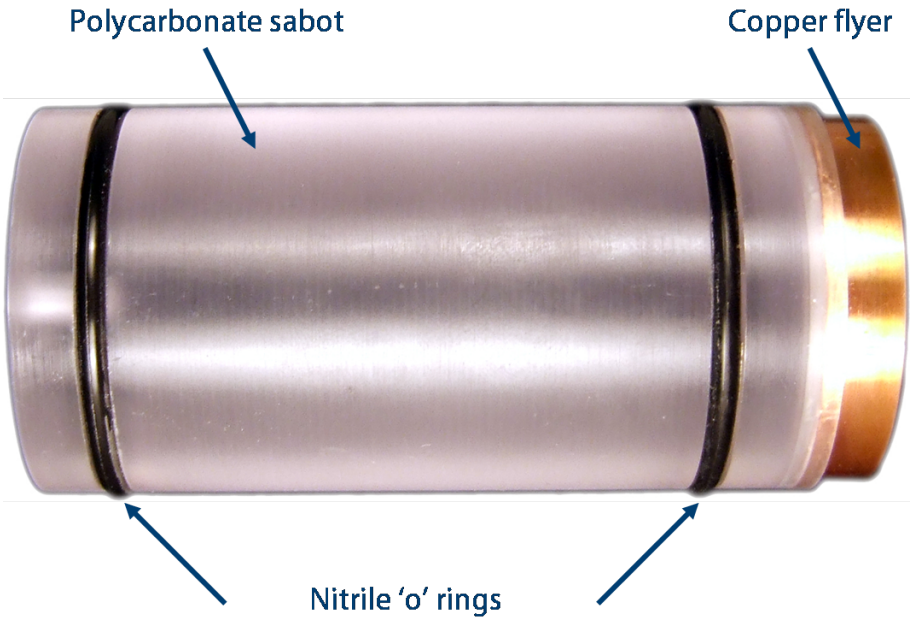

Figure 3.11: The standard 'Mark II' sabot, machined from a solid polycarbonate cylinder to an outer diameter of $50.60^{+0.00}_{-0.10}$ mm, is shown with a copper flyer plate. The 'o'-rings are placed on the sabot prior to firing, and form the seal of the firing reservoirs. The front face of the flyer plate is skimmed and/or lapped after being attached to the sabot to ensure the front face is perpendicular to the sabot's axis.

for higher velocities to be achieved for a given gas pressure; and the 'heavyweight', which has a brass cylinder inserted in it. Lower firing pressures tend to result in less reproducible projectile velocities; the increased mass of the heavyweight projectiles necessitates an increase in firing pressure and, hence, results in more reproducible velocities. In all variants there is a recess behind the flyer plate. A small hole is drilled through the sabot wall into this recess. Thus, the space behind the flyer is evacuated with the expansion chamber and barrel. In this way, the rear surface of the flyer releases fully, as a free surface, rather than partially, from the interface between the flyer and the polymer.

Figure 3.13 superposes a sabot in its pre-firing position in the breech of the gun. The two 'o'-rings seal the openings of the firing reservoirs whilst they are being filled. In order to ensure that the sabot remains in place prior to firing, a vacuum is drawn behind it. When the gun is to be fired, a small amount of air is allowed in behind the sabot. The sabot then begins to drift along

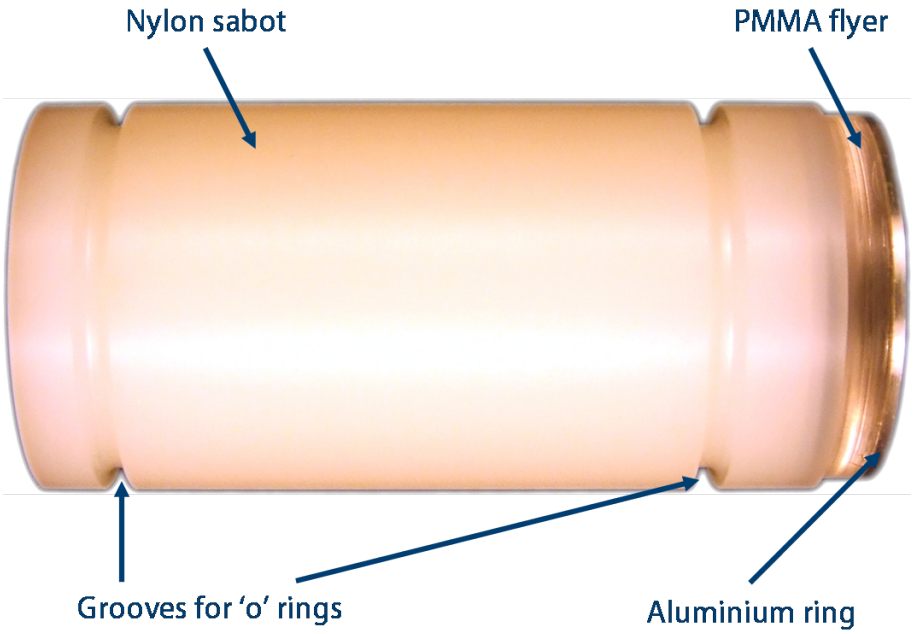

Figure 3.12: The standard 'Mark III' sabot, constructed from a nylon 6,6 rod that is preground to an outer diameter of $50.75^{+0.00}_{-0.05}$ mm, is shown with a PMMA flyer plate. An aluminium ring is placed on non-conducting flyers to enable velocity measurements. The grooves in which the 'o'-rings sit are clearly visible.

the barrel until the rear 'o'-ring no longer seals the firing reservoirs. At this point, the full pressure of the firing gas expands into the barrel, accelerating the projectile towards the target.

The diagnostic techniques described above, and the equations derived in Chapter 2, assume the propagation of a steady planar shock. In order, therefore, that the analysis remains valid, diagnostics must be employed only where the strain is uniaxial and the wave steady. Longitudinal and lateral releases will erode these conditions and, therefore, the effect of release waves must be considered when designing plate impact targets.

At impact, in addition the forward-moving shock which propagates into the target, a backward-moving shock propagates into the flyer plate. As shown schematically in Figure 3.14, interaction of this shock with the rear of the flyer plate results in a forward-moving release wave propagating into the target.

As noted in Chapter 2, this release propagates as a fan across a range of de-

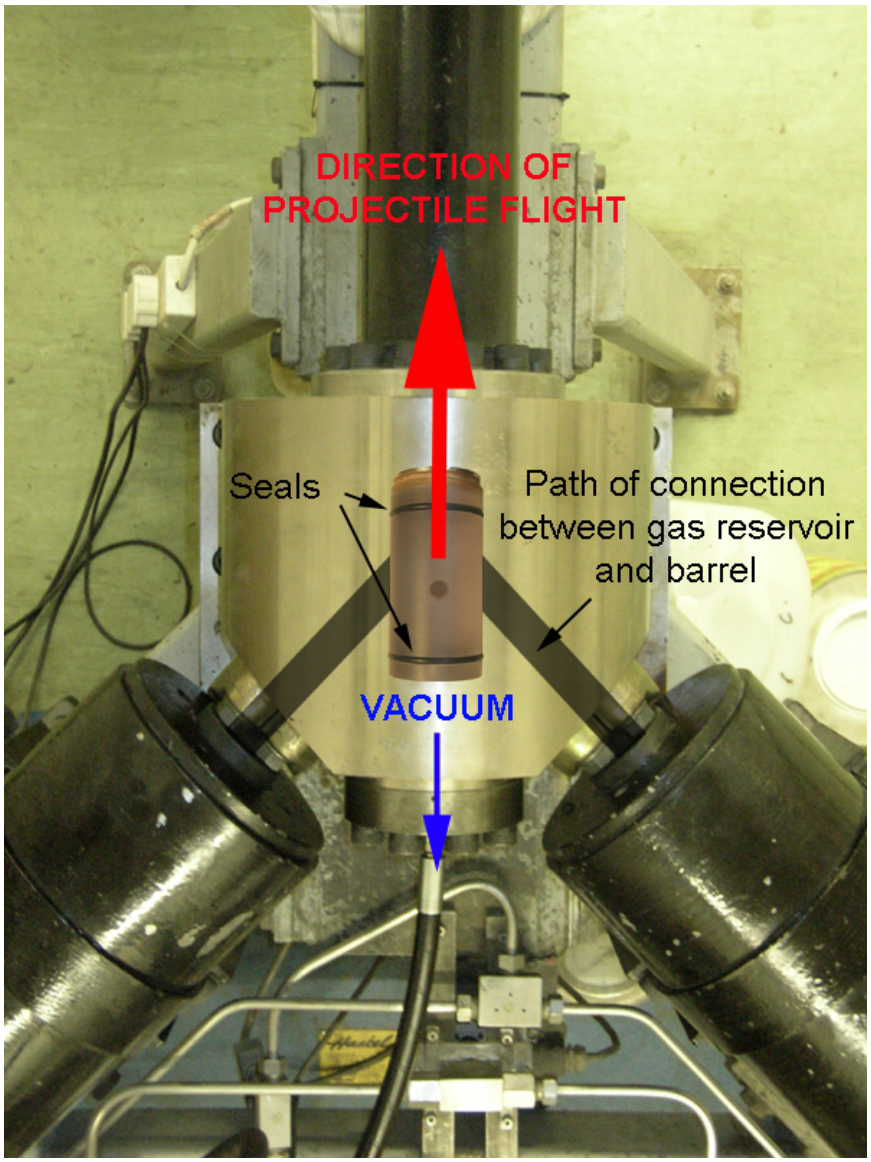

Figure 3.13: The breech of the Cavendish gun, with a sabot superposed in its pre-firing position. A vacuum is drawn behind the projectile to hold it in place, and the 'o'-rings form a seal against the openings of the firing reservoirs. When the vacuum behind the projectile is released, the projectile drifts forward and ceases to seal the firing reservoirs. At this point, the firing gas is released and accelerates the projectile along the length of the barrel. From Braithwaite [2009].

creasing velocities. The first, fastest, characteristic of the fan is an elastic wave propagating at $C + u_p$, where C is the local sound speed, and may be approximated by the ambient pressure longitudinal sound speed. The point at which the shock ceases to be steady, defined by the interaction of the shock with the first release characteristic, can be calculated by simply considering the propagation of the forward-moving shock and the backward-moving shock, and the propagation of the release wave through the partially-compressed medium.

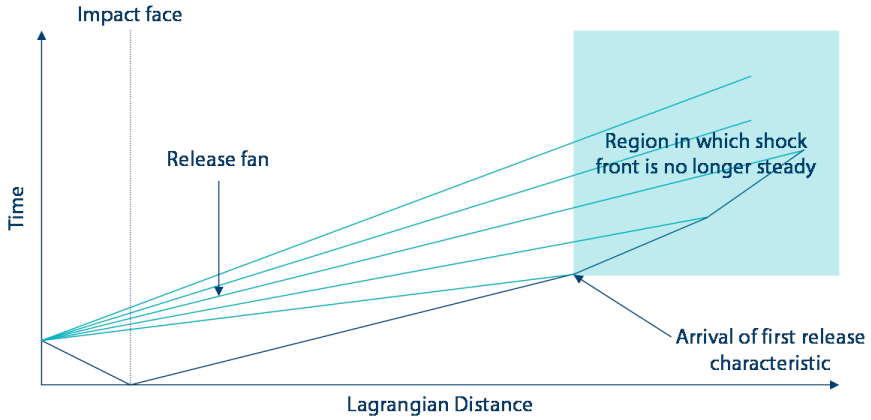

Figure 3.14: Schematic representation of longitudinal release wave propagation from the rear of a flyer plate. The shock propagating into the target remains steady until is caught by the first release characteristic.

In the conventional plate impact scenario, the flyer plate is generally of a smaller diameter than the target plate. Immediately, then, upon impact, release waves propagate into both the target and flyer from material outside the original impact area. The analysis below, following that of Swift and Kraus [2008], derives an equation governing the propagation of lateral release waves into the target. It is only necessary to consider the leading characteristic of the release fan, as it is this characteristic which first erodes the condition of uniaxial compression in the target.

Considering the frame co-moving with the shocked material, as shown in Figure 3.15, the lateral release propagates as a spherical wave moving at the bulk sound speed of the shocked state, c_r.

At a time Δt, the shock will, in this frame, have moved a distance $(U_S - u_p)\Delta_t$. The radius encompassed by the lead lateral release characteristic at this time is $c_r \Delta t$, and, hence, the angle ϕ' along which the 1D strain becomes

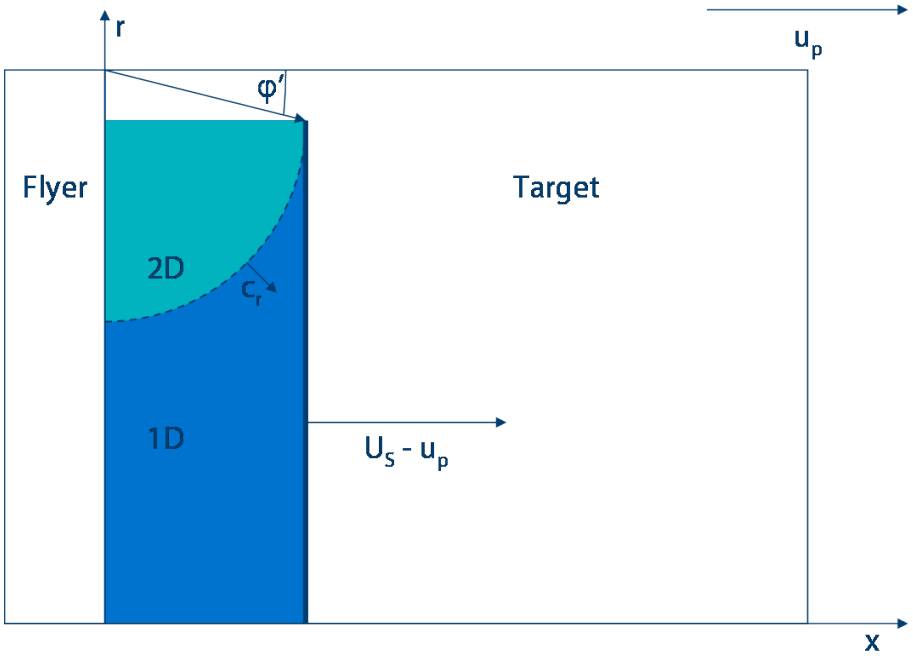

Figure 3.15: Schematic representation of lateral release wave propagation into a target in a frame co-moving with the shocked material. The vertical axis is distance from the axis of symmetry.

(in cylindrical polar co-ordinates) 2D is given, in the co-moving frame, by

$$\phi' = \cos^{-1}\left(\frac{U_S - u_p}{c_r}\right). \tag{3.7}$$

So this relation may be of use, it is necessary to find the angle ϕ along which the shock becomes two dimensional in the laboratory frame. This is accomplished by a Gallilean transformation from the shock frame, which moves at u_p with respect to the laboratory frame. Thus,

$$\phi = \tan^{-1}\left(\frac{\sqrt{c_r^2 - (U_S - u_p)^2}}{U_S}\right). \tag{3.8}$$

A similar expression holds for the release in the flyer itself. It is often convenient to assume that the ϕ is approximately $45\,^\circ$, which - in most cases - gives an over-estimate of the angle at which the releases propagate. The angle of release may be used to calculate the diameter over which the shock

remains uniaxial. For an Lagrangian distance l_0 into the target, a shock of radius r_0 leaves a radius r_1 under uniaxial compression:

$$r_1 = r_0 - 2l_0\phi. \tag{3.9}$$

In designing shock experiments, it is important to ensure that the diagnostics are within a region that has not been laterally released and, therefore, Equation 3.9 is used to determine where such diagnostics may be placed.

3.5 Measurement of impact tilt in plate-impact experiments

Consider a target at some small angle, Θ, to an impactor, travelling at velocity u_{impact}, as shown schematically in Figure 3.16. A shock is produced in the target and travels perpendicular to the impact face at U_S; the point of contact moves across the impact face at u_{contact}.

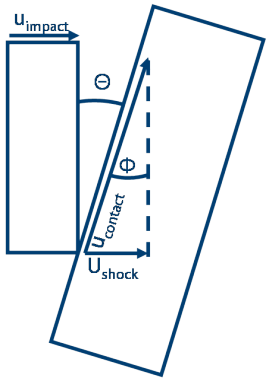

Figure 3.16: For an impactor incident on a target at some small angle Θ, the shock front moves at some greater angle, Φ, to the front surface of the target.

By the small-angle approximation, the velocity of the contact point is

$$u_{\mathrm{contact}} = \frac{u_{\mathrm{impact}}}{\sin(\Theta)} \approx \frac{u_{\mathrm{impact}}}{\Theta}. \tag{3.10}$$

The angle made by the shock to the impact face, Φ, is given by

$$\sin(\Phi) \approx \Phi = \frac{U_{\mathrm{shock}}}{u_{\mathrm{contact}}}, \tag{3.11}$$

and, hence, from Equation 3.10,

$$\Phi \approx \frac{U_{\text{shock}}}{u_{\text{impact}}}\Theta. \tag{3.12}$$

As the shock velocity is, generally, greater than the impact velocity, the tilt of the shock is larger than the physical tilt. This multiplication of the physical misalignment can have a significant effect on any measurements. For example, the tilt results in straining of manganin gauges, leading to erroneous measurements of stress.

An unknown Hugoniot is most efficiently determined by measurement of the relationship of shock velocity to particle velocity. The simplest such method is to determine the 'time of flight' of a shock wave through a known thickness of the material under consideration. Measurement of the arrival of the shock wave at two longitudinally separate points enables the transit time, and hence, shock velocity, to be determined.

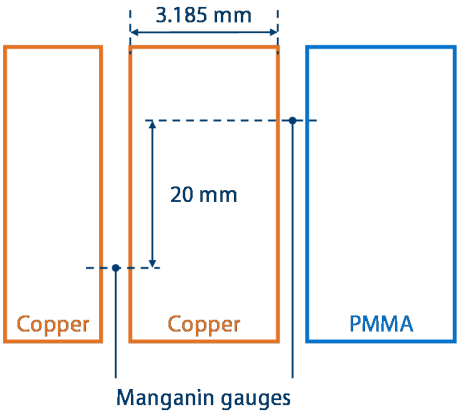

Figure 3.17: Schematic representation of the target used in Experiment E100211A. Two manganin gauges are separated longitudinally by a $3.185\,\text{mm}$-thick copper plate and laterally spaced $20\,\text{mm}$ apart. The measured shock velocity recorded between the two gauges will be sensitive to any impact tilt.

In the case where these two measurement points are separated laterally and longitudinally, then tilt of the shock wave will distort the measured shock velocity. Experiment E100211A, shown schematically in Figure 3.17, demonstrates the effect of tilt on the determination of shock velocity in copper. Comparison of the shock velocity predicted from the linear U_S–u_p Hugoniot given by Asay and Shahinpoor [1993], and that measured in E100211A, enables a measure of the tilt across the diameter on which the gauges lie. After the

impact of a copper flyer at $0.389 \pm 0.004\,\mathrm{mm}\mu\mathrm{s}^{-1}$, experiment E100211A indicated a shock velocity of $4.224 \pm 0.022\,\mathrm{mm}\,\mu\mathrm{s}^{-1}$, compared to the calculated value of $4.519 \pm 0.006\,\mathrm{mm}\,\mu\mathrm{s}^{-1}$. The impact tilt required to account for this discrepancy is approximately $30\,\mathrm{mRad}$. However, as E100211A measured shock arrival times at only two points, the tilt measurement is under-constrained, and a greater tilt could exist in some other direction. Additionally, a tilted shock introduces an uncertainty in the stress value measured by a manganin gauge, as the loading is no longer perpendicular to the gauge face and the calibration no longer applies. Therefore, in measuring impact tilt, it is desirable to use more than two points and to use a point-like diagnostic, rather than a gauge or other diagnostic with significant lateral extent.

Experiment E100312A employed two diagnostics to measure impact tilt: VISAR and optic fibres; the experimental geometry is shown schematically in Figure 3.19. As a gas is compressed adiabatically, it is strongly heated and will, ultimately, emit light. Whilst plate impact experiments are conducted under vacuum, there is sufficient residual gas between the target and flyer plate to generate an 'impact flash' as the gap between the two surfaces is closed. An optical fibre flush to front surface of a target plate is able to detect light output as the flyer impacts the target. A series of such fibres is therefore able to resolve impact tilt. Figure 3.18 shows the normalised output of a photodiode for a $400\,\mu\mathrm{m}$ silica core optic fibre flush to the front surface of an aluminium target impacted by an aluminium flyer plate at an impact velocity of $0.391\,\mathrm{mm}\mu\mathrm{s}^{-1}$. The first peak, at around $1\,\mu\mathrm{s}$, is the impact flash, the tail features of this peak depend partially on how well the fibre was polished. In around half of the photodiode traces a secondary peak, smaller in amplitude, is seen. This peak occurs at around $14\,\mu\mathrm{s}$ in Figure 3.18. This peak is attributed to triboluminescence [Smiel and Fisher, 1982]. As the silica core is fractured by the passage of the shock wave, light is generated. This process occurs on a much longer time-scale than impact flash, and the light output is observed well after the target is no longer in a state of uniaxial strain. In the determination of impact tilt, then, it is the impact flash which is considered.

Figure 3.20 shows the impact flash measured by the three silica core optic fibres, shown in Figure 3.19. Three different photodiodes were used, each with a different sensitivity; the detector outputs have been normalised for ease of comparison. One detector produced a larger-than-expected output voltage, resulting in the trace being 'clipped'.

For a series of detectors i, placed at angles ϕ_i around a circle of radius R,

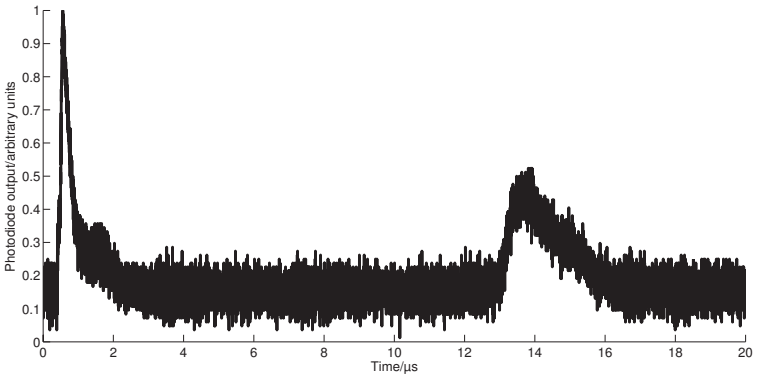

Figure 3.18: Normalised photodiode output from experiment E100312A. The initial peak, at $1\,\mu$s is due to impact flash; the secondary peak, at $14\,\mu$s is triboluminescence caused by fracture of the fibre itself.

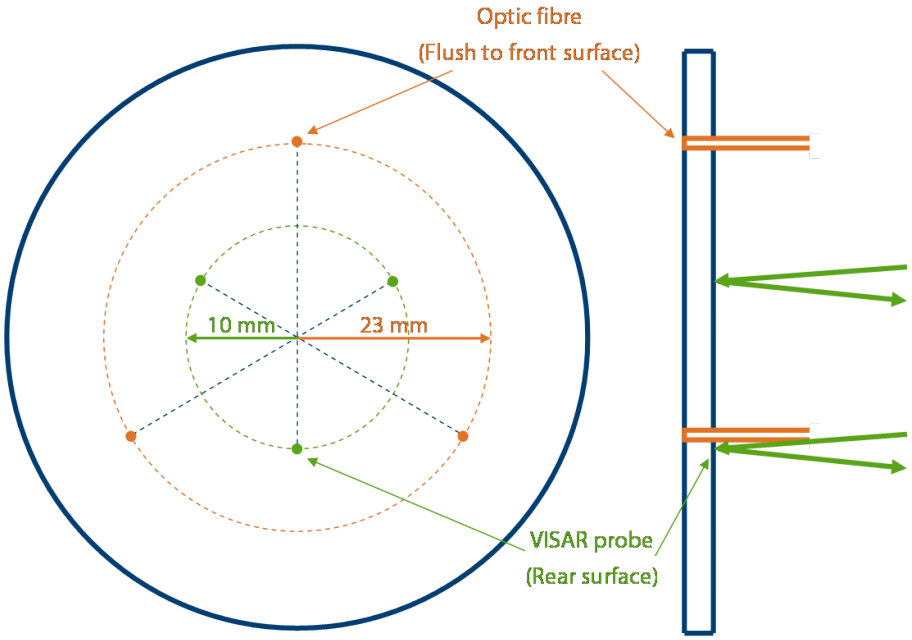

Figure 3.19: Schematic representation of the target used in experiment E100312A. The target, a $3\,\mathrm{mm}$ thick aluminium plate, held three $400\,\mu\mathrm{m}$ silica core optic fibres normal to the impact face and flush with the front surface, spaced equally around a circle of radius $23\,\mathrm{mm}$. The rear surface was illuminated with three beams from the Cavendish's multibeam VISAR system, equally spaced around a circle of radius $10\,\mathrm{mm}$, offset by 60° with respect to the silica fibres.

Mitchell and Nellis [1981] relate the deviation between the arrival time at any detector, t_i and the average arrival time, $\bar{t}$, to the tilt through the relationship

$$t_i - \bar{t} = \frac{-R}{u_{\text{impact}}} \tan(\theta) \cos(\alpha_0 + \phi_i), \tag{3.13}$$

where θ is the amplitude of the tilt; this maximal tilt occurs along a diameter at α_0 to the first diagnostic to respond ($\phi_0 = 0$). By determining the average arrival time at all three detectors and fitting the arrival time data to Equation 3.13 the maximal tilt, as measured by the three optic fibres, was found to be $9.4 \pm 0.1\,\text{mRad}$ at an angle of $77\,^\circ$ to the vertical.

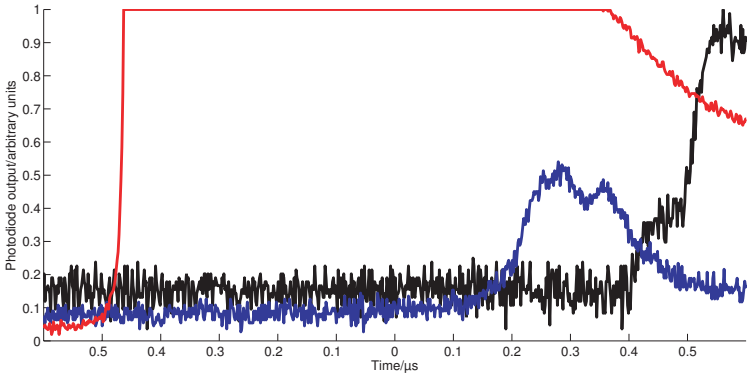

Figure 3.20: Normalised photodiode outputs, from experiment E100312A; times, in microseconds, are relative to the average arrival time at all three detectors. Deviations from the average arrival time are -0.53, $+0.12$, and $+0.40\,\mu$s indicating a tilt of $9.4 \pm 0.1\,\text{mRad}$ at an angle of $77\,^\circ$ to the vertical.

The rear surface of the target was illuminated with three probes from the Cavendish's multi-beam VISAR system, arranged around a circle of radius $10\,\text{mm}$. The arrival time of the elastic precursor, as measured by the three probes, was used to calculate the maximal tilt. The tilt, as measured by the VISAR, was $9.1 \pm 0.1\,\text{mRad}$ at an angle of $123\,^\circ$ to the vertical. That the angle of maximal tilt deduced from the VISAR data is not the same as that deduced from the photodiode data is attributed to difficulties in ensuring the mount that holds the VISAR probes is accurately positioned, and that the rear surface of the target is parallel to the front surface.

Experiment E100312A demonstrated that impact flash, as measured by embedded silica-core fibres and photodiodes, could be used to measure dy-

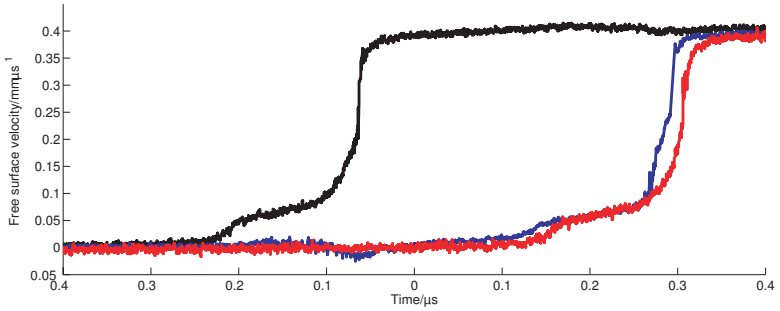

Figure 3.21: VISAR traces, from experiment E100312A. The fringe constant, K_{VPF}, was $187.5\,\mathrm{mm}\,\mu\mathrm{s}^{-1}$. The deviations from the average arrival time are -0.23, $+0.11$, and $+0.13\,\mu\mathrm{s}$ indicating a tilt of $9.1 \pm 0.1\,\mathrm{mRad}$ of $123\,^{\circ}$ to the vertical.

namic tilt in plate impact experiments. Tilt measured in this way agreed with the tilt measured by multi-beam VISAR. However, in order to accurately and reliably resolve both the magnitude and phase of the tilt, more than three measurement points are required; for this reason, the Cavendish's multi-beam VISAR system is not suited to measuring dynamic tilt. In addition, as VISAR measures shock arrival at the rear of the target, in order that lateral releases have not affected the shock, the thickness of the target would be limited. It was concluded that measuring tilt with a number of embedded silica-core fibres would be the simplest and most effective method.

Three principal contributions to the dynamic tilt measured in a plate impact experiment, shown schematically in Figure 3.22, are (i) misalignment of the target itself, (ii) misalignment of the flyer plate, and (iii) balloting of the sabot. In order to reduce the tilt at impact, each of these contributions were considered.

The adjustable alignment system, described above, is designed to allow targets to be aligned to significantly better than $1\,\mathrm{mRad}$. Over time, the threads that hold the alignment plate in place become worn and allow the alignment plate to 'slip' after it has been aligned. The system was rebuilt with reduced clearances allowed between the moving threads in order to allow for finer adjustment and reduce any 'slip' in the system. In addition, the 'alignment plug,' was re-machined to ensure its front face was perpendicular to the bore of the barrel. The conventional alignment system, described above, relies on a dial indicator that is held in place by manually applying pressure. Variations

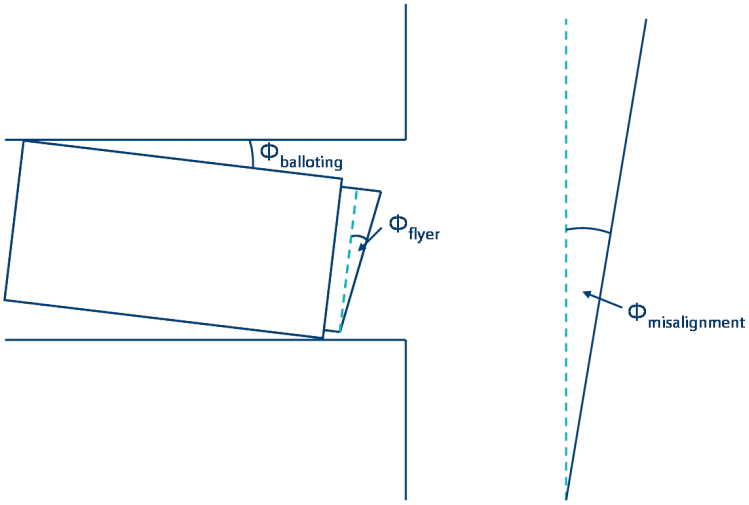

Figure 3.22: Dynamic tilt at impact, in the conventional plate impact geometry, can be considered as the sum of three independent effects: misalignment of the target plate with respect to the normal to the barrel axis; misalignment of the flyer plate with respect to the normal to the sabot axis; and balloting of the sabot.

in the force with which the indicator is held in place can result in changes in the measured displacement, thus affecting the alignment by an unquantifiable amount. A new dial indicator system was manufactured in order to eliminate this uncertainty. The dial indicator probe is mounted in a brass disc and the disc is held in place by three stiff spring steel clips; the clips provide a strong and constant force holding the indicator in place.

A Michelson interferometer has been used as an alternative method of aligning targets perpendicular to the barrel. The interferometer, shown schematically in Figure 3.23, was constructed by Dr. Daniel Eakins of the Institute of Shock Physics, Imperial College. In order to test the accuracy of the dial indicator system, the interferometer was used to align a mirrored target. The mirror was removed, and the dial indicator used to measure the position of the alignment plate. The plate was found to be perpendicular to the axis of the barrel to within $25\,\mu\mathrm{m}$. By providing an independent measurement, the interferometer demonstrates that the improved dial indicator system allows for targets to be aligned to within $0.5\,\mathrm{mRad}$. The accuracy of inteferometer system is limited by the the position of the laser beam with respect to the axis of the barrel. If the beam is off-axis, or the two ends of the barrel are not paral-

lel (i.e., the barrel is not straight), then a misalignment with respect to the dial indicator will be observed. It is therefore concluded that the dial indicator is accurate to, at worst, $0.5\,\mathrm{mRad}$.

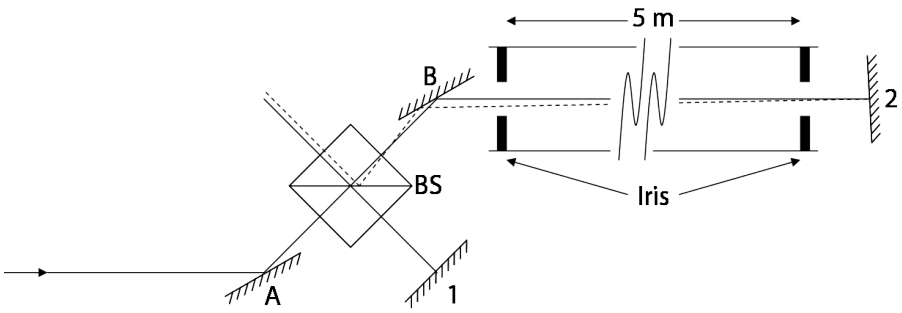

Figure 3.23: The Michelson inteferometer used for alignment in the plate impact facility. Incident laser light is directed centrally through the barrel of the gun by adjusting the mirrors A and B. An iris is inserted at each of the barrel to allow for more precise positioning of the beam. A beam splitter, BS, is used to split half the incident light; this light is reflected back to the beam splitter by mirror 1 and forms one 'leg' of the interferometer. Mirror 2 is mounted in place of a conventional target and reflects light back down the barrel to the beam splitter. If the target is not aligned correctly, the reflected light (dotted line) will not co-incide with the incident light, and two spots will be visible on the viewing screen. For light of a large enough coherence length, Fizeau fringes can be observed near perfect alignment; if mirror 2 is perfectly aligned, Haidinger fringes will be visible.

Whilst the sabot itself is machined in a single operation on a lathe, ensuring that, to within machining tolerances, the front face is perpendicular to both the sabot axis and the outer diameter, flyer plates are attached in a separate process as discussed above. Two distinct types of misalignment can exist in a completed sabot, as shown in Figure 3.24: a pure tilt of the front surface with respect to the normal to the sabot axis, and a concave (or convex) bowing of the front surface. This latter type may be introduced due to tolerances in the lathe used to 'skim' the front of the flyer. In a typical lathe, the permitted tolerance of the mechanisms that could contribute to this bowing are such that the machined surface is planar to significantly better than $5\,\mu\mathrm{m}$. The introduction of a pure tilt should not be possible in a well-maintained lathe, as the lathe's axis is perpendicular to the tool's direction of travel to within a high degree of tolerance.

In order to measure both tilt and bowing, an accurate dial indicator was

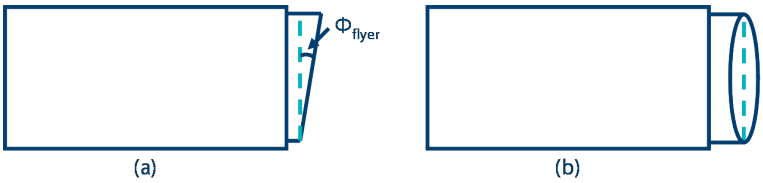

Figure 3.24: Misalignment of the flyer plate, with respect to the normal to the sabot axis, takes two forms: pure tilt (a), and concave or convex bowing (b).

placed in the toolpost of a well-aligned lathe whilst a finished sabot was rotated in the chuck. Typical measurements indicated a bowing of less than $5\,\mu\mathrm{m}$ and that flyer plates were perpendicular to the axis to within $5\,\mu\mathrm{m}$; both these measurements are at the maximum attainable measurement accuracy for the lathe used, and correspond to a pure tilt of order $1\,\mathrm{mRad}$.

Experiment E100415A employed six photodiodes, equally spaced around a radius of $20\,\mathrm{mm}$, to measure the tilt of an aluminium flyer plate, flat to $\pm 4\,\mu\mathrm{m}$, incident on an aluminium target plate ($3.056 \pm 0.010\,\mathrm{mm}$) at $0.396\,\mathrm{mm}\mu\mathrm{s}^{-1}$. The target was aligned to within $1\,\mathrm{mRad}$. Two of the detectors recorded no output; the remaining photodiode outputs are shown in Figure 3.25, with output voltages normalised. By fitting Equation 3.13 to the data, the resultant tilt at impact was found to be $4.4 \pm 0.8\,\mathrm{mRad}$. at an angle of $-40°$ to the vertical.

Balloting, the in-bore yaw of a projectile, is a well-known phenomenon in the study of interior ballistics [Ansari and Baugh, 1986]. Simplistically, the maximum possible balloting angle can be calculated by considering the angle of yaw that can be introduced due to a projectile of diameter d_{sabot} in a barrel of (larger) bore d_{bore}, as shown schematically in Figure 3.26.

For a sabot of length L_{sabot}, this maximum balloting angle occurs when

$$d_{\mathrm{bore}} = L_{\mathrm{sabot}} \sin(\Phi_{\mathrm{balloting}}) + d_{\mathrm{sabot}} \cos(\Phi_{\mathrm{balloting}}). \tag{3.14}$$

For small angles, however, the balloting angle may be expressed as

$$\Phi_{\mathrm{balloting}} \approx \frac{d_{\mathrm{bore}} - d_{\mathrm{sabot}}}{L_{\mathrm{sabot}}}. \tag{3.15}$$

The gun of the Cavendish plate impact facility has an internal bore of $50.80\,\mathrm{mm}$ near the muzzle, as measured by a dial bore gauge. The bore is approximately $50.85\,\mathrm{mm}$ near the breech, where repeated insertion of the breech plug has widened the internal diameter somewhat.

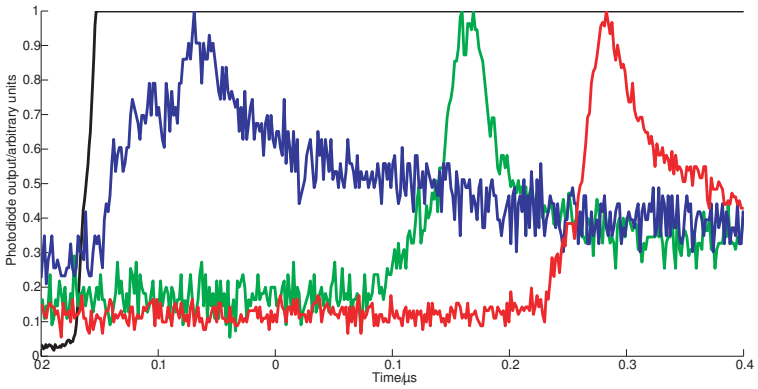

Figure 3.25: Photodiode response, from experiment E100415A. Detector output has been normalised to the range $[0 : 1]$ and times, in microseconds, are relative to the average shock arrival time of all four traces. One detector (shown in black) produced a larger than expected output voltage, resulting in 'clipping' of that trace. The deviations from the average arrival times were -0.017,-0.015,$+0.010$, and $+0.025\,\mu$s indicating a tilt of $4.4 \pm 0.8\,\mathrm{mRad}$ at an angle of -40° to the vertical.

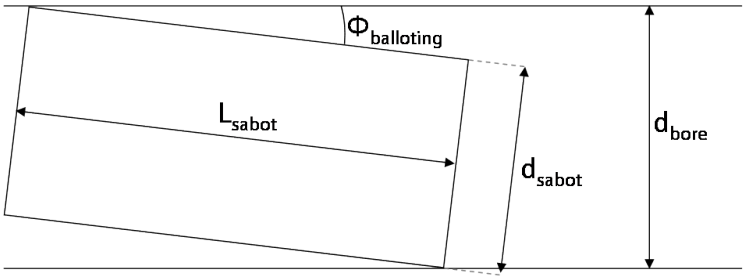

Figure 3.26: The principal contribution to balloting, or in-bore yaw, is due to the sabot necessarily having a smaller diameter than the bore through which it travels. The maximum balloting angle occurs when the leading (or, equally, trailing) edge of the sabot touches one side of the bore and the opposite end touches the opposite side of the bore.

The standard, 'Mark 2,' polycarbonate sabot has an external diameter of $50.60^{+0.00}_{-0.10}\,\mathrm{mm}$, and hence $\Phi_{\mathrm{balloting}} = 2^{+1}_{-0}\,\mathrm{mRad}$. As the experiments discussed above indicated a tilt at impact that was not attributable to misalignment of the target or the flyer, it was concluded that the magnitude of the yaw possible with a 'Mark 2' sabot was the principal contribution to tilt.

Therefore, a larger 'Mark 3' sabot was developed in conjunction with Peter Norman and Chris Summerfield of the Cavendish Laboratory's workshops. The 'Mark 3' sabots have an external diameter of $50.75^{+0.00}_{-0.05}\,\mathrm{mm}$, allowing for a maximum in-bore yaw of $\Phi_{\mathrm{balloting}} = 0.5^{+0.5}_{-0.0}\,\mathrm{mRad}$. In addition to enlarging the diameter of the sabot, it was also decided to manufacture the 'Mark 3' sabots from nylon 6,6; nylon was considered to have improved long-term storage characteristics and to be easier to machine than polycarbonate.

Experiment E100429A was a replication of experiment E100415A, using a 'Mark 3' sabot at an impact velocity of $0.395\,\mathrm{mm}\,\mu\mathrm{s}^{-1}$. Figure 3.27 shows the signal associated with impact flash for the four detectors that functioned correctly. Fitting Equation 3.13 to these data, the tilt was found to be $1.1 \pm 0.2\,\mathrm{mRad}$ at an angle of -5° to the vertical. The coefficient of determination was 0.92.

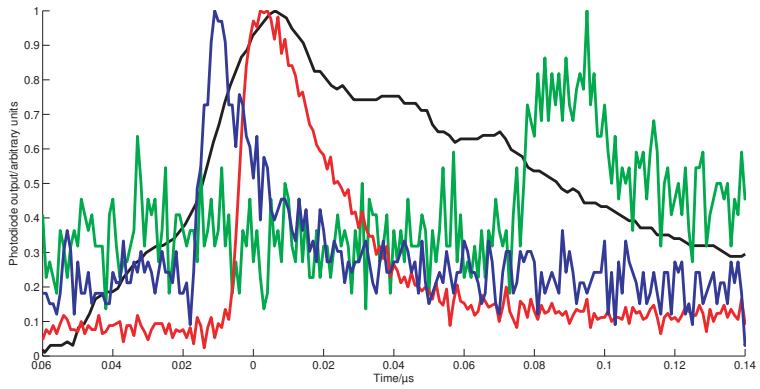

Figure 3.27: Photodiode response, from experiment E100429A. Detector output has been normalised to the range $[0 : 1]$ and times, in microseconds, are relative to the average shock arrival time of all four traces. The deviations from the average arrival times were -0.051,-0.017,-0.009, and $+0.026\,\mu\mathrm{s}$ indicating a tilt of $1.1 \pm 0.2\,\mathrm{mRad}$ at an angle of -5° to the vertical.

As further confirmation, Experiment E100528A repeated previous experiments, using a 'Mark 3' sabot at an impact velocity of $0.392\,\mathrm{mm}\,\mu\mathrm{s}^{-1}$. Figure 3.28 shows the signal associated with impact flash for the four detectors that functioned correctly. As before, Equation 3.13 was fitted to these data, and the tilt was found to be $1.6 \pm 0.1\,\mathrm{mRad}$ at an angle of $+6^{\circ}$ to the vertical. The coefficient of determination was 0.98. It is, therefore, concluded that

a 'Mark 3' sabot will reproducibly give tilts, at impact, of less than $2\,\mathrm{mRad}$. With this in mind, any experiments must be designed such that they are not sensitive to errors introduced by tilts of order $2\,\mathrm{mRad}$.

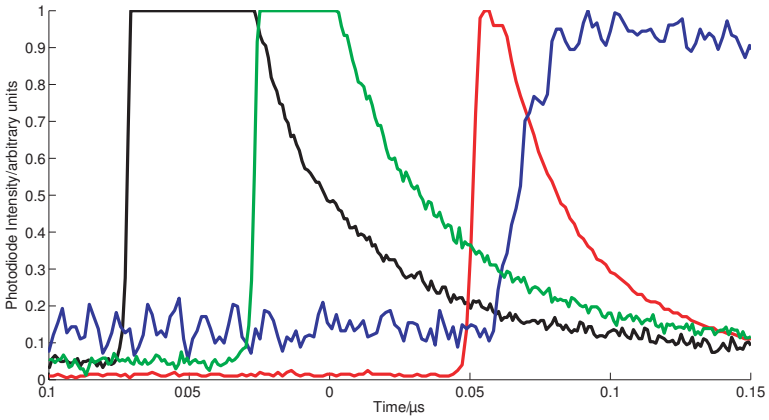

Figure 3.28: Photodiode response, from experiment E100528A. Detector output has been normalised to the range $[0:1]$ and times, in microseconds, are relative to the average shock arrival time of all four traces. The deviations from the average arrival times were -0.076,-0.030,$+0.047$, and $+0.058\,\mu\mathrm{s}$ indicating a tilt of $1.6 \pm 0.1\,\mathrm{mRad}$ at an angle of $+6^\circ$ to the vertical.

3.6 Summary

- The Cavendish Plate Impact Facility, a versatile experimental facility for gathering shock wave data, has been described.
- The principal diagnostics used in this thesis, the in-situ manganin stress gauge, and the VISAR interferometer, have been described.
- The reduction of data from these diagnostics has been described and evaluated.
- Impact tilt has been investigated in experiments conducted with the Plate Impact Facility, and significantly reduced through improvements to aspects of the facility's design.

3.7 Bibliography

K. A. Ansari and J. W. Baugh, Jr. Dynamics of a balloting projectile in a moving gun tube. Technical Report BRL-CR-605, Ballistic Research Laboratory, Aberdeen Proving Ground, 1986.

J. R. Asay and M. Shahinpoor, editors. *High-pressure shock compression of solids*. Springer, 1993.

L. Barker and R. E. Hollenbach. Laser interferometer for measuring high velocities of any reflecting surface. *Journal of Applied Physics*, 43(11):4669–4675, 1972.

L. M. Barker. The development of the VISAR, and its use in shock compression science. In M. D. Furnish, L. Chhabildas, and R. S. Hixson, editors, *Shock Compression of Condensed Matter - 1999*, pages 11–17, 2000.

E. Barsis, E. Williams, and C. Skoog. Piezoresistivity coefficients in manganin. *Journal of Applied Physics*, 41(13):5155–5162, 1970.

N. K. Bourne and Z. Rosenberg. On the ringing observed in shock-loaded piezoresistive stress gauges. *Measurement Science and Technology*, 8:570–573, 1997.

N. K. Bourne, Z. Rosenberg, D. J. Johnson, J. E. Field, A. E. Timbs, and R. P. Flaxman. Design and construction of the UK plate impact facility. *Measurement Science and Technology*, 6(10):1462–1470, 1995.

C. H. Braithwaite. *High Strain Rate Properties of Geological Materials*. PhD thesis, University of Cambridge, 2009.

P. Bridgman. The electrical resistance of metals under pressure. *Proceedings of the American Academy of Arts and Sciences*, 52(9):573–646, 1917.

D. J. Chapman. *Shock-compression of porous materials and diagnostic development*. PhD thesis, University of Cambridge, 2009.

J. S. Courtney-Pratt. *Photography of fast Transients. Interferometric study of surfaces.* PhD thesis, University of Cambridge, 1949.

D. H. Dolan. Foundations of VISAR analysis. Technical Report SAND2006-1960, Sandia National Laboratories, 2006.

L. C. Forde. *Ballistic Impact of Rods*. PhD thesis, University of Cambridge, 2000.

G. R. Fowles, G. E. Duvall, J. Asay, P. Bellamy, F. Feistmann, D. Grady, T. Michaels, and R. Mitchell. Gas gun for impact studies. *Review of Scientific Instruments*, 41(7):984–996, 1970.

R. Hammond. *Shock and ballistic properties of bainitic steels and tungsten alloys*. PhD thesis, University of Cambridge, 2004.

W. F. Hemsing. Velocity sensing interferometer (VISAR) modification. *Review of Scientific Instruments*, 50(1):73–78, 1979.

P. Horowitz and W. Hill. *The Art of Electronics*. Cambridge University, 2nd edition, 1989.

A. W. Lawson. The effect of hydrostatic pressure on the electrical resistivity of metals. *Progress in Metal Physics*, 6(1):1–44, 1956.

A. C. Mitchell and W. J. Nellis. Shock compression of aluminum, copper, and tantalum. *Journal of Applied Physics*, 52(5):3363–3374, 1981.

N. H. Murray. *The response of alumina ceramics to plate impact loading*. PhD thesis, University of Cambridge, 1997.

Z. Rosenberg and Y. Partom. Longitudinal dynamic stress measurements with in-material piezoresistive gauges. *Journal of Applied Physics*, 58(5):1814–1818, 1985.

Z. Rosenberg, D. Yaziv, and Y. Partom. Calibration of foil-like manganin gauges in planar shockwave experiments. *Journal of Applied Physics*, 51(7): 3702–3705, 1980.

A. J. Smiel and T. J. Fisher. Broadband triboluminescence in silica core fiber optic waveguides. *Applied Physics Letters*, 41(4):324–326, 1982.

D. C. Swift and R. G. Kraus. Properties of plastic ablators in laser-driven material dynamics experiments. *Physical Review E*, 77(6):066402, 2008.

G. R. Willmott. *Shock studies of kimberlite, diamond, and brittle embedded particles*. PhD thesis, University of Cambridge, 2004.

D. Yaziv, Z. Rosenberg, and Y. Partom. Release wave calibration of manganin gauges. *Journal of Applied Physics*, 51(12):6055–6057, 1980.

CHAPTER 4

SHOCK TEMPERATURE

It was demonstrated in Chapter 2 that a shock wave irreversibly increases the entropy, and hence temperature, of a material. The measurement of shock temperature is an open problem: in their 1979 review of the field of shock compression, Davison and Graham [1979] noted that

> "The problem of measuring the temperature of shock-compressed solids has a long history, but measurements of accuracy sufficient for the development of an equation of state have yet to be made. Such a measurement is of the highest value and any advance in this area most welcome."

In the subsequent three decades, much progress in the measurement of shock temperature has been reported. However, despite significant advances, a general-purpose diagnostic technique, capable of measuring temperatures to within $1\,\%$ has yet to be proposed. A review of the literature regarding these techniques is presented below, together with a discussion of new experimental results on the measurement of shock temperature using foil thermistors.

4.1 Direct temperature measurements

Thermocouples

The Seebeck effect, first reported by Seebeck [1826], is a thermoelectric phenomenon and refers to the electric field produced by a conductor in a temperature gradient. If, as shown in Figure 4.1, two different conductors are joined at two junctions and a temperature difference is maintained between the junctions then, in the open circuit configuration, a potential difference is measured. The Seebeck coefficient, S, or thermopower, of such a configuration is defined as dV/dT.

A number of authors [Crosnier et al., 1966; Palmer and Turner, 1964; Yuan and Billingsley, 1971] have fielded thermocouples as shock temperature diagnostics. It was found experimentally that the output of the thermocouple ex-

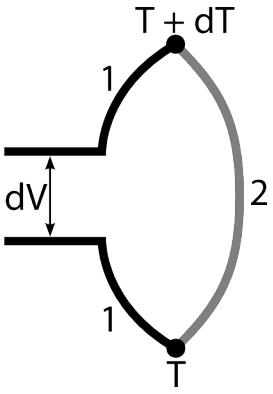

Figure 4.1: A thermocouple, after MacDonald [1962]. Material 2 is attached to material 1, and the junctions are held at different temperatures. In the open circuit configuration shown, an potential difference, dV, is measured; the ratio of dV to dT is the Seebeck coefficient, or thermopower, S, of the thermocouple materials.

ceeded, by as much as a factor of six, that which would be expected given the temperature rise in the material, as predicted by its equation of state. Whilst the effect of static pressure on thermocouple emf are known [Bundy, 1961], the dynamically measured emfs indicate that a further, dynamic, pressure effect is at work.

Bloomquist et al. [1979] attempted to address some of the previously reported uncertainties. By careful preparation of the thermocouple junction, minimising any porosity which would lead to heating of the junction itself, they were able to measure temperatures, in copper, that were within $20\,\%$ of those predicted for stresses in the range 14.5–$36.0\,\mathrm{GPa}$, as shown in Figure 4.2. Whilst it is unclear whether this discrepancy is due to inaccuracies in the measurement or the equation of state, the authors attributed it to locally higher temperatures at the junction, when compared to the bulk.

Further work [Bloomquist and Sheffield, 1980] attempted to measure the temperature rises in PMMA, epoxy, fused silica, and sapphire. As shown in Figure 4.3, the measured temperatures in PMMA do not fit well with theoretical predictions above $2\,\mathrm{GPa}$. The authors note that in PMMA there is a distinct change in the slope of the Hugoniot at this stress [Schuler, 1970], and take this as evidence of some previously-unobserved exothermic reaction. It was argued that, in the inelastic regime, an increase in the thermal diffusivity by a factor of 10^3 would allow for the thermocouples to reach equilibrium, as

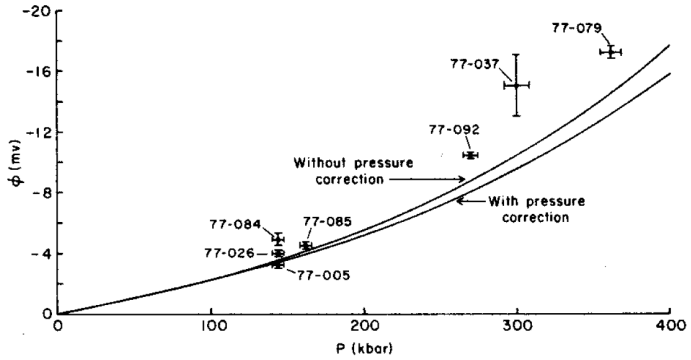

Figure 4.2: Measured thermocouple emfs in copper as a function of shock pressure, from Bloomquist et al. [1979]. Temperature rises predicted from the equation of state have been converted to emfs, and the correction due to the equivalent static pressure applied.

was suggested by the emf–time histories, and thus the measured temperatures were truly the temperature of the material under investigation. In sapphire and fused silica, which remain elastic over the stress range investigated, the temperature rises were found to more strongly correlate with the expected temperature rise in the copper of the thermocouple, and the thermocouples were therefore concluded not to be in equilibrium.

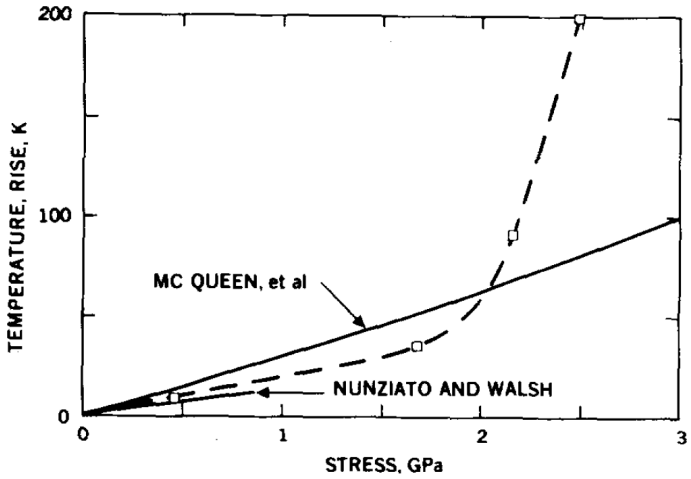

Figure 4.3: Measured temperatures in PMMA as a function of shock pressure, from Bloomquist et al. [1979], compared with predicted values from the equations of state of McQueen et al. [1970] and Nunziato and Walsh [1973].

However, Rosenberg and Partom [1982] disagree with this interpretation, suggesting that the observed response is more likely due to a strain dependence of the thermocouple emf, as the large lateral extent of the thermocouples meant they would experience significant strain. This alternative interpretation was not accepted by Bloomquist and Sheffield [1982]. It is difficult to accept the unsupported conclusion that some hitherto unknown processes are at work in PMMA, and further study is perhaps required. Whilst there have been some attempts [Ishutkin et al., 1986] to measure the the effect of dynamic pressure on thermocouple emf, the high uncertainty ($20\,\%$) associated with these measurements do not provide a reasonable constraint on the effect. In addition, the lingering questions as to what is actually being measured - a purely thermal effect, or some complex mix of heat, pressure, and strain - render thermocouples rather ineffective shock temperature diagnostics.

Radiative techniques

All hot objects radiate energy, the spectrum of which depends on their temperature. The theoretical formulations for such spectra have been discussed at length [*e.g.*, Longair, 2003]. A pyrometer is a device capable of measuring the intensity of radiation from a body at one or more wavelengths [Russell et al., 1940]. Assuming the material acts as a 'grey body' (*i.e.*, the emissivity is independent of frequency) it is possible to determine the temperature from the ratio of these radiative intensities.

Early work on optical determination of residual temperature, where the test material has been released from a free surface, in metals [Taylor, 1963], and of shock temperature in transparent media, where radiation propagates ahead of the shock through the unshocked material [Kormer, 1968; Kormer et al., 1965] found agreement with predicted temperature rises [Clark, 1959; Walsh and Christian, 1955]. However, the sensitivities of the detectors employed limited the measurements to temperatures of order $10000\,\mathrm{K}$ (*i.e.*, pressures of order $100\,\mathrm{GPa}$. The temperature sensitivity is partly determined by the detector wavelength: the 'grey body' spectrum at lower temperatures does not vary greatly in the visible wavelength range, increasing the experimental uncertainty; the use of infrared detectors is required to decrease uncertainties at these lower temperatures.

Subsequent improvements in detector technology allowed shock temperature measurements to be extended to lower regimes. Von Holle and Trimble

[1976] studied copper in the $30 - 50\,\mathrm{GPa}$ range using two-wavelength infrared pyrometry. Measured temperatures (Figure 4.4) were higher than those predicted [McQueen and Marsh, 1960]. This discrepancy was attributed to irreversible effects in the surface layer which are not counteracted by heat conduction to the bulk over the timescale of the experiment.

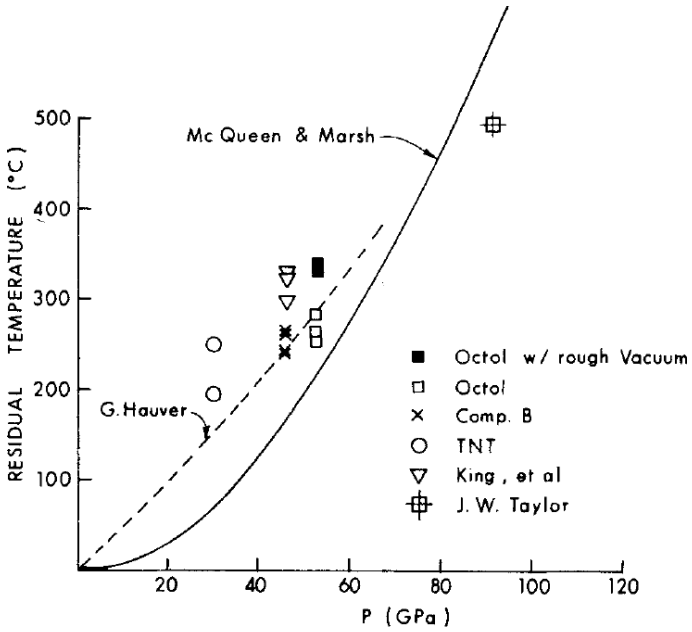

Figure 4.4: Residual temperature rises in shock-compressed copper, from Von Holle and Trimble [1976]. Experimental data are compared to predicted temperatures from McQueen and Marsh [1960]. The highest experimental data point is from Taylor [1963].

Swift et al. [2007] demonstrate that, whilst it is possible to take into account effects such as plastic work at surfaces, detailed prior knowledge of the equation of state of the material is required. In their studies of shocked molybdenum, Swift et al. [2007], were, however, unable to discriminate between various models for the temperature, as their experimental uncertainties (of order $10\,\%$ on temperatures of 600–$700\,\mathrm{K}$) were too large to facilitate this. Furthermore, a number of other challenges to pyrometric measurements have been reported. These include absorption and/or luminescence in window materials [Nellis and Yoo, 1990]; the effect of surface preparation [Shenton-Taylor et al., 2009]; surface jetting (localised plastic flow) [Swift et al.,

2007]; and hotspots/spatial inhomogeneities in the temperature, wavelength-specific emissions, and light that is non-thermal in origin (*e.g.*, impact flash or nitrogen luminesecence at the shocked surface) [Seifter and Obst, 2007]. One further challenge is the determination of spectral emissivity; emissivity is poorly constrained by pyrometric measurements [Nellis and Yoo, 1990] and its determination would enable the uncertainty in measured temperature to be reduced. Whilst some progress has been made in this area [*e.g.*, Bakshi et al., 2009; Partouche-Sebban and Pélisser, 2003; Pottlacher and Seifter, 2002; Shenton-Taylor et al., 2009], and a number of techniques have been proposed, dynamic emissivity measurements are still in their infancy and have not, as yet, proved a useful constraint on temperature measurements.

Raman scattering [Raman and Krishnan, 1928] describes the inelastic scattering of photons. Incident light, at a frequency ν_0 is scattered to a lower frequency, $\nu_0 - \nu_i$, (*i.e.*, energy is absorbed) — so-called Raman Stokes scattering — or, to a higher frequency $\nu_0 + \nu_i$ (Raman anti-Stokes scattering). ν_i is the Raman frequency. 'Incoherent spontaneous Raman scattering' [Moore and Schmidt, 1989; Schmidt et al., 1984] can be used to measure temperature. For a particular Raman frequency, the ratio of intensities of Stokes to anti-Stokes scattering is directly proportional to the temperature. As spontaneous scattering does not affect the vibrational thermal equilibrium significantly, the temperature of the test material may be determined from this intensity ratio [Holmes et al., 1984]. Raman spectroscopy has been used to measure shock temperatures in a variety of liquids [Pangilinan and Gupta, 1994, 1997a; Winey et al., 2000]. Uncertainties in the experimentally determined temperatures were of order $15\,\%$, which is comparable to pyrometric techniques. Raman spectroscopy does not suffer from the same wavelength-based limitation that pyrometry does: the Raman frequencies are independent of temperature, as it is the ratio of Stokes to anti-Stokes scattering that is temperature dependent. This suggests that Raman spectroscopy may be of use at much lower temperatures than pyrometry, although it is only applicable to systems in which active Raman modes exist. In addition, as noted by Pangilinan and Gupta [1997b], Raman-based temperature measurements, whilst conceptually better than many other techniques, suffer from practical difficulties relating to poor signal-to-noise ratios and difficulties in data analysis. Significant advances in these areas have yet to be reported in the open literature [*e.g.*, Sato et al., 2007].

Thermistors

The temperature-dependence of resistance in metals has been known for some time [Siemens, 1871]. As shock temperature diagnostics, thin foils of thermo-resisitive materials can be considered an extension of the standard thin-foil stress measurement technique, discussed in Chapter 3. A thermo-resistive material, or thermistor, subject to an incident shock wave undergoes a change in resistance due to some combination of the shock heating and its piezo-resistive response. The pressure dependence of resistance has been measured for a large number of materials by Bridgman [1964]; these results may be employed to correct for the effect of stress on resistance.

The stress can be calculated for standard materials, or a manganin gauge can employed to measure the longitudinal stress in the conventional way. Bridgman's data, tabulated in Lawson [1956], gives the relationship between resistance change and volumetric strain under hydrostatic loading conditions. To calculate the resistance change due to pressure under dynamic uniaxial loading, these values must be corrected. As reported by Barsis et al. [1970] the dynamic resistance change is increased at a given pressure by two-thirds the absolute change in volume. Once the resistance change due to the applied stress is calculated, any remaining resistance change in the thermistor must be due to a change in its temperature. Bridgman [1917a,b] demonstrated that the temperature coefficient of resistance for a number of metals is virtually independent of hydrostatic pressure. Therefore, in reducing the measured resistance change to a temperature, it is sufficient to use the temperature coefficient of resistance measured at room temperature. Nickel has a high temperature coefficient of resistance, and is one of the materials listed in Lawson [1956] in which the pressure dependence of resistance has been calculated. Therefore, it is well suited for use a thermistor. Kormer [1968] and Dremin et al. [1973] demonstrated the feasibility of using a thin-foil nickel thermistor as shock temperature diagnostic by showing that a change in resistance is measured after account has been taken of the pressure effect.

In order to further investigate the behaviour of thin nickel gauges, a series of experiments were conducted using commercially available, $5\,\mu\mathrm{m}$ thick, nickel foil gauges (ETG-50B/E, Vishay Measurements Group U.K. Ltd) to measure temperature rises in PMMA. A constant-excitation Wheatstone bridge amplifier (SGA400, Pentagon Instruments) was used with a bridge voltage of $0.2\,\mathrm{V}$. As the resistance of nickel varies strongly with temperature, a lower ex-

citation voltage can be used than with manganin gauges. This has the advantage of producing no significant self-heating of the gauge over periods of several hours, much longer than the time required to set-up and perform a plate impact experiment. Initial experiments, replicating the geometry employed, were found to be in agreement with measurements reported by Rosenberg and Partom [1981].

In order to investigate the temporal response of the nickel gauge, an experiment was conducted to measure the residual temperature in PMMA. Manganin and nickel gauges were sandwiched between two $2\,\mathrm{mm}$ thick PMMA plates. When impacted by a copper flyer at $0.672\,\mathrm{kms}^{-1}$, this results in a $2.6\,\mathrm{GPa}$ shock that persists for around $1\,\mu\mathrm{s}$ before released longitudinally from the rear of the target. The stress in this loading cycle remains entirely uniaxial. The reduced stress and temperature traces from this experiment are shown in Figure 4.5.

After the gauge plane has been released, thermal conduction should bring the nickel gauge foil into equilibrium with the surrounding PMMA. The temperature trace in Figure 4.5, however, is clearly still rising, indicating that equilibrium has not been reached. This seems to confirm the suggestion made by Rosenberg and Partom [1981] that thinner foils are required.

Producing thinner nickel foils is, however, challenging. Whilst sputter coating/vapour deposition techniques allow for thin films to be deposited, it is difficult to produce films of sufficiently large initial resistance to enable measurements to be made. The necessity to deposit such films on to some substrate, and to electrically insulate them from conducting media, will increase the time required for them to reach thermal equilibrium. Indeed, in liquids, or any material that is not identical to the substrate, understanding the gauge response becomes complex. If the substrate and test material can be considered identical, the gauge behaves as a thin layer in an infinite bulk. In the case of a gauge in a more complicated environment, it is not clear how the response of the gauge would depend on the properties of the substrate and the material it is embedded in. Whilst these gauges show some promise as shock temperature diagnositcs, the development of sub-micron thickness nickel foil temperature gauges is considered to be beyond the scope of the present work.

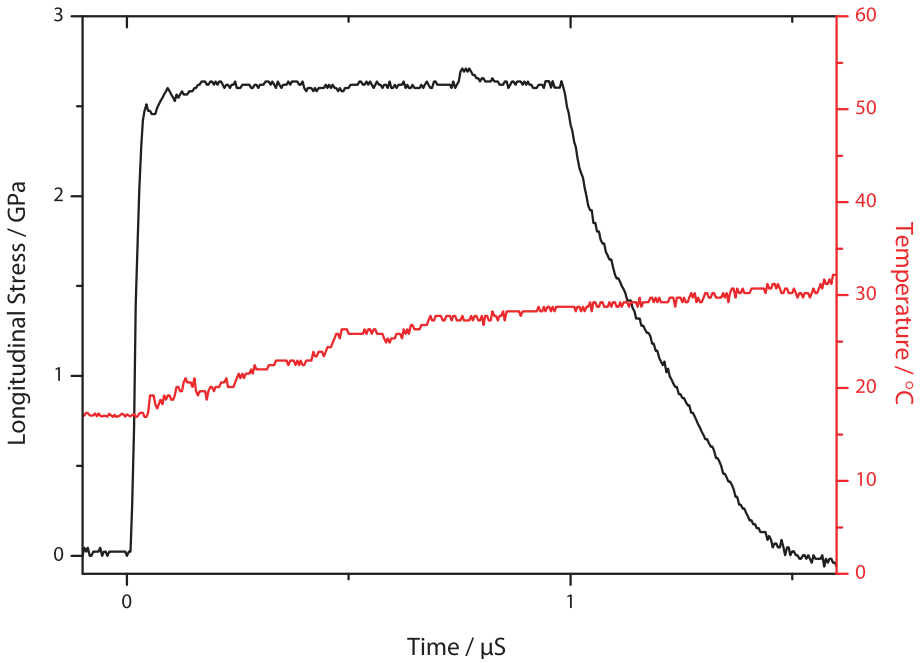

Figure 4.5: Stress-time and temperature-time histories, from Experiment E090603A. A PMMA target was impacted by a copper flyer at $0.672\,\mathrm{km\,s^{-1}}$. Manganin and nickel gauges were embedded in a plane $2\,\mathrm{mm}$ from the impact face; the total target thickness was $4\,\mathrm{mm}$. The plane is released longitudinally approximately $1\,\mu\mathrm{s}$ after the shock first enters the gauges. The temperature trace (red) is still rising at this point, indicating that thermal equilibrium has not been reached.

Conclusions

Radiative techniques - either pyrometry or Raman spectroscopy - show promise for the future, but at present are hampered by a number of significant experimental challenges limiting their accuracy and usefulness. Indeed, these techniques have generally only been deployed in materials where a pre-existing equation of state is available, in order to verify the measured temperature; at present the experimental uncertainties have proved too great to allow for choices between different material models, and currently provide only the loosest of bounds on equations of state. The present research confirms that in-material techniques, based around thin-foil thermistors, show promise as probes of temperature in shock experiments. However, experiments demonstrate that these foils must be significantly thinner than those currently avail-

able in order to reach thermal equilibrium. The development of such foils is beyond the scope of the present work.

4.2 Indirect temperature measurements

With the limitations of direct measurements of shock temperature in mind, the present work focuses on determination of shock temperature through indirect means, and specifically through determination of the equation of state. Walsh and Christian [1955] note that the temperature, T, on the Hugoniot of a material may be calculated by integration of the thermodynamic identity

$$TdS = C_v dT + T\frac{\partial P}{\partial T}\bigg|_V dV, \tag{4.1}$$

where S is the entropy and C_v is the heat capacity at constant volume

$$C_v = \frac{\partial E}{\partial T}\bigg|_V, \tag{4.2}$$

provided C_v and $\partial P/\partial T|_V$ are known. Thus, the measurement of a thermodynamically consistent equation of state enables calculation of shock temperatures. By assuming constant values for C_v and $\partial P/\partial T|_V$, Walsh and Christian [1955] calculated temperature rises in copper, aluminium, and zinc from their pressure and volume Hugoniot measurements in these materials. Walsh et al. [1957] calculated temperature rises in twenty-seven metals, having assumed a Mie-Grüneissen equation of state, where the Grüneissen parameter,

$$\Gamma = \frac{V}{C_v}\frac{\partial P}{\partial T}\bigg|_V, \tag{4.3}$$

was calculated from theoretical consideration of the vibrational modes of the metals. The validity of these equations of state was generally determined by comparing isothermal pressure-volume relationships, calculated using the equation of state and Hugoniot, with isotherms measured directly under static compression. Cowperthwaite and Shaw [1970] performed similar calculations and verified their results by direct comparison with measured temperatures in carbon tetrachloride. The accuracy of these calculations is of order $2\,\%$.

Gurtman et al. [1971] applied a Mie-Grüneissen equation of state to water under the assumption that the heat capacity C_v is constant. For a Mie-Grüneissen equation of state, Equation 4.1 becomes

$$dT = \frac{(V_0 - V)}{2C_v} dP + \left[\frac{(P - P_0)}{2C_v} - T\frac{\Gamma}{V} \right] dV. \tag{4.4}$$

Thus, temperatures along the Hugoniot may be determined by integration of Equation 4.4, providing a continous form of $\Gamma(v)$ is available. The standard assumption made in the literature, and which is made in this thesis, is that the heat capacity is constant. This assumption that the heat capacity is constant, which may or may not be justified in any given material, and which greatly simplifies the model, introduces a certain level of uncertainty to the calculation of temprature. As is discussed later in this thesis, it is the uncertainity in the heat capacity which becomes the dominant contribution to the uncertainty in calculated temperatures. By combining the experimental results of Walsh and Rice [1957] with isothermal compression data [Bridgman, 1942] for water, they constructed a functional form for $\Gamma(v)$ from $v = 1\,\mathrm{cm^3\,g^{-1}}$ to $v = 0.49\,\mathrm{cm^3\,g^{-1}}$, which is reproduced in Figure 4.6. The validity and consistency of the equation of state was checked by comparison with published adiabats and isotherms. Figure 4.7 shows the calculated shock temperatures in water from the constant C_v model proposed by Gurtman et al. [1971] together with those determined by Walsh and Rice [1957] and Cowperthwaite and Shaw [1970]. The disagreement with the model proposed by Cowperthwaite and Shaw [1970] was attributed to that model neglecting the compressional contribution to internal energy. The close agreement with Walsh and Rice [1957] was taken as evidence that constant C_v is an appropriate model for water; uncertainties were of order $2\,\%$. Hence, it is concluded that when $\Gamma(V)$, the Hugoniot, and heat capacity C_v of a material have been determined, temperatures along the Hugoniot may be determined in a consistent manner and with uncertainties of a few percent.

The remainder of this chapter describes the experimental techniques that will enable the calculation of shock temperatures in liquids. First, methods of determining the liquid Hugoniot are described, and their effectiveness compared. The equation of state is determined from shock/reshock experiments, and the analysis of these experiments is discussed with reference to standard materials.

Determination of the Hugoniot of an unknown material

As discussed in Chapter 2, the principal Hugoniot of a material is the locus of states attainable from ambient conditions due to compression by a single

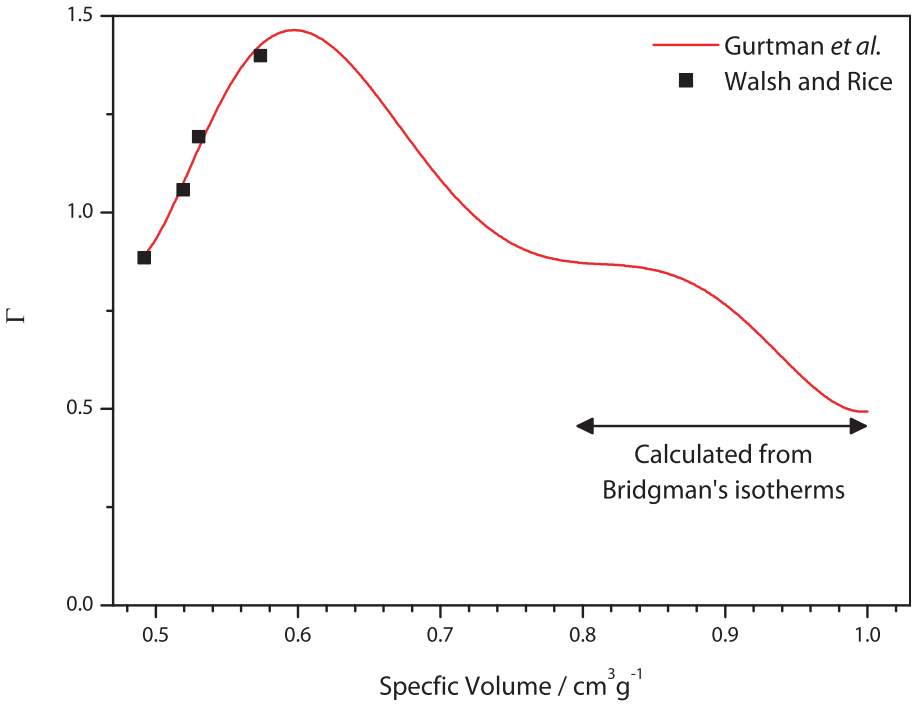

Figure 4.6: $\Gamma(v)$ for water, from the fit given by Gurtman et al. [1971]. The fit is a seventh-order polynomial through, at high volumes, the isothermal compression data given by Bridgman [1942] and, at low volumes, the shock/reload experiments reported by Walsh and Rice [1957]. These latter data were quoted without errors. It can be seen that Γ initially increases with decreasing volume, before reaching a maximum and beginning to decrease.

shock wave. Conventionally, Hugoniots are presented in terms of the shock equation of state, $U_S = c_0 + Su_p$, and therefore both the shock velocity U_S and particle velocity u_p must be determined from experiment.

Trivially, the shock velocity may be inferred from the difference in arrival time of the shock at two points separated longitudinally within a sample by some known distance. In a real sample, such a measurement is complicated by a number of factors, chief amongst which is the the passage of the shock through materials other than the sample. Where the arrival time is measured with manganin gauges, the gauges must be insulated as discussed in §3.2 and, hence, the shock propagates through the gauge package at a velocity determined by the Hugoniot of the insulating material. Furthermore, it is often

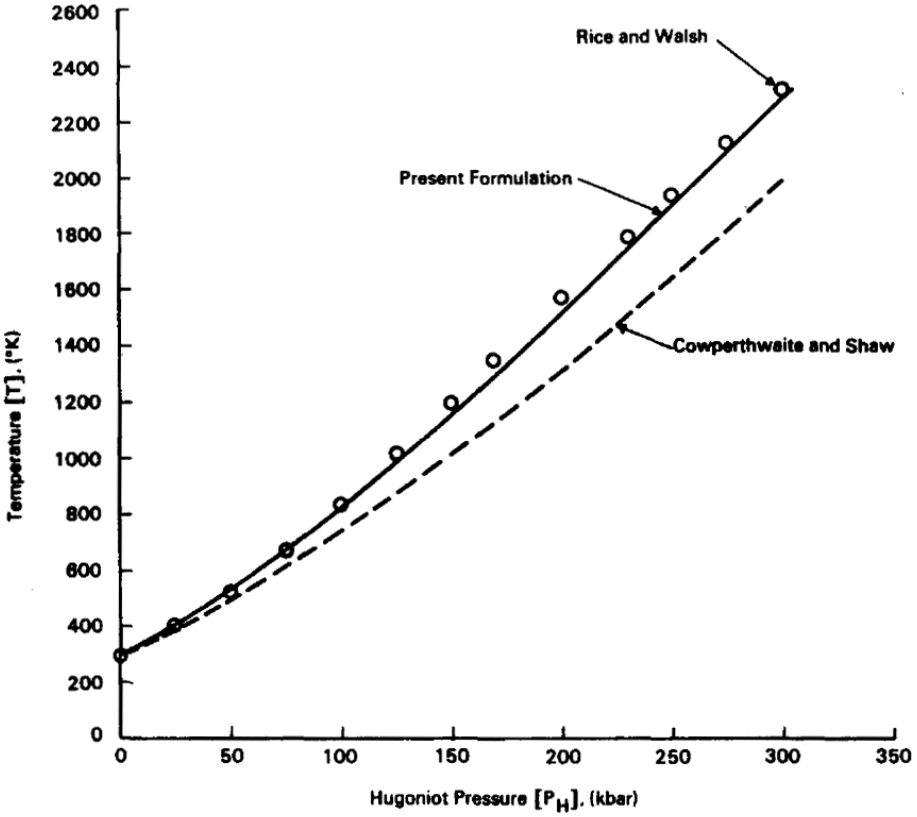

Figure 4.7: Shock temperatures in water, assuming C_V is constant, from Gurtman et al. [1971]. Their formulation was compared to other models in the literature. The disagreement with the model proposed by Cowperthwaite and Shaw [1970] was attributed the latter model neglecting the compressional contribution to internal energy. The close agreement with the calculations made by Walsh and Rice [1957] was taken as evidence that a constant C_V model is appropriate for water.

necessary to include a buffer material between the gauge package and sample and, as before, the shock velocity in this medium must be accounted for when deriving the shock velocity in the sample

For the liquid impact cell shown schematically in Figure 4.8, the total time-of-flight of the shock comprises passage through gauge packages at the front and rear, a buffer ahead of the sample, and the sample itself. The gauges are considered to be located in the middle of each package and therefore it is half the thickness of each gauge package that must be considered.

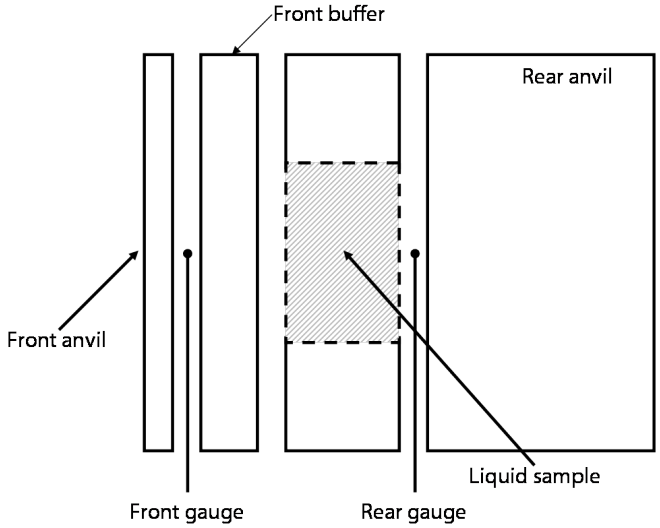

Figure 4.8: Schematic representation of a typical liquid impact cell. In this representation, the projectile would impact the left-most thin plate generating a shock that propagates through the front buffer plate and liquid sample before reaching the rear anvil. The two gauges are embedded in glue and, where necessary, insulating layers. The time-of-flight of the shock between the two gauges is a function of the thickness of the buffer and sample and the half-thicknesses of both gauge packages.

The glue, insulating material, and gauge substrate are, typically, three different materials; however, the shock response of each material is similar to the shock response of PMMA. As the gauge packages are very thin, it can be assumed, without the introduction of significant error, that the shock response of the entire package is identical to that of PMMA[1]. The shock velocity in

[1]For a gauge embedded between PMMA plates, the lack of effects due to impedance mismatches show that, within the diagnostic sensitivity of the gauge, this assumption is valid.

the front gauge package can be inferred from conventional impedance matching; whilst the shock velocity in the rear gauge package will differ (and will depend on the shock response of the sample) from that in the front gauge package, the error associated with taking the shock velocity in both packages to be identical is again insignificant. As with the gauge package, impedance matching arguments can be employed to infer the shock velocity in the buffer material. Obviously, it is important to use as a buffer a material with a well-known Hugoniot.

The thicknesses of the various relevant parts of one such cell are listed in Table 4.1. In experiment E110211B, the front buffer material was PMMA and the sample material was water at $66 \pm 2\,^{\circ}\mathrm{C}$. Figure 4.9 shows the front (red) and rear (black) gauge traces from experiment E110211B, due to the impact of a PMMA flyer at $0.589 \pm 0.006\,\mathrm{km\,s^{-1}}$.

Cell part	Thickness / mm		
Front buffer (PMMA)	2.003	$\pm$	0.003
Front gauge package (PMMA)	0.089	$\pm$	0.015
Sample thickness (Water)	3.601	$\pm$	0.001
Rear gauge package (Copper)	0.220	$\pm$	0.039

Table 4.1: Thickness of the various parts of the cell used in experiment E110211B. The front buffer material was PMMA and the sample material was water at $66 \pm 2\,^{\circ}\mathrm{C}$.

As the impact is symmetric, the Hugoniot state of the buffer can simply be determined from the impact velocity, as the particle velocity in the PMMA is half the impact velocity. The initial plateau in the front gauge trace shown in Figure 4.9 corresponds to the resultant Hugoniot state in PMMA. Thus, the shock velocity and, hence, transit time through the front buffer may be determined. The liquid has a lower impedance than the PMMA and, hence, the shock which propagates through the liquid is also reflected as a release fan into the buffer. After the release process is complete, the front gauge equilibrates at the Hugoniot stress of the liquid, corresponding to the second plateau in the front gauge trace in Figure 4.9. In experiment E110211B, this stress was measured as $0.753 \pm 0.010\,\mathrm{GPa}$. The difference in arrival time of the shock between the front and rear gauges gives the total transit time of the shock: in experiment E110211B, this was $2.470 \pm 0.014\,\mu\mathrm{s}$. A single reverberation is visible in the rear gauge profile; this reverberation is due to the impedance mismatch between the gauge package and the rear copper anvil.

The effect is small, due to the similarity in impedance between the gauge package and water, which can be deduced from the fact that the reverberation is at a similar stress to the Hugoniot stress of the water. The exact effect can be calculated using standard impedance matching techniques; it can be shown that the effect of the reverberation is less than $0.1\,\%$ on the measured stress. This means that the reverberation can be neglected as it has practically no effect on the measured reload stress.

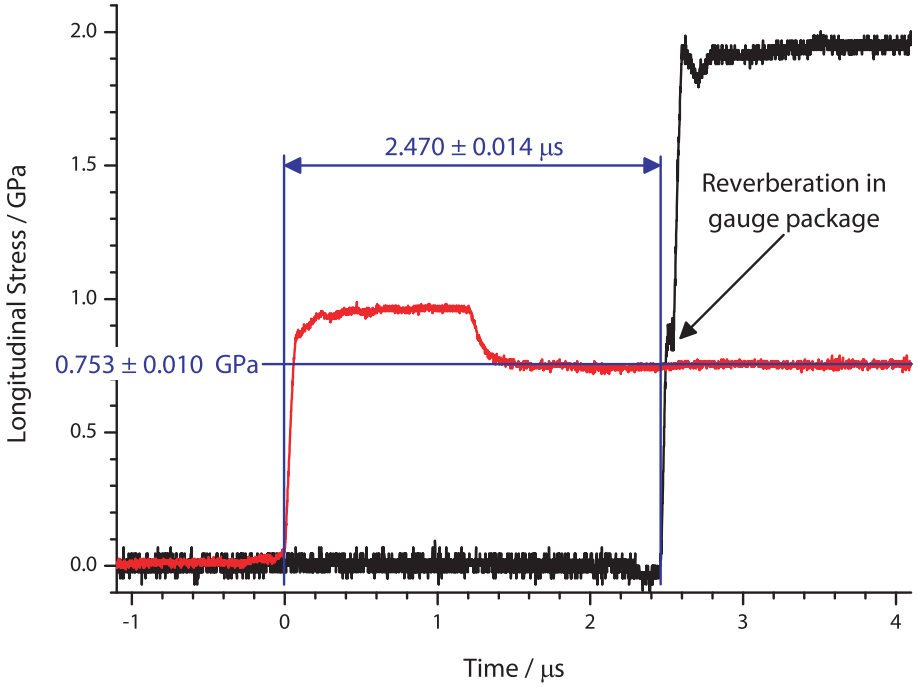

Figure 4.9: Front (red) and rear (black) stress gauge traces from experiment E110211B. The front gauge is first shocked to the Hugoniot state of PMMA, before being released to the Hugoniot state of the liquid at a stress of $0.753 \pm 0.010\,\mathrm{GPa}$; the shock reaches the rear gauge $2.470 \pm 0.014\,\mu\mathrm{s}$ after first arriving at the front gauge. A reverberation is visible in the rear gauge package, which is caused by the impedance mismatch between the water, gauge package, and rear copper anvil. The effect of this reverberation is sufficiently small that it may be neglected, as the impedance of the gauge package is virtually identical to that of the water and so it does not significantly perturb the reloading of the water.

From the measured stress and transit time, there are three methods, discussed below, which enable calculation of the particle velocity in the sample.

These methods are valid regardless of the relative impedances of the materials involved as, in all cases, a shock will propagate between the front and rear gauges.

Method 1: from σ and U_S

The first method assumes the propagation of a steady shock wave through the sample. As such, the loading path is a Rayleigh line of slope $\rho_0 U_S$. This Rayleigh line intersects the principal Hugoniot of the sample at the measured longitudinal stress σ_{1b}, as shown in Figure 4.10.

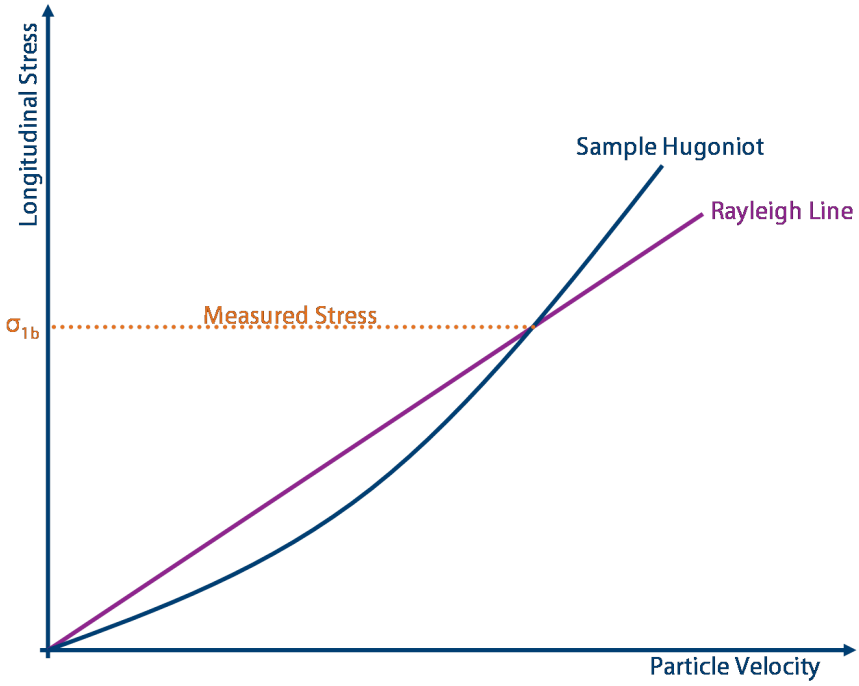

Figure 4.10: Illustration, in $\sigma - u_p$ space, of Hugoniot determination by method 1: the Rayleigh line, of slope $\rho_0 U_S$, intersects the principal Hugoniot of the sample at the measured longitudinal stress σ_{1b}.

The uncertainty in the measured shock velocity, typically $2\,\%$, and the uncertainty in the measured stress, typically $2\,\%$, combine to give an uncertainty in particle velocity of $2\,\%$. It should be noted that, as shown in Figure 4.15, if the front anvil and buffer of higher impedance than the liquid sample, then the stress σ_{1b} is a release state in the anvil and, hence, in the gauge. For stresses

above the HEL of manganin, consideration must be given to the behaviour of such gauges in release, as discussed in §3.2. The net result is to increase the uncertainty associated with the stress, and this is especially true for releases that are small in amplitude (*i.e.*, when the release propagates from an interface between two materials of similar impedance.)

In experiment E110211B, the shock velocity, determined from the transit time shown in Figure 4.9 was $2.040 \pm 0.022\,\mathrm{km\,s^{-1}}$. Using method 1, this gives a particle velocity of $0.377 \pm 0.007\,\mathrm{km\,s^{-1}}$.

Method 2: from σ and v_{impact}

The second method constrains the measured stress to lie on the release curve of the anvil material, as shown in Figure 4.11. Hence, the method requires knowledge of the release curve of the anvil material, but neglects the measured shock velocity. The release curve of the anvil is typically approximated by reflecting its Hugoniot through the state given by the intersection of the anvil Hugoniot with that of the flyer.

Uncertainties in the particle velocity and shock velocity determined[2] by this method are a function of the uncertainties in impact velocity ($1\,\%$), stress ($2\,\%$), and the Hugoniot of the flyer and/or release characteristics of the anvil ($1\,\%$). Hence, the total uncertainties are typically $2\,\%$ on particle velocity and $4\,\%$ on shock velocity.

Method 2 gives a particle velocity for experiment E110211B of $0.372 \pm 0.007\,\mathrm{km\,s^{-1}}$ and, assuming a steady shock, a shock velocity of $2.068 \pm 0.056\,\mathrm{km\,s^{-1}}$.

Method 3: from v_{impact} and U_S

The final method again constrains the Hugoniot state of the sample to the release state of the anvil, and similar arguments regarding uncertainty in that state apply here. However, as with the first method, the shock is assumed to be steady and the measured shock velocity used to define a Rayleigh line of slope $\rho_0 U_S$. The intersection of this line with the release curve, as shown in Figure 4.12, defines both the particle velocity and stress on the sample Hugoniot.

[2]The shock velocity may be determined by assuming the shock is steady and thus that stress–particle velocity Hugoniot is intersected by a Rayleigh line of slope $\rho_0 U_S$ at the measured stress. although this is not a necessary requirement of the method.

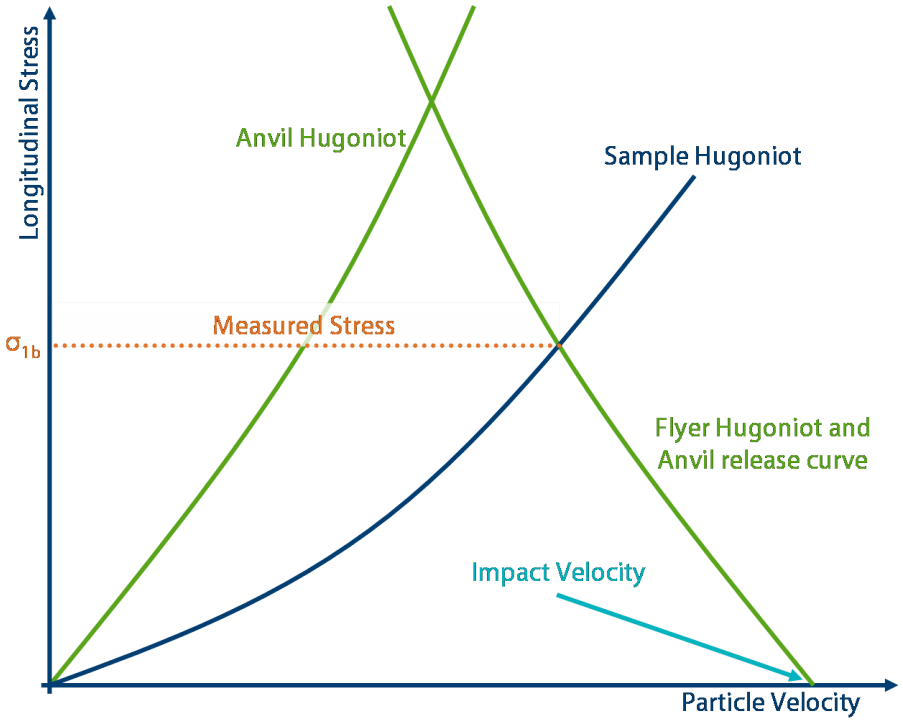

Figure 4.11: Illustration, in $\sigma - u_p$ space, of Hugoniot determination by method 2: the measured longitudinal stress, σ_{1b}, is constrained by measurement of the impact velocity v_{impact} to lie on the release curve of the flyer which, for symmetric impact is taken to be identical to the Hugoniot of the flyer. The particle velocity is therefore inferred from a single point of measurement and, hence, it is not necessary to assume that a steady shock propagates through the sample.

The uncertainties in impact velocity ($1\,\%$), shock velocity ($2\,\%$), and the Hugoniot of the flyer and/or release characteristics of the anvil ($1\,\%$) give rise to typical uncertainties of $2\,\%$ on particle velocity and $2\,\%$ on stress.

The shock velocity for experiment E110211B, is calculated from the transit time, as it was for method 1, and is $2.068 \pm 0.056\,\mathrm{km\,s^{-1}}$ at a particle velocity of $0.374 \pm 0.005\,\mathrm{km\,s^{-1}}$; the stress calculated using method 3 is $0.746 \pm 0.010\,\mathrm{GPa}$.

The three methods, as they rely on somewhat different assumptions, yield slightly different values for the shock and particle velocity state. For experiment E110211B, these states are plotted in Figure 4.13, and are found to lie within error of each other. This may not always be the case. Figure 4.14 shows the Hugoniot states in water compressed from room temperature as deter-

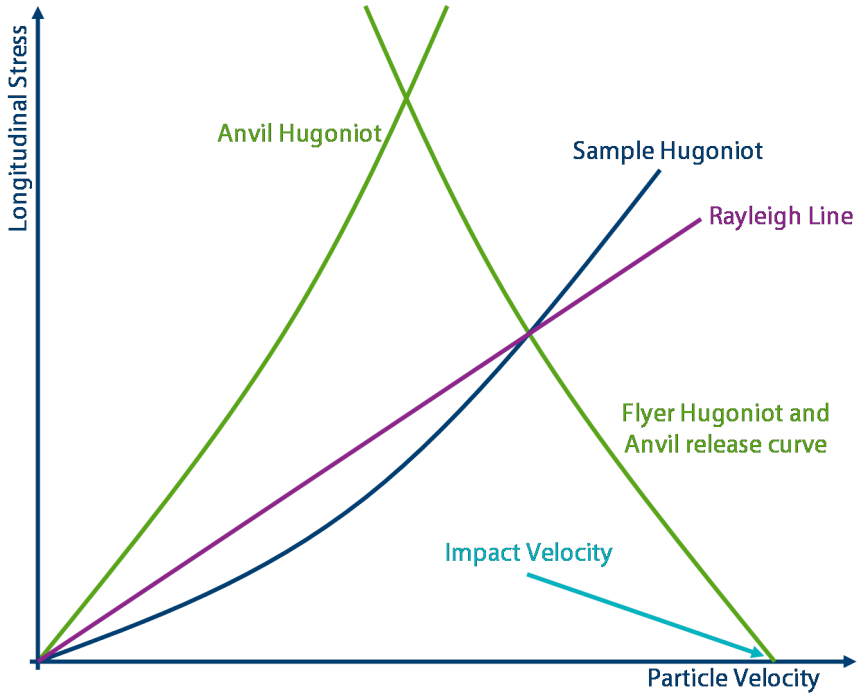

Figure 4.12: Illustration, in $\sigma - u_p$ space, of Hugoniot determination by method 3: the Rayleigh line, of slope $\rho_0 U_S$, intersects the release curve of the anvil. The particle velocity in the sample is therefore inferred from measurements of the shock velocity and impact velocity.

mined by the three methods. Method 2 is clearly at odds with the other two methods. This is due to the method relying solely on the measured stress, which is unreliable for gauges in partial release, as is the case in the experiments reported in the present work. Methods 1 and 3, which are reliant on the transit time, are considered more accurate, as there is greater confidence in the measurement of transit time than of stress. Due to its unreliability, method 2 is not subsequently used in this thesis. The systematic uncertainties in methods 1 and 3 are discussed further in Chapter 5. By conducting a series of experiments at different impact velocities, it is possible to generate a range of shock velocity/particle velocity pairs and thus determine the previously unknown Hugoniot of the test liquid.

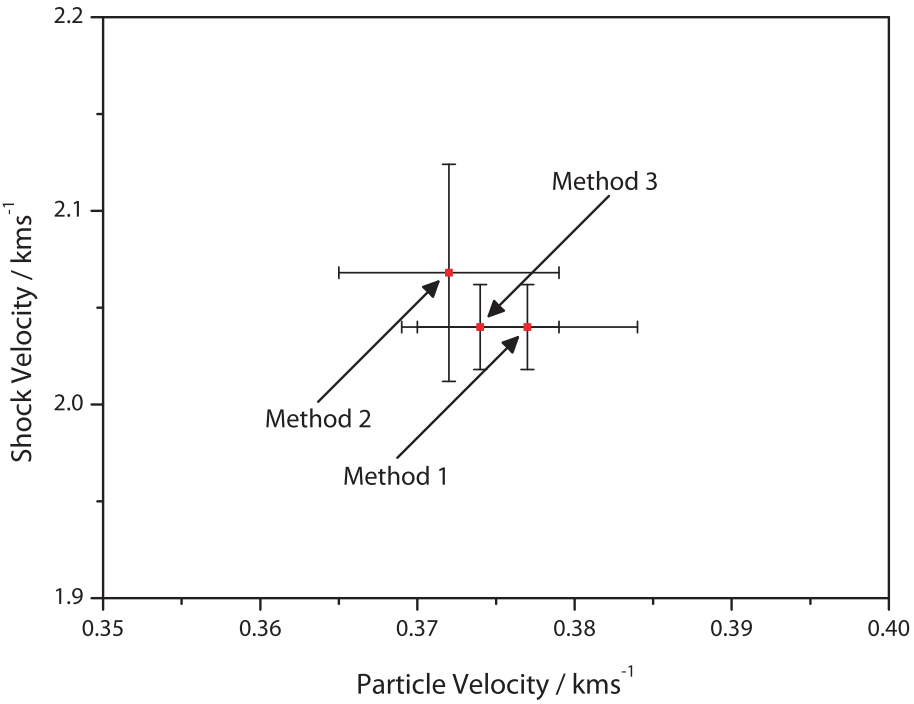

Figure 4.13: Hugoniot state, in shock velocity–particle velocity space, of experiment E110211B, as determined by the three methods described above. In this case, the three methods agree with each other within their experimental uncertainties.

Shock/reload experiments

If the rear anvil of the liquid cell shown schematically in Figure 4.8 is of a higher impedance than the liquid sample, then a shock is reflected from the interface back in to the sample. The propagation of shocks and releases in such a sample in x—t space is represented in Figure 4.15.

Assuming that the flyer and front anvil/buffer materials are identical (*i.e.*, that the impact is symmetric) and are of higher impedance than the sample liquid then the initial shock that propagates into the sample is reflected back through the buffer towards the front gauge. Thus, the front gauge is shocked first to a state on the principal Hugoniot of the buffer material before being released to the Hugoniot state of the liquid. The shock that is transmitted into the liquid sample is reflected at the interface with the rear anvil, as the anvil is of higher impedance than the sample. The reflected (backward-propagating)

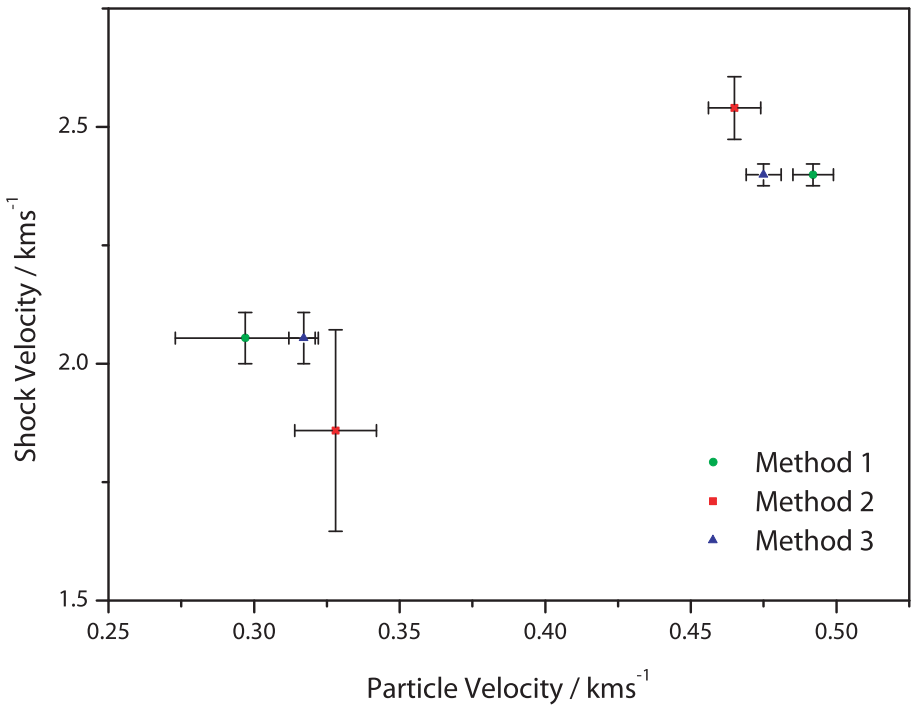

Figure 4.14: Hugoniot state, in shock velocity – particle velocity space, determined by the three methods described above in water compressed from room temperature. The unreliability of method 2 is evident, and it is not subsequently used in this thesis.

shock acts to increase the pressure and density of the sample whilst decreasing its particle velocity.

It is possible, graphically, to solve, approximately, for the states obtained in the liquid, as demonstrated in Figure 4.16. Initially, the gauge in the front anvil/buffer is shocked to the state, 1a, defined by the intersection of the Hugoniot of the anvil/buffer with that of the flyer. The gauge is subsequently released to the Hugoniot state, 1b, in the liquid. A separate release curve has been drawn for the front anvil material; as has been noted above, this release curve is conventionally approximated by the reflected Hugoniot of the anvil. The Hugoniot state can be determined using the methods described above. The reload state, 2, is constrained in P—u_p space to lie on the Hugoniot of the rear anvil. Idealised responses for the front and rear gauges, demonstrating the stress levels corresponding to the three states attained, are shown in Fig-

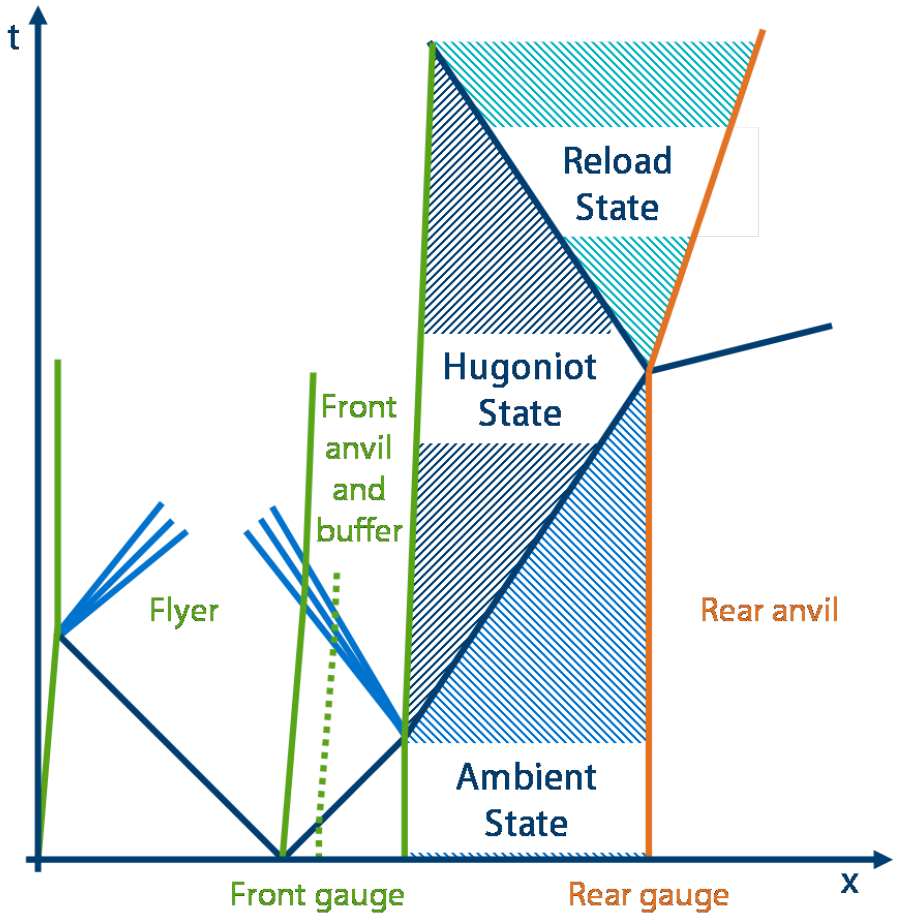

Figure 4.15: x—t diagram for shock and release propagation in the liquid impact cell (Figure 4.8) subject to a symmetric impact. Gauges are placed between the front anvil and buffer (dotted line) and at the interface between the liquid and the rear anvil. Both the front buffer and rear anvil are higher in impedance than the sample. The liquid sample is taken to a state on the principal Hugoniot by the forward-propagating shock entering from the buffer; the backward-propagating shock that is reflected from the interface with the rear anvil takes the liquid to a reloaded state that is not on the principal Hugoniot. Secondary interactions of release fans are irrelevant to the present discussion and not shown.

ure 4.17 and should be compared to the real traces shown above in Figure 4.9. Analysis of gauge traces, in particular when the measured stress is a state in partial release, is discussed in §3.2.

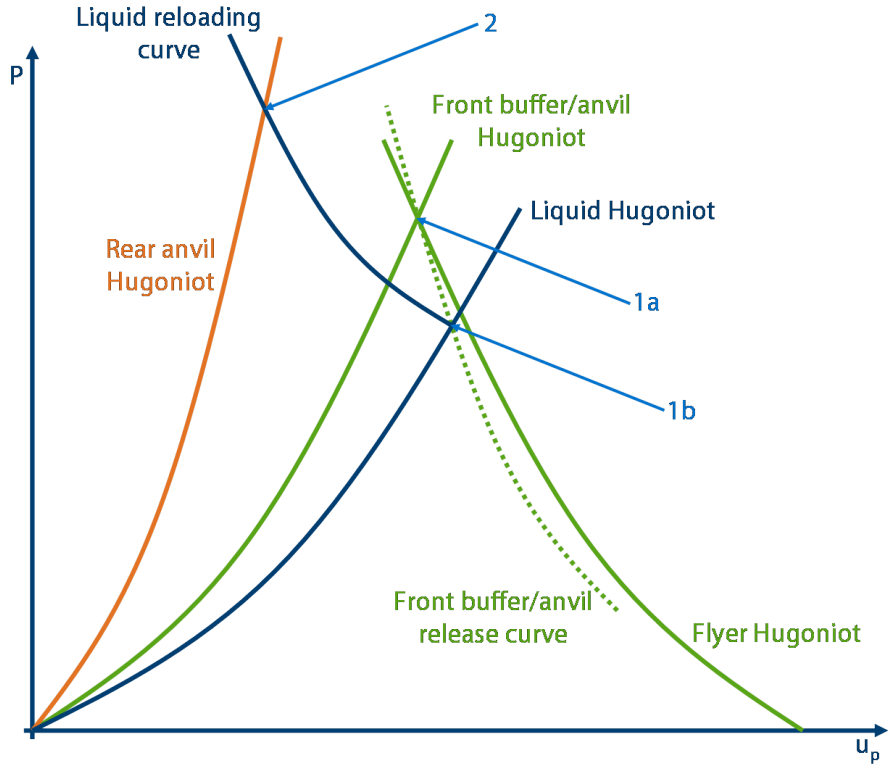

Figure 4.16: Representative graphical solution, in P—u_p space, for shock/reload experiments. Labelled states - 1a, 1b, and 2 - correspond to those that would be measured in the front and rear gauges and are, respectively, the Hugoniot state in the front anvil/buffer, the Hugoniot state in the liquid, and the reload state in the liquid. The general case, where the anvil's release curve differs from the Hugoniot, is shown; the effect of neglecting this is discussed in §4.2.

Figure 4.18 shows the relationship between the shock (*i.e.*, Hugoniot) and reload states for a typical experiment in (a) P—u_p and (b) P—V space. In the limit that the material was loaded to a given stress by an infinite number of infinitesimally small compression waves, the loading would be quasi-isentropic. The shock/reload experiment is, hence, the first step towards such a quasi-isentropic compression, and the reload state, therefore, has a lower entropy

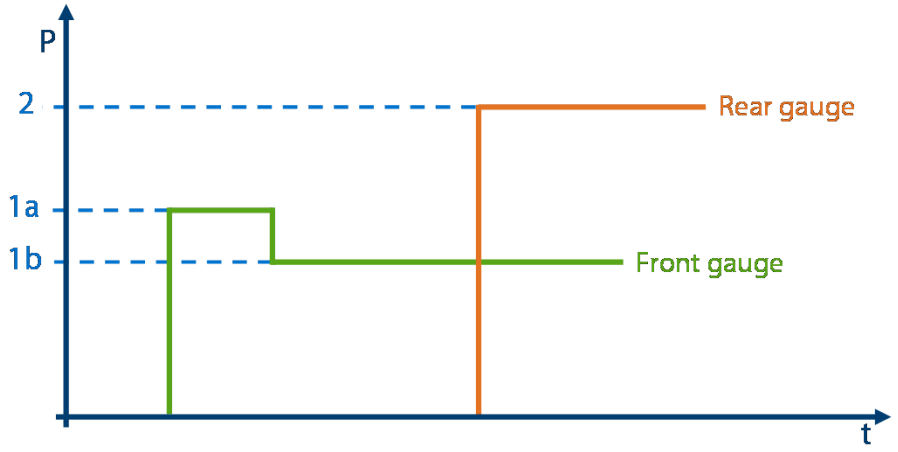

Figure 4.17: Idealised response, in P—t space for the two gauges indicated in Figure 4.8; the labelled pressures correspond to those in Figure 4.16. The gauge responses are shown for the case where the materials behave perfectly plastically: *i.e.*, there is no elastic component to either shocks or releases. The idealised response should be compared to the real experimental data shown in Figure 4.9.

and, hence, a lower pressure and temperature, for a given specific volume, and, thence, lies below the principal Hugoniot in P—V space. It is this relation, between Hugoniot and reload states along an isochor, that is required in determining a material's equation of state.

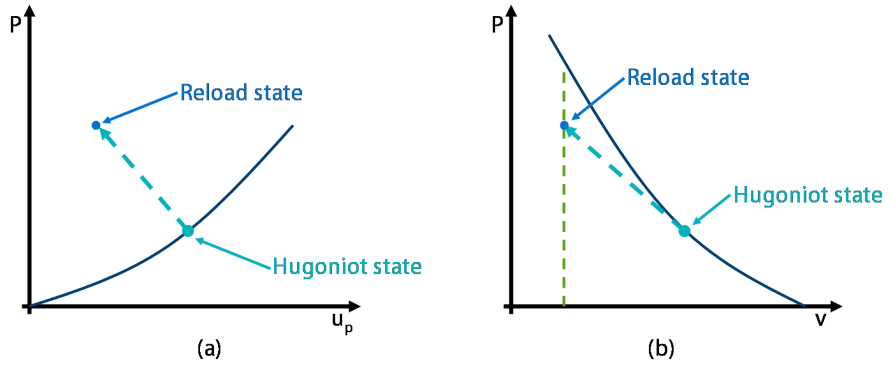

Figure 4.18: Representations of the states attained in a a typical shock/reload experiment in (a) P—u_p and (b)P—v space. In the pressure—volume representation, the reload state lies below the corresponding isochoric Hugoniot state.

Data reduction for shock/reload experiments

Hence, it is necessary to determine the specific volume corresponding to the stress measured in the reload state. The reduction of data for shock/reload experiments presented below follows the method described by Brown et al. [2007] in their experiments on the shock compression of dry sand.

The inferred Lagrangian shock velocity associated with the reloaded state, U_{S2} is

$$U_{S2} = \frac{\sigma_2 - \sigma_1}{\rho_0(u_{p1} - u_{p2})}, \tag{4.5}$$

where the subscripts 1 and 2 refer to the the measured Hugoniot and reload states respectively.

The Hugoniot state in shock/reload experiments can be determined using the methods described above for constructing the Hugoniot of an unknown material. The particle velocity in the reloaded state is constrained to lie on the Hugoniot of the rear anvil and may be inferred from the measured stress; the same stress corresponding to the reloaded state of the liquid is an Hugoniot state for the anvil.

The volume, V_2 in the reloaded state is thence

$$V_2 = V_0 \left(\frac{\rho_0}{\rho_1} - \frac{u_{p1} - u_{p1}}{U_{S2}} \right). \tag{4.6}$$

It should be recalled that the Grüneissen parameter was defined in Chapter 2 as the thermodynamic derivative of pressure with respect to internal energy at constant volume:

$$\Gamma = V \frac{\partial P}{\partial E}\Big|_v \tag{4.7}$$

and therefore, in the reloaded state, Γ is approximately given by the relation

$$\Gamma \approx V_R \frac{P_H - P_R}{E_H - E_R} \tag{4.8}$$

where subscript R denotes the measured reload state and H the Hugoniot state on the isochor through V_R. Furthermore, in an inviscid fluid, the hydrodynamic pressure and longitudinal stress in uniaxial compression are identi-

cal[3] and, therefore, Equation 4.8 may be rewritten in terms of the measured stresses viz.,

$$\Gamma \approx V_R \frac{\sigma_H - \sigma_R}{e_H - e_R}. \tag{4.9}$$

Hence, from the previously-measured principal Hugoniot, the measured stress in the reload state, and the calculated specific volume on reload, it is possible to determine the equation of state of the liquid.

Equation 4.9 may be rewritten, by substitution of Equations 4.5, 4.6 and the known Hugoniots (in the form of the shock equation of state) of the sample and rear anvil, in terms of experimentally measured quantities. The resultant equation is a function of the measured stresses in the Hugoniot and reload states, the measured shock velocity in the Hugoniot state, and the parameters ρ_0, c_0, and S for both the sample and rear anvil. Assuming the uncertainties in these nine quantities are independent, the uncertainty in Γ is given by the sum, in quadrature, of these errors.

The above analysis was applied to experiment E081105C. In this experiment, a PMMA sample plate was placed between two copper anvils. The target was impacted by a copper flyer plate at $0.458 \pm 0.005\,\mathrm{km\,s^{-}}1$. The resultant front and rear gauge traces are shown in Figure 4.19, and show the form expected from Figure 4.17.

Experiment E081105C was not originally designed for the determination of the equation of state of PMMA and the reload state is at comparatively low stress where differences between the Hugoniot and reload curve are minimal. However, the measured state does lie below the Hugoniot in stress–specific volume space, as is evident in the inset graph in Figure 4.20. The principal Hugoniot plotted in Figure 4.20 is from Asay and Shahinpoor [1993, Appendix C]. Applying Equation 4.9 gives a value of $\Gamma = 1.1 \pm 0.8$; the large uncertainty is primarily due to the close proximity of the reload state to the principal Hugoniot, in that the error bars in stress overlap with the principal Hugoniot. This measured value is within $15\,\%$ of the literature value at zero pressure, $\Gamma_0 = 0.97$ [Asay and Shahinpoor, 1993, Appendix C].

[3] This can be seen by noting that pressure is defined as one-third the trace of the stress tensor, and is equal to the longitudinal stress when the shear strength is zero [*e.g.*, Davison, 2008].

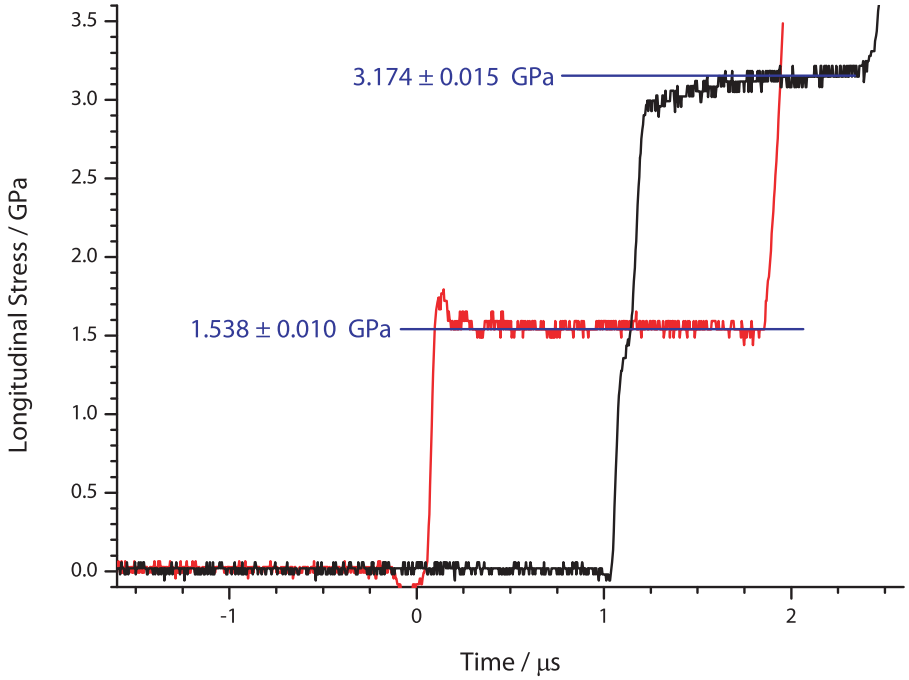

Figure 4.19: Front (red) and rear (black) stresses in experiment E081105C. Experiment E081105C consisted of a PMMA block between two copper anvils, subjected to the impact of a copper flyer plate at $0.458 \pm 0.005\,\mathrm{km\,s^{-}1}$.

4.3 Summary

- A number of techniques for direct measurement of shock temperature have been presented in the literature.
- The uncertainties in temperatures measured with these methods are generally of order $10\,\%$.
- Experiments performed with foil thermistors demonstrate that the technique shows promise, but difficulties in creating foils that are thin enough to reach thermal equilibrium over the time-scale of a shock experiment prevent their use in this thesis.
- Temperatures calculated from thermodynamically consistent equations of state generally have uncertainties of order $2\,\%$. One such equation of state is the Mie-Grüneisen equation.

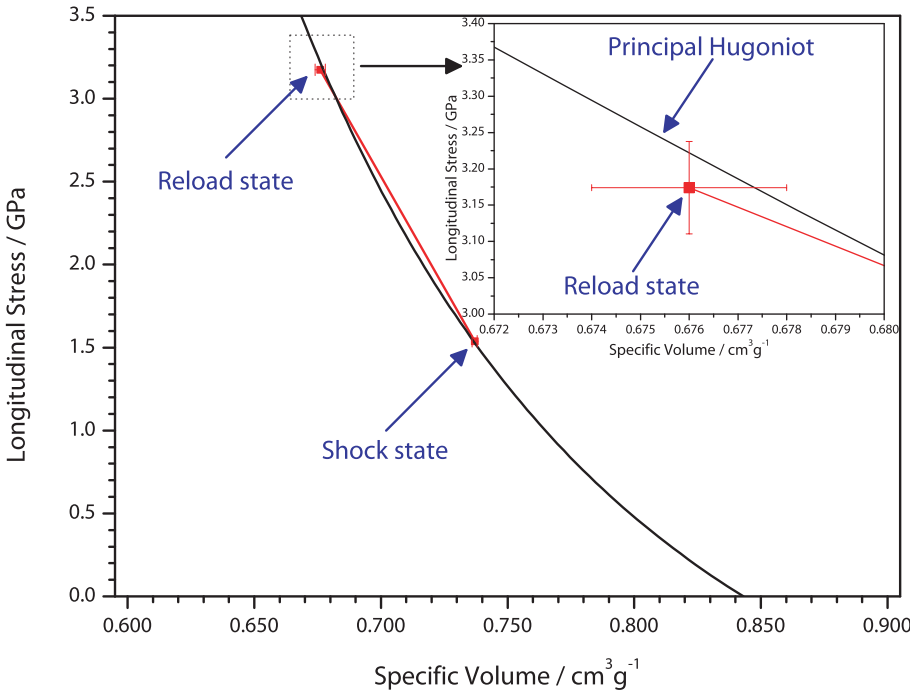

Figure 4.20: Experiment E081105C represented in stress – specific volume space. The solid black curve is the literature Hugoniot for PMMA [Asay and Shahinpoor, 1993, Appendix C]. The Hugoniot and reload states have been labeled. The inset shows a more detailed view of the stress–specific volume space near the reload state, demonstrating that it lies below the principal Hugoniot, although due to the close proximity of reload and Hugoniot stresses at low compressions, the uncertainities in stress overlap the principal Hugoniot.

- Determination of the equation of state requires characterisation of the principal Hugoniot. Experimental techniques to allow the measurement of the principal Hugoniot and determination of the Grüneisen parameter, Γ, from shock/reload experiments have been discussed and evaluated.

4.4 Bibliography

J. R. Asay and M. Shahinpoor, editors. *High-pressure shock compression of solids*. Springer, 1993.

L. Bakshi, S. Eliezer, Z. Henis, N. Nissim, L. Perelmutter, D. Moreno, M. Sudai,

and M. Mond. Equations of state and the ellipsometry diagnostics. *Laser and Particle Beams*, 27(01):79–84, 2009.

E. Barsis, E. Williams, and C. Skoog. Piezoresistivity coefficients in manganin. *Journal of Applied Physics*, 41(13):5155–5162, 1970.

D. D. Bloomquist and S. A. Sheffield. Thermocouple temperature measurements in shock-compressed solids. *Journal of Applied Physics*, 51(10):5260–5266, 1980.

D. D. Bloomquist and S. A. Sheffield. Reply to "Comment on 'Thermocouple temperature measurements in shock-compressed solids' ". *Journal of Applied Physics*, 53(8):5966–5967, 1982.

D. D. Bloomquist, G. E. Duvall, and J. J. Dick. Electrical response of a bimetallic junction to shock compression. *Journal of Applied Physics*, 50(7):4838–4846, 1979.

P. Bridgman. The electrical resistance of metals under pressure. *Proceedings of the American Academy of Arts and Sciences*, 52(9):573–646, 1917a.

P. W. Bridgman. Theoretical considerations on the nature of metallic resistance, with especial regard to the pressure effects. *Physical. Review.*, 9(4): 269–289, 1917b.

P. W. Bridgman. Freezing parameters and compressions of twenty-one substances to 50,000 kg/cm^2. *Proceedings of the American Academy of Arts and Sciences*, 74(12):399–424, 1942.

P. W. Bridgman. *Collected Experimental Papers I – VII*. Harvard University Press, 1964.

J. L. Brown, T. J. Vogler, L. C. Chhabildas, W. D. Reinhart, and T. F. Thornhill. Shock response of dry sand. Technical Report SAND2007-3524, Sandia National Laboratories, 2007.

F. P. Bundy. Effect of pressure on emf of thermocouples. *Journal of Applied Physics*, 32(3):483–488, 1961.

S. P. Clark, Jr. Effect of pressure on the melting points of eight alkali halides. *The Journal of Chemical Physics*, 31(6):1526–1531, 1959.

M. Cowperthwaite and R. Shaw. $C_V(T)$ equation of state for liquids. Calculation of the shock temperature of carbon tetrachloride, nitromethane, and water in the 100-kbar region. *The Journal of Chemical Physics*, 53(2):555–560, 1970.

J. Crosnier, J. Jacquesson, and A. Migault. Anomalous thermoelectric effect in the shock regime and application to a shock pressure transducer. In *Fourth Symposium (International) on Detonation — 1965*, pages 627–638. Office of Naval Research, 1966.

L. Davison. *Fundamentals of shock wave propagation in solids*. Springer, 2008.

L. Davison and R. A. Graham. Shock compression of solids. *Physics Reports*, 55:255–379, 1979.

A. N. Dremin, V. P. Ivanov, and A. N. Mikhailov. Investigation of the possibility of using a thermistor to measure the temperature of shock-compressed solids. *Combustion, Explosion, and Shock Waves*, 9:784–788, 1973.

G. A. Gurtman, J. W. Kirsch, and C. R. Hastings. Analytical equation of state for water compressed to 300 kbar. *Journal of Applied Physics*, 42(2):851–857, 1971.

N. C. Holmes, A. C. Mitchell, W. J. Nellis, W. B. Graham, and G. E. Walrafen. Raman spectroscopy of shocked water. In J. R. Asay, R. A. Graham, and S. G.K., editors, *Shock Compression of Condensed Matter — 1983*, pages 307–308. American Institute of Physics, 1984.

S. N. Ishutkin, G. E. Kuz'min, and V. V. Pai. Thermocouple measurement of temperature in the shock compression of metals. *Combustion, Explosion, and Shock Waves*, 22(5):582–589, 1986.

S. B. Kormer. Optical study of the characteristics of shock-compressed condensed dielectrics. *Soviet Physics USPEKHI*, 11:229–254, 1968.

S. B. Kormer, M. V. Sinitsyn, G. A. Kirillov, and V. D. Urlin. Experimental determination of temperature in shock-compressed NaCl and KCl and of their melting curves at pressures up to 700 kbar. *Soviet Physics JETP*, 21: 689–700, 1965.

A. W. Lawson. The effect of hydrostatic pressure on the electrical resistivity of metals. *Progress in Metal Physics*, 6(1):1–44, 1956.

M. Longair. *Theoretical Concepts in Physics*, pages 281–396. Cambridge University Press, 2nd edition, 2003.

D. K. C. MacDonald. *Thermoelectricty: an introduction to the principles*. John Wiley & Sons, Inc., 1962.

R. G. McQueen and S. P. Marsh. Equation of state for nineteen metallic elements from shock-wave measurements to two megabars. *Journal of Applied Physics*, 31(7):1253–1269, 1960.

R. G. McQueen, S. P. Marsh, J. W. Taylor, J. N. Fritz, and W. J. Carter. The equation of state of solids from shock wave studies. In R. Kinslow, editor, *High-Velocity Impact Phenomena*, pages 293–418. Academic, New York, 1970.

D. S. Moore and S. C. Schmidt. Experimental molecular spectroscopy in shock-compressed materials. In S. C. Schmidt and N. C. Holmes, editors, *Shock Compression of Condensed Matter — 1988*, pages 35–42. American Institute of Physics, 1989.

W. J. Nellis and C. S. Yoo. Issues concerning shock temperature measurements of iron and other metals. *High Pressure Research*, 2:159–182, 1990.

J. W. Nunziato and E. K. Walsh. Propagation of steady shock waves in nonlinear thermoviscoelastic solids. *Journal of the Mechanics and Physics of Solids*, 21:317–335, 1973.

E. P. Palmer and G. H. Turner. Response of a thermocouple junction to shock waves in copper. *Journal of Applied Physics*, 35(10):3055–3056, 1964.

G. I. Pangilinan and Y. M. Gupta. Time-resolved Raman measurements in nitromethane shocked to 140 kbar. *Journal of Physical Chemistry*, 98:4522–4529, 1994.

G. I. Pangilinan and Y. M. Gupta. Temperature determination in shocked condensed materials using raman scattering. *Applied Physics Letters*, 70(08):967–969, 1997a.

G. I. Pangilinan and Y. M. Gupta. Use of time-resolved Raman scattering to determine temperatures in shocked carbon tetrachloride. *Journal of Applied Physics*, 81(10):6662–6669, 1997b.

D. Partouche-Sebban and J. L. Pélisser. Emissivity and temperature measurements under shock loading, along the melting curve of bismuth. *Shock Waves*, 13:69–81, 2003.

G. Pottlacher and A. Seifter. Microsecond laser polarimetry for emissivity measurements on liquid metals at high temperatures — application to tantalum. *International Journal of Thermophysics*, 23(5):1281–1291, 2002.

C. V. Raman and K. S. Krishnan. A new type of secondary radiation. *nature*, 121:501–502, 1928.

Z. Rosenberg and Y. Partom. Temperature measurement of shock-loaded polymethylmethacrylate with in-material nickel gauges. *Journal of Applied Physics*, 52(10):6133–6136, 1981.

Z. Rosenberg and Y. Partom. Comment on "Thermocouple temperature measurements in shock-compressed solids". *Journal of Applied Physics*, 53(8): 5964–5965, 1982.

H. W. Russell, C. F. Lucks, and L. G. Turnbull. A new two-color optical pyrometer. *Journal of the Optical Society of America*, 30(6):248–250, 1940.

A. Sato, S. Oguchi, and K. G. Nakamura. Temperature measurement of carbon tetrachloride under laser shock compression by nanosecond raman spectroscopy. *Chemical Physics Letters*, 445(1-3):28 – 31, 2007.

S. C. Schmidt, D. S. Moore, and J. W. Shaner. Raman spectroscopies in shock-compressed materials. In J. R. Asay, R. A. Graham, and S. G.K., editors, *Shock Compression of Condensed Matter — 1983*, pages 293–302. American Institute of Physics, 1984.

K. W. Schuler. Propagation of steady shock waves in polymethyl methacyrlate. *Journal of the Mechanics and Physics of Solids*, 18:277–293, 1970.

T. J. Seebeck. Ueber die magnetische polarisation der metalle und erze durch temperatur-differenz. *Annalen der Physik*, 82(2):133–160, 1826.

A. Seifter and A. Obst. About the proper wavelength for pyrometry on shock physics experiments. *International Journal of Thermophysics*, 28:934–946, 2007.

C. Shenton-Taylor, J. De'Ath, and T. A. Ota. Pyrometry temperature studies of shocked tin including investigations exploring surface defects, anvil diameter and the integration with emissivity diagnostics. In M. L. Elert, W. T.

Butler, M. D. Furnish, W. W. Anderson, and W. G. Proud, editors, *Shock Compression of Condensed Matter — 2009*, pages 651–654. American Institute of Physics, 2009.

C. W. Siemens. On the increase of electrical resistance in conductors with rise of temperature, and its application to the measure of ordinary and furnace temperatures; also on a simple method of measuring electrical resistances. *nature*, 4:17–20, 1871.

D. C. Swift, A. Seifter, D. B. Holtkamp, and D. A. Clark. Shock and release temperatures in molybdenum: Experiment and theory. *Physical Review B*, 76(5):054122, 2007.

J. W. Taylor. Residual temperatures of shocked copper. *Journal of Applied Physics*, 34(9):2727–2731, 1963.

W. G. Von Holle and J. J. Trimble. Temperature measurement of shocked copper plates and shaped charge jets by two-color IR radiometry. *Journal of Applied Physics*, 47(6):2391–2394, 1976.

J. M. Walsh and R. H. Christian. Equation of state of metals from shock wave experiments. *Physical Review*, 97(6):1544–1556, 1955.

J. M. Walsh and M. H. Rice. Dynamic compression of liquids from measurements on strong shock waves. *The Journal of Chemical Physics*, 26(4):815–823, 1957.

J. M. Walsh, M. H. Rice, R. G. McQueen, and F. L. Yarger. Shock-wave compressions of twenty-seven metals. Equations of state of metals. *Physical Review*, 108(2):196–216, 1957.

J. M. Winey, G. E. Duvall, M. D. Knudson, and Y. M. Gupta. Equation of state and temperature measurements for shocked nitromethane. *Journal of Chemical Physics*, 113(17):7492–7501, 2000.

S. W. Yuan and J. P. Billingsley. An experimental investigation of high velocity impact. *Applied Scientific Research*, 24(1):431–451, 1971.

CHAPTER 5

SHOCK COMPRESSION OF WATER

In addition to the usual considerations of flatness and planarity discussed in Chapter 3, shock experiments involving liquids also require an effective vacuum seal around the liquid, and the chemical compatibility of the liquid with the materials surrounding it must be considered. The term 'cell' is used to describe the liquid-containing target. Careful consideration must also be given to the propagation of lateral release waves, as there will exist an impedance mismatch between the liquid and the material of the cell's wall. The first part of this chapter concerns the design of cells for shocking liquid samples. The cell must be vacuum-tight, to prevent the liquid being drawn out of the cell as the gun is evacuated. The liquid itself must be confined in such a way that it has a well-defined thickness and parallel, planar faces. The development of such a cell is discussed below.

5.1 Cell development

In order to accurately determine the Hugoniot and equation of state of the liquids considered in this thesis, several quantities must be determined from each experiment: the Hugoniot and reload stresses, and the transit time of the shock through the liquid. Thus, an experimental design that produces two stress histories, from the front and rear gauges, that have well-defined rises (associated with the arrival of the shock at each gauge) and reach steady plateaus reflecting the appropriate stresses, is required. The final cell used in this thesis was developed in several stages, which are described below. At each stage, small modifications were made to the cell design in order to obtain the desired gauge traces. A number of unexpected experimental difficulties were encountered during the development process. The first part of this chapter considers these challenges and describes their solutions.

The initial liquid cell design is shown schematically in Figure 5.1 and was constructed from three copper plates. The front and rear anvil are simple copper plates; the central plate has a $2\,\mathrm{mm}$ deep pocket machined into it forming the sample volume. The front gauge is then glued in place between the front

anvil and the central plate and the rear gauge is glued to the rear anvil. Teflon was used to insulate the gauges, as it has been suggested that it results in more robust gauge packages [Chapman, 2009b]. An 'o'-ring groove machined around the central plate allows the cell to be sealed when it is screwed together.

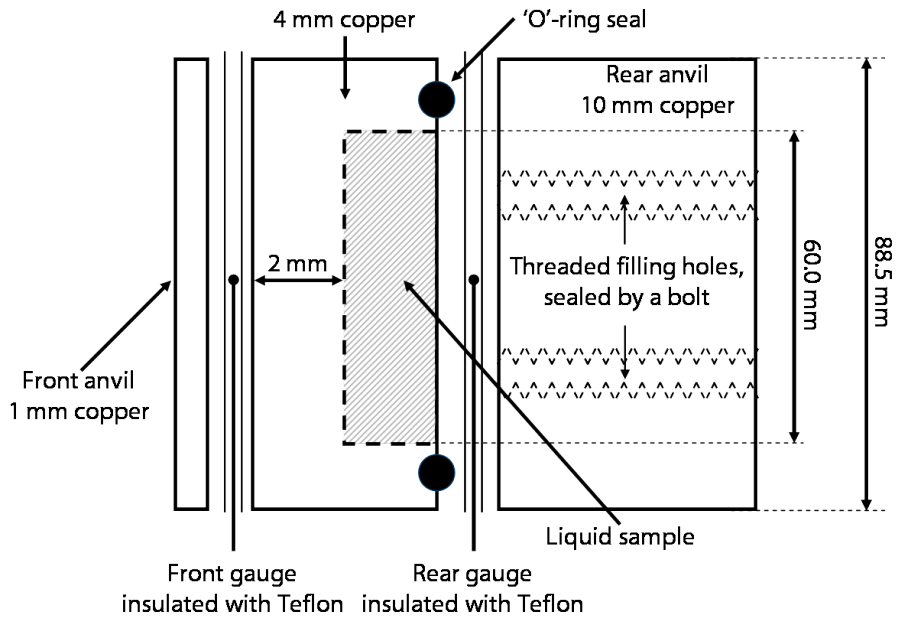

Figure 5.1: Schematic representation of the initial liquid cell; the horizontal scale is exaggerated by a factor of 10. The front anvil is a 1 mm copper plate. The sample, indicated by the shaded region, is contained within a 'cup' machined from a 4 mm copper plate: a 2 mm deep pocket is machined into this plate, leaving 2 mm of copper to form the front buffer. The front gauge is glued in place between these two copper sections, and the rear gauge is bonded to the 10 mm copper rear anvil. A groove suitable for an 'o'-ring is machined into the copper 'cup' forming a seal outside the sample volume. The cell was filled from the rear and the filling holes sealed with a bolt and PTFE sealing tape.

Figure 5.2 shows the front and rear gauge traces from experiment E090417A which resulted from the impact of a copper flyer at $0.702 \pm 0.007\,\mathrm{km\,s^{-1}}$ on the cell described in Figure 5.1 and filled with water. A number of reverberations can be seen in the front gauge trace; partly, these reverberations are due to the impedance difference between the gauge package and copper and the thickness of the gauge package. The large amplitude, and long time-scale, of the

reverberations indicate that the gauge package is of an unsatisfactory thickness. The relatively thick gauge package is a result of the use of $125\,\mu\mathrm{m}$-thick Teflon insulation which was the thinest Teflon available at the time; in order to continue to use Teflon, it must be replaced with sheets that are considerably thinner. The large reverberations may in part explain the lack of a single steady plateau in the reload state observed on the rear gauge trace. In addition, the Hugoniot state of the water is ill-defined in the front gauge trace, as the tail end of the longitudinal release from the water into the copper overlaps with what appears to be a partial release. The source of this release is unclear, and was not anticipated from consideration of the design, where the diameter of the liquid sample is greater than that of the flyer plate.

In addition, it is difficult to ensure that the central copper plate is machined in a way that ensures that its front surface is parallel to the front surface of the 'pocket'. In order to ameliorate these problems, a modified design (Figure 5.3) was implemented. The modified cell replaces the 'one piece' front buffer and sample confinement with two parts - a simple buffer plate and an aluminium annulus. An 'o'-ring is supported against the internal diameter of this annulus in order to provide a seal. This construction allows for greater control over thickness and planarity of the various parts of the target and the gauge packages themselves. Additionally, a stock of thinner ($30\,\mu\mathrm{m}$) Teflon was obtained.

The gauge traces from an impact on a water-filled cell by a copper flyer at $0.298 \pm 0.003\,\mathrm{km\,s^{-1}}$ are shown in Figure 5.4, and are representative of experiments conducted with this cell design. After reaching the Hugoniot stress of copper, the front gauge is released to the Hugoniot stress of the liquid. It was found in over half of the experiments conducted with this cell design that failure of the front gauge occured shortly after the arrival of the release wave. The electrical noise associated with the front gauge failure is 'picked up' by the rear gauge, as it acts as an antenna. The noise is such that it obscures not only the arrival time of the shock at the rear gauge, but also the stress level reached. The high failure rate makes it impractical to use this cell design. Whilst it would be possible to eliminate the front gauge and still determine the reload stress in the liquid, without the front gauge no determination of the Hugoniot is possible as neither the Hugoniot stress of the liquid, nor the transit time of the shock, would be measured. The ultimate cause of failure of the front gauge package is believed to be due to the large magnitude of the release wave that propagates into it across a significant impedance mismatch (the copper/Teflon/copper boundaries). This was not a problem in the initial

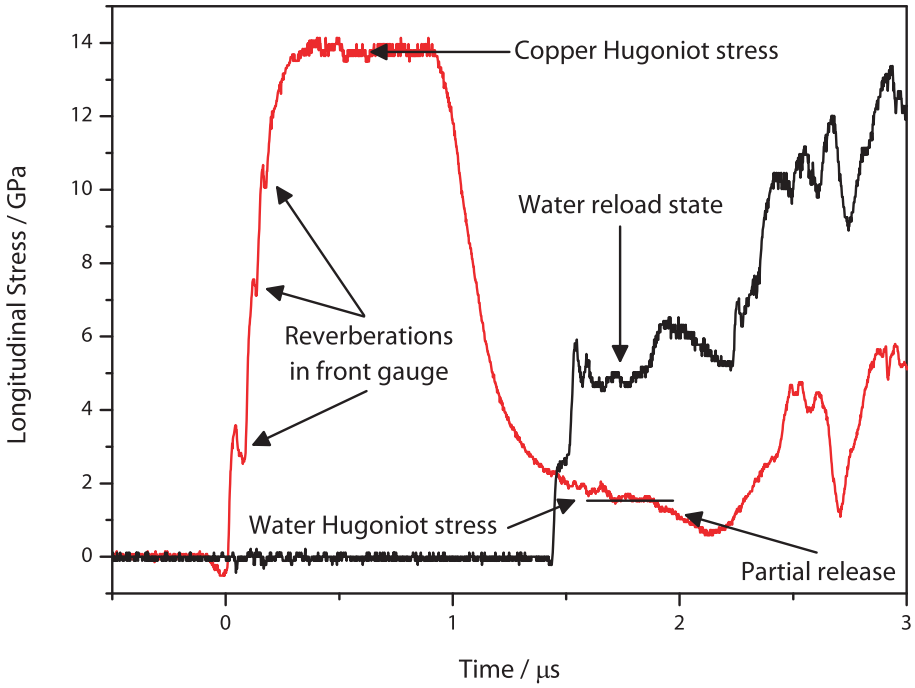

Figure 5.2: Front (red) and rear (black) gauge traces from experiment E090417A, in which the cell described in Figure 5.1 was impacted by a copper flyer at $0.702 \pm 0.007\,\mathrm{km\,s^{-1}}$. A series of reverberations in the front gauge package are evident; in part this is due to the impedance mismatch between the gauge package and the surrounding copper. The large amplitude and time-scale of the reveberations are caused by the relatively thick ($125\,\mu\mathrm{m}$) Teflon that was available to insulate the gauge at the time. These reservations suggest that there would not be a single well-defined shock entering the liquid, which may be responsible for the the rear gauge not reaching a steady plateau at the reload stress of the liquid. In addition, the Hugoniot stress in the liquid is poorly measured, as partial lateral releases affect the front gauge shortly after the longitudinal release from the water/copper interface has occurred.

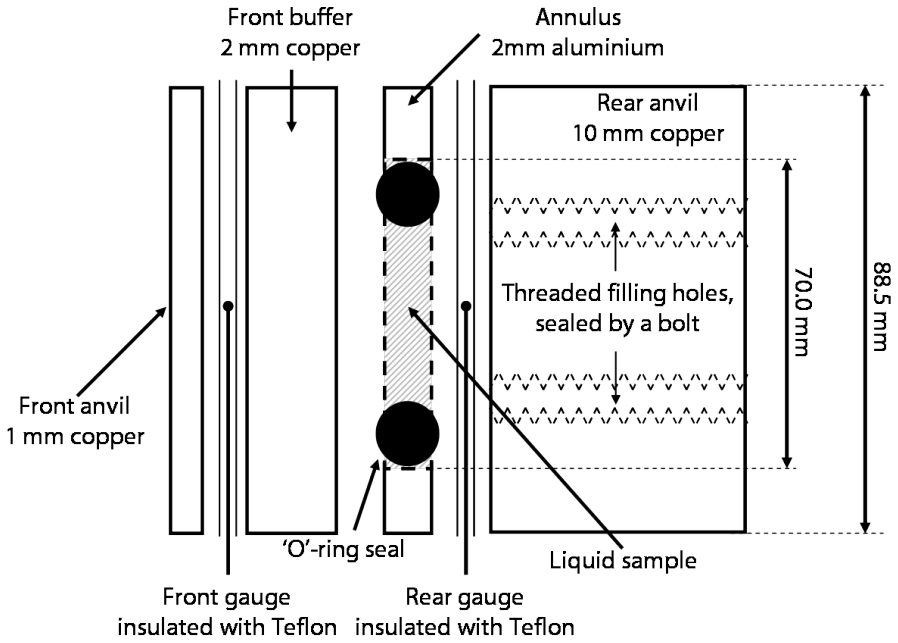

Figure 5.3: Schematic representation of the second iteration of the liquid cell design; the horizontal scale is exaggerated by a factor of 10. The front gauge is glued between two thin copper plates, and the sample (shaded region) is confined by a $2\,\mathrm{mm}$ aluminium annulus which supports an 'o'-ring against its internal diameter. The rear gauge and rear anvil are identical to those of the initial cell design (Figure 5.1.) The cell was filled from the rear and the filling holes sealed with a bolt and PTFE sealing tape.

design, as the relatively thick gauge package 'smoothed out' the effect of the impedance mismatch. That the gauge package in the new cell design is signigicantly thinner can be observed by noting the lack of reverberations in the shock rise in Figure 5.4 when compared to Figure 5.2.

In order to avoid these problems, a cell, shown schematically in Figure 5.5, was developed that employed 'off-axis' gauges. In this cell, which is not axisymmetric, the front and rear gauges do not share a common axis. The front gauge is embedded between two copper plates, and thus not subject to a release from the liquid although, for this reason, it does not measure the Hugoniot stress in the liquid which, in addition to the measured shock velocity, is used in the determination of the liquid Hugoniot.

Experiment E100623A subjected such a cell, filled with water, to the impact of a copper flyer at $0.491 \pm 0.005\,\mathrm{km\,s^{-1}}$. The resultant gauge traces are

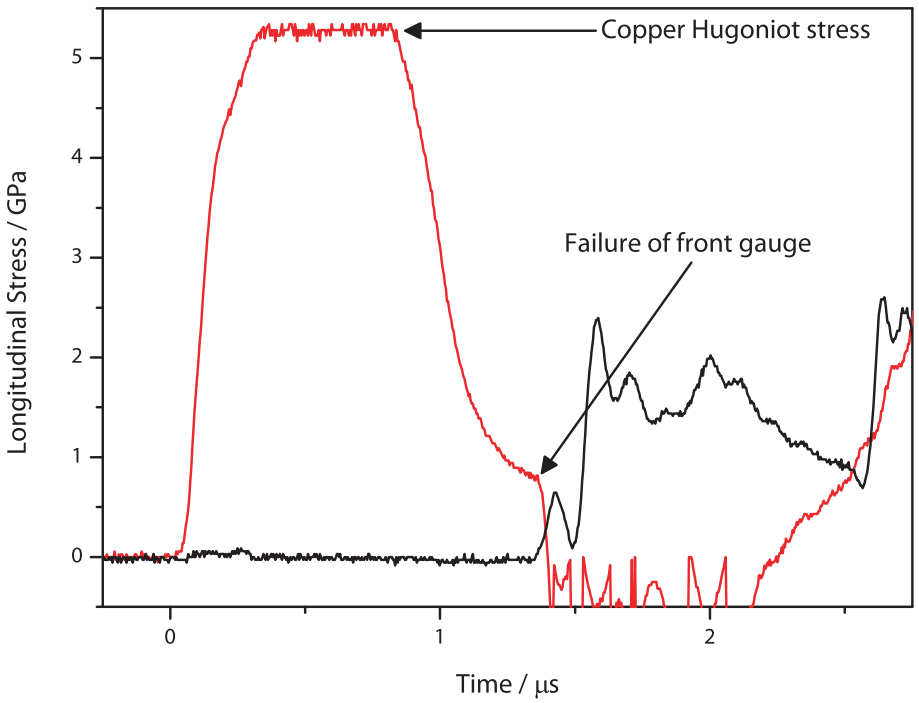

Figure 5.4: Front (red) and rear (black) gauge traces from experiment E090611B. The trace, which is representative of those conducted using the cell described in Figure 5.3 demonstrates the failure of the front gauge during the release process. The electrical noise associated with this failure is evident on the rear gauge trace, and acts to obscure both the arrival time of the shock at the rear gauge and the stress level that results. The cell was impacted by a copper flyer at $0.298 \pm 0.003\,\mathrm{km\,s^{-1}}$.

shown in Figure 5.6. Lateral release waves, in addition to propagating from the edges of the cell are also generated at the copper/water interface at the centre of the cell. The release that propagates from this interface is evident in the front gauge trace; reloading of the front gauge occurs when the shock in the water is transmitted into the copper at the copper/water interface. In addition, the rear gauge is partially released before it reaches an equilibrium value; again, it seems likely that releases at the copper/water interface are responsible for this. These release waves were not anticipated to affect the gauges until significantly later in the experiment. That they do suggests that the releases propagate much faster than was initially anticipated

The shock velocity determined from the transit time measured in experi-

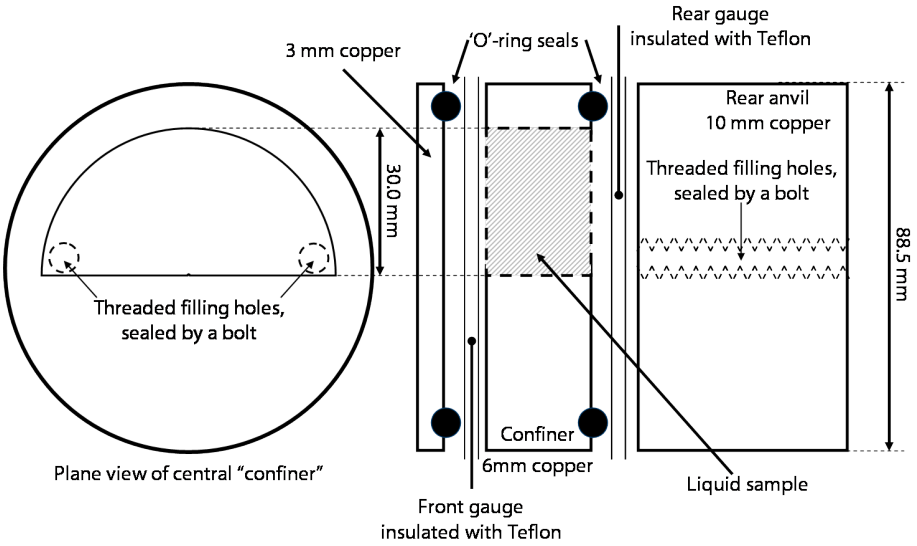

Figure 5.5: Schematic representation of the third iteration of the liquid cell design; the horizontal scale is exaggerated by a factor of 10. The entire cell is constructed from copper, 'o'-rings are placed in grooves machined in the front anvil and confining ring in order to provide a seal. The thickness of these two parts are partly defined by the available sizes of 'o'-rings. The front gauge is placed between the front anvil and copper confiner and thus does not experience a significant longitudinal release. The rear gauge is placed at the liquid/copper interface and the two gauges are placed $15\,\mathrm{mm}$ laterally from the central axis of the cell. The cell was filled from the rear and the filling holes sealed with a bolt and PTFE sealing tape.

ment E100623A is some $10\,\%$ slower than the Hugoniot of water [e.g., Asay and Shahinpoor, 1993, Appendix C] would imply. In order to bring the experimental and expected shock velocities into agreement, a tilt of the target with respect to the flyer of around $100\,\mathrm{mRad}$ is required, which is an order of magnitude greater than the maximum tilt observed in Chapter 3 and would lead to much greater rise times than are observed. It seems therefore that some property of the cell is causing this discrepancy between measured and expected shock velocities. It is not clear, however, what the precise cause of the discrepancy is, as any significant non-uniformity in the thickness of the gauge packages would have been detected when measuring the cell before assembly. It is not possible to measure impact tilt in this cell design, as the relatively thick front plate is not suitable for drilling the necessary holes for optic fibres and it would not be possible to sufficiently reduce the size of the

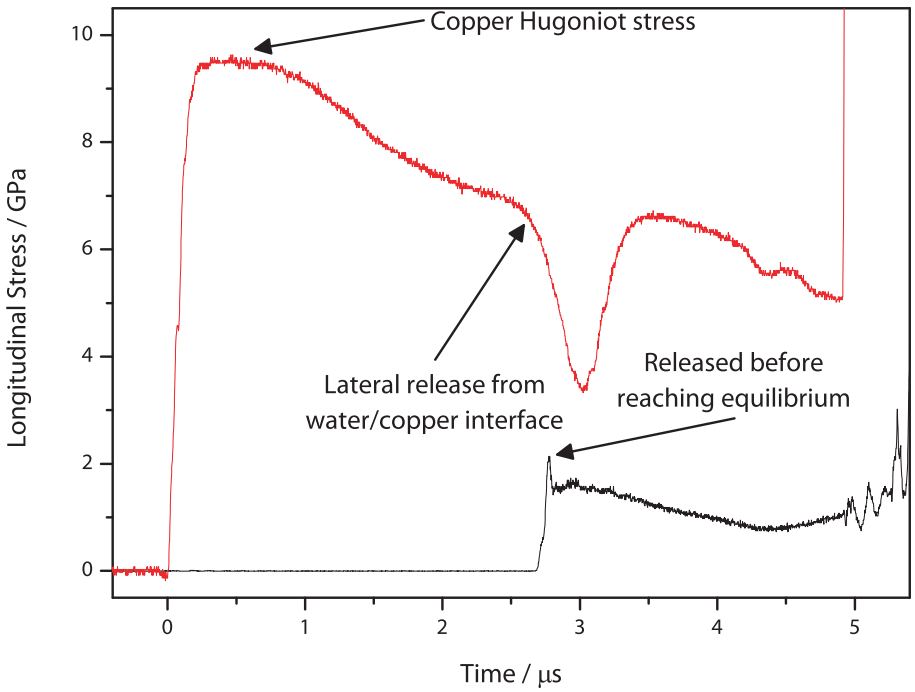

Figure 5.6: Front (red) and rear (black) gauge traces from experiment E100623A. The cell shown schematically in Figure 5.5 was impacted by a copper flyer at $0.491 \pm 0.005\,\mathrm{km\,s^{-1}}$. The front gauge is shocked to the Hugoniot state of copper and experiences a number of partial lateral releases, the greatest in magnitude of which comes from the copper/water interface. The front gauge is also partially reloaded as the shock propagating through the water is also transmitted at the copper/water interface. The rear gauge is partially released, again due to wave interactions at the copper/water interface before it has reached an equilibrium value.

sample in order to allow for placement of the fibres. The lack of measurement of the Hugoniot stress of the liquid mean that the transit time must be relied upon to determine the shock velocity; without measurement of the tilt, relying solely on the measured transit time is inaccurate. Further, the thicknesses of the various plates can not be greatly reduced due to the need to include sealing 'o'-rings - rendering it difficult, if not impossible to measure the reload stress in the liquid before releases have affected the gauges. For these reasons, it was concluded that the 'off-axis' style of cell was not suitable for the determination of either the Hugoniot of the liquid or its reload behaviour.

The final iteration of the liquid cell design returned to the on-axis design

shown in Figure 5.3, but replaced the front anvil, which had previously been made from copper, with PMMA. As the impedance of PMMA is much closer to that of the liquid, the release that propagates back into the anvil is small in magnitude. In addition, the impedance of the glue in which the gauge is embedded is conventionally taken as identical to the impedance in PMMA and thus, there no significant impedance mismatch is presented by the gauge package. This modification of the front anvil material reduces the particle velocity that can be imparted through symmetric impact, due to the lower impedance of PMMA; however, impacting the cell with a copper flyer will allow for the same particle velocities to be reached at the expense of a slight increase in uncertainty due to the use of two standard materials.

The final cell design is shown schematically in Figure 5.7. The sample thickness is defined by the thickness of the PMMA annulus, which was chosen as either $3.6\,\mathrm{mm}$ or $3.8\,\mathrm{mm}$, depending on the exact experiment, in order to maximise the transit time of the shock (and, hence, reduce the uncertainty on the measured shock velocity) whilst ensuring the rear gauge remains in a state of uniaxial strain. As the plate impact facility is fired into a rough vacuum, the cell must be vacuum tight. An 'o'-ring is used to seal the sample, with the outer diameter of the 'o'-ring being identical to the inner diameter of the PMMA annulus. To prevent bowing of the front plates, a soft (50 shore hardness) nitrile 'o'-ring was used; the 'o'-ring has a diameter of $4\,\mathrm{mm}$ and is therefore only lightly compressed. No bowing of the front plates was measurable. This 'o'-ring can clearly be seen in Figure 5.8, which is a photograph of one such cell. In order to fill the cell with a liquid, two holes were tapped in the rear anvil. A syringe was used to fill from the lower cell, with air being allowed to escape through the top hole. The transparent front plates enabled each cell to be visually inspected prior to impact to ensure that no air was left in the sample. The holes were sealed with by inserting a bolt that that had been wrapped in PTFE thread sealing tape. Whilst the insertion of a bolt into the filling hole compresses the water slightly, the effect is minimal - resulting in an increase in pressure of around $25\,\mathrm{MPa}$ - compared to the several-gigaPascal shock pressure obtained during experiments. The exact value of the pressure increase depends on how the bolt seals the hole, and the value given above is a maximum value, assuming that the bolt fills the entirety of the threaded hole; the actual pressure increase is likely to be much less than this.

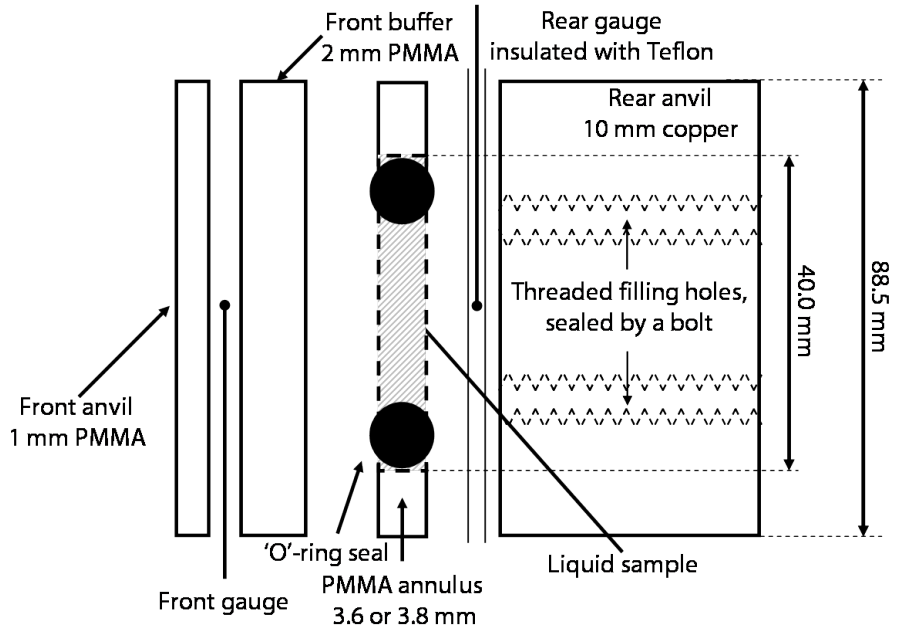

Figure 5.7: The final liquid cell design; the horizontal scale is exaggerated by a factor of 10. The front of the cell consists of two PMMA plates with a manganin gauge between them. The rear anvil is a $10\,\mathrm{mm}$ copper plate to which a manganin gauge, insulated with Teflon, has been bonded. The sample is confined by a PMMA annulus of thickness either $3.6\,\mathrm{mm}$ or $3.8\,\mathrm{mm}$. An 'o'-ring is used to seal the cell, which is sccrewed to a standard aluminium or tufnol mounting ring. Two threaded holes in the copper plate enable the cell to be filled from the rear. These holes are then sealed with a bolt used to compress a small 'o'-ring. The internal diameter of the PMMA annulus is $40\,\mathrm{mm}$, enabling the placement of optic fibres, to measure tilt, around the edge of the sample.

Release-wave propagation

The propagation of release waves in plate impact targets was discussed in §3.4. Whilst Equations 3.8 and 3.9 enable determination, approximately, of when lateral releases erode the uniaxial stress state, the more complicated propagation of releases in the liquid impact cell are not amenable to this simple analytical treatment, as has been evidenced by the unexpected arrival of release waves in the earlier cell designs. A hydrocode is a computational code capable of solving numerically the Euler equations for fluid flow, and the jump conditions for a given experimental scenario [Benson, 1992]. Hydrocode simula-

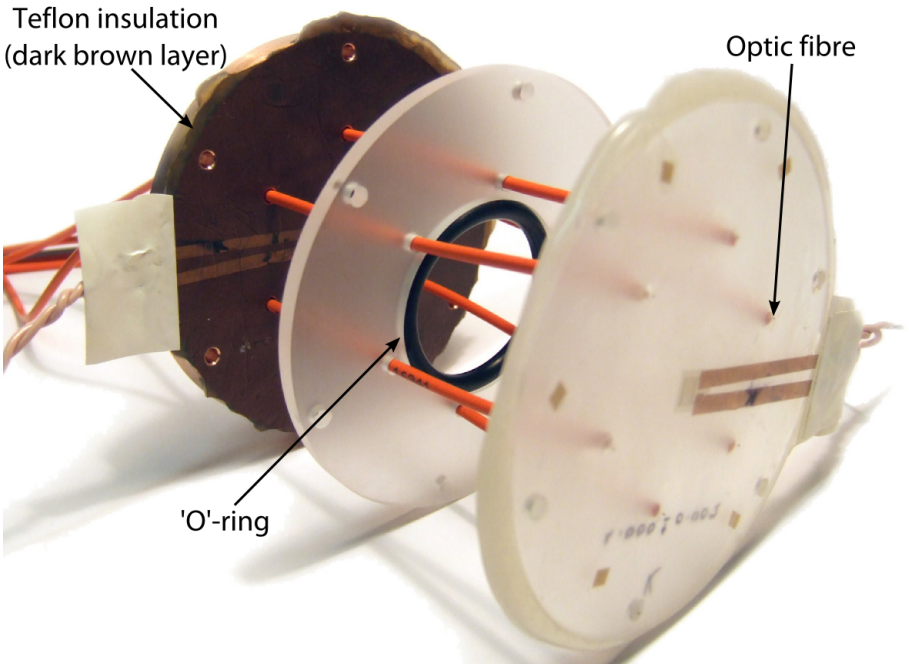

Figure 5.8: Typical cell used in studying the shock response of liquids, shown schematically in Figure 5.7. The cell is shown after optic fibres, used to measure tilt, have been inserted but before final assembly and filling. The rear gauge is insulated with Teflon, whilst the front gauge is simply glued between two PMMA plates. The central PMMA annulus holds an 'o'-ring and defines the thickness of the liquid sample.

tions of the cell described in Figure 5.7 were implemented in the C-AMR hydrocode in collaboration with Stefan Schoch [Schoch, 2011]. Figure 5.9 shows the model of the liquid cell implemented in th hydrocode simulations. The simulations are axisymmetric about $y = 0$, and the liquid is modelled as water. The buffer, anvil, and annulus shown in Figure 5.7 are considered as single continous piece of PMMA in the hydrocode. The rear anvil is modeled as a block of copper. The flyer is placed in contact with the front surface of the cell, and given an appropriate initial velocity. The red rectangles, which are not part of the simulation, indicate the approximate Lagrangian location, and lateral extent, of the front and rear gauges. Two simulations, shown below, were conducted. In the first simulation (Figure 5.10), the cell was impacted by a PMMA flyer at $0.500\,\mathrm{km\,s^{-1}}$; the second simulation (Figure 5.11) used a copper flyer at $1.000\,\mathrm{km\,s^{-1}}$. The simulation outputs have been plotted in a way

that highlights variations in density such that shocks and releases can visually be tracked. The approximate Eulerian position and sizes of the embedded manganin gauges have been overlayed on the simulation results. Both simulations show similar features: releases propagate from the edge of the flyer and from the interface between the water and PMMA as anticipated. These lateral releases can be seen as the expanding circular dark lines in the simulation results. In both cases, lateral releases do not reach the gauges until some time after the shock has reached the rear surface of the target. It is concluded, therefore, that the gauges experience uniaxial loading over the entire time-scale of the experiment.

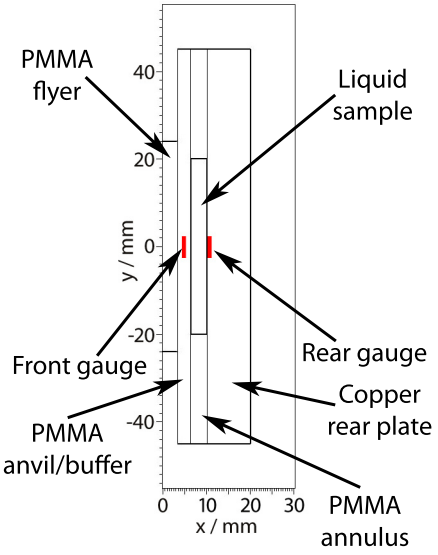

Figure 5.9: Model of the liquid cell shown in Figure 5.7 as implemented in the C-AMR hydrocode. The model is axisymmetric about $y = 0$. The appriximate Lagrangian positions of the front and rear manganin gauges is indicated by the red rectangles, which are not a part of the simulation, but have been added graphically afterwards. The PMMA parts of the cell are treated as a single piece of PMMA, with the rear anvil treated as a separate piece of copper. The liquid is modeled as water. The flyer is placed in contact with the front face of the cell, and assigned an initial velocity equal to the desired impact velocity.

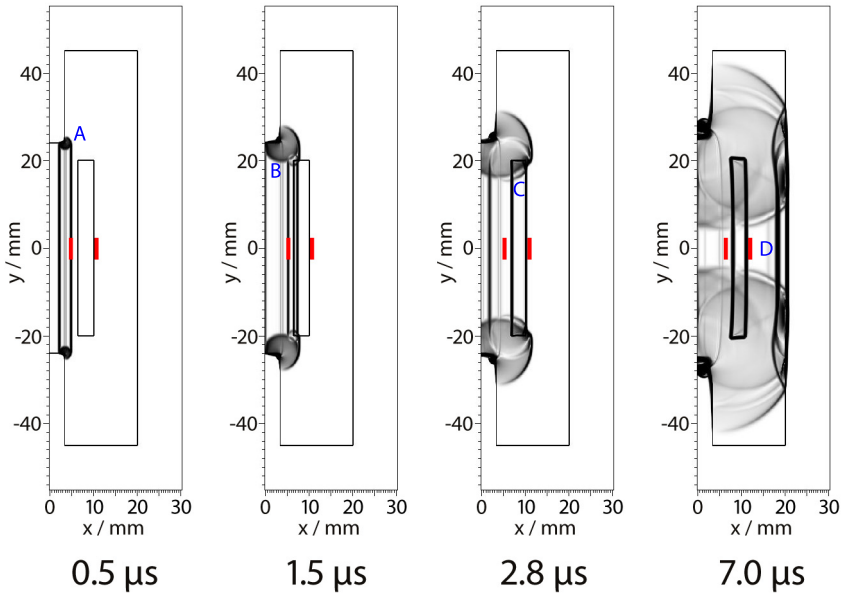

Figure 5.10: Axisymmetric hydrocode simulation of a PMMA flyer impacting the liquid cell shown in Figure 5.7 at a velocity of $0.500\,\mathrm{km\,s^{-1}}$ showing variations in density. Immediately after impact, lateral releases (A) start to encroach on the target. After $1.5\,\mathrm{mus}$, the shock has reached the liquid and the resultant release has propagated back to the front gauge. Secondary releases (B) are formed at the edge of the liquid. At around $2.8\,\mathrm{mus}$, the shock reaches the rear gauge package and releases (C) have travelled a short distance into the liquid. It is not until $7.0\,\mathrm{mus}$ after impact that releases (D) begin to approach the gauges. Therefore, the gauges can be considered to undergo unixial loading for the entire experiment.

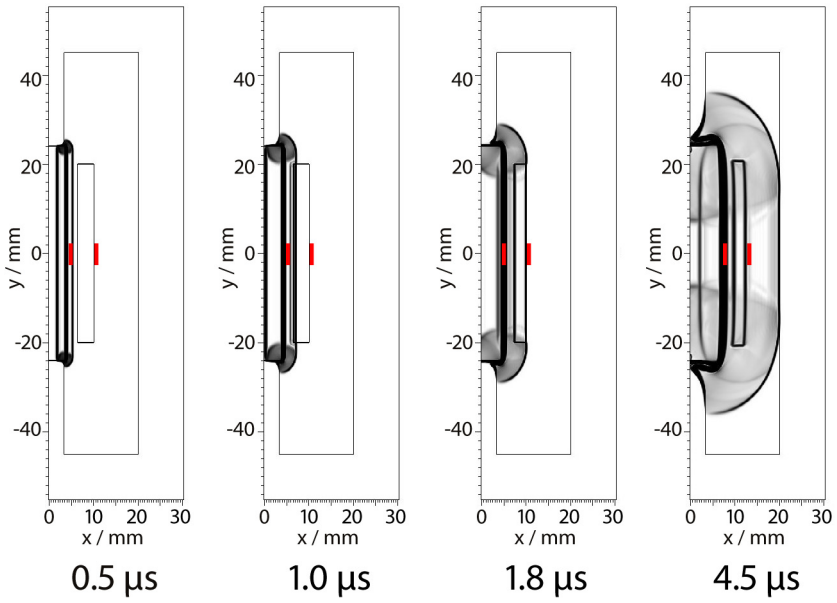

Figure 5.11: Axisymmetric hydrocode simulation of a copper flyer impacting the liquid cell shown in Figure 5.7 at a velocity of $1.000\,\mathrm{km\,s^{-1}}$ showing variations in density. Similar to those observed in Figure 5.10 are observed, although the greater shock velocity shortens the timescale over which these events occur. In the case of this high velocity impact, the gauges remain in uniaxial strain until at least $4.5\,\mathrm{mus}$ when the simulation ended due to numerical instabilities associated with the longitudinal release from the rear free surface.

Considerations regarding anvil materials

A number of different anvil materials have employed in the research described in this thesis; whilst the rear anvil has, by virtue of its relatively high impedance, been machined from copper, front anvils and buffers, and flyer plates, have been constructed from both copper and poly(methyl methacrylate) (PMMA).

The analysis discussed above, and in particular the wave diagram presented in Figure 4.15, neglects deviations from an assumed shock response that results in the emergence of only a single wave. From Chapter 2, it should be recalled that, for example, an elastic-plastic material shocked above its HEL exhibits a two-wave response that is not catered for in the present analysis. Such an approximation, of only a single-wave response, greatly simplifies the reduction of experimental data yet unavoidably introduces certain errors. The magnitude of such errors is, however, smaller than the experimental uncertainties discussed above but is presented in detail below.

Figure 5.12 shows a typical shock profile in PMMA, as recorded by an embedded manganin gauge. PMMA does not exhibit the precursor associated with an elastic-plastic material, nor does it exhibit a sharp rise to a final state; instead the longitudinal stress in PMMA jumps to an instantaneous stress (point A) around two-thirds that of the equilibrium state before ramping to the final state (point B).

By modelling PMMA as a thermoviscoelastic material, Nunziato and Walsh [1973] were able to account for these features. Barker and Hollenbach [1970] have demonstrated that, to moderate particle velocities, the behaviour of PMMA, in the shock velocity – particle velocity plane, differs markedly from the anticipated linear Hugoniot. Their data, which were quoted without errors, are reproduced in Figure 5.13.

The best, third-order, polynomial fit to these data is described by Equation 5.1 and is valid to the maximum reported particle velocity: $u_p = 0.6250\,\mathrm{km\,s^{-1}}$.

$$U_S = 2.745 + 3.534u_p - 8.834u_p^2 + 8.361u_p^3. \tag{5.1}$$

Above this stress, the Hugoniot is adequately described by that reported in the literature [Asay and Shahinpoor, 1993, Appendix C]:

$$U_S = 2.598 + 1.516u_p. \tag{5.2}$$

Further, it has been reported [Barker and Hollenbach, 1970; Chapman, 2009a] that the release path in PMMA differs markedly from the crude ap-

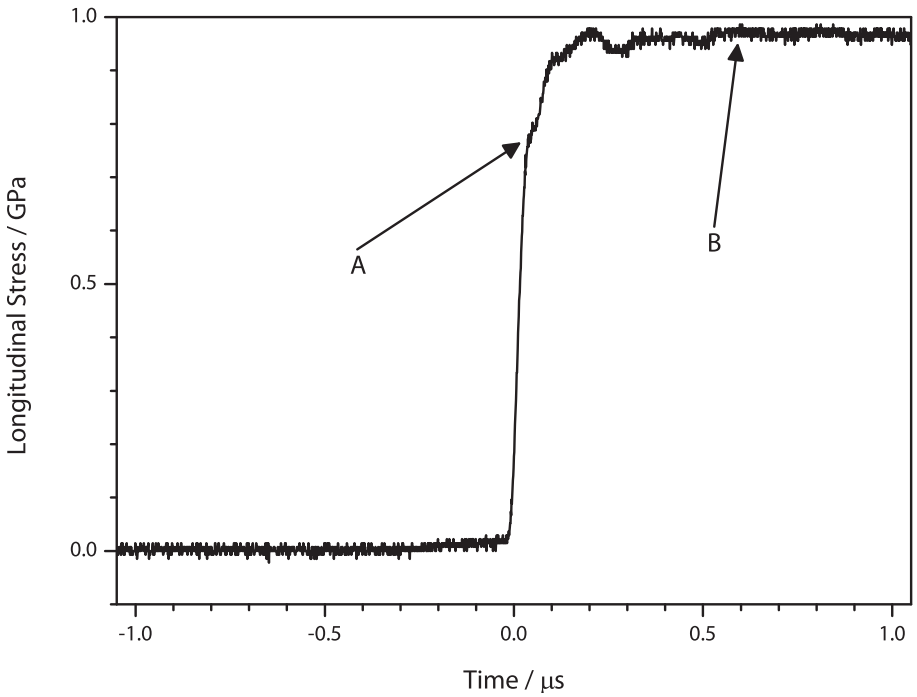

Figure 5.12: Stress history recorded by a manganin gauge embedded in PMMA, from experiment E110225A, due to symmetric impact at $0.494\,\mathrm{km\,s^{-1}}$. The trace shows an initial sharp rise, of approximately $50\,\mathrm{ns}$ duration, indicating a well-aligned shock, to the point A, which is approximately two-thirds the expected stress. The stress then gradually rises to the peak stress, B, which co-incides with the expected stress.

proximation that releases occur along a path close to the Hugoniot. Chapman [2009a] suggests that the crude approach yields, in impedance matching, a stress and particle velocity some $3\,\%$ higher than the stress that would be found by using the actual release curve. Indeed, this appears to be a worst-case scenario: for materials whose impedances are close to that of PMMA, as is the case for the liquids studied in Chapters 5 and 6, the uncertainity introduced by approximating the release by the Hugoniot is negligible, and thus ignored. Additionally, without an accurate model for the release path from a given state, it is impossible to analytically take this difference into account.

The analysis described above is greatly simplified in the case where a single, linear, Hugoniot describes the anvil's response in the U_S–u_p plane for all u_p. The experiments reported in Chapters 5 and 6 consider particle velocities

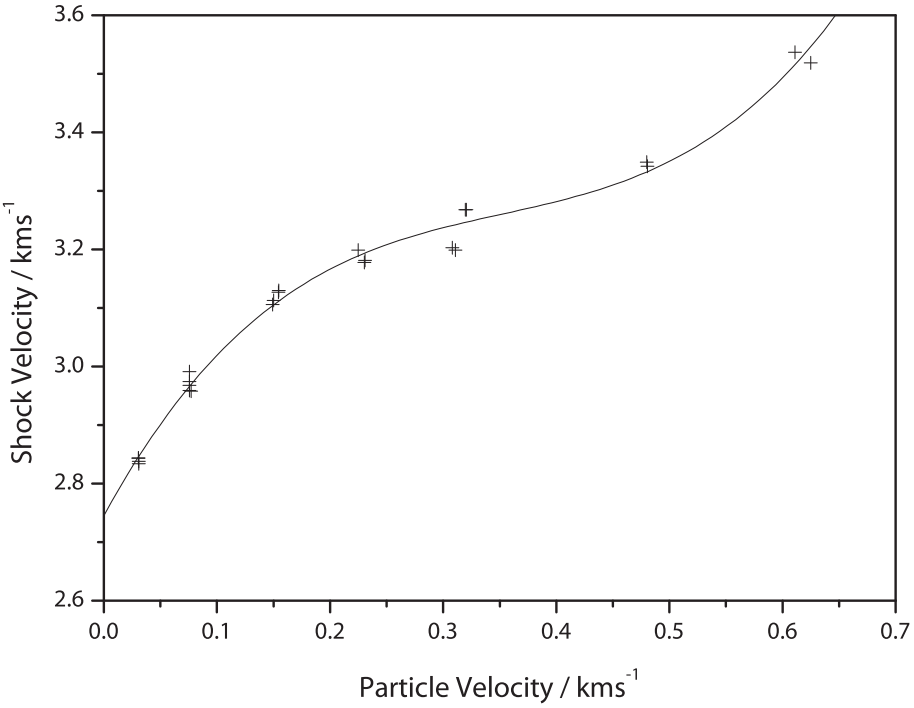

Figure 5.13: Shock velocity – particle velocity Hugoniot for PMMA, after Barker and Hollenbach [1970]. The solid line, a third-order polynomial providing the best fit to the experimental data, passes within $1\,\%$ of the data, and is described by Equation 5.1

in PMMA both above and below the particle velocity, $u_p = 0.6250\,\mathrm{km\,s^{-1}}$, at which deviations from the linear Hugoniot become significant. However, the effect of considering the more complex relation of Equation 5.1 on the determination of the liquid Hugoniots is minimal. Indeed, the more complicated analysis shifts the resultant Hugoniot by considerably less than $1\,\%$: far less than the uncertainity in the Hugoniots reported, and within the uncertainties between the different analysis methods. This latter point is discussed further below.

In addition to simplifying the analysis, relying on the linear Hugoniot introduces fewer assumptions. Without direct measurements of the shock- and particle-velocities in the specific PMMA used in this thesis, there can exist some doubt as to the validity of Equation 5.1. Whilst there are, undeniably, errors associated with this simplified approach, it is believed that they are small

in magnitude and insignificant when considered alongside other experimental uncertainties, such as the behaviour of the manganin gauges in release, impedance mismatches between the gauge package and surrounding PMMA, or variations in sample thickness. Indeed, the variation in thicknesses of target plates and gauge packages, which vary randomly between experiments, represent the dominant contribution to the uncertainty in the transit time through anvils. In dealing with cells that have been pre-heated, the room temperature Hugoniot of PMMA has been used. As PMMA is relatively well characterised, its published equation of state [e.g. Asay and Shahinpoor, 1993] can be used to calculate the effect of temperature, using the method decribed by Dai et al. [2006]. The PMMA Hugoniot at $65\,^{\circ}\mathrm{C}$ lies within error of the ambient temperature Hugoniot; thus the assumption that the effect of pre-heating on the PMMA Hugoniot can be neglected is justified, as it is substantially smaller than the other experimental uncertainties.

Strength effects in Copper

Copper is widely used in shock experiments, as it has a high impedance, low elastic limit, does not exhibit any phase transitions, and is both easy to machine and available as a reproducible stock material [Davison and Graham, 1979].

Figure 5.14 shows experimentally-determined stress–particle velocity states in copper (Cu101), as measured by embedded manganin gauges under symmetric impact. The data are collected from previous work conducted in this laboratory, and have been re-analysed for the present work. The experimental configurations are reported elsewhere [Chapman, 2009c]. The re-analysed data are shown together with the linear shock equation of state for copper, Equation 5.3, given by Asay and Shahinpoor [1993, Appendix C]:

$$U_S = 3.940 + 1.489 u_p. \tag{5.3}$$

The data of Figure 5.14, which lie within experimental error of Equation 5.3, would suggest that there are no appreciable strength effects in copper. However, the existence of an HEL in Cu101 has been demonstrated experimentally by Chapman [2009a]. Figure 5.15 (ibid.) shows the free surface velocity, determined by VISAR, in Cu101 under low-velocity symmetric impact. The two-wave structure consists of an elastic precursor, of stress amplitude $\sigma_{HEL} = 0.3 \pm 0.1\,\mathrm{GPa}$, and a second wave which increases the longitudinal

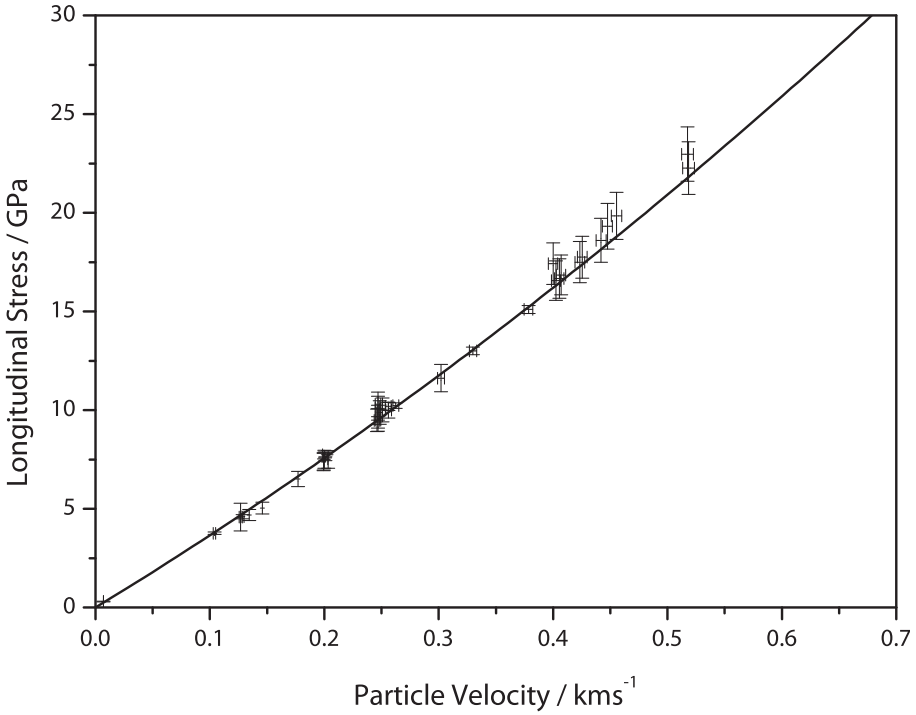

Figure 5.14: Copper Hugoniot states, measured with embedded manganin gauges, under symmetric impact, re-analysed from experiments reported in Chapman [2009c]. The solid line is the linear shock velocity–particle velocity Hugoniot given by Equation 5.3.

stress to that of the shock; the yield strength at the HEL is found by applying the Tresca or von Mises yield criterion and is $Y_{HEL} = 0.14 \pm 0.05\,\mathrm{GPa}$.

The elastic precursor becomes overdriven, leaving a single wave response, when the elastic loading line, of slope $\rho_0 C_e$ (where C_e is the elastic wave speed) intersects the linear shock velocity Hugoniot in the stress–particle velocity plane. For the elastic wave speed in copper, $4.76\,\mathrm{km\,s^{-1}}$ [Chapman, 2009a], this occurs at a stress of approximately $23.5\,\mathrm{GPa}$.

Figure 5.16 considers the deviation of longitudinal stress from hydrodynamic pressure in a material with finite strength. The low yield strength of copper, however, means that there is little difference between these curves. Indeed, it is unlikely that a manganin gauge would be sensitive to this slight offset, and, furthermore, the impedance mismatch between the gauge package and copper would 'smooth out' the elastic precursor wave. The close agree-

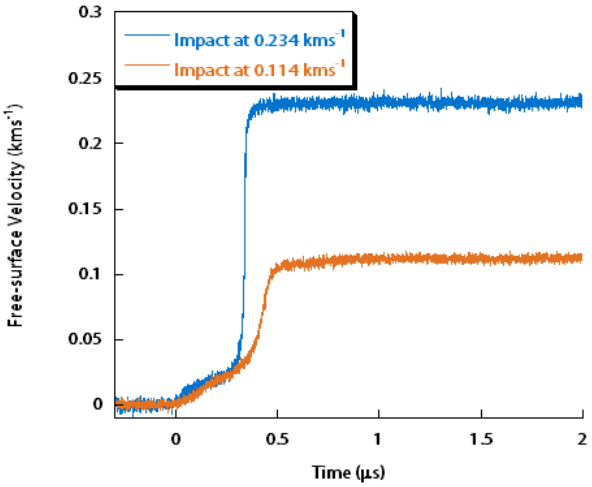

Figure 5.15: From Chapman [2009a]. The two-wave structure measured by VISAR at the free surface of Cu101 during symmetric impact at two different impact velocities.

ment between longitudinal stresses measured by manganin gauges and the linear shock velocity equation derived from over-driven experiments (Equation 5.3), shown in Figure 5.14 indicate that, within the diagnostic sensitivity of manganin gauges, this effect can be ignored.

Figure 5.17 shows the wave profile that would be observed at the interface between an ideal elastic-plastic material and a lower impedance window. The unloading portion would occur along the lower line of 5.16.

The ideal elastic-plastic material provides the 'worst case' scenario: in a material which is not perfectly elastic-plastic, the longitudinal stress lies closer to the hydrostat. Johnson et al. [1992] report measurements of the release wave structure in oxygen-free electronic copper (OFEC), interpreting the observed 'quasi-elastic' behaviour in terms of internal stresses and dislocation motion. Figure 5.18, from Johnson et al. [1992], is representative of the release wave profile in OFEC.

The release wave structure of OFEC, whilst more ideally elastic-plastic than in other materials, still deviates from the ideal case, and the release state lies closer to the Hugoniot than Figure 5.16 implies. Coupling this with the low yield strength measured in C101, it is concluded that the error introduced by approximating the release of copper by its Hugoniot is negligible and may

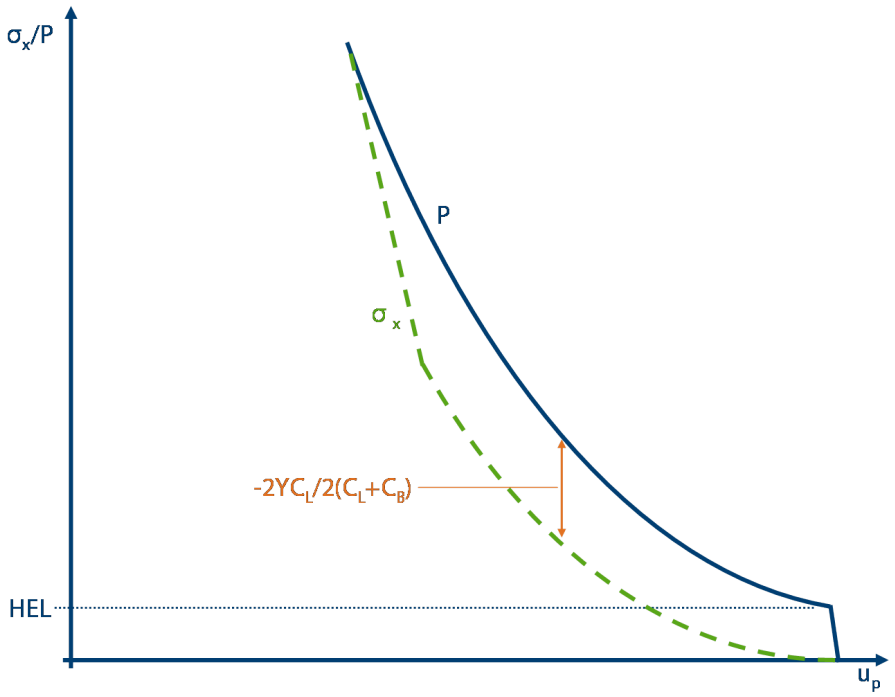

Figure 5.16: Ideal elastic-plastic unloading, in P–u_p space. The longitudinal stress in release is displaced below the pressure, P (calculated using the, strengthless, linear shock-velocity Hugoniot, by $-\frac{2}{3}\frac{C_L}{C_L+C_B}Y$ where C_L and C_B are the ambient pressure longitudinal and bulk sound speeds respectively. The additional factor of $\frac{C_L}{C_L+C_B}$ when compared to the stress-volume curve of Figure 2.9 reflects the fact that the displacement is smaller in stress–particle velocity space, and is derived by Davison [1998].

be ignored.

5.2 Pure water, ambient temperature

The water used in experiments in this thesis was de-ionised and vacuum degassed prior to performing each experiment. The shock response of pure water has been widely reported in the literature [Gurtman et al., 1971; Mitchell and Nellis, 1982; Nagayama et al., 2002], and thus a small number of experiments on pure water at ambient temperature were perfomed to demonstrate the validity of the experimental design described above and of the data analysis methods described in Chapter 4. The gauge traces resulting from such an experiment, at an impact velocity of $0.787 \pm 0.008\,\mathrm{km\,s^{-1}}$ with a PMMA

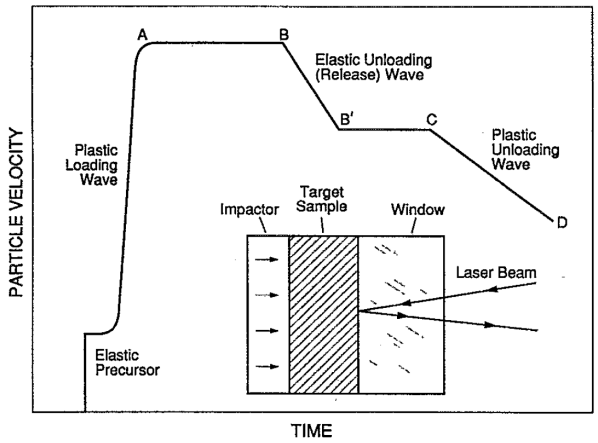

Figure 5.17: From Johnson et al. [1992]. An experimental geometry to measure the release wave structure in a test material. The particle velocity-time history for an ideal elastic-plastic material in this geometry is shown.

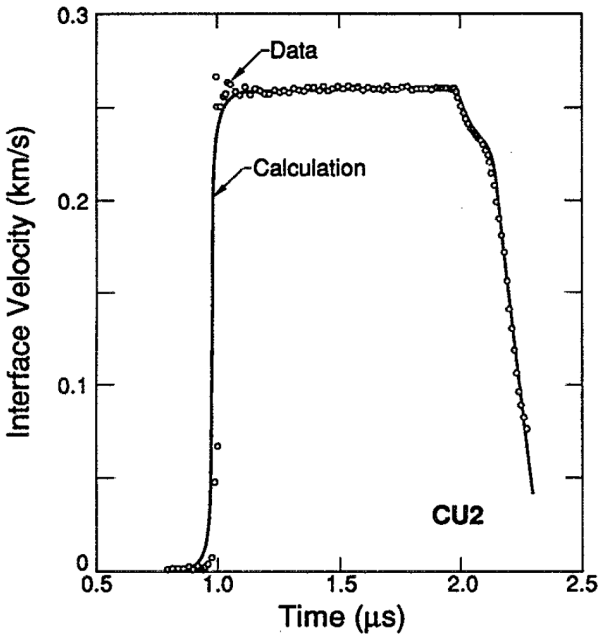

Figure 5.18: From Johnson et al. [1992]. Measured interface velocity for OFCE shocked to 10 GPa in the geometry shown in Figure 5.17. The quasi-elastic nature of the release wave is evident.

flyer are shown in Figure 5.19. The trace is representative of those obtained in the experiments discussed in the remainder of this chapter and in Chapter 6. The tilt in this experiment was measured as $1.8 \pm 1.1\,\mathrm{mRad}$. Comparison should be made between these gauge traces, those shown in Figure 5.2 obtained with the initial cell design, and with the idealised responses shown in Figure 4.17. Clearly, the final design produces siginificantly better stress histories from both gauges; the arrival of the shock at each is clearly visible, and identifiable stress levels, associated with the Hugoniot and reload state of the liquid, persist for significant periods of time. The reverberation visible on the rear gauge trace is due to the impedance mismatch between water and Teflon; the effect of this mismatch was discussed in §4.2 and is sufficiently small that it may be neglected.

Principal Hugoniot

In order to demonstrate that the reduction of the Hugoniot data yields appropriate values, two experiments were conducted on water at an initial temperature of at $18 \pm 2\,^{\circ}\mathrm{C}$. Figure 5.20 shows the experimentally determined Hugoniot states in water, analysed using the first and third analysis methods discussed in §4.2. The solid line is the linear Hugoniot of water given by Nagayama et al. [2002] as $U_S = 1.45 + 1.99u_p$, and the dashed lines represent the quoted uncertainties in the intercept and slope of the Hugoniot. Both methods of analysis yield shock and particle velocities that lie within error of this Hugoniot, indicating that both methods produce sensible results; the slight differences between the two methods are discussed further in §5.3.

Rybakov [1996] note that there is a slight break in the gradient of the Hugoniot of water at $P = 2.86\,\mathrm{GPa}$, suggesting this is due to the onset of a partial phase change, $0.8\,\%$ by mass, to ice VII. Dolan and Gupta [2003] report on the quasi-isentropic compression of water. Their pressure–temperature phase diagram for water is reproduced in Figure 5.21; the temperatures on the Hugoniot are calculated using the model proposed by Gurtman et al. [1971]. The temperatures calculated in this way suggest that the principal Hugoniot of water does not cross the ice VII boundary; Dolan and Gupta [2003] note that the freezing of water under shock compression is an open question. In considering the relevant literature, Duvall and Graham [1977] had previously concluded similarly, citing the work of Kormer and Krishkevich [1968]: the freezing of water into ice VII only occurs in isentropic loading. It seems, therefore,

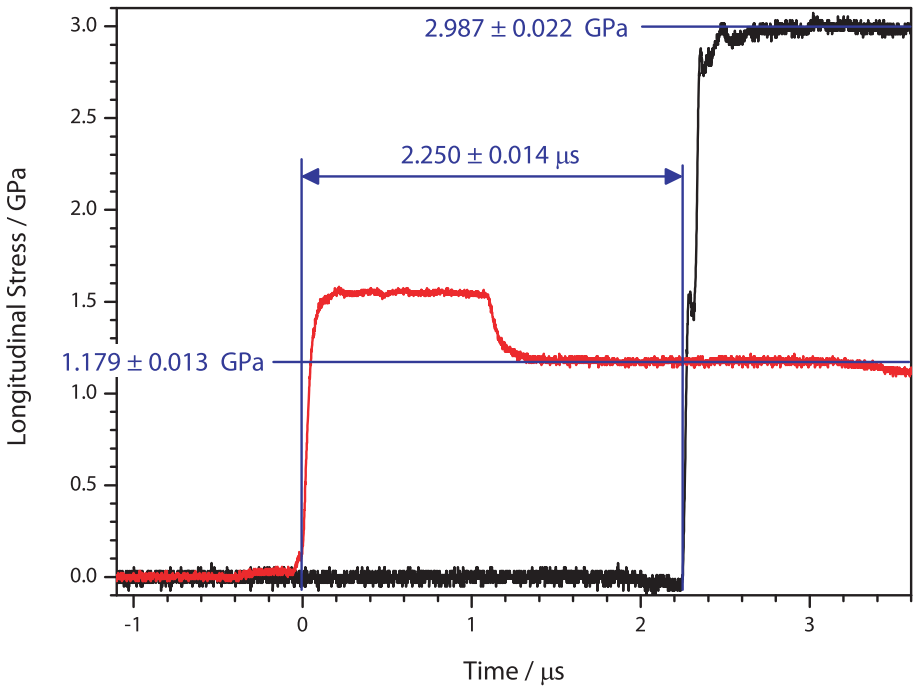

Figure 5.19: Front (red) and rear (black) stress gauge traces from experiment E100927A. A liquid cell, containing water at $18 \pm 2\,^{\circ}\mathrm{C}$, was impacted by a PMMA flyer at $0.787 \pm 0.008\,\mathrm{km\,s^{-1}}$. The front gauge is first shocked to the Hugoniot state of PMMA, before being released to the Hugoniot state of water at a stress of $1.179 \pm 0.013\,\mathrm{GPa}$; the shock reaches the rear gauge $2.250 \pm 0.014\,\mu\mathrm{s}$ after first arriving at the front gauge. The stress in the rear gauge, corresponding to the reload state of water, is $2.987 \pm 0.022\,\mathrm{GPa}$. Comparing these gauge traces with those obtained with the initial cell design (Figure 5.2), it is clear that the final cell design represents a significant improvement. The reverberation visible on the rear gauge trace is due to the impedance mismatch between water and Teflon; the effect of this mismatch was discussed in §4.2 and is sufficiently small that it may be neglected.

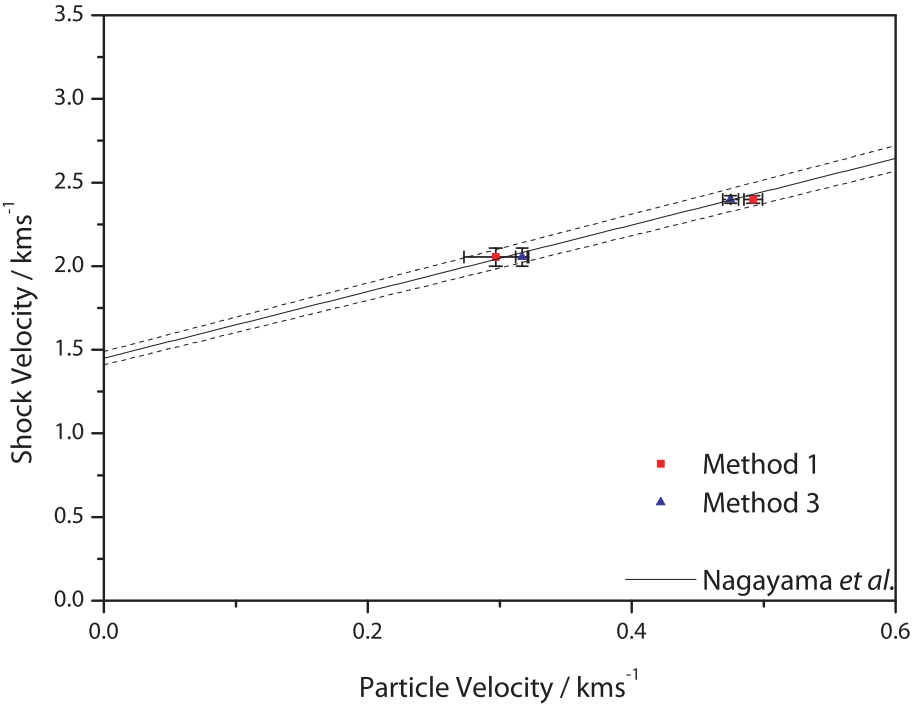

Figure 5.20: Measured Hugoniot states in water at $18 \pm 2\,^{\circ}\mathrm{C}$, compared to the linear Hugoniot, $U_S = 1.45 + 1.99u_p$, given by Nagayama et al. [2002]; the dashed lines reflect the quoted 3 % uncertainty in the fitting constants. The data analysed by methods 1 and 3 lie within error of the fit, demonstrating the validity of these analysis methods.

that the gradient change in the water Hugoniot reported by Rybakov [1996], which has not been reported elsewhere in the literature, is not due to to a freezing transition and the results presented may be in error.

Dolan [2003] has noted that the Hugniot given by Nagayama et al. [2002] does not extrapolate well to particle velocities outside the experimental range. In order to examine the reload behaviour of water, a Hugoniot which can be extrapolated to higher particle velocities is required. Figure 5.22 presents the Hugoniot states in water determined by method 3, and the data for water given by Marsh [1980] for particle velocities below $1.5\,\mathrm{km\,s^{-1}}$. The fitted line is the best-fit linear Hugoniot through these data and is given by $U_S = 1.50 \pm 0.04 + 1.85 \pm 0.04u_p$. The data are well-described by this fit, and it is therefore concluded that a single linear Hugoniot represents the best fit to the data to $u_p = 1.5\,\mathrm{km\,s^{-1}}$, and it is this Hugoniot which will be used in the analysing

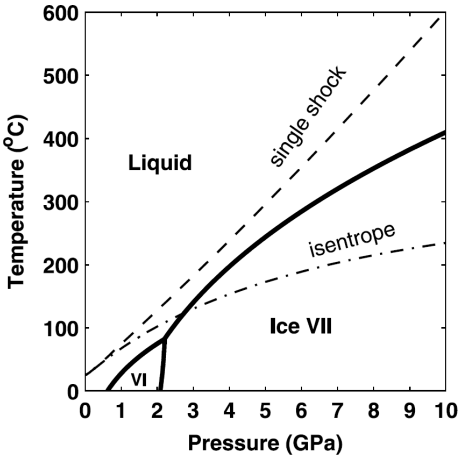

Figure 5.21: Pressure–temperature phase diagram for water, from Dolan and Gupta [2003]. The two dashed curves represent the limiting temperature curves - the Hugoniot at the upper temperature range, calculated using the model propsed by Gurtman et al. [1971], and the isentrope.

reload experiments.

Reload experiments

The Mie-Grüneisen equation of state has been applied to the shock/reload behaviour of water by a number of authors [e.g., Gurtman et al., 1971; Mitchell and Nellis, 1982; Nagayama et al., 2002]. Indeed, Gurtman et al. [1971] provide a form for the volume-dependent Grüneisen parameter, Γ, against which it is possible to compare experimental results. Using the Hugoniot shown in Figure 5.22, and the methodology described in §4.2, it is possible to obtain a value for Γ from experiment E100927A (Figure 5.19). At a volume in the reloaded state of $0.707 \pm 0.010\,\mathrm{cm^3 g^{-1}}$, the value of Γ determined in this way is 1.07 ± 0.57, compared to the value given by Gurtman et al. [1971] of 1.05. The uncertainty in Γ is determined by analysis, in quadrature, of the uncertainties in the measured stresses, shock velocity, and the parameters defining the Hugoniots of both the water and the rear copper anvil; it is believed that this method gives rise to a larger uncertainty than would be suggested by the data, as it neglects covariance in the uncertainties on these quantities. The covariance arises as the Hugoniot of the liquid has been generated from the experimental data, and these data are used in conjunction with the Hugoniot when

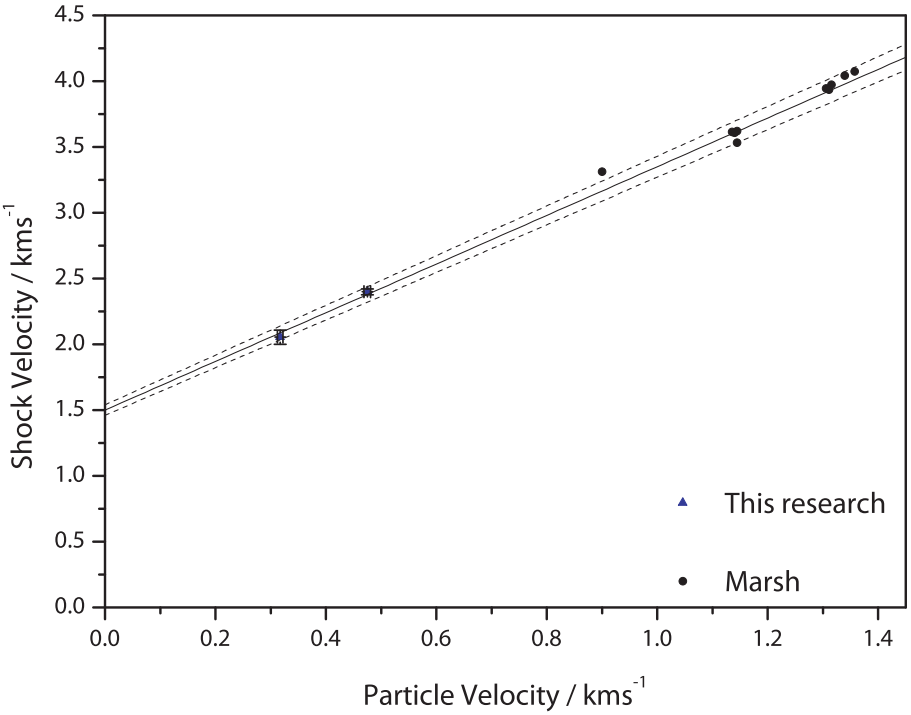

Figure 5.22: Hugoniot of water below $u_p = 1.5\,\mathrm{km\,s^{-1}}$. The data comprise the present research, as determined by method 3, together with that of Nagayama et al. [2002] and Marsh [1980]. The line fitted through these data is given by $U_S = 1.50 \pm 0.04 + 1.85 \pm 0.04 u_p$ and is shown by the solid line, with the dashed lines representing the upper and lower bounds of this fit. The coefficient of determination of the fit is 0.99. It is therefore concluded that the Hugoniot of water over this particle velocity range is best described by the present fit.

calculating Γ. It is not apparent how this covariance may be accounted for in the present analysis. It is felt that the agreement demonstrated between the determined value of Γ, and that given by Gurtman et al. [1971], demonstrates the validity of the experimental techniques presented. Experiment E100816A, which had a reload stress of $1.678 \pm 0.040\,\mathrm{GPa}$ yields a value of Γ with an uncertainty of around $500\,\%$. As Γ is, ultimately, dependent on the difference between the Hugoniot and reload stresses, when this difference is very small (as is the case at low reload stresses), the proportionate uncertainties are large. Γ can only be generally determined from the experiments in this thesis when the reload stress is at least $3\,\%$ below the Hugoniot; this criterion is satisfied

when the reload stress is around $3\,\mathrm{GPa}$.

5.3 Pure water, elevated temperature

The method adopted in this thesis to determine the shock temperature rise in a material requires first the measurement of the principal Hugoniot of the material. Thence, shock/reload experiments enable an empirical fit to the Mie-Grüneisen equation of state to be made. Combining these two measurements with a suitable model for the heat capacity, it is possible to calculate shock temperatures along the Hugoniot. The remainder of this chapter discusses a series of experiments conducted on water, at an initial temperature of $66 \pm 2\,^{\circ}\mathrm{C}$, to measure the Hugoniot and volume dependence of the Grüneisen parameter, Γ. These measurements will then be combined to calculate the shock temperatures in water.

In order to investigate liquids at different initial temperatures, it was necessary to pre-heat the cell described above. Heating was achieved by attaching two metal clad resistors to the rear copper anvil, and applying around $1\,\mathrm{A}$ at $30\,\mathrm{V}$. During plate impact experiments, the initial temperature was determined by a single thermocouple mounted on the rear anvil. Prior to conducting any plate impact experiments on the heated cells, the effects of heating the cell were investigated by placing thermocouples on the front anvil and within the liquid itself . It was found that if the cell was heated over a period of several hours, and then filled with the test liquid, which had been separately heated, no significant thermal gradients were introduced. A series of experiments were conducted on de-ionised water at an initial temperature of $66 \pm 2\,^{\circ}\mathrm{C}$. The initial density, ρ_0, of water at this temperature is $0.878\,\mathrm{g\,cm^{-3}}$ [Washburn, 2003].

Principal Hugoniot

Figure 5.23 shows the experimentally determined Hugoniot states, as determined by the three methods given in §4.2, in shock velocity–particle velocity space.

In addition to the experimental uncertainties discussed earlier, various systematic errors are associated with the two methods. Principally, these can be considered to come from two sources: firstly, the uncertainty associated with stress measurements made in release and, secondly, the precise nature of the

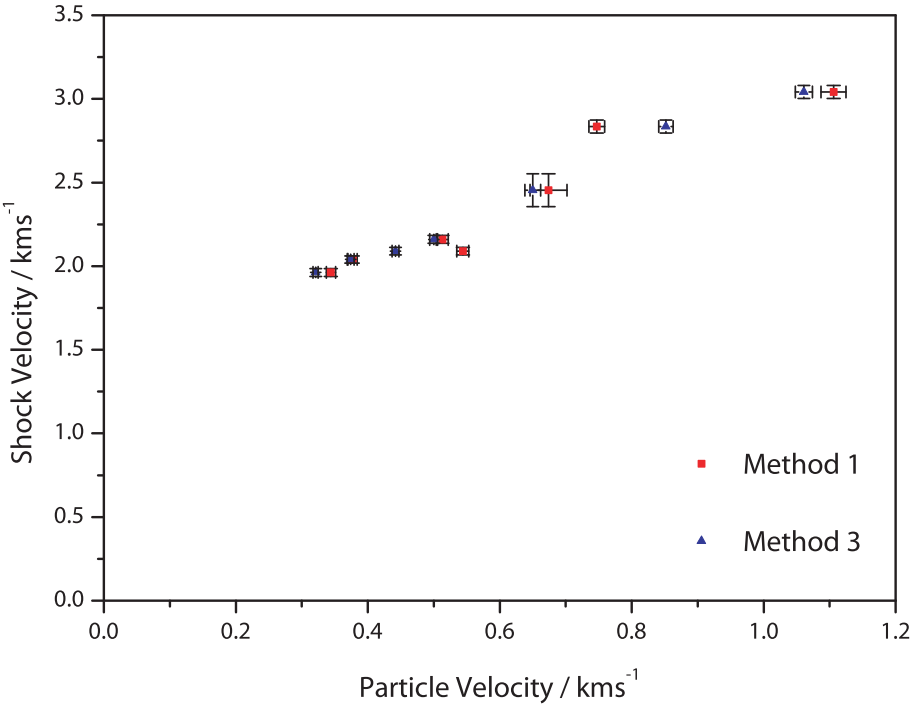

Figure 5.23: Measured Hugoniot states for water at $66 \pm 2\,^{\circ}\mathrm{C}$, determined using using two of the methods described in §4.2. The two methods yield somewhat different results for the Hugoniot state for each experiment. Method 3 is considered to give the most accurate determination of the Hugoniot. The systematic uncertainties relating to each method are discussed in the text.

release path of the front anvil material. As the water has a lower impedance than PMMA, the Hugoniot state lies on the release curve of PMMA. The stress measured by a gauge embedded in PMMA, therefore, also lies on the release curve of the PMMA with the gauge itself in a state of partial release.

Considering first the determination of stress from the resistance change of the manganin gauge, it should be recalled that the resistance of manganin is subject to hysteresis on unloading. It is assumed that, when the peak stress experienced by the gauge is below $1.5\,\mathrm{GPa}$, the gauge behaves elastically. For peak stresses above this elastic limit, a second calibration curve [Yaziv et al., 1980] can be applied, which gives stresses in the release state of the gauge. This calibration is, however, somewhat uncertain for stresses that are above $80\,\%$ of the peak stress. Figure 5.24 shows the front stress gauge trace, from experiment E101126A, which resulted from the impact of a cop-

per flyer at $0.590 \pm 0.006\,\mathrm{km\,s^{-1}}$. The peak stress (PMMA Hugoniot) was $2.034 \pm 0.011\,\mathrm{GPa}$, and the release stress (water Hugoniot/PMMA release curve) was $1.964 \pm 0.015\,\mathrm{GPa}$. This latter figure is around $97\,\%$ of the peak stress, and is therefore in the uncertain region of the calibration.

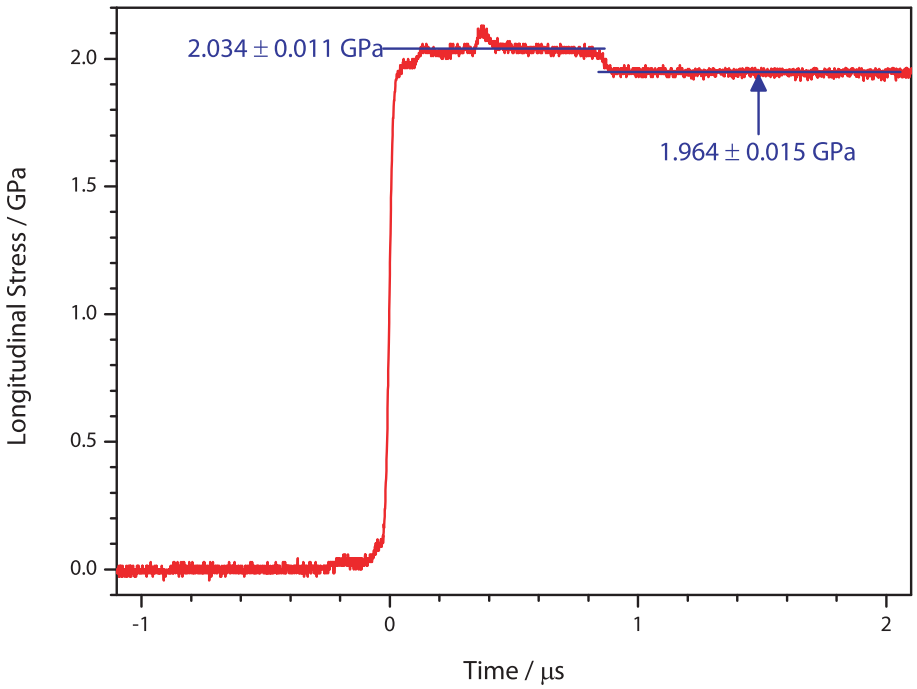

Figure 5.24: Front stress gauge trace from experiment E101126A. The peak stress, $2.034 \pm 0.011\,\mathrm{GPa}$, corresponds to the Hugoniot stress of PMMA. The second plateau, at $1.964 \pm 0.015\,\mathrm{GPa}$, is the Hugoniot stress of the liquid, and lies on the release curve of PMMA. It is also, evidently, a state in release of the manganin gauge and thus subject to the release calibration given by [Yaziv et al., 1980].

§5.1 discussed the behaviour of PMMA in release. It was concluded that, in general, the widely-used approximation that the release curve of a material may be approximated by the Hugoniot, was inappropriate for PMMA, which demonstrates a complex, non-linear, thermo-visco-elastic, rate-dependent response. For states in partial release that lie close to the Hugoniot state from which they are released, the uncertainty introduced by neglecting the exact nature of the release curve of PMMA is negligble, as the strain involved is small. Further, as there is no analytical description of the release behaviour of

PMMA, without detailed experimental determination of the release path for each experiment, it is not clear how this effect could be applied to the present analysis.

The uncertainty introduced by not including the exact release behaviour of PMMA in the data analysis is, as has been noted, considered to be negligible. Further evidence for this is provided by Figure 5.25, which shows the Hugoniot states determined by methods 1 and 3 in stress–particle velocity space. The close agreement demonstrated by the two methods is considered evidence that the uncertainties in the release behaviour of the gauges and of PMMA are small. It is concluded that the uncertainity in the gauge behaviour in states of partial release is, however, significantly larger than the uncertainity introduced by neglecting the true release behaviour of PMMA. For these reasons, it is concluded that method 3 gives the most accurate determination of the Hugoniot states of the water in the shock velocity–particle velocity plane, and these data will be used to construct a relationship for the Hugoniot. Measurements of the shock response of low-density granular systems by Chapman [2009a] yielded similar conclusions.

The resultant Hugoniot for water at $66 \pm 2\,^{\circ}\mathrm{C}$ is shown in Figure 5.26. The fit, which is weighted by the errors on the data, has a coefficient of determination of 0.98, and is given by $U_S = 1.44 \pm 0.05 + 1.53 \pm 0.09 u_p$. The dashed lines represent confidence bounds at $95\,\%$. That the data are well-fitted by a single linear relationship is taken as evidence that no phase changes occur. The quality of fit also suggests that a linear relationship is the appropriate description of the present data.

Reload experiments

In addition to measuring the principal Hugoniot, the reported experiments measured the reload stress in water at $66 \pm 2\,^{\circ}\mathrm{C}$. These stress measurements allow for the determination of the volume of the reload state in the way described in the preceeding chapter, and are presented as the open symbols in Figure 5.27 together with the Hugoniot states (blue symbols) and fitted Hugoniot (blue curve). By using the Mie-Grüneisen equation of state to describe these reload states, we will be able to calculate temperature rises along the Hugoniot. The fitted Hugoniot, and its uncertainties (dashed curves) were calculated from the U_S–u_p relationship using the equation

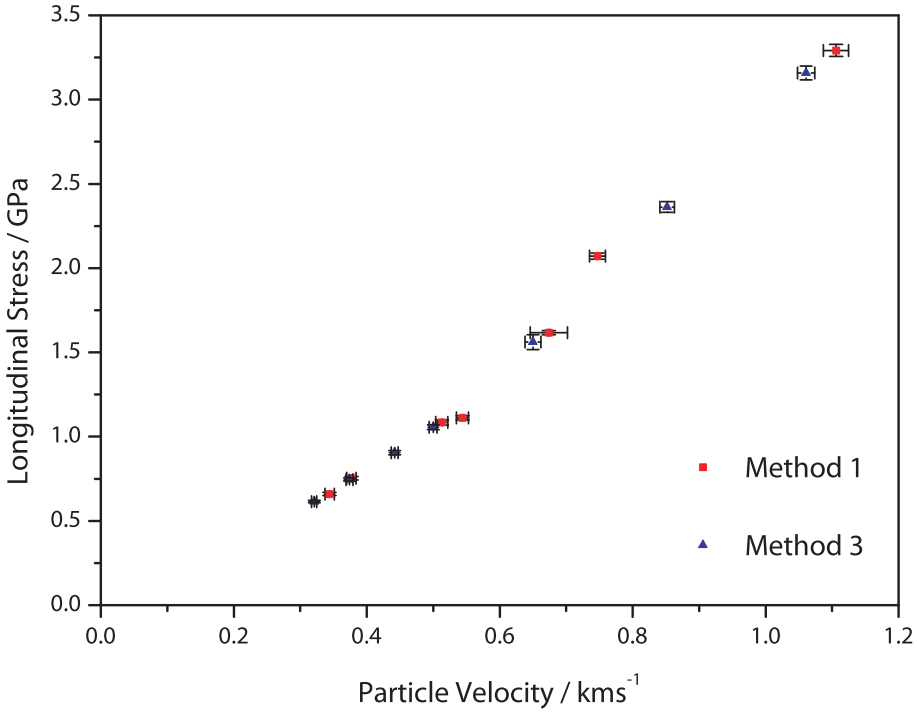

Figure 5.25: Measured Hugoniot states for water at $66 \pm 2\,^{\circ}\mathrm{C}$. In P–u_p, the three analysis methods yield similar Hugoniots, indicating that the approximations made yield only small uncertainties. Method 2, which neglects the measured transit time of the shock wave, in which there is greatest confidence, is considered unreliable. Methods 1 and 3 are in close agreement, indicating that neglecting the exact release behaviour of PMMA introduces only a small uncertainty in the calculations.

$$P = \frac{\rho_0 c_0^2 \Delta}{(1 - S\Delta)^2}, \tag{5.4}$$

where Δ is the Lagrangian compression, $\rho_0(v_0 - v_1)$ and c_0 and S are, respectively, the intercept and slope of the U_S–u_p Hugoniot.

The arrows in Figure 5.27, linking the Hugoniot and reload stress for the experiments with reload stresses above $3.5\,\mathrm{GPa}$, correspond in each case to the Rayleigh line describing the loading path taken in these experiments. These states lie below the Hugoniot on isochors through their respective reload volumes. The lower stress experiments do not differ markedly from the Hugoniot, with two experiments found to be exactly on the Hugoniot. It is not clear why the remaining two reload states lie above the Hugoniot. It is unlikely that

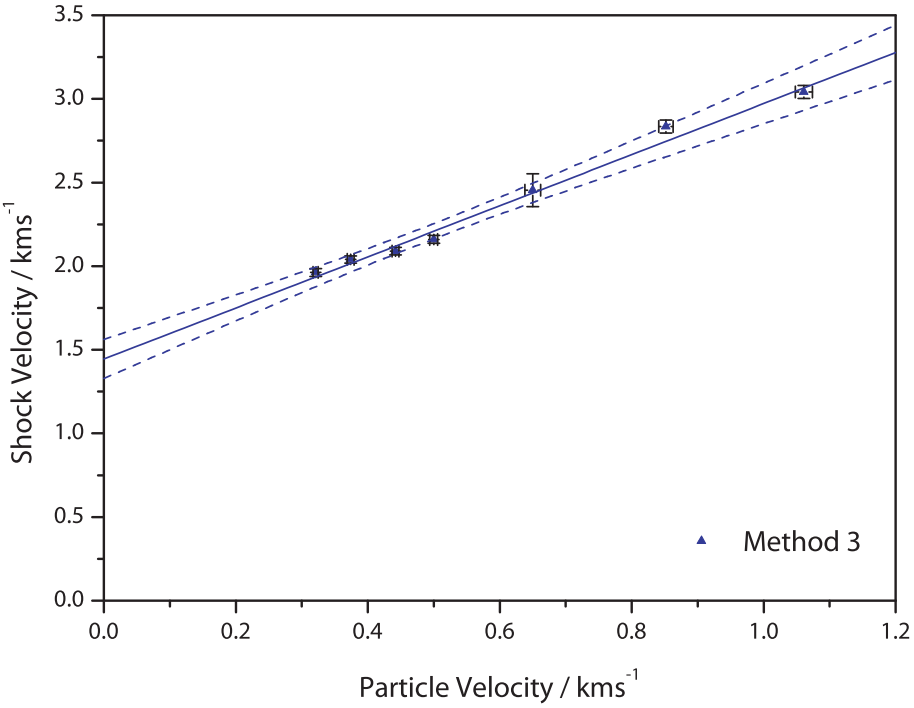

Figure 5.26: Hugoniot of water at $66 \pm 2\,^{\circ}\mathrm{C}$. The data points are determined from the experimental values using the third analysis method described in §4.2. The solid line is the weighted best fit to the data and is given by $U_S = 1.44 \pm 0.05 + 1.53 \pm 0.09 u_p$; the dashed lines are confidence bounds at $95\,\%$.

this is due to a phase change, as this would require the states to be at a lower temperature than the isentrope centered on ambient conditions shown in Figure 5.21, which is clearly unphysical. It is likely that the deviation in these states is an artefact of the particular experiments involved, as at low stresses, a small offset in the measured reload stress would manifest as proportionately larger offset in the calculated volume.

For those states which lie below the Hugoniot, it is possible to determine a value of the Grüneissen parameter, Γ,

$$\Gamma \approx v_R \frac{p_H - p_R}{e_H - e_R}, \tag{5.5}$$

where the subscripts R and H refer to the reload state and the Hugoniot state on an isochor through the reload volume. The energies are calculated

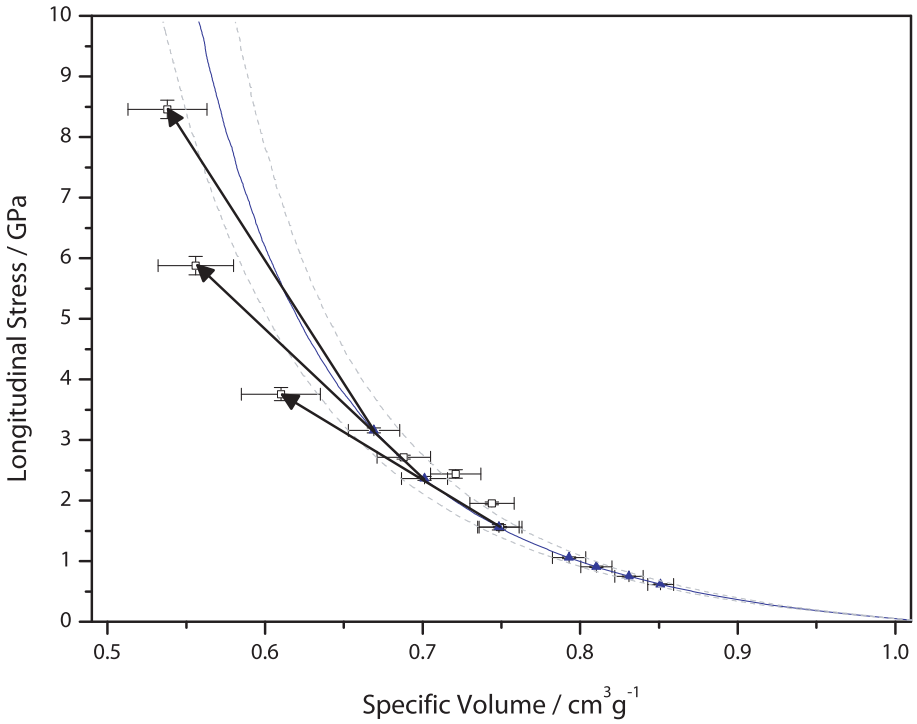

Figure 5.27: Reload states in water at $66 \pm 2\,^{\circ}\mathrm{C}$. The solid points are the previously determined Hugoniot states, and the blue curve is given by the Hugoniot $U_S = 1.44 \pm 0.05 + 1.53 \pm 0.09 u_p$, where the dashed lines represent the uncertainities in this relationship. The open symbols are the measured reload states. Arrows indicating the Rayleigh line between the Hugoniot and reload state have been added for three of the experiments.

using the generalised jump condition for energy between the states (V, P) and (V_1, P_1)

$$E - E_1 = \frac{1}{2}(P + P_1)(V_1 - V). \tag{5.6}$$

These values for Γ are shown in Figure 5.28, where the uncertainties in Γ have been determined in quadrature. The calculation of Γ relies on the measured U_S–u_p Hugoniot and the measured stress and volume in the Hugoniot state. However, the U_S–u_p Hugoniot is determined from the stress measurement, and the volume is, in turn, determined from the stress measurement and the U_S–u_p Hugoniot. The errors in these quantities are, therefore, to an extent, covariant and the determination of errors in quadrature will lead to an

over-estimate of the error.

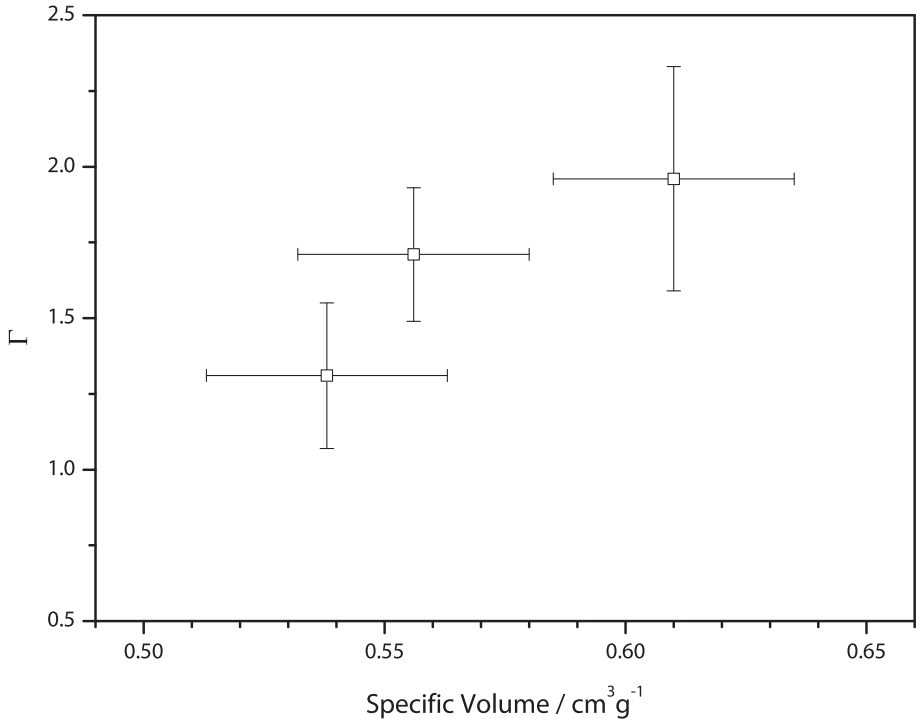

Figure 5.28: Experimentally determined values of the Grüneissen parameter, Γ, in water at $66 \pm 2\,^{\circ}\mathrm{C}$. The uncertainties in Γ have been determined in quadrature from Equation 5.5 and are believed to be an over-estimate, as the quadrature analysis neglects covariance of the errors in the measured Hugoniot stresses and the fitted U_S–u_p Hugoniot.

The data presented in Figure 5.28 suggest that Γ decreases with increasing density in the range investigated. Dolan [2003] suggests that, in water compressed from ambient conditions, a maximum is observed in Γ at a specfic volume of around $0.675\,\mathrm{cm^3\,g^{-1}}$, likely due to the collapse of the hydrogen bonding which would allow for greater compaction.

In order to calculate temperatures along the Hugoniot, a form of $\Gamma(v)$ is required that is defined for all v; following the methodology given by Gurtman et al. [1971], a polynomial fit to Γ is found. In order to ensure correct behaviour at low compressions, the $60\,^{\circ}\mathrm{C}$ and $70\,^{\circ}\mathrm{C}$ isotherms of water given by Grindley and Lind [1971] are used in the equation

$$\frac{C_v\Gamma(V)}{V} = \frac{P_i(V) - P_j(V)}{T_i - T_j}. \tag{5.7}$$

Gurtman et al. [1971] suggest that the heat capacity, C_v, of water shock compressed from an initial temperature of $20\,^{\circ}\mathrm{C}$ is within $10\,\%$ of $3.2\,\mathrm{J\,g^{-1}\,K^{-1}}$. This is in agreement with the value of $3\,\mathrm{J\,g^{-1}\,K^{-1}}$ used by Dolan [2003], and is lower than the heat capacity at ambient pressure ($4\,\mathrm{J\,g^{-1}\,K^{-1}}$). The following analysis assumes that the value given by Gurtman et al. [1971] is approximately correct for water at an initial temperature of $66 \pm 2\,^{\circ}\mathrm{C}$. The isotherms are described by a Murnaghan equation

$$P(v) = \frac{K}{g}\left[\left(\frac{v_0}{v}\right)^g - 1\right], \tag{5.8}$$

where K was chosen to match the bulk isothermal modulus at ambient pressure [Kell, 1975] and the temperature of the isotherm, leaving g, which is the rate that the isothermal modulus varies with pressure, as the only adjustable parameter. The resultant values for Γ are plotted in Figure 5.29 together with a fifth-order polynomial fit to the data

$$\begin{aligned}\Gamma(v\,\mathrm{cm^3\,g^{-1}}) = \quad & - \quad 253 \\ & + \quad (1510\,\mathrm{g\,cm^{-3}})v \\ & - \quad (3521\,\mathrm{g^2\,cm^{-9}})v^2 \\ & + \quad (4057\,\mathrm{g^3\,cm^{-27}})v^3 \\ & - \quad (2324\,\mathrm{g^4\,cm^{-81}})v^4 \\ & + \quad (531\,\mathrm{g^5\,cm^{-243}})v^5,\end{aligned} \tag{5.9}$$

which is the lowest-order polynomial that can describe the behaviour of Γ at high and low specific volumes.

It is not possible, generally, to integrate the the equation for Hugoniot temperatures, Equation 4.4, in closed form. McQueen [1989] gives a centered difference equation that enables the temperature at some point on the Hugoniot, (P_i, V_i, T_i), to be calculated from some other point $(P_{i-1}, V_{i-1}, T_{i-1})$:

$$T_i = \frac{T_{i-1}[1 + \overline{\rho}\overline{\Gamma}\Delta V/2] + [(V_0 - \overline{V})\Delta P + (\overline{P} - P_0)\Delta V]/2\overline{C_v}}{1 + \overline{\rho}\overline{\Gamma}\Delta V/2}, \tag{5.10}$$

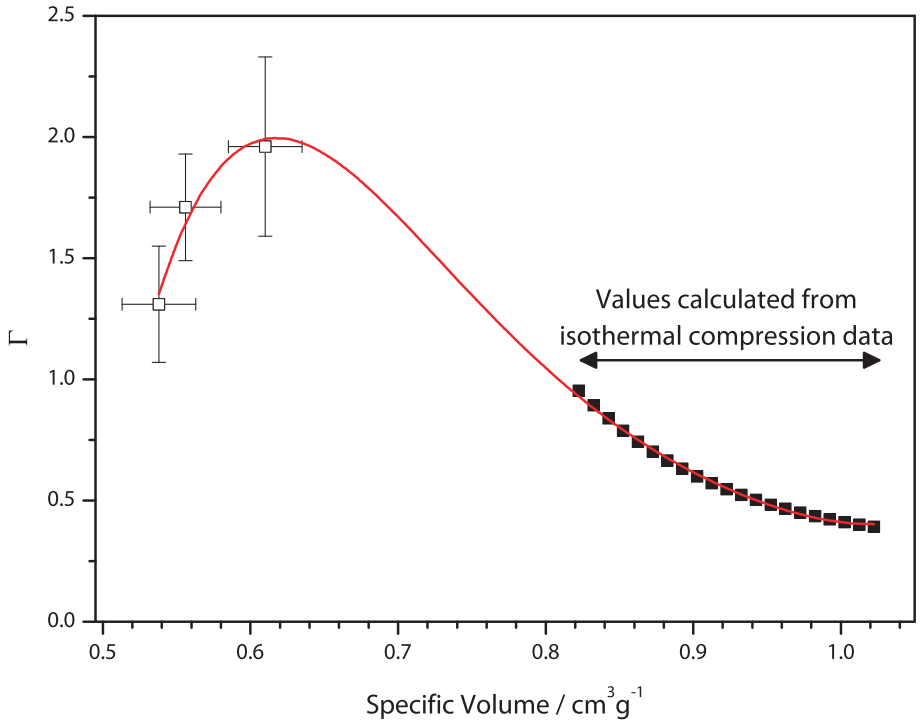

Figure 5.29: Volume-dependent Grüneissen parameter, Γ, in water at $66 \pm 2\,^{\circ}\mathrm{C}$ from shock/reload experiments (open squares) and isotherms (closed squares, Equation 5.7). The fit is a fifth-order polynomial described by Equation 5.9 and is the lowest-order polynomial that can describe the behaviour of Γ at high and low specific volumes.

where the quantities $\overline{\rho}$, $\overline{\Gamma}$, $\overline{C_v}$, $\overline{V}$, and $\overline{P}$ refer to the density, Grüneissen parameter, heat capacity, volume, and pressure averaged between the two states and ΔV, ΔP the differences in volume and pressure between the two states. By specifying the temperature T_0 at the initial volume V_0 and pressure $P = P_0 = 0$, it is possible construct a full temperature Hugoniot by iterative application of Equation 5.10 using the polynomial form for Γ. The calculated shock temperatures, as a function of pressure, are shown in Figure 5.30. The present analysis has been conducted for three values of the specific heat - the expected value of $C_v = 3.2\,\mathrm{J\,g^{-1}\,K^{-1}}$, and the upper and lower bounds that are within $10\,\%$ of this value, as suggested by Gurtman et al. [1971]. This variation in C_v yields uncertainties in the shock temperature of around $7\,\%$, and represents the dominant contribution the uncertainty in the temperature cal-

culation. As is standard in the literature, the heat capacity has been assumed to be constant; as is discussed in Chapter 7 this approximation may not be valid, and C_v is likely to increase slightly over the stress range considered. The magnitude of the variation is uncertain, and it is believed the present $10\,\%$ variation is an appropriate description; a $50\,\%$ variation in the heat capacity would increase the uncertainty in the calculated temperature rise to approximately $25\,\%$. Combining the $10\,\%$ variation in C_V with the uncertainties in the experimentally determined Hugoniot and the polynomial fit for Γ, it is felt that the present results enable calculation of the shock temperature in water, at an initial temperature of $66\,^{\circ}\mathrm{C}$, to within $\pm 10\,\%$ for stresses to $8\,\mathrm{GPa}$. The assumptions underpinning these calculations of temperature are discussed in detail in Chapter 7.

5.4 Summary

- A cell has been developed which allows for well-defined shocks to be generated in liquids, and the ability to pre-heat the liquid has been demonstrated.

- Manganin gauges at the front and rear of the liquid show sharp rises, at the arrival of the shock, and steady plateaus in the Hugoniot and reload states.

- Comparison with literature values for the Hugoniot and Grüneisen parameter, Γ, for water compressed from room temperature, demonstrate the cell and analysis techniques produce consistent and reliable data.

- The Hugoniot of water for water compressed from $66 \pm 2\,^{\circ}\mathrm{C}$ has been determined experimentally.

- The Grüneisen parameter has been determined from shock/reload experiments, and combined with appropriate isothermal compression data to produce a polynomial fit describing the volume-dependence of Γ.

- Shock temperatures have been calculated along the principal Hugoniot of water compressed from $66 \pm 2\,^{\circ}\mathrm{C}$ to $8\,\mathrm{GPa}$ with uncertainties of $10\,\%$.

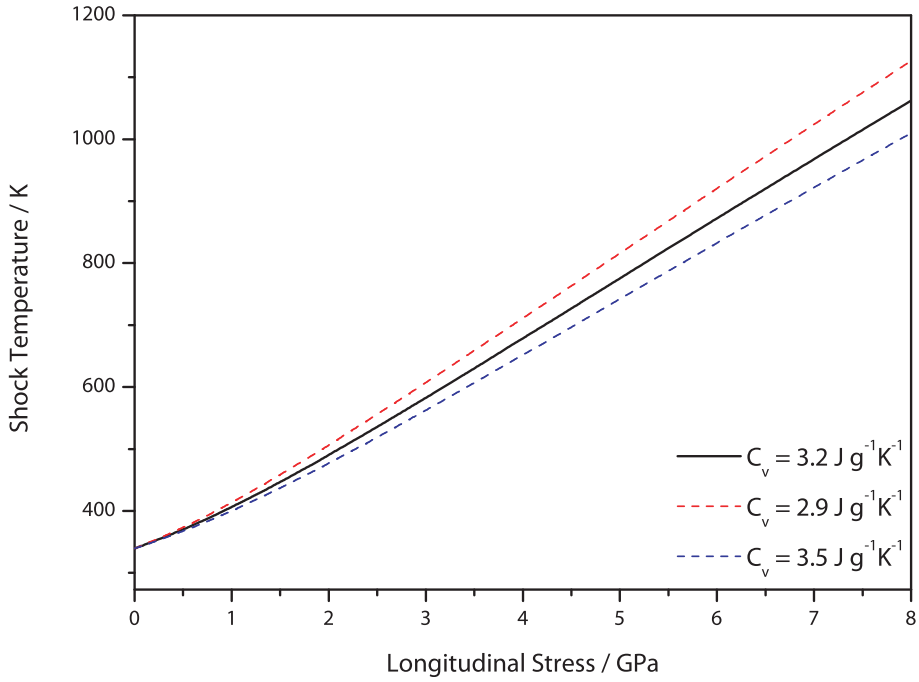

Figure 5.30: Calculated shock temperatures in water at $66 \pm 2\,^{\circ}\mathrm{C}$, using the measured Hugoniot $U_S = 1.44 + 1.53u_p$ and polynomial expression for Γ (Equation 5.9), assuming a constant heat capacity $C_v = 3.2\,\mathrm{J\,g^{-1}\,K^{-1}}$. The dashed lines are calculated for heat capacities $10\,\%$ above and below $C_v = 3.2\,\mathrm{J\,g^{-1}\,K^{-1}}$. The variation in heat capacities uncertainties in calculated temperature of approximately $7\,\%$. To account for uncertainties in the experimentally determined Hugoniot and the polynomial fit for Γ, it is concluded that the present results give the shock temperature in water at $66 \pm 2\,^{\circ}\mathrm{C}$ for pressures to $8\,\mathrm{GPa}$ to within $\pm 10\,\%$.

5.5 Bibliography

J. R. Asay and M. Shahinpoor, editors. *High-pressure shock compression of solids*. Springer, 1993.

L. M. Barker and R. E. Hollenbach. Shock-wave studies of pmma, fused silica, and sapphire. *Journal of Applied Physics*, 41(10):4208–4226, 1970.

D. Benson. Computational methods in Lagrangian and Eulerian hydrocodes. *Computer Methods in Applied Mechanics and Engineering*, 99:235–394, 1992.

D. J. Chapman. *Shock-compression of porous materials and diagnostic development*. PhD thesis, University of Cambridge, 2009a.

D. J. Chapman. Personal communication, 2009b. Fracture and Shock Physics, Cavendish Laboratory.

D. J. Chapman. Standard materials for use with the Cavendish plate-impact facility. Technical report, University of Cambridge, 2009c.

C. Dai, H. Tan, J. Hu, Y. Yu, and J. Zheng. Hugoniot evaluation of the pre-heated metal from its principal hugoniot. *Journal of Applied Physics*, 99(5): 056102, 2006.

L. Davison. Attenuation of longitudinal elastoplastic pulses. In L. Davison and M. Shahinpoor, editors, *High-pressure shock compression of solids III*, pages 277–327. Springer, 1998.

L. Davison and R. A. Graham. Shock compression of solids. *Physics Reports*, 55:255–379, 1979.

D. H. Dolan. *Time dependent freezing of water under multiple shock wave compression*. PhD thesis, Washington State University, 2003.

D. H. Dolan and Y. M. Gupta. Time-dependent freezing of water under dynamic compression. *Chemical Physics Letters*, 374(5-6):608 – 612, 2003.

G. E. Duvall and R. A. Graham. Phase transitions under shock-wave loading. *Reviews of Modern Physics*, 49(3):523–579, 1977.

T. Grindley and J. E. Lind. PVT properties of water and mercury. *The Journal of Chemical Physics*, 54(9):3983–3989, 1971.

G. A. Gurtman, J. W. Kirsch, and C. R. Hastings. Analytical equation of state for water compressed to 300 kbar. *Journal of Applied Physics*, 42(2):851–857, 1971.

J. N. Johnson, R. S. Hixson, G. T. Gray, III, and C. E. Morris. Quasielastic release in shock-compressed solids. *Journal of Applied Physics*, 7(2):429–441, 1992.

G. S. Kell. Density, thermal expansivity, and compressibility of liquid water from $0\,^{\circ}\mathrm{C}$ to $150\,^{\circ}\mathrm{C}$ correlations and tables for atmospheric pressure and

saturation reviewed and expressed on 1968 temperature scale. *Journal of Chemical and Engineering Data*, 20(1):97–105, 1975.

K. B. Kormer, S. B. Yushko and G. V. Krishkevich. Phase transformation of water into ice VII by shock compression. *Soviet Physics JETP*, 27:879–881, 1968.

S. P. Marsh, editor. *LASL Shock Hugoniot Data*. University of California Press, 1980.

R. G. McQueen. Shock-waves in condensed media: Their properties and the equation of state of materials derived from them. In *Enrico Fermi summer course CX11: nuclear collisions from the mean field into the fragmentation regime*, 1989.

A. C. Mitchell and W. J. Nellis. Equation of state and electrical conductivity of water and ammonia shocked to the 100 GPa (1 Mbar) pressure range. *Journal of Chemical Physics*, 76:6273–6281, 1982.

K. Nagayama, Y. Mori, K. Shimada, and M. Nakahara. Shock hugoniot compression curve for water up to 1 GPa by using a compressed gas gun. *Journal of Applied Physics*, 91(1):476–482, 2002.

J. W. Nunziato and E. K. Walsh. Propagation of steady shock waves in nonlinear thermoviscoelastic solids. *Journal of the Mechanics and Physics of Solids*, 21:317–335, 1973.

A. Rybakov. Phase transformation of water under shock compression. *Journal of Applied Mechanics and Technical Physics*, 37:629–633, 1996.

S. Schoch. Personal communication, 2011. Laboratory for Scientific Computing, University of Cambridge.

E. Washburn, editor. *International Critical Tables of Numerical Data, Physics, Chemistry and Technology*. Knovel, 1st electronic edition, 2003.

D. Yaziv, Z. Rosenberg, and Y. Partom. Release wave calibration of manganin gauges. *Journal of Applied Physics*, 51(12):6055–6057, 1980.

CHAPTER 6

SHOCK COMPRESSION OF AMMONIUM NITRATE SOLUTIONS

The liquid impact cell developed in previous chapters was applied to the study of aqueous solutions of ammonium nitrate. Specifically, measurements were made of the principal Hugoniot and shock/reload response of a series of ammonium nitrate solutions. From these measurements, an empirical fit describing the volume-dependence of the Grüneisen parameter, Γ in each solution is determined. Shock temperatures can then be calculated along the Hugoniot, as has been discussed in the preceeding chapters.

The 'solubility limit' of a solution is defined as the temperature below which, for a given concentration (*i.e.*, weight-percentage) of the solute, crystalisation would begin to occur. The solubility limit for the ammonium nitrate–water system, as a function of the weight-percentage of ammonium nitrate, is shown in Figure 6.1.

The emulsion explosives used in the mining industry were discussed in Chapter 1. The 'water' phase of these emulsions is an aqueous solution of ammonium nitrate, typically containing $70\,\%$ or more ammonium nitrate by weight [Sudweeks, 1985]. From Figure 6.1, it is clear that such solutions have solubility limits above room temperature. Indeed, the manufacture of emulsion explosives occurs at elevated temperatures, and it is only after the emulsion matrix has been formed that the resultant explosive may be cooled to room temperature [Hustrulid, 1999].

Thus, it is clear that the ammonium nitrate solutions of interest are saturated at room temperature and experiments on them must be conducted at an elevated initial temperature. It is not immediately obvious what effect raising the initial temperature will have on the behaviour of the solution. A second solution, which has a solubility limit below room temperature, can be used to investigate any effects by conducting experiments on it at room temperature and at the temperature of the more concentrated solution.

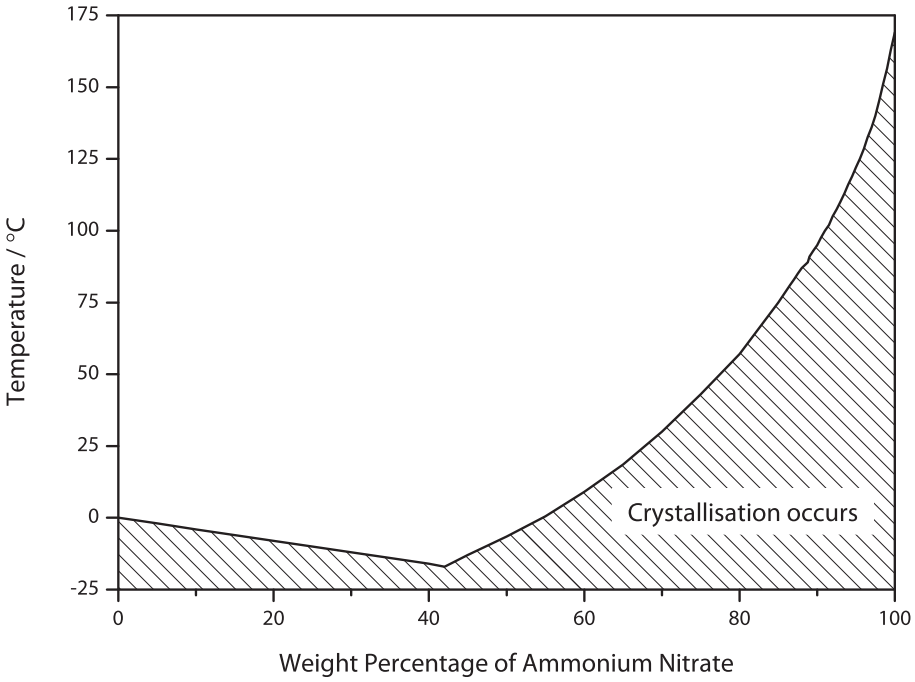

Figure 6.1: Phase diagram for the ammonium nitrate/water system as a function of weight-percentage of ammonium nitrate and temperature [data supplied by Chan, 2011]. Stable solutions exist for temperatures above the 'solubility limit', shown by the solid curve. For a given concentration, crystallisation will occur at temperatures below this line.

6.1 Ammonium nitrate solutions

The 'o'-ring used in the liquid cell ceases to provide an effective seal for temperatures above $70\,^{\circ}\mathrm{C}$, thus limiting the maximum concentration which may be experimented upon. From Figure 6.1, it can be seen that this limiting concentration is approximately $82\,\%$. To provide some margin of error, both in terms of the efficacy of the 'o'-ring seal and the solubility limit data, the maximum concentration was set at $80\,\%$ ammonium nitrate by weight. The solubility limit for this solution is $57\,^{\circ}\mathrm{C}$. A solution of $50\,\%$ ammonium nitrate by weight, which has a solubility limit below room temperature, was used to investigate what effect changing the initial solution temperature has on the calculated shock temperatures.

Solutions were prepared using vacuum-de-gassed and de-ionised water, and reagant grade ammonium nitrate. The ammonium nitrate was $> 98\,\%$

purity, and purchased in granular form from Sigma Aldrich. Appropriate quantities of water and ammonium nitrate were weighed using a balance accurate to $\pm 0.005\,\mathrm{g}$ and mixed in a sealed container at $70\,^{\circ}\mathrm{C}$ in an oil bath for several hours until the ammonium nitrate had fully dissolved. As the analysis of shock wave data require knowledge of the initial density of the material being shocked, it was necessary to determine the density of the solution. At ambient temperature, this can be accomplished by using a density bottle. A density bottle is a glass vessel whose volume is accurately known. Measuring the mass of fluid the bottle contains allows for the density of the fluid to be determined. At elevated temperatures, the volume of the density bottle is no longer precisely known, and attempting to compensate for this would introduce unnecessarily large uncertainties into subsequent calculations. Densities of the solutions at elevated temperature were determined from the literature [Washburn, 2003]; it is not clear what method was used to measure these densities. The physical properties of the solutions discussed in this chapter are summarised in Table 6.1.

6.2 Principal Hugoniots

Hugoniots were determined for the three solutions described above using the methods already presented. As with the pure water experiments described in Chapter 5, different methods of analysing the data yield subtly different results. These differences are attributed to the systematic uncertainties associated with the assumptions used by each method. As in the previous chapter, it is felt that the measured Hugoniot stresses are less reliable, as they lie in states of partial release of the gauge. Method 1 combines the measured stress with the shock velocity deduced from the transit time to calculate the Hugoniot particle velocity in the solution. It is therefore considered unreliable, whereas method 3, which constrains the Rayleigh line defined by the measured shock velocity to lie on the release curve of PMMA, is believed to provide a more accurate determination of the Hugoniot state. That both these uncertainties are small is evidenced by the generally close agreement between both methods. As before, however, method 3 is considered the more reliable method, and has hence been used to fit the shock velocity–particle velocity Hugoniots.

The Hugoniot of the $50\,\%$ ammonium nitrate solution at a temperature of $14 \pm 1\,^{\circ}\mathrm{C}$ is presented in shock velocity–particle velocity space in Figure 6.2, and in stress–particle velocity space in Figure 6.3, and the Hugoniot is given

Concentration / Weight % ammonium nitrate	Initial temperature / K	Density / $\mathrm{g\,cm^{-3}}$	c_v/ $\mathrm{J\,g^{-1}\,K^{-1}}$	Γ_0
50	14 ± 1	1.220 ± 0.005	2.572	1.13 ± 0.05
50	65 ± 2	1.190 ± 0.005	2.590	0.57 ± 0.05
80	64 ± 2	1.370 ± 0.005	1.706	0.68 ± 0.05

Table 6.1: Properties of the ammonium nitrate solutions used in the present work. Densities at elevated temperatures are from Washburn [2003], the other data were provided by Chan [2011]. c_v is the isochoric heat capacity at zero pressure. Γ_0 is the Grüneisen parameter, also at zero pressure.

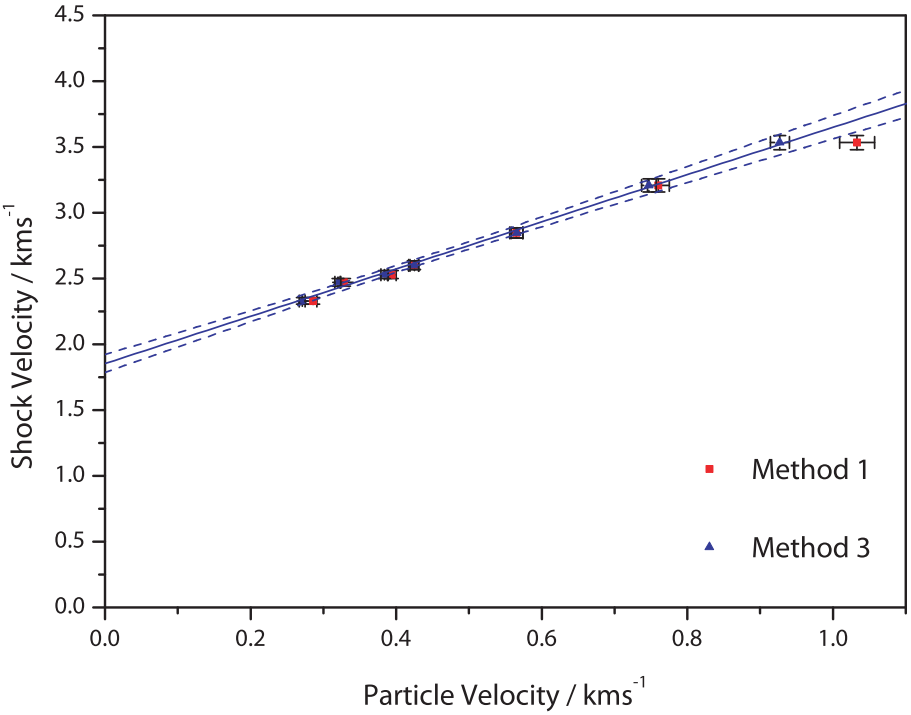

Figure 6.2: Measured Hugoniot states for a solution of $50\,\%$ ammonium nitrate by weight at $14\pm1\,^{\circ}\mathrm{C}$. The methods described in §4.2 yield somewhat different results for the Hugoniot state for each experiment. The blue line is the fit through the states determined by method 3, which is considered to provide the most accurate determination of the Hugoniot states, and is given by the equation $U_S = 1.86 \pm 0.03 + 1.80 \pm 0.06 u_p$. The dashed lines are the $95\,\%$ confidence bounds of the fits, and suggest that data is well represented by a linear relationship. The large discrepancy between the two methods for the highest particle velocity datum are likely due to mismeasurement of the stress, potentially due to a fault in the construction of the gauge package. There is no evidence from the data for a phase change over the range of particle velocities investigated.

by the linear relationship $U_S = 1.86\pm0.03+1.80\pm0.06u_p$. It is not clear why the two methods give markedly different results for the highest particle velocity experiment. Such a discrepancy could be due to the stress being recorded incorrectly in this particular experiment, possibly due to a fault, such as a gas bubble in the glue layer, introduced when the cell was constructed.

The Hugoniot of the $50\,\%$ ammonium nitrate solution at a temperature of $65 \pm 2\,^{\circ}\mathrm{C}$ is presented in shock velocity–particle velocity space in Figure 6.4,

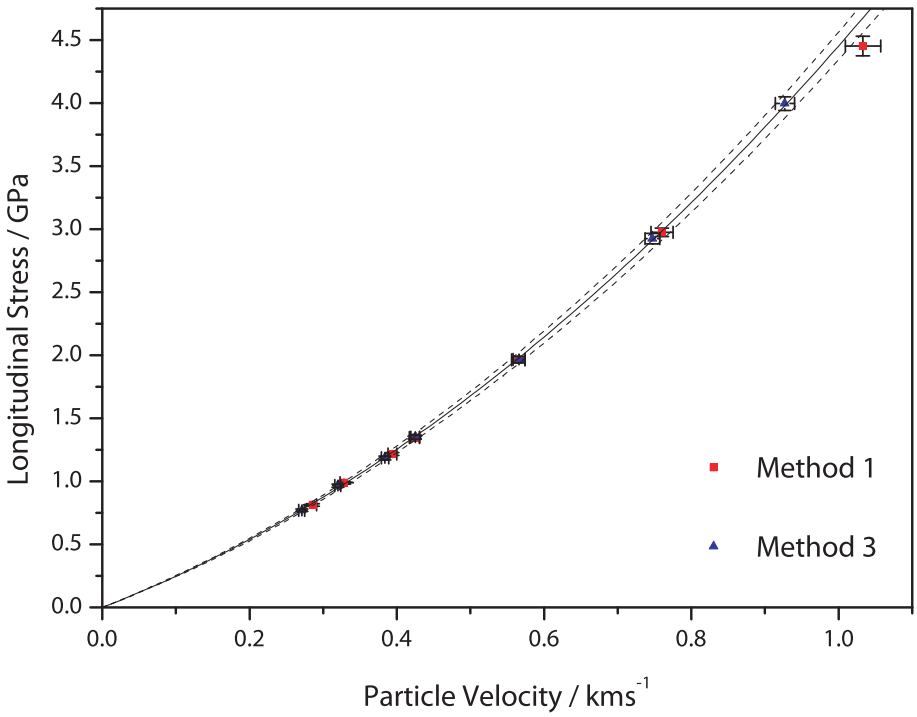

Figure 6.3: Stress–particle velocity Hugoniot for a solution of $50\,\%$ ammonium nitrate by weight at $14 \pm 1\,^{\circ}\mathrm{C}$, determined by two analysis methods, and presented with the Hugoniot given by $U_S = 1.86 \pm 0.03 + 1.80 \pm 0.06 u_p$. That the highest datum analysed by method 1 is not well-described by the fit is considered further evidence that the Hugoniot stress in the liquid was mismeasured in this experiment.

and in stress–particle velocity space in Figure 6.5. The fitted Hugoniot is given by the equation $U_S = 1.73 \pm 0.05 + 1.49 \pm 0.10 u_p$, and therefore lies below the ambient temperature Hugoniot in both spaces. Chapman [2009] reported the Hugoniots for samples of silica powder at various initial densities; the lower initial density samples were found to lie below those of higher initial densities. Similar results can be seen in the Hugoniot data given by Marsh [1980] for a number of different materials. The present results act to confirm the conclusion that lower density forms of a given material in general will have lower Hugoniots. From a phenomenological view point, the elevated temperature solution can be considered to be a less dense modification of the ambient temperature solution, and therefore has a lower shock impedance. By definition of the impedance, it must, therefore, have a lower Hugoniot, as

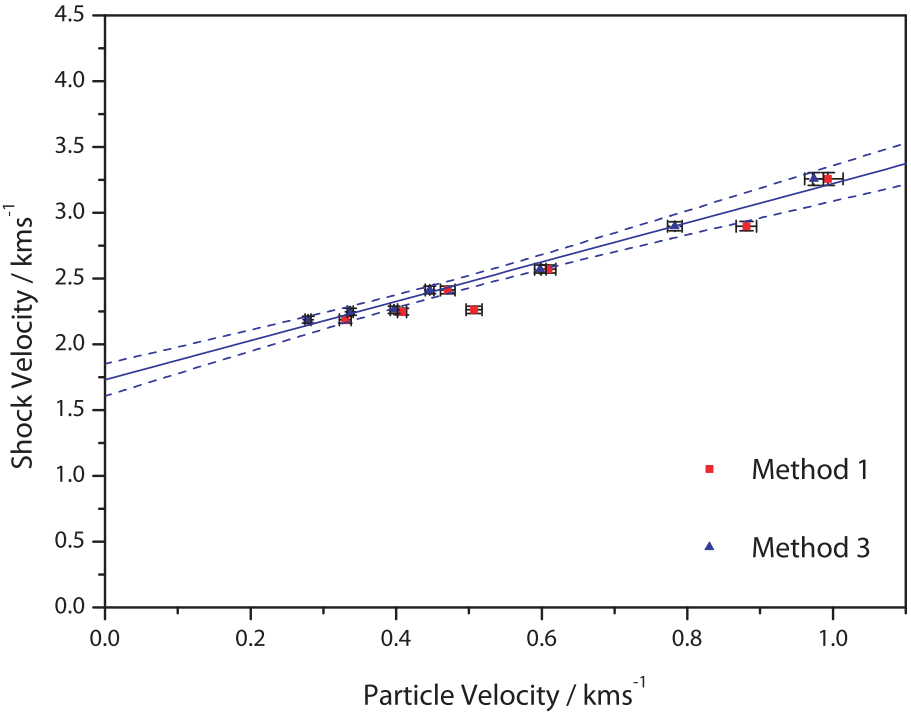

Figure 6.4: Measured Hugoniot states for a solution of $50\,\%$ ammonium nitrate by weight at $65 \pm 2\,^{\circ}\mathrm{C}$. The methods described in §4.2 yield somewhat different results for the Hugoniot state for each experiment. The blue line is the fit through the states determined by method 3, which is considered to provide the most accurate determination of the Hugoniot states, and is given by the equation $U_S = 1.73 \pm 0.05 + 1.49 \pm 0.10 u_p$. The dashed lines are the $95\,\%$ confidence bounds of the fits, and suggest that data is well represented by a linear relationship. As with the ambient temperature experiments, there is no evidence of any phase changes occurring over the range of particle velocities investigated.

the sound speed is unlikely to increase with decreasing density.

The Hugoniot of the $80\,\%$ ammonium nitrate solution at a temperature of $64 \pm 2\,^{\circ}\mathrm{C}$ is presented in shock velocity–particle velocity space in Figure 6.6, and in stress–particle velocity space in Figure 6.7. The Hugoniot is given by the equation $U_S = 1.83 \pm 0.04 + 1.73 \pm 0.09 u_p$. There is no evidence in any of the presented Hugoniots to suggest that any phase changes occur in the solutions over the stress/particle velocity ranges investigated, nor is there any suggestion from the data of non-linearity of the shock velocity–particle velocity Hugoniot.

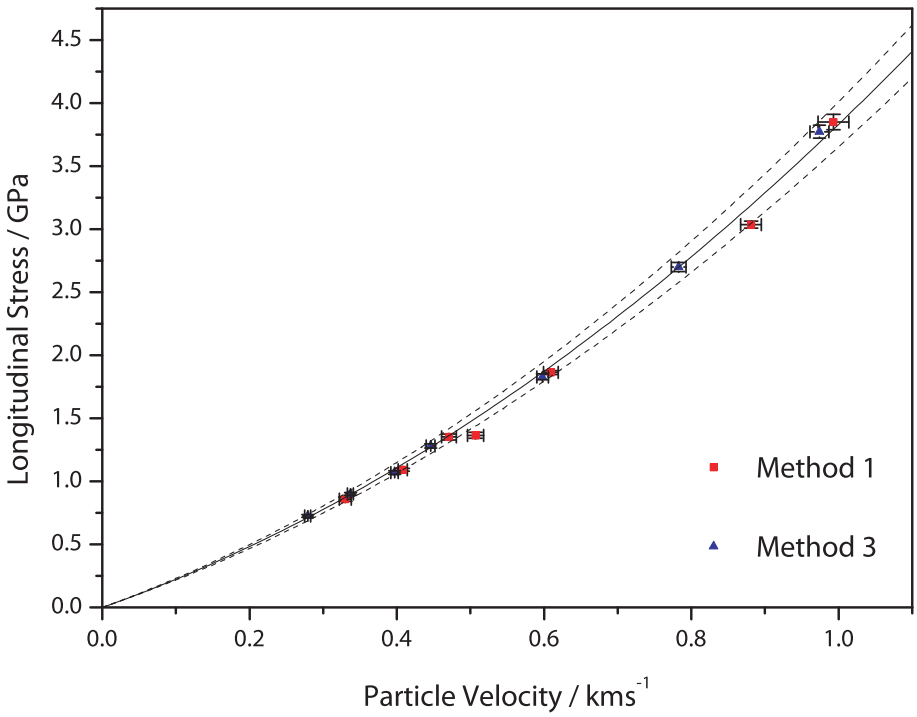

Figure 6.5: Stress–particle velocity Hugoniot for a solution of $50\,\%$ ammonium nitrate by weight at $65 \pm 2\,^{\circ}\mathrm{C}$, determined by two analysis methods, and presented with the Hugoniot given by $U_S = 1.73 \pm 0.05 + 1.49 \pm 0.10 u_p$. The stress–particle velocity data determined by both methods are well-described by the present fit.

The Hugoniots of the three solutions, in stress–particle velocity space, are presented in Figure 6.8 together with their associated uncertainties. These Hugoniots have been extrapolated to particle velocities approximately twice the maximum particle velocity in the experiments ($\approx 1\,\mathrm{km\,s^{-1}}$). As has already been discussed, the elevated temperature Hugoniot of the $50\,\%$ ammonium nitrate solution lies below the ambient temperature Hugoniot due to the decreased density. The $80\,\%$ ammonium nitrate solution Hugoniot lies above the two $50\,\%$ ammonium nitrate solution Hugoniots, principally due to its increased density.

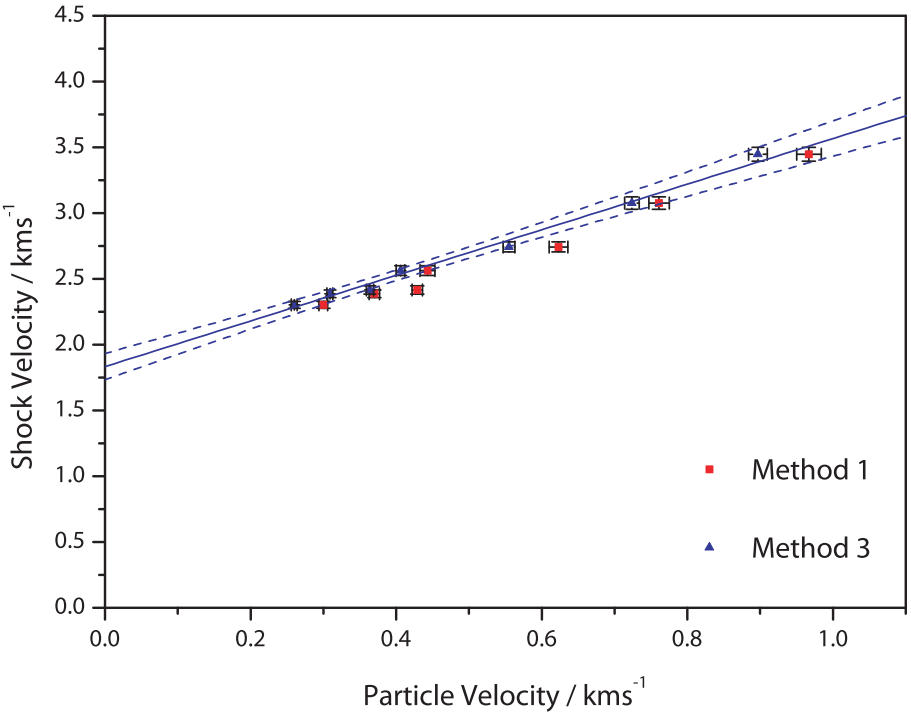

Figure 6.6: Measured Hugoniot states for a solution of $80\,\%$ ammonium nitrate by weight at $64 \pm 2\,^{\circ}\mathrm{C}$. The three described in §4.2 yield somewhat different results for the Hugoniot state for each experiment. The blue line is the fit through the states determined by method 3, which is considered to provide the most accurate determination of the Hugoniot states, and is given by the equation $U_S = 1.83 \pm 0.04 + 1.73 \pm 0.09 u_p$. The dashed lines are the $95\,\%$ confidence bounds of the fits, and suggest that data is well represented by a linear relationship. As with the $50\,\%$ ammonium nitrate solutions, there is no evidence that any phase changes have taken place.

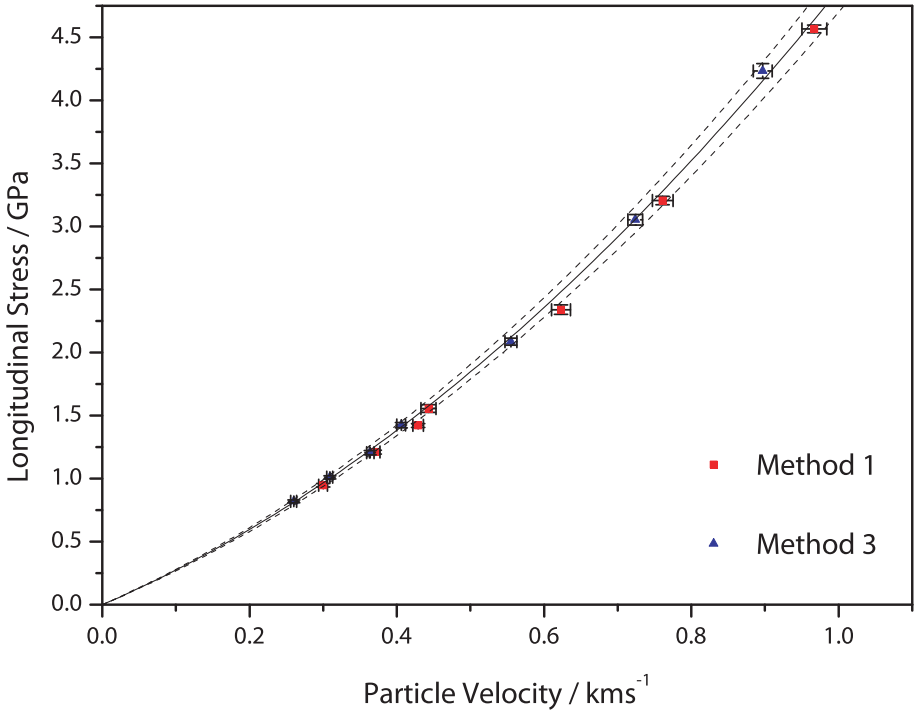

Figure 6.7: Stress–particle velocity Hugoniot for a solution of $80\,\%$ ammonium nitrate by weight at $64 \pm 2\,^{\circ}\mathrm{C}$, determined by two analysis methods, and presented with the Hugoniot given by $U_S = 1.83 \pm 0.04 + 1.73 \pm 0.09 u_p$. As with the $50\,\%$ ammonium nitrate solutions, the data reduced by both methods are well-described by the fitted linear Hugoniot.

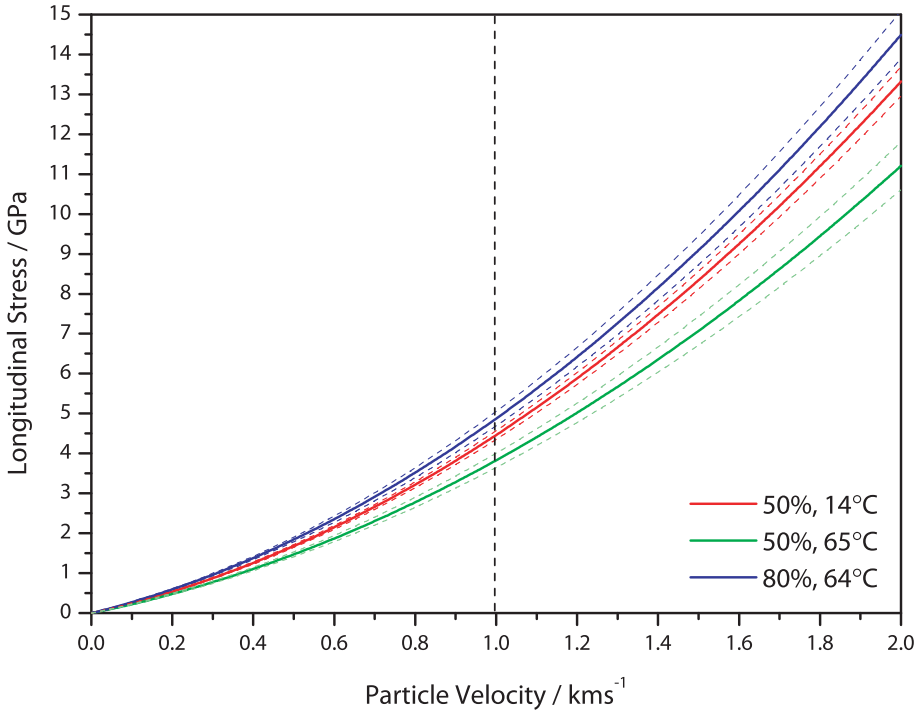

Figure 6.8: Stress–particle velocity Hugoniots for the ammonium nitrate solutions; the solid curves are given by the fitted Hugoniots, and the dashed lines represent the uncertainties in the intercept and slope of the linear shock velocity–particle velocity Hugoniots. The elevated temperature $50\,\%$ ammonium nitrate solution can be considered as a less dense version of the ambient temperature $50\,\%$ solution, and it is expected that this should result in a decrease in the impedance of the material. The $80\,\%$ ammonium nitrate solution, which has a higher density than the other solutions, consequently has a higher impedance. The experimental Hugoniot data are limited to particle velocities of around $1\,\mathrm{km\,s^{-1}}$; the lack of any evidence for non-linearity in the present data allow for the Hugoniots to be extended to higher particle velocities with ease, as the linear Hugoniots are well-behaved at all particle velocities, whereas a quadratic relationship between particle velocity and shock velocity would not behave well in stress–volume space when extrapolated.

6.3 Reload experiments

The reported experiments, in addition to measuring the principal Hugoniots of the solutions, enabled determination of the reload state of the solutions. These reload states are plotted for the various solutions in Figures 6.9, 6.10, and 6.11. In some of the experiments, the rear gauge failed before reaching an equilibrium value; these experiments have been neglected in the analysis of reload states, and are indicated by the circled points on the principal Hugoniots in the figures below. Rayleigh lines, connecting the Hugoniot and reload states, have been added to the graphs. As expected, the reload states generally lie below the principal Hugoniot; one exception is the reload state with lowest stress in Figure 6.10, which lies somewhat above the Hugoniot. This is likely due to the inherently larger proportional uncertainties at lower stresses causing the reload volume to be miscalculated slightly.

The measured reload states can be used to obtain values of the Grüneisen parameter, Γ. Generally, the method for determining values of Γ discussed in the preceeding chapters is only reliable for reload stresses above $3\,\mathrm{GPa}$. Below this reload stress, when the Hugoniot stress is of order $1\,\mathrm{GPa}$, the relative uncertainties in the measured stresses are sufficient to prevent an accurate determination of Γ, and the calculation of Γ produces unphysically large values. The calculation of temperature on the Hugoniot requires a form for Γ that can be integrated from the initial specific volume, v_0. Whereas, in water, accurate compressional isotherms are reported in the literature enabling determination of the behaviour of Γ at low compressions, for the solutions reported, the low compression behaviour is limited to a single value of Γ at the initial density [Chan, 2011]. In analysing the volume-dependence of Γ, a linear form has been assumed. Whilst the data in water suggest that a more complicated form might be appropriate, without isothermal compression data, it is not possible to ensure appropriate low compression behaviour for higher-order polynomials. Thus, as values of Γ are only available above $3\,\mathrm{GPa}$ and at the initial density, a linear dependence on volume is the simplest admissible form.

Figure 6.12 shows the measured values of Γ in a solution of $50\,\%$ ammonium nitrate by weight at $14 \pm 1\,^{\circ}\mathrm{C}$ together with the zero-pressure value and the linear fit, $\Gamma = 3.65 - 3.62v$, through the data. The fact that Γ decreases with decreasing volume in the reload experiments suggests that there is a maximum in Γ near $v = 0.6\,\mathrm{cm}^3\,\mathrm{g}^{-1}$, as was demonstrated in the water experiments. However, without further measurements of Γ at low compressions, it

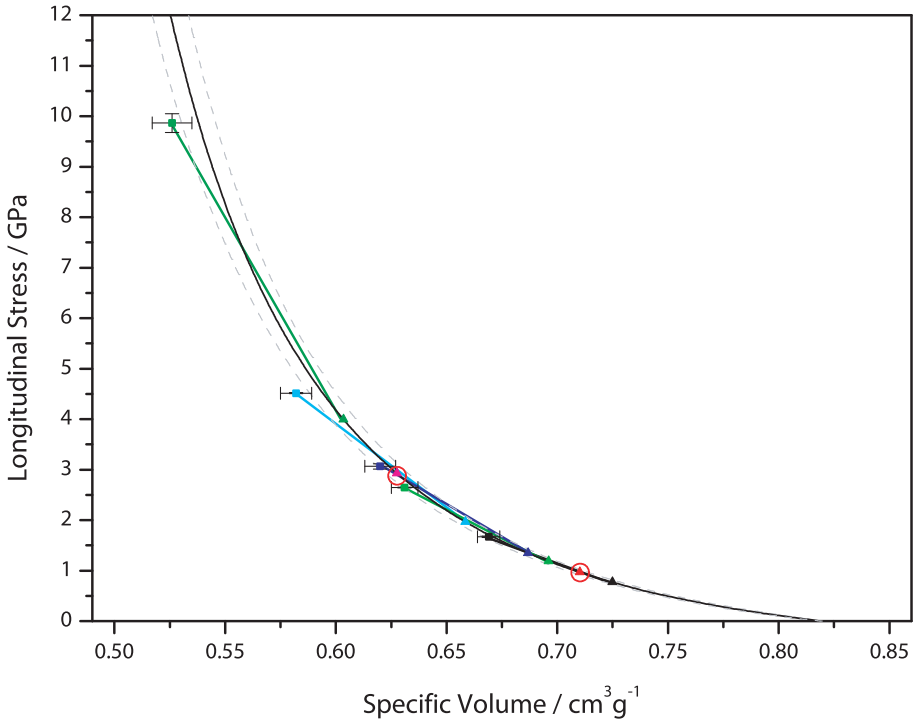

Figure 6.9: Hugoniot and reload states, in stress–specific volume space, for a solution of $50\,\%$ ammonium nitrate by weight at $14 \pm 1\,^{\circ}\mathrm{C}$. The triangular symbols are the measured Hugoniot states; the error bars, which are generally smaller than the symbols, have been omitted for clarity. The solid straight lines are the Rayleigh lines linking each Hugoniot state to its corresponding reload state (square symbols). The solid black curve is the fitted Hugoniot for the solution. The two circled points on the Hugoniot do not have measured reload states, as the rear gauges in these experiments failed before reaching equilibrium stress values.

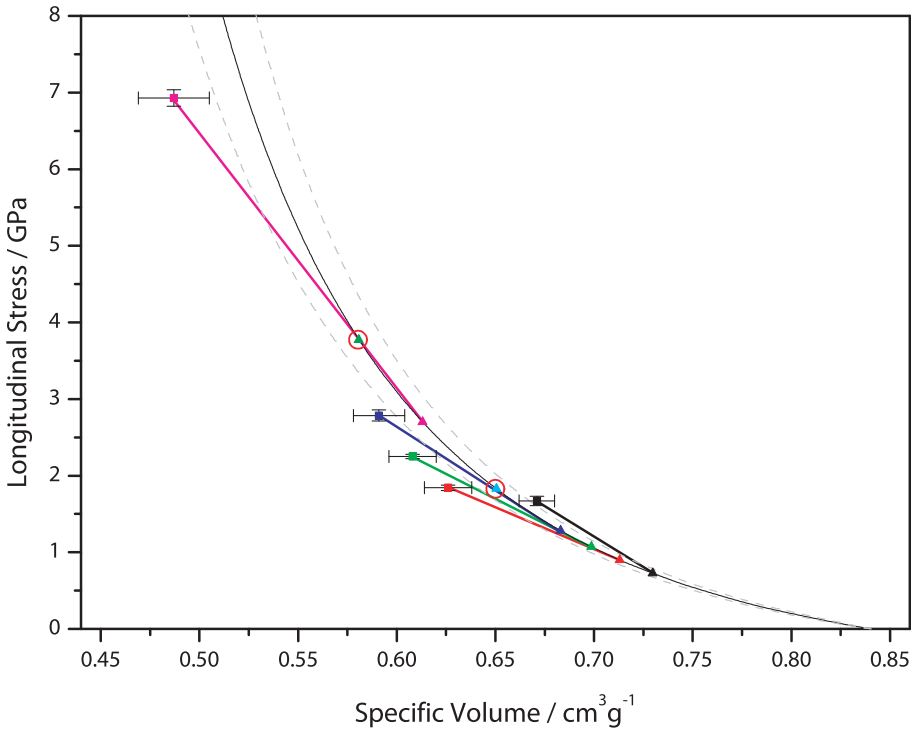

Figure 6.10: Hugoniot and reload states, in stress–specific volume space, for a solution of 50 % ammonium nitrate by weight at $65 \pm 2\,^{\circ}\mathrm{C}$. The triangular symbols are the measured Hugoniot states; the error bars, which are generally smaller than the symbols, have been omitted for clarity. The solid straight lines are the Rayleigh lines linking each Hugoniot state to its corresponding reload state (square symbols). The solid black curve is the fitted Hugoniot for the solution. The two circled points on the Hugoniot do not have measured reload states, as the rear gauges in these experiments failed before reaching equilibrium stress values. The lowest stress reload state appears to lie above the Hugoniot, probably due to the reload stress being incorrectly measured in this experiment.

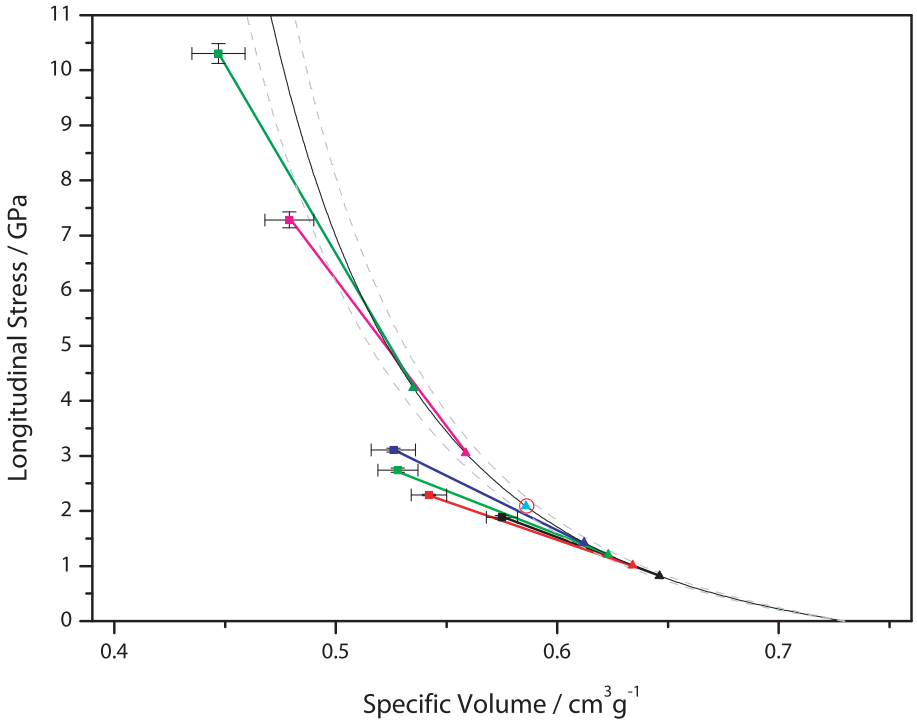

Figure 6.11: Hugoniot and reload states, in stress–specific volume space, for a solution of 80 % ammonium nitrate by weight at $64 \pm 2\,^{\circ}\mathrm{C}$. The triangular symbols are the measured Hugoniot states; the error bars, which are generally smaller than the symbols, have been omitted for clarity. The solid straight lines are the Rayleigh lines linking each Hugoniot state to its corresponding reload state (square symbols). The solid black curve is the fitted Hugoniot for the solution. The circled point on the Hugoniot does not have a measured reload state, as the rear gauge in this experiment failed before reaching an equilibrium stress value.

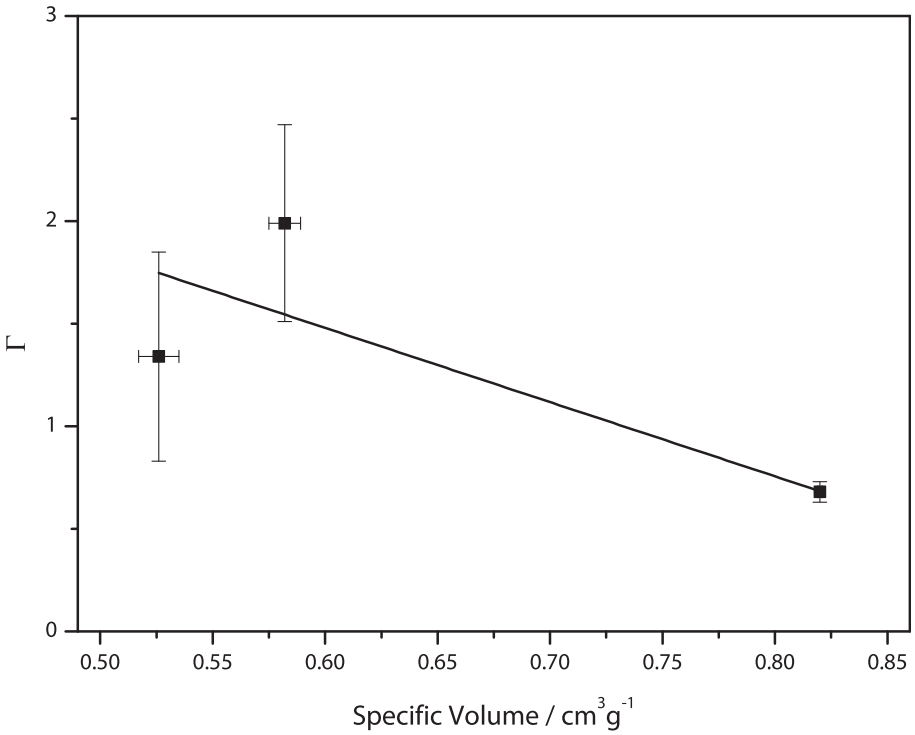

Figure 6.12: Γ in a solution of $50\,\%$ ammonium nitrate by weight at $14 \pm 1\,^{\circ}\mathrm{C}$ determined from shock/reload experiments, together with the calculated value of Γ at v_0 [Chan, 2011]. The linear fit through these data is given by $\Gamma = 3.65 - 3.62v$. The data derived from shock/reload experiments suggest that Γ reaches a maximum near a specific volume of $0.6\,\mathrm{cm}^3\,\mathrm{g}^{-1}$; without further data near v_0, however, it is not possible to fit a higher-order polynomial through the data that behaves physically for all volumes.

is not possible to fit a more complicated function whilst maintaining realistic behaviour as v tends to v_0. These results imply that there is a temperature-dependence of Γ at constant volume; this point is discussed further in Chapter 7.

Increasing the initial temperature of the solution to $65 \pm 2\,^{\circ}\mathrm{C}$ has little effect on the measured values of Γ, which are presented in Figure 6.13. Again, the data seem to imply that there is a maximum in Γ near $v = 0.6\,\mathrm{cm}^3\,\mathrm{g}^{-1}$, but the lack of data in the low compression region do not enable a higher-order polynomial to be fitted to the data. The linear fit is given by $\Gamma = 3.93 - 4.01v$.

The variation of Γ with volume in a solution of $80\,\%$ ammonium nitrate by

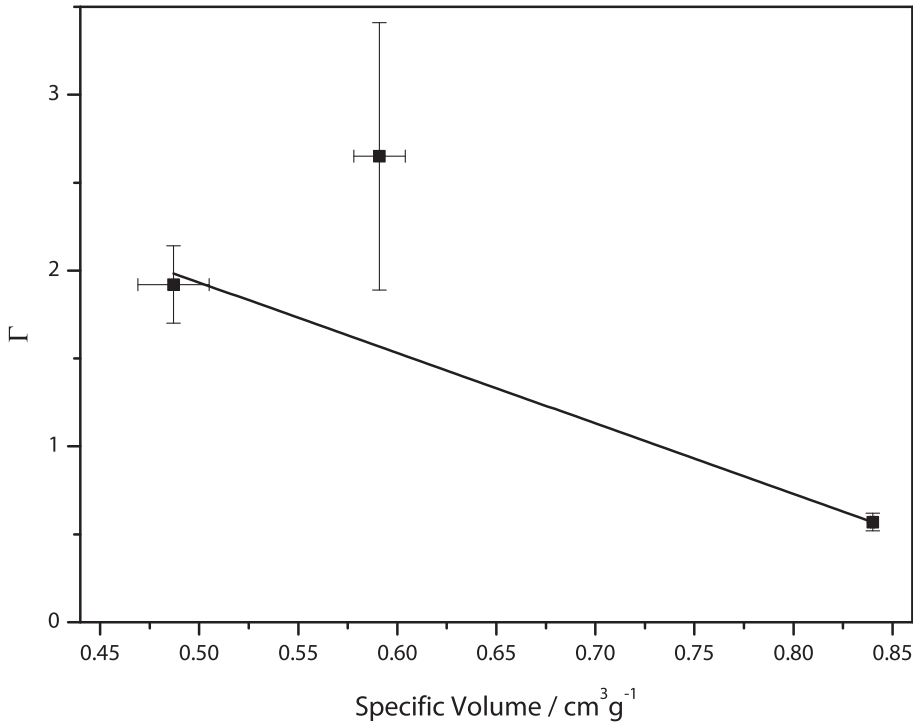

Figure 6.13: Γ in a solution of $50\,\%$ ammonium nitrate by weight at $65 \pm 2\,^{\circ}\mathrm{C}$ determined from shock/reload experiments, together with the calculated value of Γ at v_0 [Chan, 2011]. The linear fit through these data is given by $\Gamma = 3.93 - 4.01v$. The data derived from shock/reload experiments suggest that Γ reaches a maximum near a specific volume of $0.6\,\mathrm{cm}^3\,\mathrm{g}^{-1}$; without further data near v_0, however, it is not possible to fit a higher-order polynomial through the data that behaves physically for all volumes.

weight at $64 \pm 2\,^{\circ}\mathrm{C}$ is shown in Figure 6.14. In contrast to the experiments on the $50\,\%$ ammonium nitrate solution, there is no evidence for a maximum in Γ over the range of volumes investigated, and the linear relationship $\Gamma = 3.87 - 3.76v$ provides a good fit through the data from shock/reload experiments and the calculated value of Γ at v_0.

The linear fits for the volume dependence of Γ in each solution have similar gradients, and the reported values of Γ lie close to each other. This suggests that the response of the three solutions is quite similar, a suggestion supported by the similarity of the solution Hugoniots reported above.

In order to calculate temperatures along the Hugoniot, in addition to de-

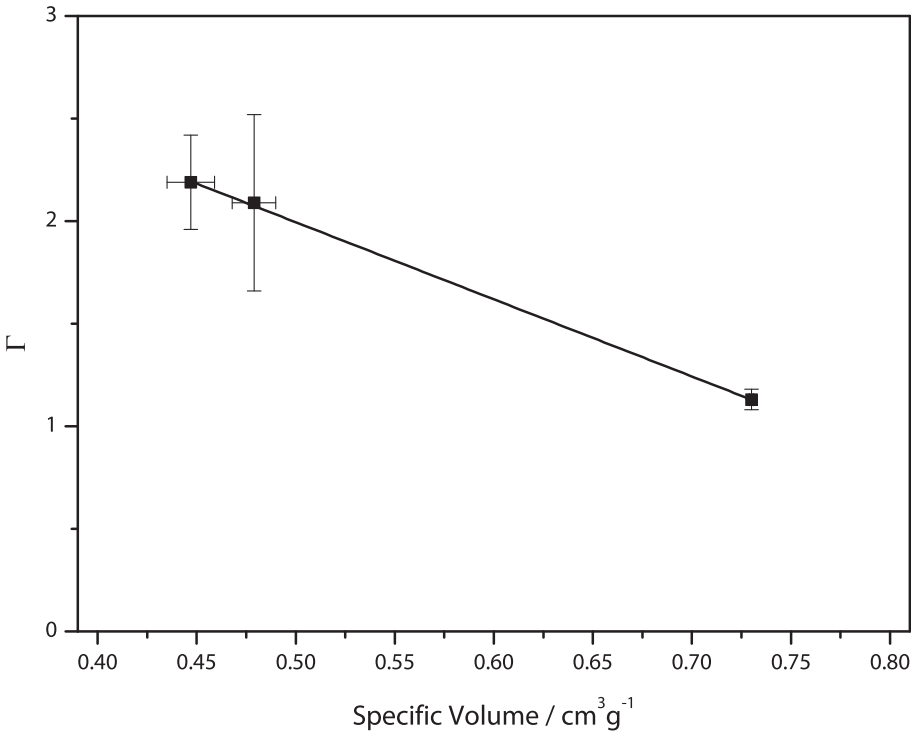

Figure 6.14: Γ in a solution of $80\,\%$ ammonium nitrate by weight at $64 \pm 2\,^{\circ}\mathrm{C}$ determined from shock/reload experiments, together with the calculated value of Γ at v_0 [Chan, 2011]. The linear fit through these data is given by $\Gamma = 3.87 - 3.76v$. In contrast to the the other experiments reported in this thesis, there is no evidence that Γ reaches a maximum value over the range of specific volumes investigated.

termining the Hugoniot and the volume-dependence of Γ, a model for the heat capacity at constant volume, c_v, is required. In the present analysis, the value of c_v has been taken to be identical to the value at zero pressure given by Chan [2011]. That c_v is constant is the standard assumption made in the literature, and is usually justified by assuming the material is well above its Debye temperature; without detailed data on the behaviour of c_v under dynamic compression, constant c_v is also the simplest assumption. These heat capacities are given in Table 6.1. The calculated temperature rises in the solutions are presented in Figure 6.15, along with the temperatures in water determined in Chapter 5, as a function of the Lagrangian compression, $\rho_0(v_0 - v)$. The data are presented as a function of compression, rather than pressure or density, as

the liquids have different initial densities and different impedances. Giving the temperatures as a function of compression allows for easier comparison between the materials. Errors have been calculated by considering the effect of uncertainties in the measured Hugoniots and the heat capacity used, and are of order $10\,\%$ on the temperature rise.

Given the similarities in the Hugoniots and values of Γ, the variations in calculated shock temperatures in the solutions can chiefly be explained through their different heat capacities. As lower heat capacities would give rise to larger calculated temperature rises, the lower heat capacity in the $80\,\%$ ammonium nitrate solution, compared to the $50\,\%$ solution at the same initial temperature, explains the majority of the difference in calculated shock temperatures for these experiments. As with the water, the effect of increasing the initial temperature for the $50\,\%$ solution is predominantly to increase the shock temperatures by the difference in initial temperature.

Changes in the functional form or values of Γ are manifested by changes in the curvature of the temperature-compression curves shown in Figure 6.15. The present temperature calculations are relatively insensitive to the exact form of Γ. McQueen [1989] has commented that Γ cannot be taken as constant, however, as this results in unphysical behaviour being predicted. For the $50\,\%$ ammonium nitrate solutions, replacing the single linear fit with a fit that is piecewise linear between the three values changes the calculated temperatures by only one or two percent, and is thus significantly smaller than the other experimental uncertainties. Variations in the value of c_v change the magnitude of the temperature rise but not the curvature. The assumptions that the heat capacity is constant and within $10\,\%$ of that at zero pressure, and that Γ takes the linear form described above, yield an uncertainty in the calculated shock temperature rises of $10\,\%$. As with the previous results in this thesis, variation of the heat capacity along the Hugoniot has been neglected, as is generally the case in the literature. It is unclear what form such variation may take in these solutions. It is felt that, over the compression range of interest, the present $10\,\%$ uncertainty in the calculated temperatures is sufficient to account for any such variations. The calculated temperature rises are only valid over the compression range measured along the Hugoniot, where the maximum compression was approximately 0.25. However, as is discussed in the following chapter, these calculations must be considered as only approximations.

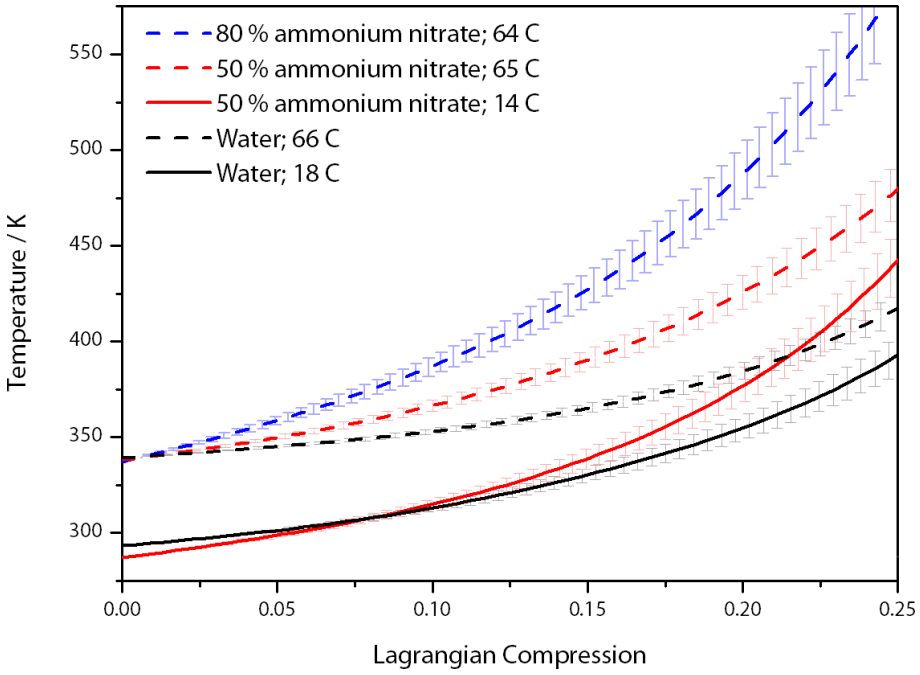

Figure 6.15: Calculated temperature rises, assuming a constant value of c_v equal to the zero pressure heat capacity, in the ammonium nitrate solutions, and temperatures in water determined in Chapter 5, as a function of the Lagrangian compression, $\rho_0(v_0 - v)$. The calculated temperatures are only valid over the compression range of the Hugoniots measured above. The uncertainty on the temperatures is $10\,\%$.

6.4 Summary

- The principal Hugoniots of three ammonium nitrate solutions have been determined experimentally.
- The shock velocity–particle velocities are linear over the range of particle velocities studied.
- The Hugoniots are similar to each other, and the variations seem most strongly correlated with the variations in initial density.
- Stress and specific volume in states off the principal Hugoniots have been measured through shock/reload experiments.
- Extrapolation of the principal Hugoniots to compressions enabled determination of the Grüneisen parameter, Γ.

- By assuming c_v was constant and equal to the zero pressure value, temperatures along the Hugoniot were calculated for each solution.
- To Lagrangian compressions of 0.25, these temperatures have uncertainties of $10\,\%$.
- Within the present experimental uncertainties, for a given solution, the shock temperatures at a higher initial temperature can be found by adding the increase in initial temperature to the calculated shock temperatures for the lower initial temperature.

6.5 Bibliography

J. Chan. Personal communication, 2011. Orica Mining Services.

D. J. Chapman. *Shock-compression of porous materials and diagnostic development*. PhD thesis, University of Cambridge, 2009.

W. Hustrulid. *Blasting principles for open pit mining*, volume 1 - General design concepts. A. A. Balkema, 1999.

S. P. Marsh, editor. *LASL Shock Hugoniot Data*. University of California Press, 1980.

R. G. McQueen. Shock-waves in condensed media: Their properties and the equation of state of materials derived from them. In *Enrico Fermi summer course CX11: nuclear collisions from the mean field into the fragmentation regime*, 1989.

W. B. Sudweeks. Physical and chemical properties of industrial slurry explosives. *Industrial & Engineering Chemistry Product Research and Development*, 24(3):432–436, 1985.

E. Washburn, editor. *International Critical Tables of Numerical Data, Physics, Chemistry and Technology*. Knovel, 1st electronic edition, 2003.

CHAPTER 7

ANALYSIS AND DISCUSSION

The preceding chapters have described a series of experiments that were conducted to investigate the response of water and of ammonium nitrate solutions to shock loading. The Mie-Grüneisen equation of state has previously been used to describe the thermodynamic behaviour of water under shock loading and, under the assumption that the heat capacity C_v is constant, has been used to calculate shock temperature rises [Gurtman et al., 1971]. The present work applied this model to water at an elevated initial temperature (Chapter 5) and to solutions of ammonium nitrate (Chapter 6). Attention is now turned to the validity of the assumptions made in the present model and, hence, to the applicability of the Mie-Grüneisen equation of state to the behaviour of water and ammonium nitrate solutions. Firstly, the effect of preheating on a material's Hugoniot is considered and comparison between the experimentally-determined and theoretically-predicted Hugoniots made. Secondly, the functional dependencies of Γ are examined, and it is demonstrated that the present results show a dependence on temperature in addition to volume. Finally, the theoretical understanding of the shock compression of water is examined, with particular reference to the behaviour of Γ and the heat capacity C_V.

7.1 Relationships amongst the Hugoniots

The experimentally-determined Hugoniots for water at initial temperatures of $18 \pm 2\,^{\circ}\mathrm{C}$ and $66 \pm 2\,^{\circ}\mathrm{C}$ are shown in stress–particle velocity space in Figure 7.1. The elevated temperature Hugoniot lies significantly below the ambient temperature Hugoniot, suggesting that a significant softening has occurred. Softening has been experimentally observed in preheated metal samples [*e.g.*, Dai et al., 2006], although the level of softening is typically much smaller than that shown in Figure 7.1.

The Mie-Grüneisen equation can be used to calculate Hugoniots at elevated temperatures. Using the principal Hugoniot as the reference curve, the Mie-Grüneisen equation becomes

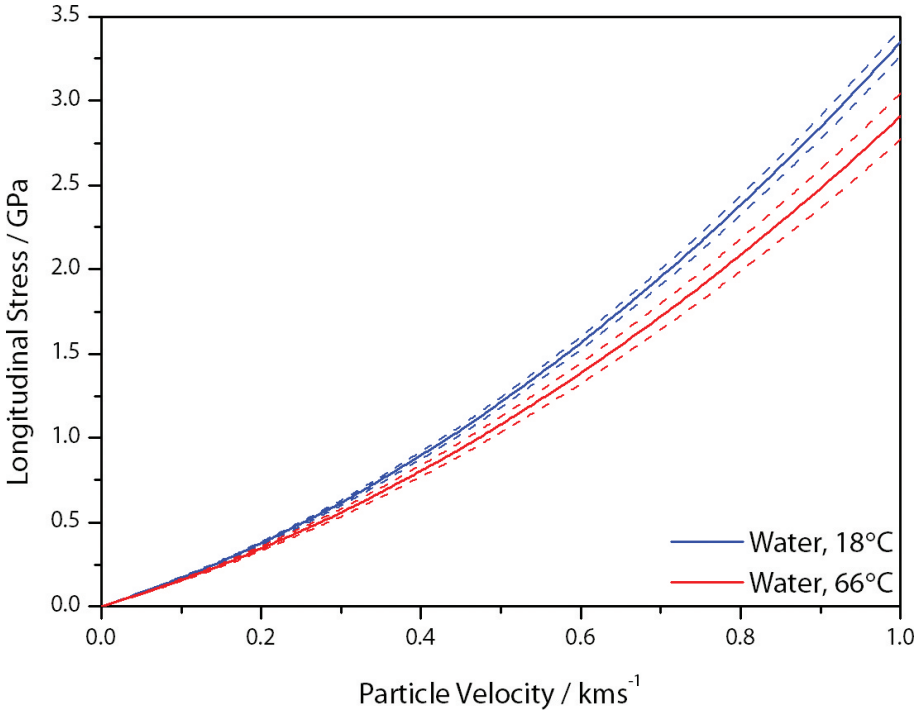

Figure 7.1: Pressure–particle velocity Hugoniots of water at $18 \pm 2\,^{\circ}\mathrm{C}$ (blue) and $66 \pm 2\,^{\circ}\mathrm{C}$ (red), from the results described in Chapter 5. The elevated temperature Hugoniot lies below the ambient temperature Hugoniot, indicating a reduction in shock impedance with temperature over this range of temperatures and particle velocities.

$$P_H^{'} - P_H = \frac{\Gamma}{v}(E_H^{'} - E_H). \tag{7.1}$$

where $E_H^{'}$ and $P_H^{'}$ are the respectively the energy and pressure on the elevated temperature Hugoniot. Considering the generalised energy jump condition (Equation 2.7), we have, on the principal Hugoniot

$$E_H - E_0 = \frac{1}{2}P_H(V_0 - V), \tag{7.2}$$

and, similarly, on the elevated temperature Hugoniot

$$E_H^{'} - E_0^{'} = \frac{1}{2}P_H^{'}(V_0^{'} - V), \tag{7.3}$$

where $E_0^{'}$ is the specific internal energy at ambient pressure at the elevated temperature and is simply $E_0 + C_p\Delta T$, where C_p is the heat capacity at con-

stant pressure, which is typically assumed to be constant - in water, over the temperature range of interest, the variation of C_p with temperature is less than one part in a thousand [Washburn, 2003]. Combining this result with Equations 7.1, 7.2, and 7.3, the pressure–volume Hugoniot at elevated temperature is

$$P_H^{'} = P_H \left(\frac{1 - \frac{\Gamma}{v}\left(\frac{v_0 - v}{2}\right)}{1 - \frac{\Gamma}{v}\left(\frac{v_0^{'} - v}{2}\right)} \right) + \frac{\frac{\Gamma}{v} c_p \Delta T}{1 - \frac{\Gamma}{v}\left(\frac{v_0^{'} - v}{2}\right)}, \tag{7.4}$$

and thus may be calculated from the principal Hugoniot provided Γ is known. Using the principal Hugoniot for water determined experimentally in Chapter 5 and the polynomial form for $\Gamma(v)$ given by Gurtman et al. [1971], the elevated temperature Hugoniot for water in pressure–volume space has been calculated; the heat capacity was taken to be $4.2\,\mathrm{J\,g^{-1}\,K^{-1}}$ [Washburn, 2003]. This calculation is presented in Figure 7.2, together with the experimentally determined principal and elevated temperature Hugoniots.

The calculation suggests that the elevated temperature Hugoniot should, in pressure-volume space, lie to the right of the ambient temperature Hugoniot, with the shift being partly due to the change in initial volume and partly due to the increase in specific internal energy at zero pressure. The calculated elevated temperature Hugoniot crosses the measured ambient Hugoniot at a stress of around $7\,\mathrm{GPa}$. The implication of this crossing over is that the specific internal energy at a given volume for the elevated temperature material is lower than that of the ambient temperature material; it should however be recalled that an additional term $C_p \Delta T$ must be added to the energy of the elevated temperature material to reflect the energy added by pre-heating it. The measured elevated temperature Hugoniot does not agree well with the calculated Hugoniot, as it crosses the ambient Hugoniot at around $0.5\,\mathrm{GPa}$ and thence lies significantly below it at most stresses. A similar discrepancy between the calculated and measured elevated temperature Hugoniots occurs in pressure–particle velocity space, as is shown in Figure 7.3. As expected, the calculation shows a softening of the water, which results in the calculated elevated temperature Hugoniot lying below the principal Hugoniot. However, the calculation is, within error, the same as the ambient temperature Hugoniot. The measured elevated temperature Hugoniot shows a much greater degree of softening. It has been noted by a number of authors [Jonas et al., 1976; Postorino et al., 1993; Tromp et al., 1994] that, as the pressure and temperature

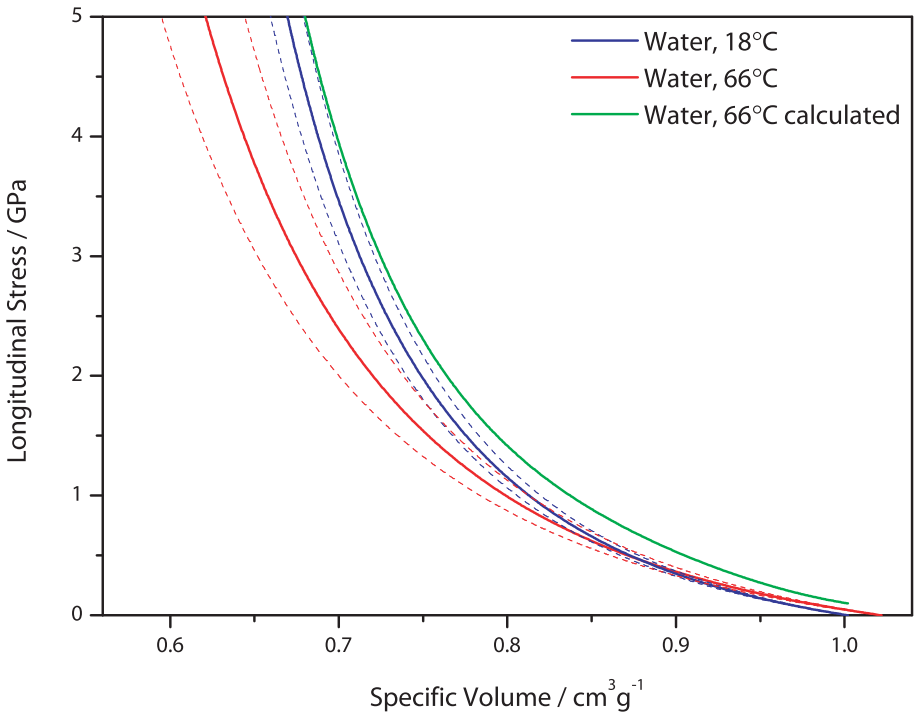

Figure 7.2: Pressure–volume Hugoniots of water at initial temperatures of $18 \pm 2\,^{\circ}\mathrm{C}$ (blue) and $66 \pm 2\,^{\circ}\mathrm{C}$ (red), from the results described in Chapter 5. The green curve has been calculated using Equation 7.4, the experimentally determined water Hugoniot, and the form of Γ for ambient temperature water given by Gurtman et al. [1971] under the assumption that the heat capacity c_p at ambient pressure is independent of temperature. The calculations suggest that, in pressure–volume space, the increase in specific internal energy at zero pressure, together with the reduction in initial density, dominate the behaviour of the higher temperature Hugoniot. The calculations indicate that Hugoniots will cross over at a stress of around $7\,\mathrm{GPa}$. The experimentally determined elevated temperature Hugoniots crosses the ambient Hugoniot at $0.5\,\mathrm{GPa}$, the the errors cease to overlap at around $1.5\,\mathrm{GPa}$.

of water are increased, significant structural changes occur and there appears to be a transition from behaviour that is dominated by hydrogen bonds to a more 'normal' liquid response. The implication of these studies is that, for a given pressure, the elevated temperature water would be significantly denser; Bradley and Pitzer [1979] note that these structural changes begin to become important at temperatures above $50\,^{\circ}\mathrm{C}$. Due to these structural changes, it would appear that water at elevated temperature is a fundamentally different material than water at ambient temperature. The increase in temperature appears to increase markedly the compressibility of water and reduce significantly its impedance.

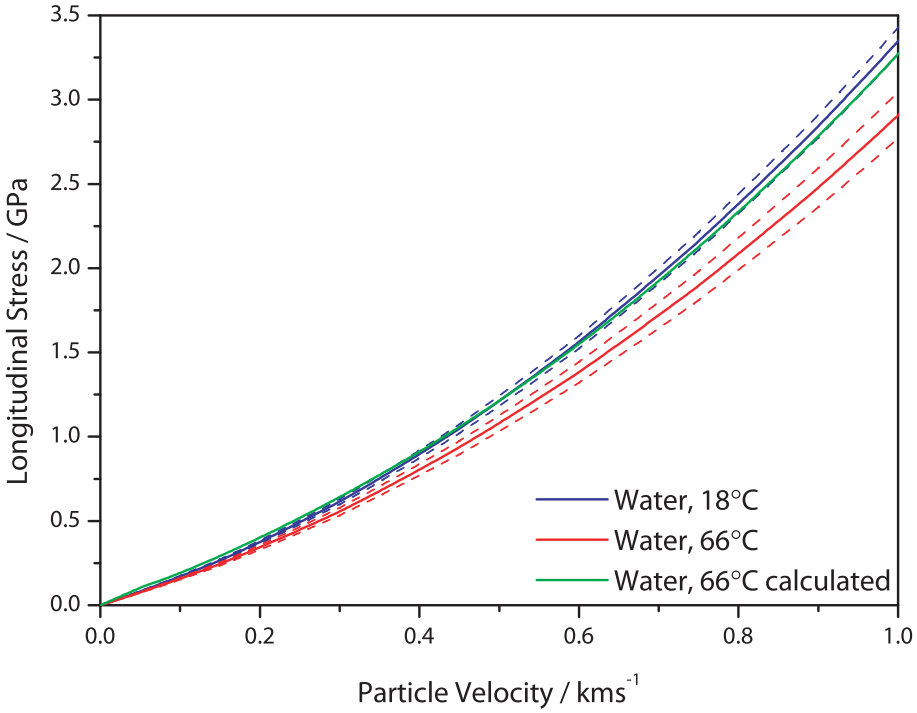

Figure 7.3: Pressure–particle velocity Hugoniots of water at initial temperatures of $18 \pm 2\,^{\circ}\mathrm{C}$ (blue) and $66 \pm 2\,^{\circ}\mathrm{C}$ (red), from the fits described in Chapter 5. Particle velocities corresponding to the calculated elevated temperature Hugoniot shown in Figure 7.2 have been calculated using the relationship $u_p^{'} = \sqrt{P'(v_0' - v')}$, where the primes indicate that the values are on the elevated temperature Hugoniot. The calculation suggests that the elevated temperature should lie below, but within error of, the ambient temperature Hugoniot. The measured elevated temperature Hugoniot is significantly softer than the ambient temperature Hugoniot and is not within error of it.

A similar behaviour, of softening (reduction in impedance) is observed in the compression of a solution of $50\,\%$ ammonium nitrate by weight at $14\pm1\,^{\circ}\mathrm{C}$ and $65\pm2\,^{\circ}\mathrm{C}$. The Hugoniots determined in Chapter 6 for this solution are presented in Figure 7.4. Such behaviour is to be expected: whilst the weight percentages of ammonium nitrate and water are equal, an ammonium nitrate molecule is four-times heavier than a water molecule and, thus, there are many more water molecules in the solution. The solution can be considered as ammonium (NH_4^+) and nitrate (NO_3^-) ions completely surrounded by water and therefore the response of the solution will be dominated by the response of water.

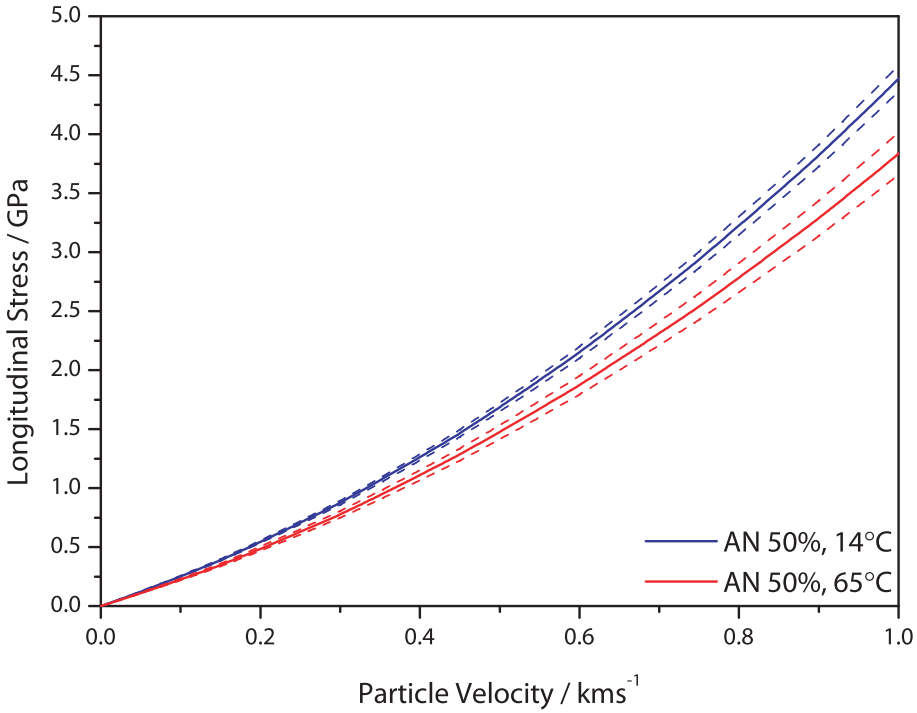

Figure 7.4: Pressure–particle velocity Hugoniots of a solution of $50\,\%$ ammonium nitrate by weight at $14\pm1\,^{\circ}\mathrm{C}$ (blue) and $65\pm2\,^{\circ}\mathrm{C}$ (red), from the fits described in Chapter 6. As with the water Hugoniots shown in Figure 7.1, the elevated temperature Hugoniot lies below the ambient temperature Hugoniot, indicating a reduction in shock impedance with temperature over this range of temperatures and particle velocities.

Figure 7.5 shows the pressure–particle velocity data given by Galbraith [1997] for a solution of $54\,\%$ ammonium nitrate by weight at $20\pm1\,^{\circ}\mathrm{C}$ and $80\pm$

1 °C. The uncertainties associated with this data were discussed in Chapter 1. For ease of comparison, a quadratic (constrained through the origin) has been fitted to Galbraith's data. As with the liquids discussed above, it is clear that the elevated temperature solution has a lower impedance than the ambient temperature solution.

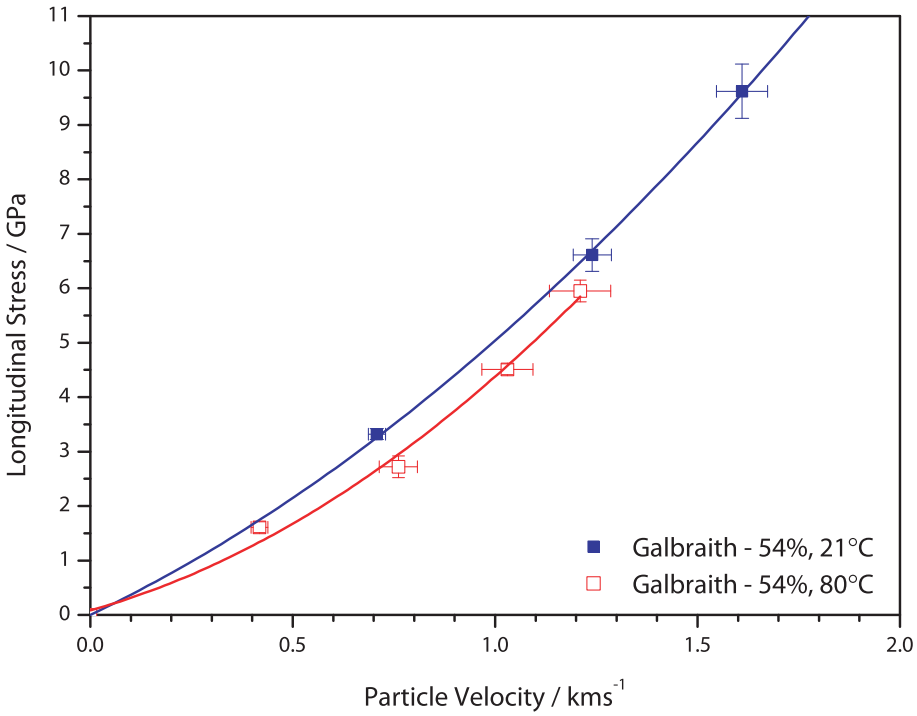

Figure 7.5: Hugoniots, in pressure–particle velocity space, of a solution of 54 % ammonium nitrate by weight at $20 \pm 1\,^{\circ}\mathrm{C}$ (blue) and $80 \pm 1\,^{\circ}\mathrm{C}$ (red). The data are from Galbraith [1997], and have been re-analysed to give the present Hugoniots, which are taken as quadratic relationships between pressure and particle velocity, and have been forced through the origin. Again, the higher temperature Hugoniot lies below that at lower temperature, indicating a softening of the liquid and effective reduction in impedance.

The present experimental results, together with those of Galbraith [1997] and the Mie-Grüneisen calculations described above, demonstrate that water, and water-dominated solutions, become significantly softer as they are preheated to an extent that is not described by the Mie-Grüneisen equation of state. In water, it is not possible to achieve agreement between the measured and calculated elevated temperature Hugoniots for any physically plausible

values of Γ or the heat capacity C_p. As has been noted in the literature, it seems that there is a significant reduction in the effect of the peculiar structural properties of water as temperatures increase. It is, perhaps, therefore unwise to consider ambient and elevated temperature water as being the same material.

7.2 Functional dependencies of Grüneissen's parameter

Throughout this thesis, it has been assumed that Γ is a function of volume alone; indeed this is required if one is to use the Hugoniot, and not the cold compression curve, as the reference pressure-energy curve. In discussing the field of shock compression and of equations of state, McQueen [1989] stated that

> "One of the basic results from these studies is that Γ is a function of volume alone. To our knowledge this has never really been tested, since Γ has never been measured at two temperatures at the same density."

Whilst it is true that such measurements of Γ from shock compression experiments have not been reported in the literature, other experimental measurements of Γ have been reported, but are largely neglected by the shock physics community. Knopoff and Shapiro [1969] discuss the applicability of the Mie-Grüneisen equation of state to shock wave data, noting the logical contradiction between the derivation of the Mie-Grüneisen equation of state (which assumes a crystalline solid) and the jump conditions (which assume an inviscid fluid). From the thermodynamic definition of Γ (Equation 2.19), we have

$$\begin{aligned}
\Gamma &= V \left.\frac{\partial P}{\partial E}\right|_V && (7.5)\\
&= V \left.\frac{\partial P}{\partial T}\right|_V \Big/ \left.\frac{\partial E}{\partial T}\right|_V && (7.6)\\
&= \frac{V}{C_V}\left(-\left.\frac{\partial V}{\partial T}\right|_P \Big/ \left.\frac{\partial P}{\partial V}\right|_T\right) && (7.7)\\
&= \frac{\alpha K_T V}{C_V} && (7.8)
\end{aligned}$$

where $C_V = \left.\frac{\partial E}{\partial T}\right|_V$ is the heat capacity at constant volume, $K_T = -V \left.\frac{\partial P}{\partial V}\right|_T$ is the isothermal bulk modulus, and $\alpha = \frac{1}{V}\left.\frac{\partial V}{\partial T}\right|_P$ is the volumetric coefficient of

thermal expansion. These quantities have been measured at a variety of temperatures under static loading for a number of materials, and as Knopoff and Shapiro [1969] note, the resultant values of Γ determined in a variety of solids are independent of temperature. Knopoff and Shapiro [1969] determined values of Γ as a function of both temperature and pressure in water from literature data of the heat capacity, bulk modulus, and thermal expansivity. Their results are shown in Figure 7.6.

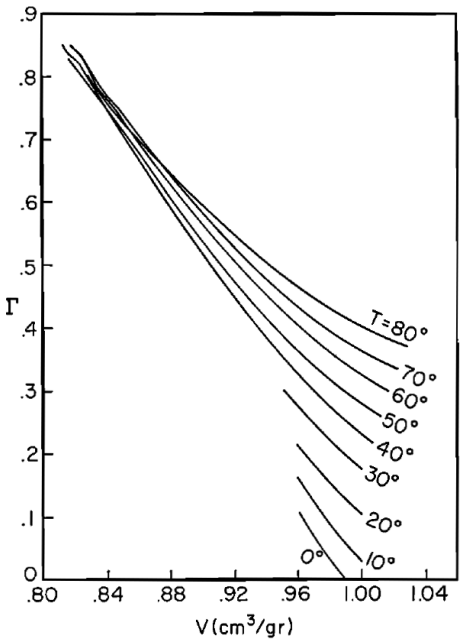

Figure 7.6: Variation of Γ with volume at different temperatures in water, from Knopoff and Shapiro [1969]. The values were calculated from published isostatic compression data, and indicate a dependence of Γ on temperature. The variation with temperature appears to decrease with increasing pressure (decreasing volumes).

One interesting feature is that Γ increases with decreasing V, which is the opposite to the behaviour found in sold metals [McQueen, 1989]. This behaviour, of Γ increasing with decreasing V, has also been observed in mercury (Figure 7.7) which, whilst metallic, is also a liquid; there is also a temperature dependence of Γ at constant volume. It is obvious from Figure 7.6 that in water there is a significant dependence of Γ on temperature, and at larger temperatures Γ is larger. However, as the pressure increases and the volume decreases,

the temperature dependence decreases. Knopoff and Shapiro [1969] conclude that at high pressures the Mie-Grüneisen equation of state provides a valid description of liquids, suggesting that the effect of compression is to increase the spatial correlation of the water molecules to a point at which the lattice dynamic description becomes more appropriate. They note that further experimentation is required, at higher compressions, to investigate the temperature dependence of Γ in liquids. The present study, therefore, represents a test of the validity of the assumption that Γ is independent of temperature.

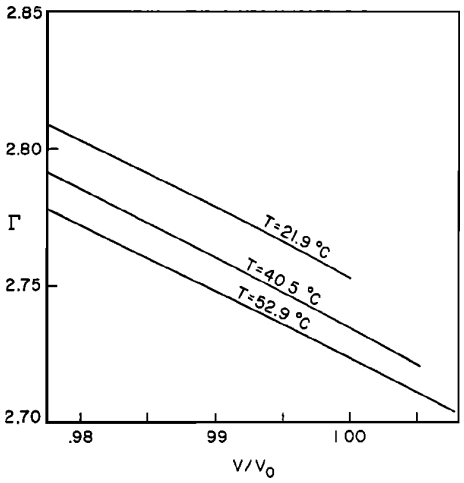

Figure 7.7: Variation of Γ at different temperatures in mercury as a function of the relative volume V/V_0 (where V_0 is the volume at room teperature and pressure), from Knopoff and Shapiro [1969]. The values were calculated from published isostatic compression data, and indicate a dependence of Γ on temperature. Γ is observed to increase with decreasing volume, in contrast to the standard behaviour in solid metals [McQueen, 1989].

Figure 7.8 shows the values of Γ measured in water at $66 \pm 2\,^{\circ}\mathrm{C}$, from the experiments described in Chapter 5. These data, and the fit derived from them, are compared to the fit for Γ in water at ambient temperature given by Gurtman et al. [1971]. It is clear from the values of Γ determined from the shock/reload experiments conducted that even a moderate degree of heating ($48 \pm 3\,^{\circ}\mathrm{C}$) significantly alters the value of Γ. The present results, therefore, support the trend suggested by the results of Knopoff and Shapiro [1969]. In producing their fit, Gurtman et al. [1971] constructed the low-compression data from isothermal compression curves, choosing the isotherms at $75\,^{\circ}\mathrm{C}$ and $175\,^{\circ}\mathrm{C}$ to provide the best fit to the shock data; that different pairs of

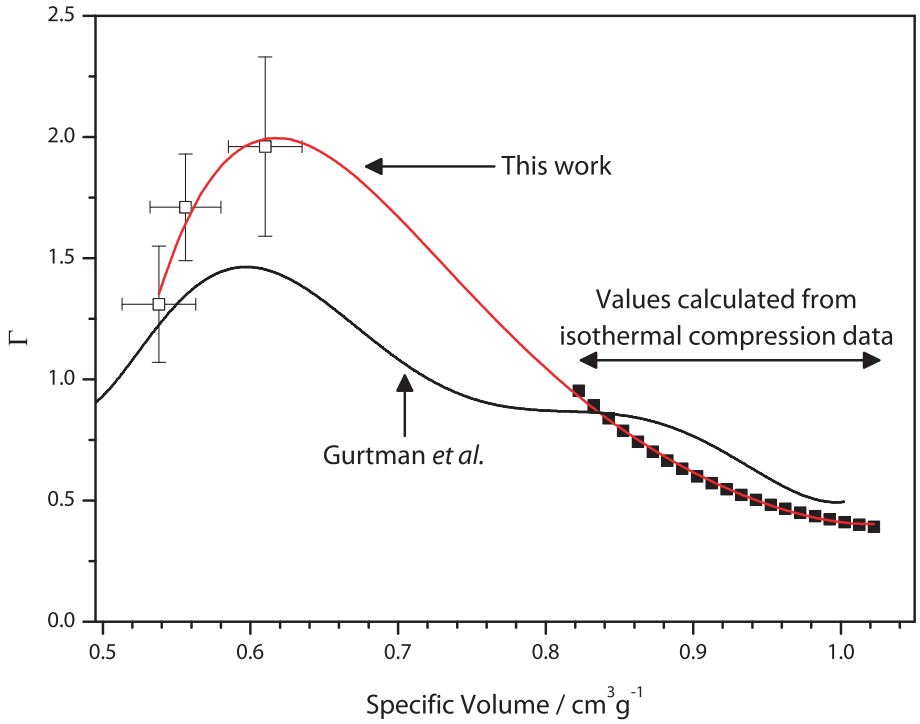

Figure 7.8: Variation of Γ with volume for water at $66 \pm 2\,^{\circ}\mathrm{C}$, from the experiments described in Chapter 5. The fit given by Gurtman et al. [1971] for water at ambient temperature is shown for comparison. The present results indicate that Γ has a temperature dependence over a wide range of specific volumes.

isotherms produce different values of Γ is a clear suggestion that there is a temperature dependence of Γ. It is surprising that the isothermal data suggest that Γ is lower in the higher temperature water, as the opposite result is found from the shock data. This could be due to uncertainties in the value used for C_V when calculating Γ from isotherms, which has been discussed in the preceeding chapters.

Similar results were found for a solution of $50\,\%$ ammonium nitrate by weight at $14 \pm 1\,^{\circ}\mathrm{C}$ and $65 \pm 2\,^{\circ}\mathrm{C}$. Values of Γ determined from the experiments described in Chapter 6 are shown in Figure 7.9. As with water, the ambient pressure values of Γ (calculated by Chan [2011] using Equation 7.8) suggest that, initially, Γ is smaller in the higher temperature liquid; again, this trend is reversed in the dynamic experiments.

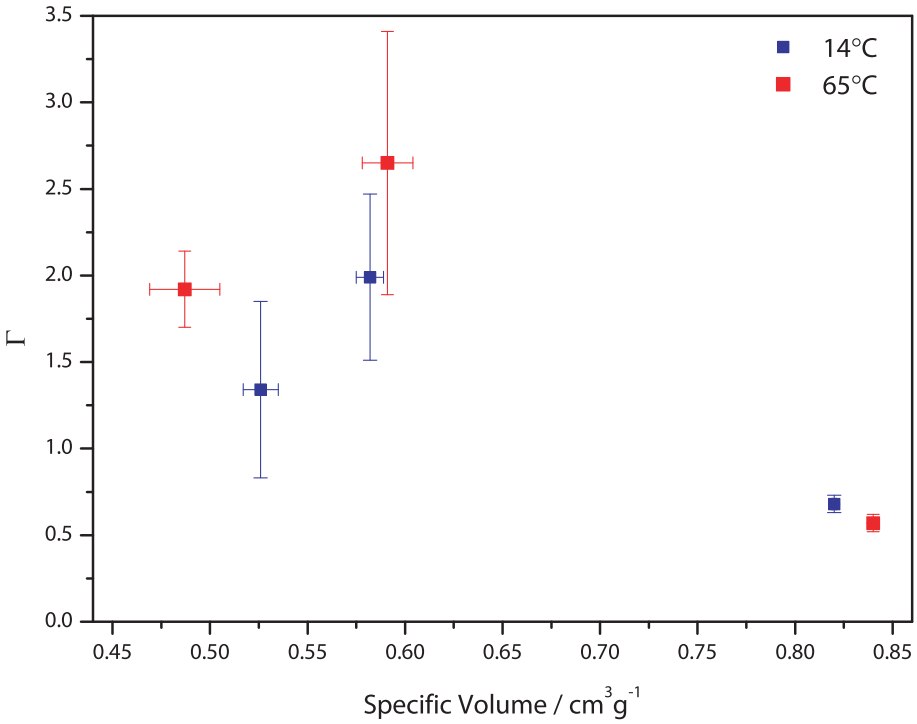

Figure 7.9: Variation of Γ with volume for a solution of $50\,\%$ ammonium nitrate by weight at $14 \pm 1\,^{\circ}\mathrm{C}$ (blue) and $65 \pm 2\,^{\circ}\mathrm{C}$ (red), from the experiments described in Chapter 6. The present results indicate that Γ has a temperature dependence over a wide range of specific volumes.

The implication, then, of the present experimental results is that in water and ammonium nitrate solutions, at pressures below $10\,\mathrm{GPa}$, there is significant dependence of Γ on temperature and, hence, as noted by Anderson [2000], the Mie-Grüneisen equation of state is a poor model of the thermal pressure. In light of this conclusion, the temperature calculations presented in the preceeding chapters should be considered only as rough approximations. Further, Anderson [2000] suggests that the Mie-Grüneisen equation of state is only applicable to systems that have a high level of coordination; it seems likely then that water, and ammonium nitrate solutions, will not be amenable to the simple treatment that is generally applied in the literature. It should be stressed that the standard form of the Mie-Grüneisen equation of state, which uses the principal Hugoniot as a reference curve, is only valid when Γ is a function of volume alone.

7.3 Pathological behaviour of water

The foregoing sections have discussed the results presented in this thesis in the context of the Mie-Grüneisen equation of state. It has been shown the Mie-Grüneisen equation provides a poor description of the effect of preheating on the water Hugoniot, and that the present results indicate a significant variation of Γ with temperature. There is some suggestion from the literature that structural effects in water may be responsible for both of these phenomena. It has also been noted in earlier chapters that uncertainties in the heat capacity C_V limit the ability to calculate Γ from isothermal compression data, and have an effect on calculated shock temperatures. The remainder of this chapter concerns the theoretical understanding of the behaviour of water, with particular reference to the functional form and dependencies of C_V and Γ.

Water is a pathologically complex molecule, and its properties vary dramatically with temperature and pressure [Nellis, 2008]. In the liquid form, water molecules auto-dissociate into hydronium (H_3O^+) and hydroxide (OH^-) ions:

$$2H_2O \rightleftharpoons H_3O^+ + OH^-. \tag{7.9}$$

Under shock compression, single water molecules also dissociate:

$$H_2O \rightleftharpoons H^+ + OH^-, \tag{7.10}$$

and the proportions of the various ions and molecules varies strongly with both pressure and temperature [Goldman et al., 2009a; Holzapfel, 1969]. The complex interaction between these various ionic species, and the non-spherical potentional of the water molecule itself, have hampered *ab initio* modelling efforts. Ree [1982] opted to focus on modeling higher pressures and temperatures in order that the complex interactions could be neglected. Their calculated value of Γ as a function of temperature and density on the Hugoniot is reproduced in Figure 7.10.

The calculated values of Γ are markedly lower than the experimentally determined values [*e.g.* Gurtman et al., 1971], which Ree attributed to uncertainties in the experimental measurements, having noted that the molecular potential used was able to accurately reproduce the principal Hugoniot, and also commented that the finite-difference approximation used to calculate Γ leads to an over-estimate of the value of Γ. The dashed portion of the curve

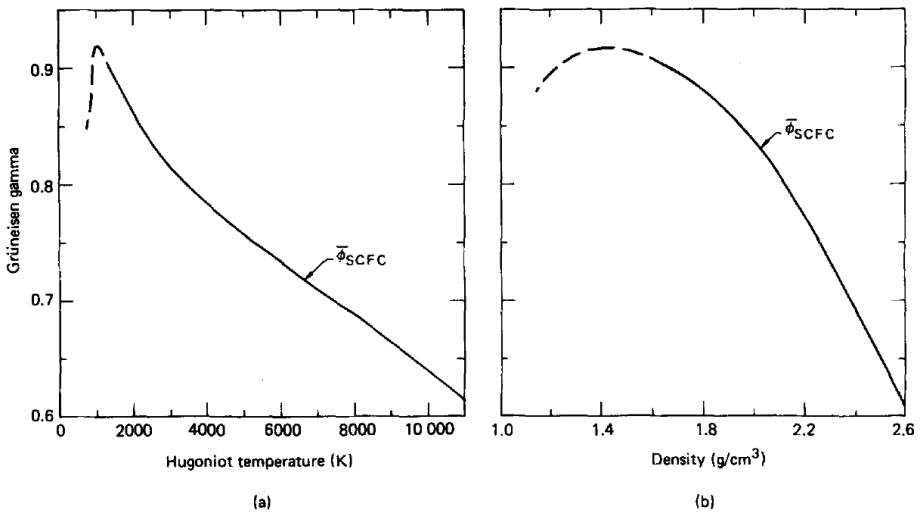

Figure 7.10: *Ab initio* calculations of the variation of Γ with (a) temperature and (b) density on the Hugoniot, from Ree [1982]. The dashed portions of the curves represent the low temperature region where complex interactions neglected in the calculations become important. The calculated values of Γ are significantly lower than those measured experimentally; this discrepancy was attributed to errors in the experiments.

represents the lower temperature region where the calculations become uncertain. This is the region of densities and temperatures of interest to the present work. The decrease in Γ at high pressures is attributed to an increase in the compressibility due to the collapse of the hydrogen bonding structure of water. In contrast Nellis [2008] suggests this behaviour indicates that the energy is being absorbed internally as well as thermally. Nigmatulin and Bolotnova [2008] note that experiments suggest Γ in water must have a temperature dependence, and explicity included this in their construction of an equation of state for water and steam. Their calculation of Γ as a function of volume at different temperatures is reproduced in Figure 7.11.

Whilst not directly comparable to the form for Γ given by Gurtman et al. [1971] or the calculations made by Ree [1982] (Figure 7.10), comparison can be made to the values of Γ deduced from isothermal compression data discussed in Chapter 5, some of which are shown in Figure 7.8 above. The calculated values of Γ shown in Figure 7.11 do not agree with those determined from isothermal compression, both in terms of their value and the variation with volume. The calculations made by Nigmatulin and Bolotnova [2008] appear

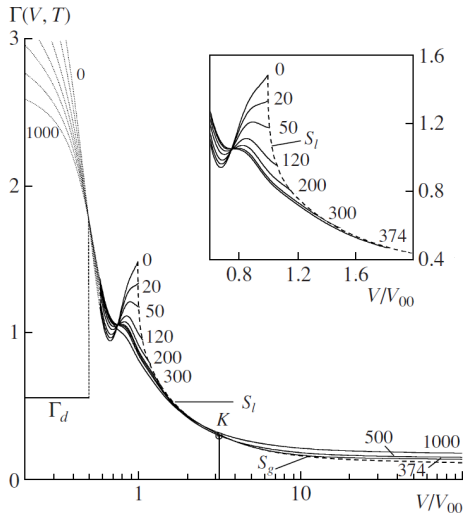

Figure 7.11: Variation of Γ with volume at different temperatures, from Nigmatulin and Bolotnova [2008]. In the figure, V_{00} corresponds to the initial volume at room temperature, which has been referred to as v_0 elsewhere in this thesis. Whilst not directly comparable to the preceeding results, and the calculations given by Ree [1982], it is reasonably clear that the functional form given by Nigmatulin and Bolotnova [2008] does not match well with the experimentally determined values of Γ. For example, at all temperatures, the figure shows Γ increasing with decreasing volume below $V/V_{00} \approx 0.6$, whereas the experiments show a decrease in Γ at these volumes.

also to contradict the calculations made by Ree [1982]. It is unclear what the origin of this discrepancy is, and no explanation is offered in the paper. In a subsequent paper [Nigmatulin and Bolotnova, 2011], the authors offer a form for Γ that neglects any temperature dependence, arguing that it applies to states where the anomalous behaviour of water is unimportant. It is not clear what pressure and temperature range this applies to, although it is implied this is the gaseous phase. In general, recent modeling efforts [*e.g.*, French and Redmer, 2009; Goldman et al., 2009a,b] have been concerned with the temperatures and pressures that are relevant to water in planetary interiors, which are much higher than those dealt with in the present thesis, and the temperature dependence of Γ is generally neglected.

The heat capacity of water at constant volume, C_v, is often, for simplicity, assumed to be constant Dolan [2003]; Gurtman et al. [1971]. This assumption can be justified by arguing that effective Debye temperature of water is

lower than the actual temperature. Kor and Tripathi [1974] applied a quasi-crystaline model to water, assuming that over short time-scales, the molecules behaved in a similar way to those in solids, and calculated effective Debye temperatures as a function of both temperature and pressure. From their calculations, it was concluded that the Debye temperature remained constant, at around $170\,\mathrm{K}$, as the temperature was varied at ambient pressure. However, it was found that the Debye temperature increases rapidly with pressure at constant temperature, rising to over $400\,\mathrm{K}$ at a pressure of $0.3\,\mathrm{GPa}$ and temperature of $30\,^{\circ}\mathrm{C}$. It seems likely, therefore, that the Debye temperature will be close to the Hugoniot temperature and the approximation that the heat capacity is constant may not be valid. Ree [1982] calculated the variation of the heat capacity along the Hugoniot of water, noting it decreased from a maximum of around $11.5R$ to a near-constant $7.6R$, as is shown in Figure 7.12.

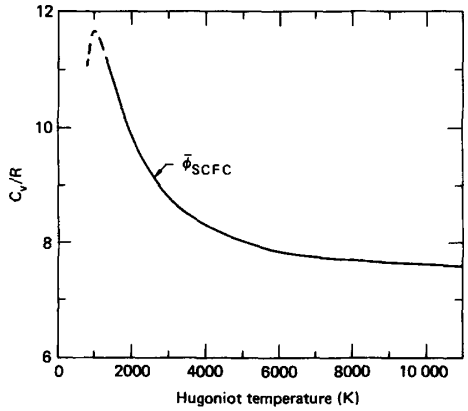

Figure 7.12: Variation of C_v/R as a function of Hugoniot temperature in water, from Ree [1982]. The dashed portion of the curve represents the low temperature region where complex interactions neglected in the calculations become important. Significant variation of the heat capacity with temperature is predicted.

Ree [1982] comments that the maximum greatly exceeds the value of $6.94R$ that would be expected from summing the ideal-gas translation, rotational, and bond vibration contributions ($3.94R$) and the potential energy contributions from translational and librational modes for each molecule. The high temperature value is close to the ideal gas contribution of $6R$ and the the potential energy contribution of $1.5R$. The variation is attributed to the complex interplay of the increasing density and temperature along the Hugoniot - the

shock compression tends to increase C_v through enhanced librational motion, whereas the shock temperature tends to promote bond vibration (increasing C_v) and molecular rotation over libration (decreasing C_v). Ree [1982] suggests in light of these calculations, the constant-C_v model of Gurtman et al. [1971] may require modification; no explanation as to the apparent agreement between that model and experimental measurements of temperature is offered. Nigmatulin and Bolotnova [2008] also calculated the variation in heat capacity; these calculations as functions of volume at different temperatures and temperature at different volumes are shown in Figure 7.13. As with the Γ calculations discussed above, a direct comparison between Figure 7.13 and Figure 7.12 is not possible; however, it should be noted that values of C_v calculated by Nigmatulin and Bolotnova [2008] are wildly different from those calculated by Ree [1982], which themselves differ markedly from the constant values used by Gurtman et al. [1971] and Dolan [2003].

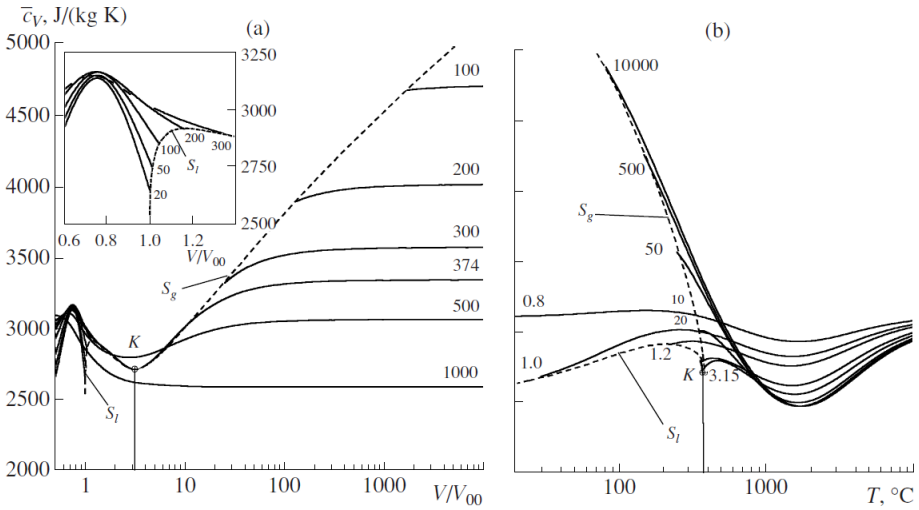

Figure 7.13: Variation of heat capacity with (a) relative volume at different temperatures and (b) temperature at different relative volumes, from Nigmatulin and Bolotnova [2008]. Whilst not directly comparable to calculations shown in Figure 7.12, it is reasonably clear that the calculations made by Ree [1982] and by Nigmatulin and Bolotnova [2008] give fundamentally different forms and values for the heat capacity as a function of both volume and temperature.

The picture, then, which emerges from these modeling results is an unclear one. The variation, value, and even functional dependencies of Γ are still not

agreed upon; the same is true of the heat capacity C_v. It is puzzling that the molecular models suggest a constant value for C_v is inappropriate and yet empirical models, such as that proposed by Gurtman et al. [1971] are able to accurately calculate shock temperatures in water using a constant value for C_v determined from experiments. There are no comparable calculations in the open literature for ammonium nitrate solutions. In considering the softening of the Hugoniot that occurs when a material is pre-heated, it has been experimentally demonstrated that a solution of $50\,\%$ ammonium nitrate behaves in a similar way to water, with both undergoing significant softening on pre-heating. This is taken as evidence that the behaviour of the solution is dominated by the behaviour of water. In both the solution and in water, it has been shown that pre-heating results in an increase in the value of Γ, demonstrating that the standard assumption that Γ is a function of volume alone, is invalid over the stress range investigated. The present results are believed to be the first test of this assumption in shock-compressed liquids at low stresses. It follows from this result that the Mie-Grüneisen equation of state is a poor model for the thermal pressure in water and ammonium nitrate solutions at low stresses and, therefore, further work on the theoretical description of these materials is required.

7.4 Summary

- Measured Hugoniots in water and ammonium nitrate for different initial temperatures indicate a significant softening (reduction in impedance) with increasing temperature.
- Calculations using the Mie-Grüneisen equation of state are unable to correctly account for this softening.
- From the literature, it is believed that water (and hence the solutions) undergo significant structural changes affecting their behaviour as temperature increases. These changes would lead to a marked softening, and it is believed this may explain the observed behaviour.
- It is arguable that upon heating, water and ammonium nitrate solutions change sufficiently as to effectively be different materials.
- The variation of Γ with temperature, which has been observed experimentally, is largely ignored in the literature.

- The present work suggest that the variation of Γ with temperature is significant under shock loading.
- There is no widely accepted method for incorporating a temperature-dependent Γ into equations of state, as it invalidates the standard form of the Mie-Grüneisen equation of state.
- Water is a pathologically complex material that has not proved amenable to modeling efforts. Published models of water show different, and contradictory, variations in Γ and C_v.
- In lieu of more concrete modeling on the behaviour of C_v the simplest approximation is to assume that it remains constant as a function of pressure and temperature.
- Most modeling efforts are concerned with the pressures and temperatures that may exist in planetary interiors, and thus are not relevant to the present work.
- A surprisingly small amount is known for certain about the behaviour of water and aqueous solutions under shock compression, and it is believed that the present work represents the first published test of many of the commonly used assumptions.

7.5 Bibliography

O. L. Anderson. The Grüneisen ratio for the last 30 years. *Geophysical Journal International*, 143(2):279–294, 2000.

D. J. Bradley and K. S. Pitzer. Thermodynamics of electrolytes. 12. Dielectric properties of water and Debye-Hückel parameters to 350°C and 1 kbar. *The Journal of Physical Chemistry*, 83(12):1599–1603, 1979.

J. Chan. Personal communication, 2011. Orica Mining Services.

C. Dai, H. Tan, J. Hu, Y. Yu, and J. Zheng. Hugoniot evaluation of the preheated metal from its principal hugoniot. *Journal of Applied Physics*, 99(5): 056102, 2006.

D. H. Dolan. *Time dependent freezing of water under multiple shock wave compression*. PhD thesis, Washington State University, 2003.

M. French and R. Redmer. Estimating the quantum effects from molecular vibrations of water under high pressures and temperatures. *Journal of Physics: Condensed Matter*, 21(37):375101, 2009.

S. Galbraith. *The responses of potassium chloride, ammonium nitrate solutions, and emulsion explosives to plate impact loading*. PhD thesis, University of Cambridge, 1997.

N. Goldman, E. Reed, I.-F. W. Kuo, L. E. Fried, C. J. Mundy, and A. Curioni. Ab initio simulation of the equation of state and kinetics of shocked water. *The Journal of Chemical Physics*, 130(12):124517, 2009a.

N. Goldman, E. J. Reed, and L. E. Fried. Quantum mechanical corrections to simulated shock hugoniot temperatures. *The Journal of Chemical Physics*, 131 (20):204103, 2009b.

G. A. Gurtman, J. W. Kirsch, and C. R. Hastings. Analytical equation of state for water compressed to 300 kbar. *Journal of Applied Physics*, 42(2):851–857, 1971.

W. B. Holzapfel. Effect of pressure and temperature on the conductivity and ionic dissociation of water up to 100 kbar and 1000[degree]c. *The Journal of Chemical Physics*, 50(10):4424–4428, 1969.

J. Jonas, T. DeFries, and D. J. Wilbur. Molecular motions in compressed liquid water. *The Journal of Chemical Physics*, 65(2):582–588, 1976.

L. Knopoff and J. N. Shapiro. Comments on the interrelationships between Grüneisen's parameter and shock and isothermal equations of state. *Journal of Geophysical Research*, 74(6):1439–1450, 1969.

S. K. Kor and N. D. Tripathi. Temperature and pressure dependence of effective debye temperature in associated liquids based on quasi crystalline model. *Journal of the Physical Society of Japan*, 36(2):552–554, 1974.

R. G. McQueen. Shock-waves in condensed media: Their properties and the equation of state of materials derived from them. In *Enrico Fermi summer course CX11: nuclear collisions from the mean field into the fragmentation regime*, 1989.

W. J. Nellis. Water at high dynamic pressures and temperatures. *Zeitschrift für Naturforschung*, 63b(6):605–607, 2008.

R. Nigmatulin and R. Bolotnova. Wide-range equation of state for water and steam: Calculation results. *High Temperature*, 46:325–336, 2008.

R. Nigmatulin and R. Bolotnova. Wide-range equation of state for water and steam: simplified form. *High Temperature*, 49:303–306, 2011.

P. Postorino, R. H. Tromp, M.-A. Ricci, A. K. Soper, and G. W. Neilson. The interatomic structure of water at supercritical temperatures. *Nature*, 366: 668–670, 1993.

F. Ree. Molecular interaction of dense water at high temperature. *The Journal of Chemical Physics*, 76(12):6287–6302, 1982.

R. H. Tromp, P. Postorino, G. W. Neilson, M. A. Ricci, and A. K. Soper. Neutron diffraction studies of H_2O/D_2O at supercritical temperatures. A direct determination of $g_{HH}(r)$, $g_{OH}(r)$, and $g_{OO}(r)$. *The Journal of Chemical Physics*, 101(7):6210–6215, 1994.

E. Washburn, editor. *International Critical Tables of Numerical Data, Physics, Chemistry and Technology*. Knovel, 1st electronic edition, 2003.

CHAPTER 8

CONCLUSIONS AND FUTURE WORK

The aim of this thesis has to been to further develop an understanding of the behaviour at high dynamic pressures of materials relevant to the mining industry. The specific materials considered have been aqueous solutions of ammonium nitrate; such solutions are employed as the oxidising component of the 'emulsion' explosives that are widely used in the industry.

The experiments reported in this thesis were performed on the Cavendish's Plate Impact Facility, a versatile experimental apparatus constructed sixteen years ago [Bourne et al., 1995], which has not been significantly altered or improved upon. Worn parts, particularly of the alignment mechanism, were rebuilt at the author's instigation. Minimisation of the impact tilt in such an apparatus has been identified as a key requirement in ensuring high fidelity data are obtained. Measurements of impact tilt on the Cavendish's Plate Impact Facility have not previously been reported. As such, a technique for characterising impact tilt, using optic fibres, was developed. Using this technique, impact tilt was measured in a number of experiments, and found to be of order $10\,\mathrm{mRad}$. This has subsequently been reduced to less than $2\,\mathrm{mRad}$, chiefly through the design and use of a new projectile.

A survey of the literature indicated that a number of experimental techniques have been proposed to measure the temperature rise associated with shock compression. A brief investigation of the use of thin-foil thermistors demonstrated that their response is chiefly limited by their thickness. The technical challenges in making ultra-thin foils prevented their use in the present investigation. Other methods, including Raman spectroscopy, show promise for future research, but represent a significant capital investment beyond the scope of this investigation.

Accurate shock temperatures may be calculated from a thermodynamically consistent equation of state. Historically, such equations have not been used, with simplified analytic expressions being used instead. The simplest such equation, which has been applied widely in the shock compression field, is the Mie-Grüneisen equation of state, which relates the energy in a given state to the energy on some reference curve (typically the Hugoniot) through

the Grüneisen parameter, Γ. A 'Mie-Grüneisen' material is one in which Γ is assumed to be a function of volume alone. If this parameter can be determined then, under assumptions regarding the heat capacity of the material, shock temperatures can in general be calculated to accuracies of a few percent.

To this end, it was necessary to develop an experimental configuration and technique that would enable characterisation of the principal Hugoniot and equation of state of liquids under shock loading. The study of shocks in liquids presented several experimental challenges, as generating well-defined shocks in liquids of precise thickness is markedly more complex than doing the same in a solid sample. A cell was designed that would enable the measurement of the shock response of liquids. A number of unanticipated problems were encountered during the testing of the cell, requiring significant modifications to be made to the design. An iterative design process resulted in the cell employed in the present work. Shock velocities in the liquids were determined from measurement of the transit time through a known thickness. Embedded manganin gauges allowed accurate measurement of the Hugoniot and reshock stresses in shock compressed liquids. The measured Hugoniot states were fitted by linear shock velocity–particle velocity relations and, extrapolated to higher compressions. Thus, the reshock stresses enabled parameterisation of the Mie-Grüneisen equation of state. The validity and consistency of the cell and analysis techniques were demonstrated by studying the behaviour of water compressed from room temperature, which has previously been reported in the literature [Gurtman et al., 1971].

A series of experiments were then conducted on a number of liquids: water, at an initial temperature of $66 \pm 2\,^{\circ}\mathrm{C}$, a solution of $50\,\%$ ammonium nitrate by weight at initial temperatures of $14 \pm 1\,^{\circ}\mathrm{C}$ and $65 \pm 2\,^{\circ}\mathrm{C}$, and a solution of $80\,\%$ ammonium nitrate by weight at an initial temperature of $64 \pm 2\,^{\circ}\mathrm{C}$. Shock velocities of these materials were studied to a maximum particle velocity of around $1\,\mathrm{km\,s^{-1}}$, enabling determination of the Hugoniot. The reported Hugoniots show no evidence of phase changes or, in the ammonium nitrate solutions, shock-induced reaction, and have uncertainties in the intercept and slope of less than $5\,\%$. The Hugoniots were shown to lie close to each other in both shock velocity–particle velocity space and stress–particle velocity space. As might be expected, increasing the initial density of the liquid (*i.e.,* increasing the weight-percentage of ammonium nitrate), resulted in increased shock impedances. For this reason, the Hugoniot of the $50\,\%$ ammonium nitrate so-

lution at an initial temperature of $65 \pm 2\,^{\circ}\mathrm{C}$ lies below the Hugoniot for the same solution at an initial temperature of $14 \pm 1\,^{\circ}\mathrm{C}$. In water, the softening that occurs on heating exceeds greatly that which is predicted from the equation of state; from a review of the literature, it is believed that this softening is the result of structural changes in the liquid as it is heated.

Shock/reload experiments on water at an initial temperature of $66 \pm 2\,^{\circ}\mathrm{C}$ enabled the determination of the Grüneisen parameter, Γ, at specific volumes between 0.64 and $0.54\,\mathrm{cm^3\,g^{-1}}$. Combining these data with reported compressional isotherms [Grindley and Lind, 1971], a fifth-order polynomial was used to describe the volume dependence of Γ, as this is the lowest order polynomial which can correctly describe the isothermal compression data and dynamically measured values. Shock/reload experiments also enabled determination of Γ in the ammonium nitrate solutions. In water and the solution of $50\,\%$ ammonium nitrate by weight, a temperature dependence of Γ at constant volume was found. There have been some reports in the literature concering such a temperature varation [e.g. Knopoff and Shapiro, 1969], but such investigations have been generally neglected [e.g. McQueen, 1989]. There is no widely accepted method for incorporating a temperature-dependent Γ into equations of state, as it invalidates the standard form of the Mie-Grüneisen equation of state. There is no consensus in published models of the behaviour of water [e.g. Nigmatulin and Bolotnova, 2008, 2011; Ree, 1982] on the functional form or values of Γ that might expected, and most recent modeling efforts [e.g., French and Redmer, 2009; Goldman et al., 2009a,b] have been devoted to pressures in planetary interiors, which far exceed those relevant to this study.

Neglecting these concerns, and under the assumption that the heat capacity c_v is constant, and, for water, within $10\,\%$ of $3.2\,\mathrm{J\,g^{-1}\,K^{-1}}$ [Gurtman et al., 1971], temperatures on the Hugoniot, which exceeded $1000\,\mathrm{K}$ at $8\,\mathrm{GPa}$, were calculated with an uncertainity of $10\,\%$. Temperatures were determined in the ammonium nitrate solutions, by assuming that c_v was constant and equal to the zero pressure value, and combining the dynamic data with the calculated zero pressure value of Γ [Chan, 2011]. The calculated temperatures, which have uncertainties of $10\,\%$ are valid to Lagrangian compressions of 0.25 (equivalent to stresses of approximately $4.5\,\mathrm{GPa}$). It was found that increasing the initial temperature for a given concentration resulted in higher temperatures on shock loading, the difference in shock temperature being approximately equal to difference in initial temperatures. At the same initial temperature, higher concentrations yielded higher shock temperatures. The

lowest calculated temperature rise, of around $100\,\mathrm{K}$ at a compression of 0.25, was found for the $50\,\%$ ammonium nitrate by weight at initial temperatures of $14 \pm 1\,^{\circ}\mathrm{C}$. A temperature rise of $250\,\mathrm{K}$ at the same level of compression was calculated for the $80\,\%$ ammonium nitrate by weight at an initial temperature of $64 \pm 2\,^{\circ}\mathrm{C}$. Even though these calculations must be considered only as approximations, it is believed that these results represent the first calculations of shock temperatures in ammonium nitrate solutions in the open literature. The assumption of constant c_v is justified if the Debye temperature is significantly lower than the temperature of the material. There is some suggestion [Kor and Tripathi, 1974] that this may not be the case as water is compressed. Again, however, literature models [e.g. Nigmatulin and Bolotnova, 2008; Ree, 1982] present a confused and contradictory picture.

8.1 Future work

In order to reduce uncertainties in the calculated temperatures, four areas must be addressed in future work. Firstly, the measurement of the principal Hugoniots should be extended to higher particle velocities. This would reduce the need to extrapolate the Hugoniot beyond its measured region when analysing shock/reload experiments, and would reduce the uncertainties in the intercept and slope of the fitted linear shock velocity–particle velocity relationship. Such measurements are not possible with the present experimental facilities. The highest particle velocities in the liquid were obtained by using copper flyer plates at near the maximum velocity of the Cavendish's Plate Impact Facility. No significant increase in velocity is possible, as the wrap-around breech design imposes certain constraints on the wall thickness, and hence mass, of the sabot. Some increase in particle velocity could be achieved through the use of higher-impedance flyer materials, such as tungsten or tantalum. A well-characterised stock of these materials is not available at the present time, and characterising the shock response of either of these materials to a suitable degree of accuracy is itself a significant experimental programme. To achieve particle velocities that would cover the full compression range of the reshock measurements, experiments would need to be conducted at around twice the maximum particle velocities reported in the present work. Such particle velocities would require projectile velocities that are not physically possible with a single-stage gas gun, requiring instead a two-stage gas gun, powder gun, or explosive plane-wave generator [Asay and Shahinpoor,

1993, §3.2 – §3.4].

Accurate measurement of the compressional isotherms of the ammonium nitrate solutions would provide a stronger constraint on the behavior of Γ at volumes close to the initial specific volume. To be of use, measurements of the specific volume to pressures below $1\,\mathrm{GPa}$, with an accuracy of $0.01\,\%$, comparable to the isotherms reported by Grindley and Lind [1971] for water, would be required. This would allow for an improved fit describing the volume-dependence of Γ to be determined by constraining the behaviour at low compressions, thus increasing the accuracy of the calculated temperatures.

The calculations of shock temperature have assumed that c_v is constant and, in the ammonium nitrate solutions, equal to the zero-pressure value. An accurate experimental technique for measuring c_v in shock experiments has not been reported in the open literature. Some success has been had in applying density functional theory to the calculation of heat capacities during compression. Ree [1982] calculated c_v along the Hugoniot of water, but report that the calculations are only approximate for temperatures near $1000\,\mathrm{K}$, yielding uncertainties larger than those reported by Gurtman et al. [1971]. More recent calculations for water [French and Redmer, 2009; Goldman et al., 2009b] do not significantly improve on these uncertainties in the pressure/temperature region relevant to the present work. More accurate calculations of the heat capacity of shock compressed minerals have been reported [de Koker, 2010; de Koker et al., 2008], although the applicability of the calculations to the temperatures and pressures in the liquids studied in the present work is not clear. Future experimental work should also attempt the direct measurement of shock temperature in these liquids, which could then be used to improve the calculations by constraining the value of c_v.

Finally, it is evident from the present work that the behaviour of water at low stresses is poorly understood from a theoretical viewpoint, as published models give contradictory results. The application of the Mie-Grüneisen equation to describe the thermal pressure appears to be invalid, as there is a strong variation of Γ with temperature at constant volume. Therefore, it must be concluded that a better model of thermal pressure is needed; the results presented in this thesis provide a constraint on the behaviour of such a model and thus act as a useful constraint on future developments. The mining industry must, therefore, in developing the desired holistic models of the blasting process, attempt to capture the underlying physical processes that occur, at a level that is not currently considered.

8.2 Bibliography

J. R. Asay and M. Shahinpoor, editors. *High-pressure shock compression of solids*. Springer, 1993.

N. K. Bourne, Z. Rosenberg, D. J. Johnson, J. E. Field, A. E. Timbs, and R. P. Flaxman. Design and construction of the UK plate impact facility. *Measurement Science and Technology*, 6(10):1462–1470, 1995.

J. Chan. Personal communication, 2011. Orica Mining Services.

N. de Koker. Structure, thermodynamics, and diffusion in $CaAl_2Si_2O_8$ liquid from first-principles molecular dynamics. *Geochimica et Cosmochimica Acta*, 74(19):5657–5671, 2010.

N. de Koker, L. Stixrude, and B. B. Karki. Thermodynamics, structure, dynamics, and freezing of Mg_2SiO_4 liquid at high pressure. *Geochimica et Cosmochimica Acta*, 72(5):1427–1441, 2008.

M. French and R. Redmer. Estimating the quantum effects from molecular vibrations of water under high pressures and temperatures. *Journal of Physics: Condensed Matter*, 21(37):375101, 2009.

N. Goldman, E. Reed, I.-F. W. Kuo, L. E. Fried, C. J. Mundy, and A. Curioni. Ab initio simulation of the equation of state and kinetics of shocked water. *The Journal of Chemical Physics*, 130(12):124517, 2009a.

N. Goldman, E. J. Reed, and L. E. Fried. Quantum mechanical corrections to simulated shock hugoniot temperatures. *The Journal of Chemical Physics*, 131 (20):204103, 2009b.

T. Grindley and J. E. Lind. PVT properties of water and mercury. *The Journal of Chemical Physics*, 54(9):3983–3989, 1971.

G. A. Gurtman, J. W. Kirsch, and C. R. Hastings. Analytical equation of state for water compressed to 300 kbar. *Journal of Applied Physics*, 42(2):851–857, 1971.

L. Knopoff and J. N. Shapiro. Comments on the interrelationships between Grüneisen's parameter and shock and isothermal equations of state. *Journal of Geophysical Research*, 74(6):1439–1450, 1969.

S. K. Kor and N. D. Tripathi. Temperature and pressure dependence of effective debye temperature in associated liquids based on quasi crystalline model. *Journal of the Physical Society of Japan*, 36(2):552–554, 1974.

R. G. McQueen. Shock-waves in condensed media: Their properties and the equation of state of materials derived from them. In *Enrico Fermi summer course CX11: nuclear collisions from the mean field into the fragmentation regime*, 1989.

R. Nigmatulin and R. Bolotnova. Wide-range equation of state for water and steam: Calculation results. *High Temperature*, 46:325–336, 2008.

R. Nigmatulin and R. Bolotnova. Wide-range equation of state for water and steam: simplified form. *High Temperature*, 49:303–306, 2011.

F. Ree. Molecular interaction of dense water at high temperature. *The Journal of Chemical Physics*, 76(12):6287–6302, 1982.

APPENDIX A

SELECTED GAUGE TRACES

In Chapter 6 it was noted that in some experiments, the stress in the reshock state was not measured, due to failure of the rear gauge. These rear gauge traces are presented in this appendix. Figure A.1 shows the front and rear gauge traces from experiment E100927A, where the plateau associated with the stress in the reshock state is clearly visible. The trace is typical of those used in the analyses in Chapters 5, 6, and 7. The front gauge trace shows two plateaus, corresponding to first the Hugoniot stress in PMMA and then to the Hugoniot stress in the test liquid. The rear trace rises to the reload stress of the test liquid. The reverberation evident on the rear gauge rise is due to the impedance mismatch presented by the Teflon used to insulate the gauge. As noted in Chapter 4, this reverberation has no significant effect on the measured reload stress and can be neglected. Comparing the following traces to Figure A.1, the failure of the rear gauge is evident.

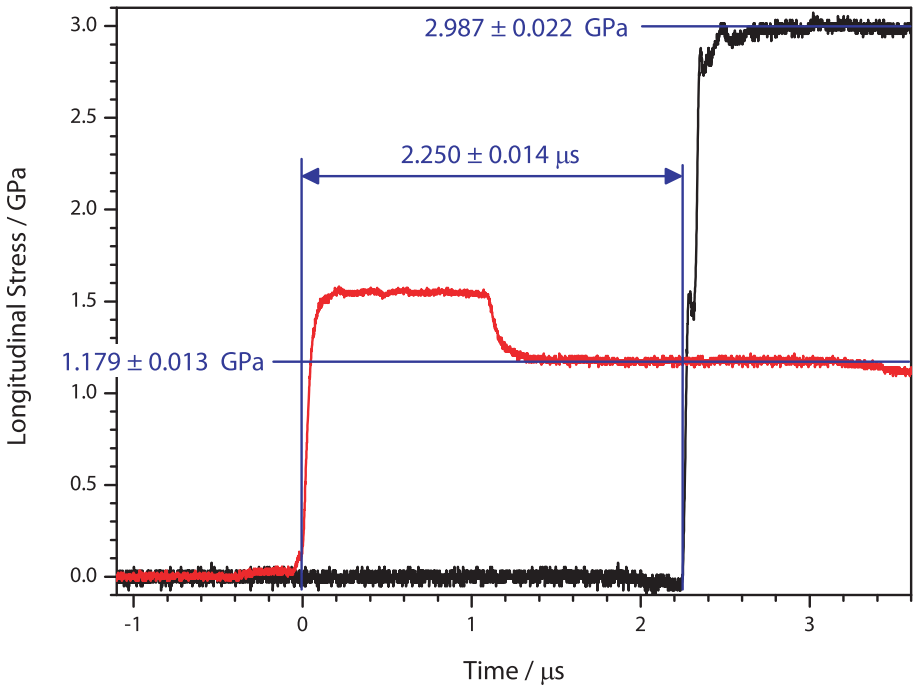

Figure A.1: Front (red) and rear (black) stress gauge traces from experiment E100927A. A liquid cell, containing water at $18 \pm 2\,^{\circ}\mathrm{C}$, was impacted by a PMMA flyer at $0.787 \pm 0.008\,\mathrm{km\,s^{-1}}$. The front gauge is first shocked to the Hugoniot state of PMMA, before being released to the Hugoniot state of water at a stress of $1.179 \pm 0.013\,\mathrm{GPa}$; the shock reaches the rear gauge $2.250 \pm 0.014\,\mu\mathrm{s}$ after first arriving at the front gauge. The stress in the rear gauge, corresponding to the reload state of water, is $2.987 \pm 0.022\,\mathrm{GPa}$.

A.1 $50\,\%$ ammonium nitrate, $14 \pm 1\,^{\circ}\mathrm{C}$

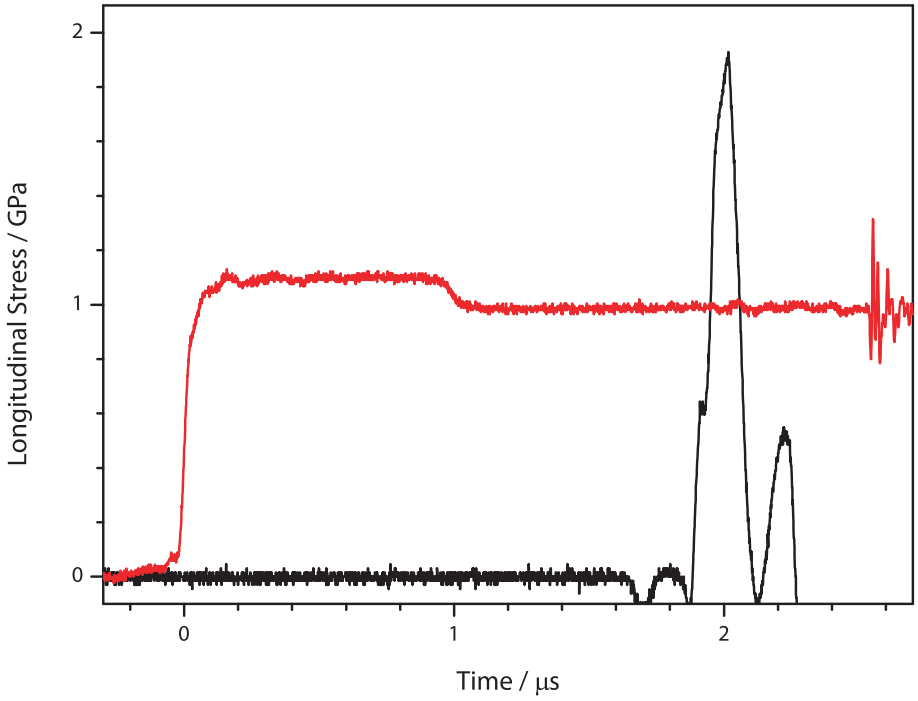

Figure A.2: Front (red) and rear (black) stress gauge traces from experiment E101118A. A liquid cell, containing $50\,\%$ ammonium nitrate at $14 \pm 1\,^{\circ}\mathrm{C}$, was impacted by a PMMA flyer at $0.591 \pm 0.006\,\mathrm{km\,s^{-1}}$. The failure of the rear gauge at around $2\,\mu\mathrm{s}$ is evident. Electrical noise associated with this failure appears on the front gauge trace at around $2.5\,\mu\mathrm{s}$.

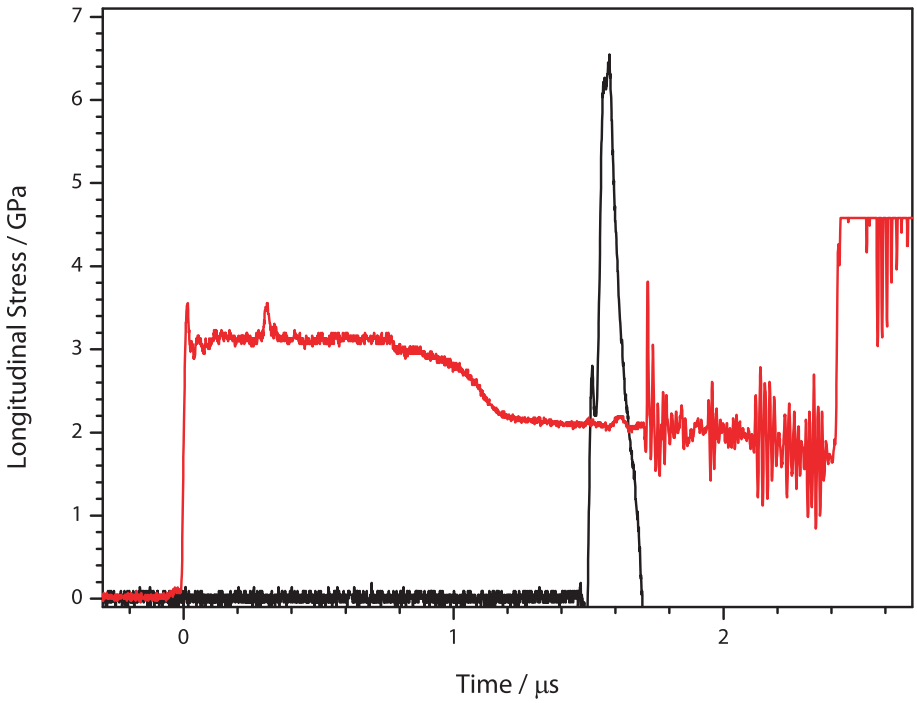

Figure A.3: Front (red) and rear (black) stress gauge traces from experiment E101130A. A liquid cell, containing $50\,\%$ ammonium nitrate at $14\pm1\,^{\circ}\mathrm{C}$, was impacted by a copper flyer at $0.799 \pm 0.008\,\mathrm{km\,s^{-1}}$. The failure of the rear gauge at around $1.5\,\mu\mathrm{s}$ is evident. Electrical noise associated with this failure appears on the front gauge trace at around $1.7\,\mu\mathrm{s}$.

A.2 $50\,\%$ ammonium nitrate, $65 \pm 2\,^{\circ}\mathrm{C}$

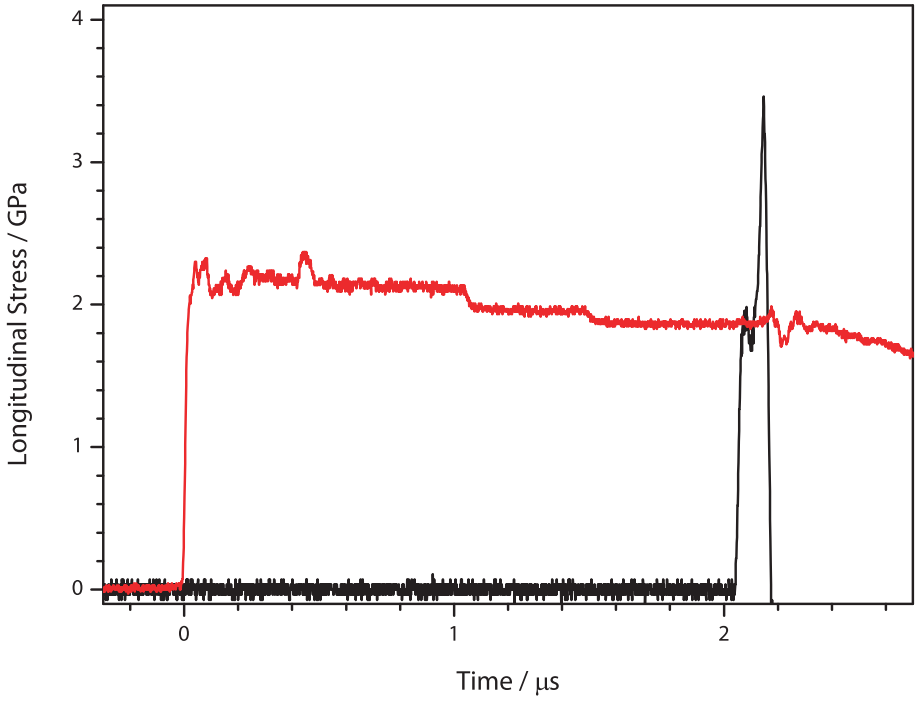

Figure A.4: Front (red) and rear (black) stress gauge traces from experiment E110305A. A liquid cell, containing $50\,\%$ ammonium nitrate at $65 \pm 2\,^{\circ}\mathrm{C}$, was impacted by a PMMA flyer at $0.592 \pm 0.006\,\mathrm{km\,s^{-1}}$. The failure of the rear gauge at around $2.1\,\mu\mathrm{s}$ is evident.

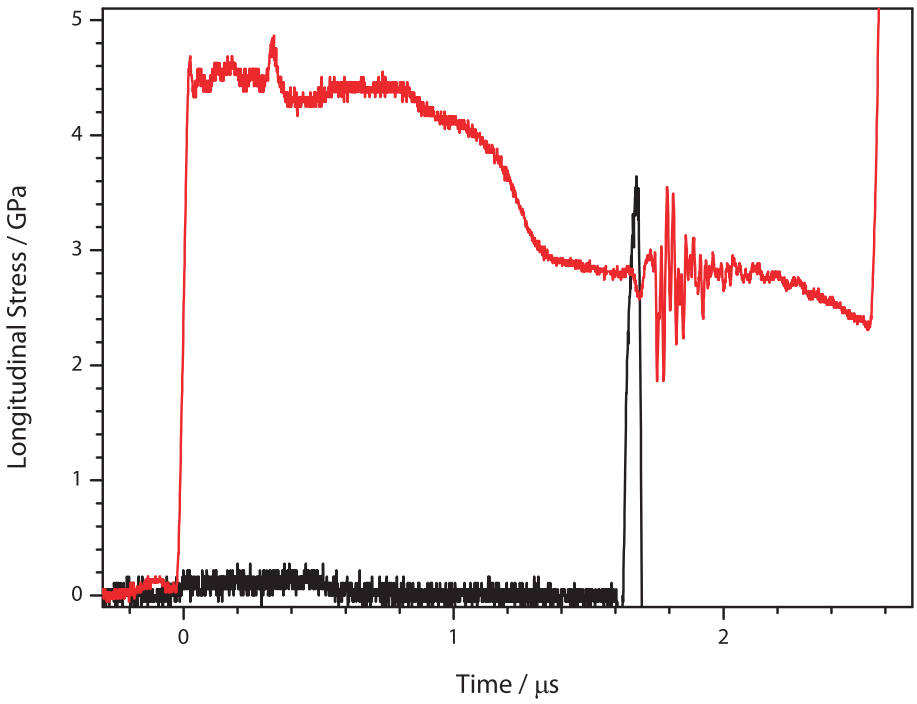

Figure A.5: Front (red) and rear (black) stress gauge traces from experiment E110308B. A liquid cell, containing $50\,\%$ ammonium nitrate at $65 \pm 2\,^{\circ}\mathrm{C}$, was impacted by a PMMA flyer at $1.014 \pm 0.010\,\mathrm{km\,s^{-1}}$. The failure of the rear gauge at around $1.7\,\mu\mathrm{s}$ is evident. Electrical noise associated with this failure appears on the front gauge trace at around $1.8\,\mu\mathrm{s}$

A.3 $80\,\%$ ammonium nitrate, $64 \pm 2\,^{\circ}\mathrm{C}$

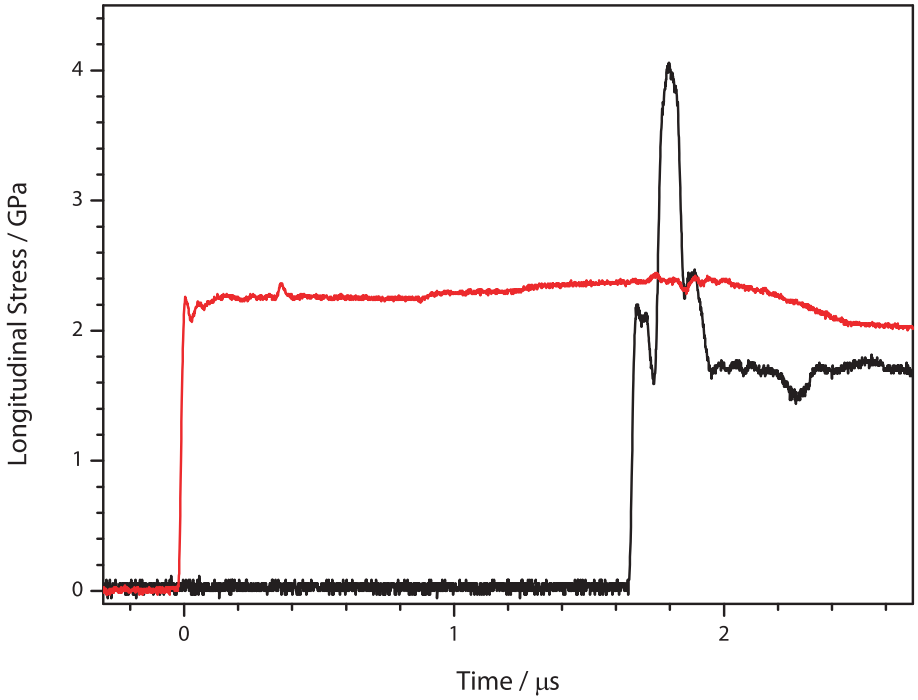

Figure A.6: Front (red) and rear (black) stress gauge traces from experiment E110228B. A liquid cell, containing $80\,\%$ ammonium nitrate at $65 \pm 2\,^{\circ}\mathrm{C}$, was impacted by a PMMA flyer at $0.598 \pm 0.006\,\mathrm{km\,s^{-1}}$. The failure of the rear gauge at around $1.8\,\mu\mathrm{s}$ is evident. It is not clear why the rear gauge seems to then equilibrate at around $1.6\,\mathrm{GPa}$, although this may indicate mechanical failure (*e.g.*, the gauge de-bonding) rather than the electrical failure seen in the other figures.